Characterisation and Probability of Detection Analysis of Rolling Contact Fatigue Cracks in Rails Using Eddy Current Pulsed Thermography

Junzhen Zhu

B.Sc., M.Sc.

A thesis submitted for the degree of

Doctor of Philosophy

School of Engineering

Newcastle University

April 2020

This page is intentionally left blank.

CERTIFICATE OF ORIGINALITY

This is to certify that the thesis entitled ‘Characterisation and Probability of Detection Analysis of Rolling Contact Fatigue Cracks in Rails Using Eddy Current Pulsed Thermography’ and the work presented has been generated by me as own original research. I confirm that:

- This work has been done for a research degree at Newcastle University;
- Where I have cited from the work of others, the source is always given;
- I have acknowledged all main sources of help;
- Parts of this work have been published and these publications are listed in the List of Publication pages. All the relevant papers are properly cited in the thesis.

…….(Signed)

2 April 2020.(Date)

This page is intentionally left blank.

Abstract

With transportation volumes continuously increasing, railway networks are now facing problems of greater axle loads and increasing vehicle speeds. The most direct consequence is the initiation of rolling contact fatigue (RCF) defects in rails, which have become safety issues for all types of railway systems and received more attention due to lack of timely examination and management. Among different RCF defects, the RCF crack probably presents the biggest hazard in rails. Detection and characterisation of RCF cracks aim to provide detailed guidelines for safety management and preventative grinding. Unfortunately, current nondestructive testing and evaluation techniques are still facing several challenges and research gaps. One outstanding challenge is the characterisation of RCF cracks under their complex geometries and clustered distributions. One major research gap is how to evaluate the probabilistic performance in crack characterisation via a proper framework.

By combining the advantages of eddy current pulse excitation and infrared thermography, this thesis proposes the use of eddy current pulsed thermography (ECPT) technique to address the detection and characterisation of RCF cracks in rails. To quantitatively investigate the ECPT's performance in crack characterisation, a performance evaluation framework based on probability of detection (POD) analysis is proposed.

The major contributions of the thesis are summarised as follows: (1) implementations of three-dimensional FEM models and a lab-based ECPT system for investigating the characterisation of RCF cracks under clustered distributions and geometric influences; (2) temporal/spatial-thermal-feature-based ECPT for angular slots and RCF cracks detection and characterisation; (3) investigations into the capability and the performance of ECPT for characterising angular slots and natural RCF cracks via a POD analysis framework.

The thesis concludes that the proposed feature-based ECPT system can characterise RCF cracks in both light and moderate stages. Based on feature comparison and POD evaluation, tempo-spatial-based patterns are better fits for pocket length characterisation. Temporal domain-based features show better performances for inclination angle characterisation. A spatial domain-based feature, SS_T, can characterise vertical depths with reasonable POD values. One tempo-spatial-based pattern at the early heating stage, $I_{ET\text{-}PCA}$, gives the best performance for characterising surface lengths. Still, several issues need to be further investigated in future work, such as feature selection for crack characterisation, three-dimensional reconstruction of RCF cracks, model-assisted POD frameworks for improving the effectiveness of POD analysis with a limited number of physical specimens.

Acknowledgements

Firstly, I would like to kindly express my sincere appreciation to my supervisors, Professor Gui Yun Tian and Dr Mohsen Naqvi for the continuous guidance and support of my PhD study. Professor Gui Yun Tian, who leads me into the electromagnetic world and insightfully guides me throughout all three years. He devotes loads of precious time to encouraging me to discover and maximise own strengths. Without his consistent support, the completion of my PhD study would not have been possible.

Thanks also go to all the group members, Dr Yunlai Gao, Dr Kongjing Li, Dr Ruslee Sutthaweekul, Dr Chaoqing Tang, Mr Xiaotian Chen, Mr Yachao Ran, Mr Adi Marindra, and Mr Qiuji Yi. Also, thanks to research colleagues, Mr Sergey Gartsev from Fraunhofer-IKTS and Mr Abdoulaye Ba from IREENA. I am grateful for the suggestion and help from all the academics as follows, Professor Fuzhou Feng, Professor Jianbo Wu, Dr Zijun Wang, Professor Feng Liu, Dr Song Ding, Professor Jie Zeng, Dr. Wenbo Duan, Professor Helena Maria Geirinhas Ramos, Professor Hongjun Wang, and Professor Yifei Gao. I extend my appreciation to all the staff and technicians, especially Mr Paul Killan, Mr John Smith and Mr Samuel Burn, from Newcastle University for their continuous support.

Special thanks go to Professor Philip John Withers (FRS, FREng) and Ms Julia Behnsen from the University of Manchester for their advice and support of specimen scanning and following-up discussions. I acknowledge the Henry Royce Institute for enabling access to the Henry Moseley X-ray Imaging Facility to obtain the X-ray computed tomography data. I would like to express thanks to Dr Ding Wang from Northumbria University for his support of optical microscopy images in this work.

Ultimately, I voice a special note of gratitude to my family. Their love, encouragement and support have been far greater than I can now express in words.

List of Publications

Journal Papers

1. **J. Zhu**, P.J. Withers, J. Wu, F. Liu, G.Y. Tian, and Q. Yi, "Characterization of Rolling Contact Fatigue Cracks in Rails by Eddy Current Pulsed Thermography," *IEEE Transactions on Industrial Informatics*. (major revision)

2. **J. Zhu**, G.Y. Tian, Q. Min, and J. Wu, "Comparison Study of Different Features for Pocket Length Quantification of Angular Defects Using Eddy Current Pulsed Thermography," *IEEE Transactions on Instrumentation and Measurement*, vol. 68, pp. 1373-1381, 2019.

3. **J. Zhu**, Q. Min, J. Wu, and G.Y. Tian, "Probability of detection for eddy current pulsed thermography of angular defect quantification," *IEEE Transactions on Industrial Informatics*, vol. 14, pp. 5658-5666, 2018.

4. F. Liu, **J. Zhu** (corresponding author), G.Y. Tian, C. Ulianov, and Z. Wang, "Investigations for inclination angle characterization of angular defects using eddy current pulsed thermography," *Infrared Physics & Technology*, vol. 100, pp. 73-81, 2019.

5. J. Wu, **J. Zhu**, and G.Y. Tian, "Depth quantification of surface-breaking cracks in ferromagnetic materials using DC-biased magnetization based induction thermography," *Mechanical Systems and Signal Processing*, vol. 141, p. 106719, 2020.

6. J. Wu, **J. Zhu**, H. Xia, C. Liu, X. Huang, and G.Y. Tian, "DC-biased Magnetization Based Eddy Current Thermography for Subsurface Defect Detection," *IEEE Transactions on Industrial Informatics*, vol. 15, pp. 6252-6259, 2019.

7. Z. Wang, **J. Zhu**, G.Y. Tian, and F. Ciampa, "Comparative analysis of eddy current pulsed thermography and long pulse thermography for damage detection in metals and composites," *NDT&E International*, vol. 107, p. 102155, 2019.

8. J. Wu, **J. Zhu**, G.Y. Tian, H. Xia, X. Huang, and C. Tang, "Study of rotating magnet array-based motion-induced eddy current thermography," *IEEE Transactions on Magnetics*, vol. 54, pp. 1-5, 2018.

9. Q. Min, **J. Zhu**, J. Sun, and F. Feng, "Investigation of heat source reconstruction of thickness-through fatigue crack using lock-in vibrothermography," *Infrared Physics & Technology*, vol. 94, pp. 291-298, 2018.

Conference Papers

1. **J. Zhu**, J. Wu, G.Y. Tian, and Y. Gao, "Detection and Reconstruction of Rolling Contact Fatigue Cracks Using Eddy Current Pulsed Thermography," *in Proceeding of IEEE Far East NDT New Technology & Application Forum*, 2018, pp. 1-7. (First Award)

2. **J. Zhu**, Z. Wang, and G.Y. Tian, "Comparative Study of Eddy Current Pulsed and Long Pulse Optical Thermography for Defect Detection in Aluminium Plate," *in Proceeding of IEEE International Conference on Automation and Computing*, 2018, pp. 1-5.

3. **J. Zhu**, W. Duan, and G.Y. Tian, "Investigation of a new feature for angular defect quantification by eddy current pulsed thermography," *in Proceeding of IEEE International Instrumentation and Measurement Technology Conference*, 2018, pp. 1-6.

Table of Contents

Abbreviations

ACFM	Alternating Current Field Measurement
ECPT	Eddy Current Pulsed Thermography
ECT	Eddy Current Testing
EMAT	Electromagnetic Acoustic Transmission Technique
EOF	Empirical Orthogonal Function
FEM	Finite Element Modelling
FOV	Field of View
IRT	Infrared Thermography
LED	Light Emitting Diode
LT	Laser Thermography
MAPOD	Model Assisted Probability of Detection
MFL	Magnetic Flux Leakage
MT	Microwave Thermography
NDT&E	Nondestructive Testing and Evaluation
NETD	Noise Equivalent Temperature Difference
OT	Optical Thermography
PCA	Principal Component Analysis
POD	Probability of Detection
ROI	Region of Interest
RCF	Rolling Contact Fatigue
SNR	Signal Noise Ratio
VI	Visual Inspection

List of Figures

List of Tables

Chapter 1. Introduction

This chapter briefly provides the background to rolling contact fatigue (RCF) defect detection and the motivations for proposing eddy current pulsed thermography (ECPT) technique for the detection and characterisation of RCF cracks in rails, and investigating the performance of crack characterisation via the probability of detection (POD) analysis. Research methods are determined to achieve the proposed aim and objectives. Accordingly, the overall structure of this thesis is outlined.

1.1 Background

Nowadays, with transportation volumes continuously increasing, railway networks are facing the challenges of continuously increasing axle loads and vehicle speeds [1]. Since the railway accident at Hatfield, UK, in 2000, RCF defects in rails have become a safety challenge for all types of railway systems and received more attention due to short examination times [2, 3]. RCF defects removal has already been the major reason to carry out rail grinding and polishing in Europe [4]. Among types of RCF defects, the RCF crack probably presents the biggest hazard in rails. To minimise the possible in-service failures of rails and provide detailed guidelines for preventative grinding, it is important to conduct regular inspections via nondestructive testing and evaluation (NDT&E) techniques. Up to date, different types of NDT&E techniques, such as ultrasonic testing (UT), eddy current testing (ECT), alternating current field measurement (ACMF), magnetic flux leakage (MFL) testing, radiography, visual inspection (VI), have been developed to detect and characterise RCF cracks. Although these techniques have been accepted as common tools, they have own limitations for RCF crack characterisation. For instance, it is difficult for UT to detect shallow surface cracks and the testing results of the high-speed inspection usually need to be verified by manual inspections. ECT is prone to overestimating the depth because the complex geometries and the clusters of small RCF cracks can lead to large defect signals. Additionally, it is difficult for ECT to detect defects deeper than the eddy current penetration depth. The capability of ACFM to characterise natural RCF cracks with short surface lengths still needs to be further verified. Performances of MFL sensors are limited at lower inspection speeds due to rapid decreasing of magnetic flux density. Radiography involves potential health risks and the three-dimensional reconstruction of defects using computed tomography always needs defective samples cut off from rails, which is time-consuming and not applicable to in-situ inspections. VI can achieve high-speed inspection relying on a high lift-off distance to the rail surface but it is impossible for VI to provide any information about subsurface defects. As a promising candidate, ECPT, as known as induction thermography and electromagnetic

thermography, exploits electromagnetic excitation and thermal diffusion. These enable ECPT to easily heat clustered cracks and characterise their geometric parameters. On the other hand, in crack characterisation using ECPT, material factor, geometry factor, equipment factor and human factor, can influence whether the inspection will result in the correct decision as to the absence or presence of a defect. All these factors contribute to the inspection uncertainty, which leads to a probabilistic performance in crack characterisation. This probabilistic performance can be expressed by the probability of detection, which describes the likelihood of correctly characterising cracks.

By utilising the ECPT technique, the thesis carries out two in-depth investigations. One aspect is investigating temporal/spatial features and patterns for angular defect and RCF crack characterisation. Another aspect is investigating the performance of feature-based characterisation.

1.2 Aim and Objectives

The aim of the thesis is to systematically study the characterisation of RCF cracks in rails via ECPT technique and carry out the POD analysis for evaluating the performance of crack characterisation, which lays emphases on the following main objectives:

- To undertake a systematic review of RCF defects in rails and their detection, identify major challenges of current NDT&E techniques for characterising RCF cracks, and propose the use of ECPT and POD analysis;
- To build three-dimensional finite element modelling (FEM) models and a laboratory ECPT setup for numerically and experimentally investigating the characterisation of RCF cracks under the clustered distributions and geometric influences;
- To prepare dedicated man-made specimens with angular slots and cut-off specimens containing natural RCF cracks for the studies of investigating the capability of ECPT system for characterising idealised defects and RCF cracks;
- To propose and compare types of temporal/spatial thermal features and patterns for RCF crack detection and characterisation;
- To develop a POD analysis framework of guiding the performance evaluation of feature-based characterisation.

1.3 Research Methodology

To achieve the above aim and objectives, this work combines both numerical and experimental studies. Specifically, the FEM-based numerical studies and the lab-based experimental studies are carried out.

FEM aims to gain a deep understanding of the whole induction heating process (the electromagnetic field coupling between the coil and the specimen, induced eddy currents, Joule heating, and heat diffusion) before conducting the experimental studies. This makes it possible to use models for designing and optimising experimental procedures. In addition, after model calibration, the simulated results can be further used for feature extraction. COMSOL Multiphysics is selected for FEM because of its ability to easily couple numbers of physics phenomena or user-defined physics descriptions together by using partial differential equations.

For the experimental studies, a lab-based ECPT system is built to investigate the characterisation and POD analysis of angular defects and RCF cracks. Experimental studies begin with carefully configuring ECPT setups for testing different specimens. Various features are introduced and their capabilities of characterising angular defects and RCF cracks are experimentally investigated. Based on the proposed POD analysis framework, these features' performances are further evaluated and compared by using POD curves. Finally, the best features for characterising a specific parameter, e.g., pocket length, inclination angle, vertical depth or surface length, are obtained.

Figure 1.1 presents the overall diagram of the methods used to fulfil the objectives.

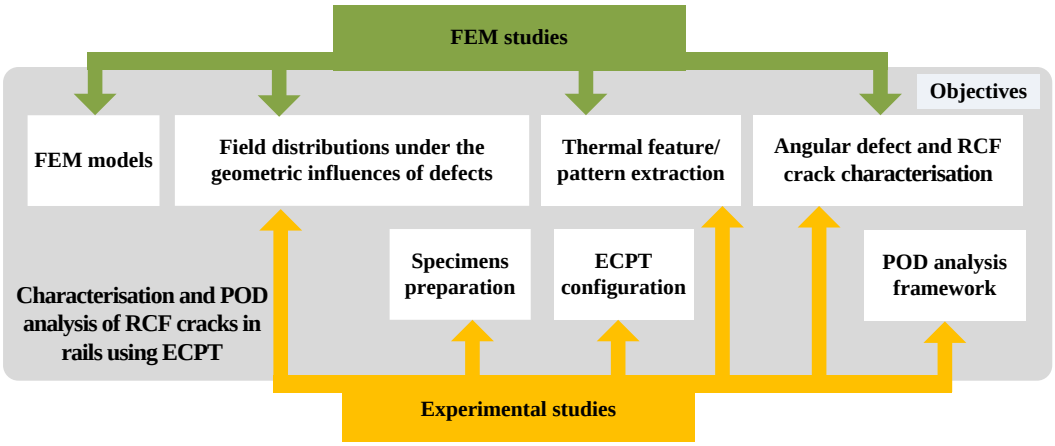

Figure 1.1 Overall diagram of the research methodology.

1.4 Thesis Overview

Figure 1.2 presents the structure of this thesis. It starts by introducing the thesis background and presenting a thorough review to identify current challenges for RCF cracks detection. Then, fundamentals of ECPT technique, POD analysis, as well as various thermal features are discussed. Greater details are presented in two case studies to test the capabilities of these features for angular defect and RCF crack characterisation. Lastly, based on the findings of the case studies, the conclusions and future investigations are summarised and their importance to modern railway industry is highlighted.

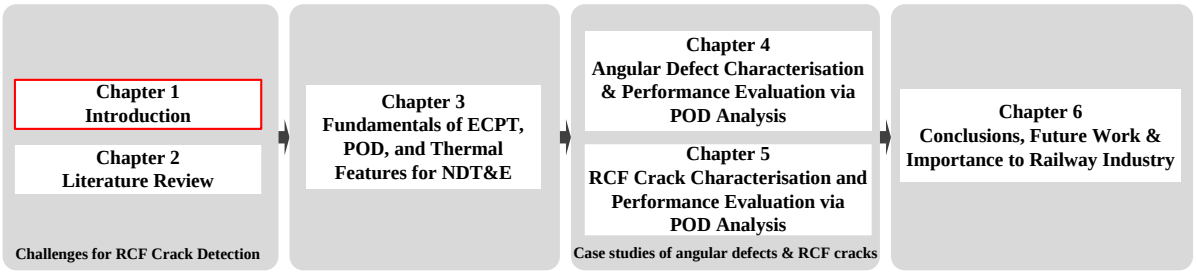

Figure 1.2 Thesis structure.

Each chapter of this thesis is briefly described below.

Chapter 1 introduces the research background of this thesis, which highlights the requirement for proposing a new NDT&E technique to handle the challenges in characterising geometric parameters of RCF cracks and introducing POD analysis to address the challenges in evaluating the characterisation performance. The aim and objectives of the thesis are determined. The structure of the thesis is presented with a brief description of each chapter.

Chapter 2 presents a literature review on RCF defects in rails and their detection. It starts by finding out the RCF induced hazards threatening railway transportation. Special attention is paid to the challenges of RCF crack characterisation using current NDT&E techniques. To overcome the problem of characterising RCF cracks when they are clustered as fish scales, ECPT with its advantages of high heating efficiency and fast testing speed is proposed. The challenges facing ECPT for RCF crack characterisation are summarised at the last of this chapter.

Chapter 3 briefly describes the theoretical backgrounds to ECPT technique and POD analysis. Based on these backgrounds, types of thermal features/patterns for defect characterisation and POD analysis are proposed, which are thoroughly discussed in case-study chapters.

Chapter 4 shows a case study of angular defect characterisation and performance evaluation by using POD analysis. It starts by proposing a POD analysis framework to quantitatively

evaluate thermal features/patterns performances for defect characterisation. Then, the ECPT configuration and three dedicated specimens that contain artificial angular slots are introduced. Features/patterns for characterising three main parameters, i.e., pocket length, inclination angle, and vertical depth, of angular defects are discussed and compared. Lastly, based on the proposed POD analysis framework, the performances of angular defect characterisation using these features are evaluated.

Chapter 5 provides another important case study focusing on RCF crack characterisation and performance evaluation via POD Analysis. The detailed descriptions of the ECPT configuration and the cut-off specimens from rails are presented. Four main parameters of RCF cracks, i.e., pocket length, inclination angle, and surface length, are characterised by different thermal features/patterns. The POD analyses are conducted to evaluate the performances of RCF crack characterisation using these features.

Chapter 6 summarises the conclusions and the main contributions of this thesis. In addition, further work and the importance to the railway industry are suggested.

1.5 Chapter Summary

This chapter briefly outlines an introduction to the thesis. The background shows that the initiation of RCF defects in rails is the most direct consequence of the increasing transportation volume and these defects have become one major safety concern of railway networks. The research gaps are summarised focusing on the characterisation of RCF cracks and the evaluation of the probabilistic performance in crack characterisation. Lastly, the research methodology and the thesis structure are present.

The next chapter presents a thorough review of RCF defect detection and characterisation by using various NDT&E methods.

Chapter 2. Literature Review

2.1 Introduction

This chapter presents a literature review of RCF defects in rails and their detection through NDT&E techniques. Based on the identified problems of current NDT&E techniques for detecting RCF cracks and the comparison of three active infrared thermography techniques, the use of ECPT for characterising RCF cracks is proposed. Importantly, this chapter highlights the challenges facing ECPT for RCF crack characterisation that need to be carefully investigated with research studies. The flow chart of this chapter is shown in figure 2.1.

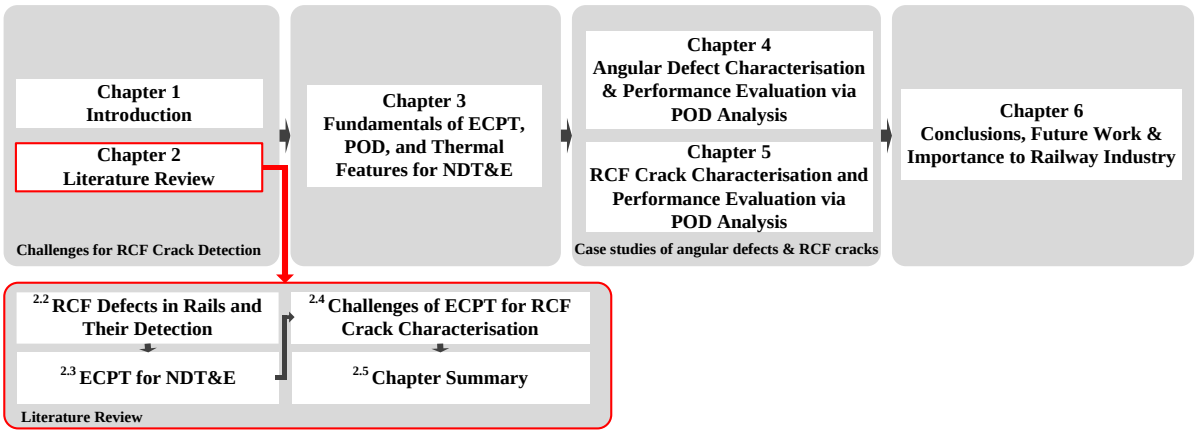

Figure 2.1 Flow chart of Chapter 2.

2.2 RCF Defects in Rails and Their Detection

As introduced in the background, rail grinding has become an important maintenance method for controlling RCF in Europe [4]. Rail grinding can be categorised into corrective and preventative maintenance. Corrective grinding needs to be carried out if a rail's condition has sufficiently deteriorated, e.g., excessive corrugation, severe fatigue defects. Preventative grinding is undertaken with predetermined intervals and procedures to reduce the probability of rail degradation, which is considered as a good practice to remove longitudinal irregularities and surface-initiated cracks, as well as restore rail's transverse profile. Indeed, the frequency of preventative grinding highly depends on the condition of rail degradation. Figure 2.2 shows two cut-off specimens containing RCF cracks in the light stage (left one) and the moderate stage (right one). The ability to detect RCF cracks at their early propagation stages is a priority for planning routine preventative grinding. Greater details of RCF cracks are given in Section 2.2.3.1.

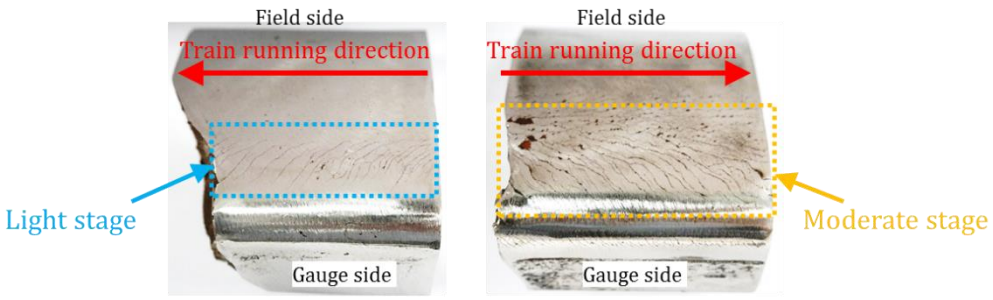

Figure 2.2 Two cut-off specimens containing RCF cracks.
The left one and the right one show cracks in the light and the moderate stages, respectively.

2.2.1 *Rail/Wheel damages by high contact stresses*

Rails are inevitably facing very high contact stresses from wheel-rail contact, which mainly determines the condition of rail degradation. Considering economic benefits, the wheel-rail contact should build a strong connection with the costs, which needs to be operated at the optimal condition with the minimum cost [4]. As shown in figure 2.3, four main aspects of wheel-rail contact are considered, i.e., rail/wheel materials, rail/wheel dynamics, contact mechanics, and friction management. These critical aspects are all linked by rail/wheel damage modes. Taking special care of these aspects contributes to the increase of rail-wheel life and profits, and the decrease of spending and maintenance costs. If any of these aspects is not treated seriously, rail/wheel damages may exist, such as wear [5], RCF [6, 7], plastic deformation [8], etc. Most of them are interlinked, such as wear and RCF. If wear is reduced, RCF defects may initiate. However, if the propagation of defects is truncated, wear failures are likely to occur.

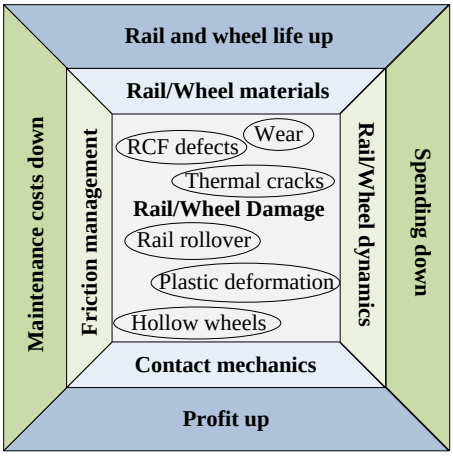

Figure 2.3 Main aspects of wheel-rail contact and their contributions to rail/wheel life and economic costs. Adapted from Ref [9].

Different damages are likely to occur at specific positions of wheel-rail contact. The position of the wheel-rail contact may continuously vary when a train is running along different

sections of a track. For example, in a straight track, the wheel tread and the rail head are likely to contact, whereas, in a curved track, a contact position probably occurs at the wheel flange and the rail gauge corner contact. Three possible regions of the wheel-rail contact are shown in figure 2.4.

Region A is the wheel-rail contact close to the field side. Contact rarely occurs in this region. If it happens, high contact stresses are induced, which leads to undesirable wear behaviour. Region B is the wheel tread-rail head contact, i.e., the running band. Normally, wheel-rail contact often occurs in this region when a train is running on straight tracks or large-radius curves. Compared with other regions, the contact stress and the lateral force are the lowest in this region. Region C is the wheel flange-rail gauge corner contact at the gauge side. Compared with Region B, this contact region is much smaller, which yields much higher contact stresses and wear rates.

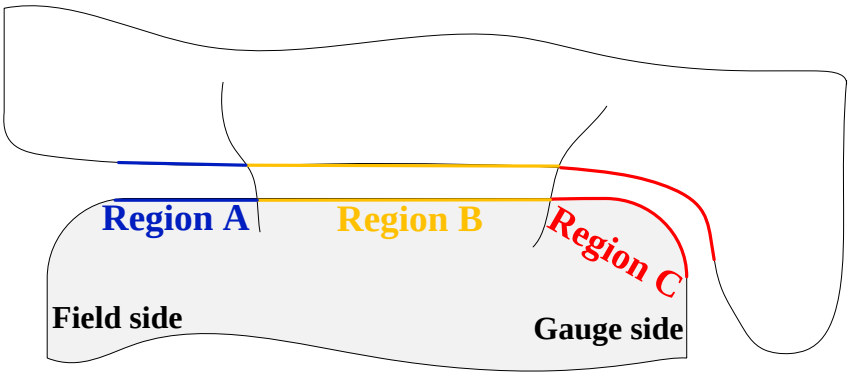

Figure 2.4 Possible regions of wheel-rail contact. Adapted from Ref [10].

Because of wear and material flow, contact regions and profile shapes of the wheel and rail will change as time progresses. Therefore, a good understanding of wheel-rail contact contributes to predicting how profiles may evolve [11]. In the wheel-rail contact, rolling/sliding behaviour often exists. Because of the rolling/sliding behaviour, a repeated-cycle of plastic deformation may occur beneath the material surfaces [12]. It is this behaviour that leads to wear and rolling contact fatigue occurring. Normally, rail wear results from sliding, whereas rail rolling contact fatigue dominates in rolling situations although some micro-sliding may occur.

2.2.2 *Rail surface wear and fatigue*

It can be seen from the discussions above that wear and fatigue are two common results of the rolling/sliding behaviour of wheel-rail contact. The following sections give descriptions of wear, fatigue and their interactions.

2.2.2.1 *Rail wear and fatigue*

A mild degree of wear can remove initial defects from the surface of the rail. However, excessive wear may shorten rail in-service life. Problems resulting from excessive wear mainly includes loss of rail profile, poor wheel-rail dynamics and, in extreme cases, a loss of rail cross-section. Sliding may result in types of wear [13], such as adhesive wear, abrasive wear, corrosive wear, thermal wear. Among them, abrasive wear accounts for approximately 50 % of wear problems [10].

With a rolling motion, the principal mechanism is rail fatigue. Surface fatigue mechanisms involve the initiation and propagation of cracks, which lead to particle loss from the rail surface, a process also known as ratcheting [14]. In severe cases, these cracks can turn down via bending moments in rails, which may eventually lead to rail breakages [15]. Types of defects caused by rail fatigue are described in detail in Section 2.2.3.

2.2.2.2 *Interaction of wear and fatigue*

As discussed above, wear and fatigue coexist in the rolling/sliding behaviour. Figure 2.5 shows the relationship between the crack growth rate and the crack pocket length under two different wear rates. For a high wear rate, the wear rate is higher than the maximum crack growth rate in Phase I and cracks are probably worn away within Phase I. There is no crack growth in Phases II and III. Instead, if the wear rate is lower than the minimum crack growth rate in Phase I, the crack pocket length may enter to Phase II and then continue propagating. In Phase II, the crack grows at a high rate until it extends through the depth of maximum shear stress rate and then at a relatively slow rate as it grows outside the region influenced by rolling contact stresses [16]. If the wear rate is still lower than the intersection point of Phase II and Phase III, the crack will enter Phase III, which may lead to rail branching.

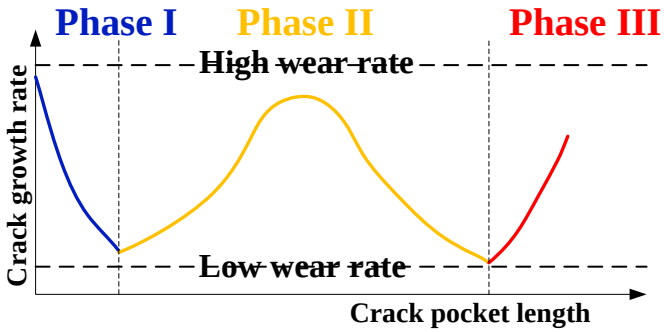

Figure 2.5 Crack growth rate vs. crack pocket length. Adapted from Ref [15].

2.2.3 *Types of RCF defects in rails*

As discussed in the aforementioned sections, high wheel-rail contact stresses, arising from traction, braking, or steering, lead to the deformation of the surface material and the development of RCF defects. There is a wide range of terms to describe different types of RCF defects [3, 17-21]. In the UK, railhead defects usually categorised as RCF cracks, squats, and tongue lipping [10], as illustrated in figure 2.6.

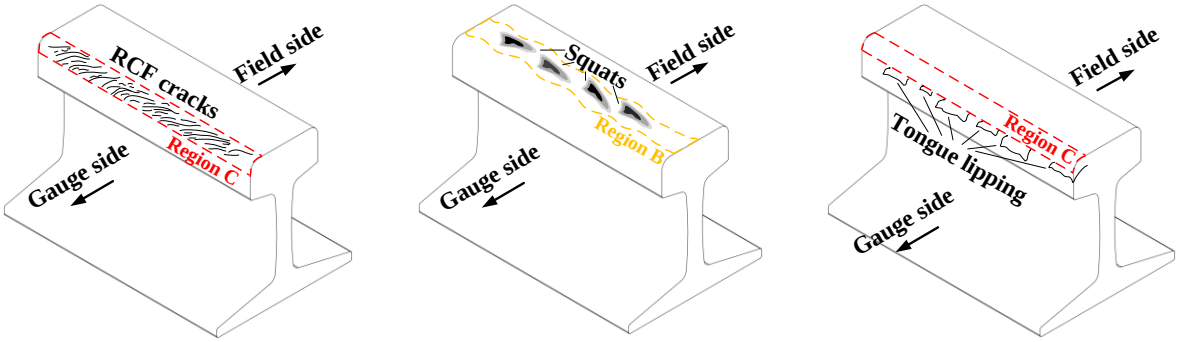

(a) (b) (c)

Figure 2.6 Schematic illustrations of common RCF defects in rails.
(a) RCF cracks in gauge corner. (b) Squats in rail crown. (c) Tongue lipping in gauge face. Adapted from Ref [10].

2.2.3.1 *RCF cracks*

RCF cracks, also known as head checks or gauge corner cracking when it occurs at the rail gauge corner (Region C in figure 2.4), probably present the biggest problem in rails. RCF cracks often appear as a group of tightly spaced cracks of similar shapes [10], and the previous figure 2.2(a) shows two typical surface appearances of them. It also can be seen that these cracks are not vertical to the train running direction and their inclined angles show possible high lateral forces of the rail-wheel contact in curves.

As mentioned in Section 2.2.2.2, the propagation phases of a RCF crack in the railhead consist of three stages: crack initiation (Phase I), crack propagation under a constant angle (Phase II), and crack propagation with potential of vertical or horizontal branching (Phase III) [15]. These three stages are also illustrated in figure 2.7. Phase I is driven by ratcheting in the plastically deformed layer with up to hundreds of microns in size [10]. Phase II is mainly controlled by applied stresses. Phase III is driven by bending stresses in rails. At this stage, if a crack reaches a critical length, there is a high possibility of a rail breakage. Usually, this stage of crack propagation is rapid since the crack becomes very large. In both Phases I and II, rail grinding can be used as an artificial wear process to remove small cracks. In addition, driving stresses for any remaining defects can also be reduced [10]. In Phases III, cracks are

too large to be removed by grinding, and the only way is replacing the defective rails. Thus, the ability to detect cracks and estimate their propagation stages is a priority for planning routine preventative grinding.

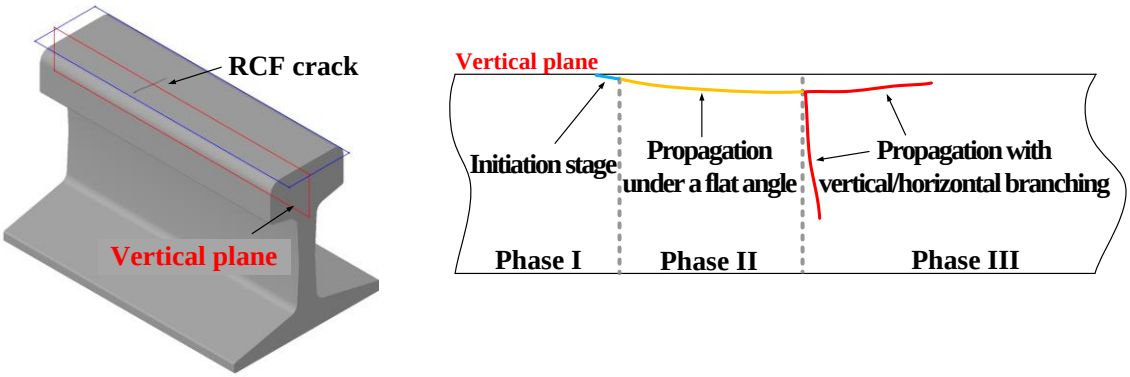

Figure 2.7 Illustration of a RCF crack propagation broken into three main stages [22].

2.2.3.2 *Squats*

Squats are another type of RCF defects [23]. Squats often occur at the running band in straight track and large curves (Region B in figure 2.4). Now it has become one of the major sources of RCF damages on many railways [24, 25].

A squat can be identified by the darkening area of rail surfaces, as illustrated in figure 2.6(b). This appearance is because of a surface depression which collects dirt and becomes corroded [10]. Typically, a squat starts from a horizontal subsurface crack which allows the near-surface material to flow sideways, thereby widening the running band, and produces a surface depression. Squats can initiate as a result of ratcheting and fluid pressurisation and also from white etching layers [26].

2.2.3.3 *Tongue lipping*

Tongue lipping is also a form of plastic deformation initiated by surface cracks. These cracks partially separate a layer of material from the bulk of rail. Tongue lipping can be distinguished by the extrusion of thin slivers or tongues of material from the running band, often extending down the rail gauge face by several millimetres [10]. Cracks form below the extruded region and grow into the railhead in a near-horizontal plane. Branches can then form running either up or down, leading to a rail breakage.

Among different RCF defects, the RCF crack appears to be the most frequent and biggest problem in rails, which has become the problem of greater interest [3]. The next section discusses current NDT&E techniques for detecting RCF cracks.

2.2.4 *Detection of RCF cracks*

Up to now, lots of research has been focused on different areas of the RCF management [27-29], e.g., RCF damage model building [30-32], wheel-rail profile management [33-35], friction management [36, 37], rail grinding [38, 39], nondestructive rail inspection [40-43], etc. Among them, NDT&E of rails is of critical importance to control risks and minimising catastrophic accidents. On the other hand, rail grinding is a well-established method to remove surface defects and profile rails. However, decisions on economical or optimal rail grinding interval should take vehicle track interaction, rail defect, and rail wear data into consideration. If a NDT&E testing technique can accurately measure rail profiles and quantify geometries of cracks, it will provide great values in the effectiveness of rail grinding practices and achieve condition-based rail grinding.

Nowadays, many NDT&E techniques have been developed for inspecting rails, such as UT, ECT, ACFM, MFL testing, radiography, VI, etc. In the following sections, six representative techniques for detecting RCF defects are briefly introduced and reviewed. Special attention is focused on their capabilities of detecting RCF cracks.

2.2.4.1 Ultrasonic testing

UT is one of the commercialised and traditional techniques for rail inspection. UT can be either manually [44] or automatically deployed [45]. During rail inspection, ultrasonic energy generated by a transducer is introduced into the rail. When defects exist in the ultrasonic wave path, part of the energy will be reflected back. The reflected signals together with their occurring times can provide useful information about the location and type of defects [46]. UT for rail inspection can be deployed by using test trains, the inspection speeds achieved varies from 40 to 80 km/h [47]. Inspection speeds can be much lower if any suspicious results need to be further verified by manual inspection. Recent developments of UT facilitate a new generation of test trains that can achieve inspection speeds as high as 100 km/h [47, 48]. However, their performances are very limited at such speeds [40]. Rail defects may locate in various positions, to avoid missing some critical defects, multiple transducers can be used to transmit ultrasonic energy at different incident angles [41].

Although UT has been proved to be a practical and effective technique for detecting internal flaws in rails, the main disadvantage is that it is difficult for UT to find surface and subsurface defects. It is because near-surface signals are always influenced by high-level noises and complex scattering. It is reported that conventional UT could be used to detect larger (>4 mm) surface defects such as deep head checks and gauge corner cracking [40].

Recently, phased array UT has been used for rail inspection [49-52]. Phased array UT is another advanced technique of UT since the beam produced from a phased array can be electronically focused, swept, and steered without moving the probe. Due to the possibility of controlling beam angles and focal distances, phased array UT can efficiently detect discontinuities, such as cracks, porosity, and lack of fusion in rails. Unfortunately, because the data volume generated during inspections is quite large, data processing of phased array UT takes much time compared to conventional UT. It is reported that the maximum inspection speeds achieved by phased array UT systems are around 5-6 km/h [40]. Recently, more research attention has been paid to developing novel software of signal processing and optimising the hardware of phased array UT to increase inspection speeds. To address the data processing issue, a new concept is looking for the coherence between signals without presuming a defect response, also known as the fast automated angle scan technique, which has been recently developed by SOCOMATE [53].

Guided wave UT is another method to inspect rails. This technique can employ various modes of acoustic waves, such as Lamb and Rayleigh waves, propagating along the boundaries of rails. This kind of propagation allows waves to travel a long distance with little loss in energy. Based on the arrival times of reflected echoes and the speeds of wave modes, cracks or corrosion in rails can be detected. Several studies have shown the results of using guided wave UT in the field test of rail inspection [54-60]. A commercial hi-rail vehicle equipped with guided wave UT, as known as Prism, has been developed by Wavesinsolids LLC [61]. It is reported that Prism can detect large transverse defects in the rail head with the maximum inspection speed of 15 km/h [61]. However, guided wave UT is likely to miss some surface-initiated cracks unless they have already reached critical sizes.

Laser/air hybrid UT has been recently used for rail inspection to address the coupled contact problem. It combines the generation of ultrasonic waves using pulsed lasers and the detection using air-coupled acoustic transducers [62-64]. A laser/air hybrid UT prototype installed in a hi-rail vehicle has been developed by Tecnogamma SPA and evaluated by Transportation Technology Centre Inc. [65]. Early tests show that this prototype can be used for detecting transverse defects, horizontal and vertical splits, and shelling in the rail head with the inspection speed up to 32 km/h [65].

Electromagnetic acoustic transmission technique (EMAT) is another non-contact way of deploying UT for rail inspection. This technique generates ultrasonic waves through magnetic field interaction, which is achieved by passing an alternating current through an inductive coil in the presence of a strong static or a quasi-static magnetic field [66]. Via the magnetic field

interaction, electromagnetic acoustic transmission transducers can generate ultrasonic waves within the skin depth without any physical contact [66]. A commercial hi-rail inspection vehicle using EMAT, as known as RailPro, has been developed by Tektrend in Canada [67, 68]. RailPro can use different configurations of transducers to generate surface or bulk ultrasonic waves, which can detect several types of defects, such as horizontal and vertical head splits, split webs, bolt hole cracking, and RCF defects at inspection speeds between 5-9 km/h [67, 68]. EMAT for high-speed rail inspection and quantification of RCF defects has been reported by several studies [69-76]. However, it is reported that in principle it is difficult for EMAT to find defects with their depths smaller than 2 mm [40]. Therefore, the combination of EMAT with ECT is a possible way to increase the detectability of shallow cracks [77].

2.2.4.2 Eddy current testing

ECT has been successfully applied in many industries [78-86], e.g., pipeline, nuclear, aircraft, etc. For rail inspection, several studies have been carried out [87-89]. A surface or subsurface defect in the rail head will divert eddy currents, which leads to fluctuations in the secondary magnetic field and the impedance changes are measured. Based on this principle, ECT is suitable for detecting RCF cracks.

The combination of ECT with UT is reported for high-speed measurements of rail defects [47, 90]. This combined system utilises ten ultrasonic probes with different incident angles and four eddy current probes, which can not only detect internal flaws but also surface cracks. Another practical application of ECT for rail inspection is optimising the grinding process by real-time monitoring depths of defects. HC Grinding Scanner developed by SPENO International SA is a good example of using ECT to provide information on the location and depth of head-check-type defects during the grinding process [91].

Because the density of eddy currents only concentrates within the skin depth, only the surface and near-surface cracks can be detected [92]. In addition, the result of eddy current testing is very sensitive to the distance between the coil and the material, i.e., lift-off distance. Typically, the lift-off distance is set to 1-2 mm, which is difficult to keep consistent at high speeds with continually varying rail head shapes.

2.2.4.3 Alternating current field measurement

ACFM is another electromagnetic technique with good potential for rail inspection. Its working principle is remotely inducing uniform alternating currents, which flow in a thin skin near the surface of the rail. Defects in the rail surface distort current paths which are reflected

by the magnetic field change above the surface. Any changes in the magnetic field can be measured by a sensor array located across the rail head. Several studies have verified the capabilities of using ACFM to detect RCF cracks [93-98]. Compared to ECT, a maximum 5 mm lift-off distance is possible without significant loss of signal when using ACFM [93]. This is due to the fact that the signal strength diminishes with the square of lift-off, not with its third power which is the case for eddy current sensors. This enables the ACFM technique to cope with much larger lift-off distances [93]. Additionally, ACFM does not suffer from the problems of conventional UT where clustered defects can render a rail untestable [17].

One commercial ACFM walking stick is developed by Technical Software Consultants Ltd. [17]. To improve the reliability of this ACFM walking stick, the empirical corrections to the sizing models have been incorporated for the use on the UK rail network [99, 100]. However, most of the sizing models are based on the assumption of isolated cracks. Although one recent publication reports the characterisation of clustered cracks via an ACFM sensor [98], its capabilities of characterising natural RCF cracks with short surface lengths still needs to be further verified.

2.2.4.4 Magnetic flux leakage testing

MFL testing has been widely used for NDT&E of ferromagnetic components in many industries [101-106]. In rail inspection with MFL, permanent magnets or DC electromagnets are first used to magnetise the rail letting the magnetic flux lines couple into it. Magnetic field sensors are placed at a constant distance from the rail head to detect any leakage in the magnetic field [41]. MFL sensors are particularly good at detecting subsurface or surface transverse defects [107], such as RCF cracks. For the low-speed inspection by using MFL-based walking stick system, MRX-RSCM is an example used for rail inspection in London Underground [108].

Unfortunately, MFL is affected by high inspection speeds since the magnetic flux density in the rail head will be largely reduced [109]. Thus, MFL is commonly used as a complementary technique to ultrasonic inspection. It is reported that the maximum inspection speed achieved by a combined ultrasonic-MFL system is limited by 35 km/h [41]. Additionally, if cracks run parallel to the magnetic flux lines, they can hardly be detected by MFL because of insufficient flux leakage.

2.2.4.5 Radiography

Radiography testing of rails can be implemented by using either gamma or X-ray sources [40]. This technique is particularly powerful for inspecting internal flaws via computed tomography

[110-115]. X-ray images taken from different angles can reproduce the three-dimensional crack shapes while avoiding the inaccuracy in detecting shallow or overlapped cracks [110]. X-ray or neutron diffraction results can also be used to evaluate residual stresses near the surface of the rail head [116-118]. However, radiography testing inherently involves health and safety drawbacks. Furthermore, since the inspection is time-consuming and costly, radiography testing is usually applied as a verification method in places where defects have already been detected by other NDT&E techniques or in rail areas where inspection with other NDT&E methods is unreliable [119].

2.2.4.6 Visual inspection

VI is probably the most direct and widely used NDT&E method. Previously, VI is manually carried out by railway engineers. Recently, via machine vision, automated visual camera-based systems for railway networks have been implemented [120]. Automated VI systems can operate at a high speed and are typically used to measure track profiles [121, 122], inspect fastening bolts/clips [123-126], and detect RCF defects [127-129]. Recently, a commercial track inspection system (V-CUBE) has been developed by MERMEC [130]. It is advertised that through the use of V-CUBE, more than 50 different types of defects on rail surface, fastenings, sleepers and trackbed can be automatically identified.

However, another report concluded that although VI systems can be used for scanning and recording various track features, none appear to provide a quantitative assessment of RCF cracks since they are an order-of-magnitude more difficult to distinguish than spalls [131]. In addition, the capability of VI highly depends on the illumination condition. Moreover, automated vision systems do not provide any information with regards to the presence of internal defects and therefore cannot be used to substitute ultrasonic inspection [40]. It is suggested that VI combined with ECT is probably an effective way for inspection rails [132].

2.2.5 *Challenges of RCF cracks detection*

From the discussions above, challenges of detecting RCF cracks can be summarised as follows:

(1) Conventional UT is still the most practical rail inspection method. However, the coupled contact of conventional UT is inevitable. Improved ultrasonic systems can be achieved by using the laser pulse excitation, the phased array, and the electromagnetic acoustic transmission. Still, it is difficult for UT to detect surface and subsurface defects because of strong noises and complex near-surface signals.

(2) ECT shows potential to not only detect but also quantify RCF cracks. Unfortunately, limited by the concentrated skin depth, it can only measure the surface and near-surface defects. Apart from this, the testing results of ECT highly depends on the lift-off distance, which is difficult to keep constant with the rail profile changing.

(3) ACFM shows good potential of detecting clustered cracks. However, the capability of ACFM to characterise natural RCF cracks with short surface lengths still needs to be further verified.

(4) MFL testing is good at detecting surface and subsurface transverse cracks. However, it is challenging for MFL testing for high-speed inspection. Moreover, it is difficult for MFL testing to detect cracks that are parallel to the magnetic flux lines because of insufficient flux leakage.

(5) Radiography is normally used to verify the testing results of other NDT&E techniques. But radiography testing is time-consuming and costly. Also, for three-dimensional characterisation, specimens need to be cut off from rails, which means it is impossible to conduct the in-situ testing. In addition, radiography involves health and safety drawbacks.

(5) VI is probably the most direct and widely used NDT&E method. However, its capability highly depends on the illumination condition and the experience of the inspector. In addition, VI can only obtain the surface information and it is impossible to measure the subsurface distributions of cracks.

As shown above, only a solo technique alone cannot successfully achieve the detection and characterisation of RCF cracks in rails. A better way is integrating two or more techniques to maximise their strengths and minimum their deficiencies. In other words, a multi-physics-based system, such as the previously mentioned UT plus ECT, is more suitable to achieve RCF cracks detection and characterisation. From this point of view, ECPT, an emerging multi-physics-based technique for detecting fine surface-breaking cracks, is introduced to address the aforementioned challenges in the following section.

2.3 ECPT for NDT&E

In the recent few decades, infrared thermography (IRT) has become a rapidly growing area in both science and industry [133]. Compared with the above-mentioned NDT&E techniques, IRT has the advantage of non-contact sensing and easy visualisation of tiny thermal variations that are invisible to the human eye [134-139]. IRT methods can be divided into active IRT and passive IRT depending on whether they are external stimulated or self-radiating. With the

advantage of fast testing and high signal-to-noise-ratio (SNR), active IRT is increasingly used in a wide range of applications [140-145]. Active IRT can be used for quick detection of surface and subsurface defects in materials with a large inspection area. Based on different excitation sources, excitation waveforms, modes, and states, figure 2.8 illustrates some main branches and working principles of active IRT.

From figure 2.8, it can be seen that active IRT requires an external excitation with a specific waveform to provide thermal contrasts between the defective area and the sound area. External excitation sources may vary from optical heating, laser heating, vibration-induced heating, microwave heating, to induction heating. In the following, based on the excitation source, five main branches of active IRT are briefly discussed. By comparing these five techniques, the use of eddy current pulsed thermography to detect and characterise RCF cracks is clarified.

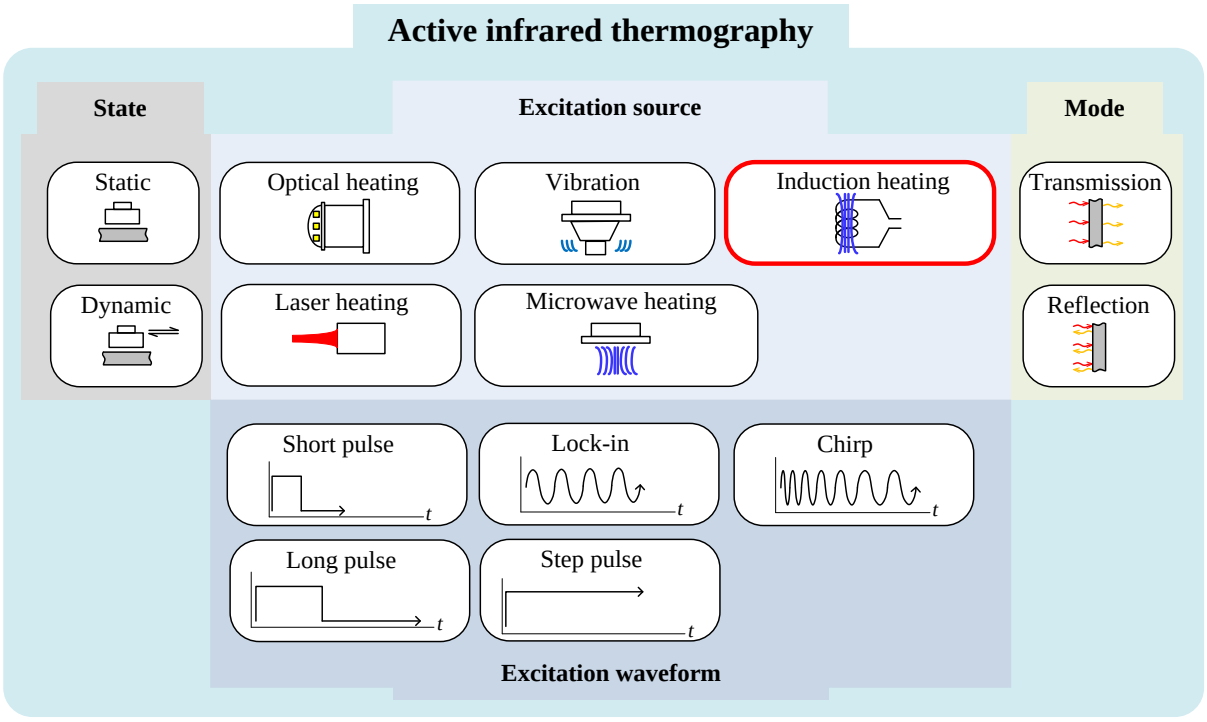

Figure 2.8 Main branches and working principles of active IRT.

Optical thermography (OT) is probably the most widely-used branch of active IRT. It is based on using three main optical stimulation devices, i.e., Xenon flashes, halogen lamps, and power light emitting diode (LED) arrays. Excitation principles of these devices determine the excitation waveforms can be deployed. Normally, high-energy and short heat pulses are used by Xenon flashes [146-152]. On the other hand, although the output energy of halogen lamps and LED arrays are much lower than Xenon flashes, various excitation waveforms can be applied, such as long pulse [153-156], lock in [157-160], step pulse [161-164], chirp

[165-168], etc. Up to date, OT has been used for various applications [169-179]. Among them, more attention is paid to characterising thermal properties of composite materials and their defects, such as impact damages, delamination, etc.

Laser thermography (LT) can be considered as a variation of OT, which mainly uses a high-power laser source to heat the material under test [180,181]. The advantage of laser excitation is that almost all types of excitation waveforms can be applied. In addition, the detection area of LT can be expanded by using a focused lens array, i.e., the laser spot heating becomes the laser array heating [182]. Compared with OT, the research and applications of LT are wider-ranging from metallic materials to biological samples [183-190] and LT is more suitable for the detection of defects perpendicular to the surface [142]. However, laser spots may result in non-uniform heating. Additionally, compared with OT, high power lasers used by LT are expensive and it can be difficult to direct the laser beam if the wavelength is long and an optical fibre cannot be used [187].

Vibrothermography is based on the frictional, plastic, and viscoelastic heating at the defect vicinity by employing high power excitation to vibrate the material under test [191-193]. The major advantage of vibrothermography is finding barely visible and closed defects with high contrasts since only the defect vicinity has the strongest thermal response. With this advantage, vibrothermography can be applied to detect fatigue flaws in most materials [194-202]. However, vibrothermography always needs a direct/indirect contact with the test material and its performance is hindered by poor repeatability [203].

Microwave thermography (MT) is a recent technique of active IRT [204-206]. This technique mainly based on the dielectric loss of medium, i.e., in a varying electric field, loss of energy dissipates into heat. Although MT has the advantage of controlled microwave energy and noncontact heating, an improved thermal contrast for defect detection in composites needs much longer heating time than pulsed excitation used in LT [205].

Eddy current pulsed thermography (ECPT), also known as induction thermography and electromagnetic thermography, is another branch of active IRT, which enjoys the capabilities of combining the responses from electromagnetic induction and heat diffusion [207-211]. Defects such as RCF cracks within the range of effective skin depth disturb the eddy current density distribution, where higher levels of Joule heating are achieved in the regions of increased current density and thereby influence the temperature distribution. Thus, the defect can be detected from thermal images [212]. Relying on this specific principle, ECPT has been found to detect the smallest cracks, i.e. sensitivity, with higher reliability and reproducibility

compared to vibrothermography and LT [213]. In addition to these, the superior performance of ECPT, e.g., pulse excitation, robust to lift-off variations and effective for defect orientation and depth estimation, significantly leads it for fast quantitative evaluation [214]. Up to now, ECPT has been deployed to various applications [215-228].

Further, table 2.1 briefly summarises the advantages and limitations of these five techniques. As can be seen, although limited for detecting subsurface defects and testing non-conductive materials, ECPT is the most suitable way to detect small and fine surface-breaking cracks with high repeatability and heating efficiency, which reasonably clarifies the use of ECPT in this thesis to achieve the RCF crack characterisation.

Table 2.1 Summary of five main branches of active IRT

Active IRT based on excitation source	**Advantages**	**Limitations**
OT	- Various waveforms - More suitable for voids and delamination	- Non-uniform heating - Limited for surface-breaking cracks
LT	- Various waveforms - Suitable for surface-breaking cracks	- Non-uniform heating - Longer scanning time in the absence of a focused lens array
Vibrothermography	- Various waveforms - Suitable for all types of closed natural defects - Uniform heating	- Low repeatability - Frictional faces are needed - Contact excitation is required - May introduce further damages
MT	- Relatively uniform heating - Adjustable excitation frequency and polarisation	- Limited for subsurface defects in metallic materials - Longer heating time
ECPT	- More suitable for small and fine surface-breaking cracks - High repeatability - High heating efficiency - High SNR	- Limited for subsurface defects. - Non-uniform heating - Limited for non-conductive materials - Relatively expensive

2.4 Challenges of ECPT for RCF Crack Characterisation

It can be seen from the above section that ECPT shows the best capability of detecting and characterising RCF cracks. However, there are still several challenges and research gaps need to be addressed before this technique is further applied to the in-situ testing.

One outstanding challenge is that under the clustered distribution of RCF cracks, it is difficult to characterise the geometric parameters, i.e., pocket length, inclination angle, vertical depth, and surface length, of RCF cracks. It is because that the clustered cracks with narrow spacings

may lead to complex eddy current and thermal distributions. In this situation, it is more difficult to extract useful thermal features for RCF crack characterisation.

One major research gap is how to quantitatively evaluate the probabilistic performance in crack characterisation. Repeated tests of a specific crack can produce different feature responses because of variations in the excitation setup, infrared camera, background environment, etc. All these variations contribute to feature uncertainty and lead to probabilistic performances in crack characterisation. It is important to propose a proper framework to evaluate these probabilistic performances.

To address these two aspects, i.e., the quantitative characterisation of RCF cracks under their clustered distributions and the performance evaluation of crack characterisation, this thesis proposes the use of the feature-based ECPT technique to achieve the detection and characterisation of RCF cracks. Additionally, a POD analysis framework is proposed to evaluate the ECPT's performance in crack characterisation.

2.5 Chapter Summary

A literature review of modern NDT&E techniques for rail inspection is presented in this chapter. Specifically, RCF defects in rails and their detection by different NDT&E techniques are first reviewed and compared. Based on the identified challenges of current NDT&E techniques and a brief review of active IRT for NDT&E, ECPT is proposed as a promising candidate for characterising RCF cracks inspection. Lastly, the challenges of ECPT for RCF crack characterisation are highlighted.

The next chapter will provide the fundamentals of ECPT technique, POD analysis, and thermal features. Based on the proposed features, the challenges pointed out in Section 2.4 will be addressed and discussed in the case study chapters. Greater details can be found in Chapter 4 and Chapter 5.

Chapter 3. Fundamentals of ECPT, POD, and Thermal Features for NDT&E

3.1 Introduction

In this chapter, theoretical backgrounds related to ECPT technique and POD analysis are first introduced. Based on these backgrounds, types of thermal features/patterns for further defect characterisation and POD analysis are discussed. The last section presents the chapter summary. The flow chart of this chapter is shown in figure 3.1.

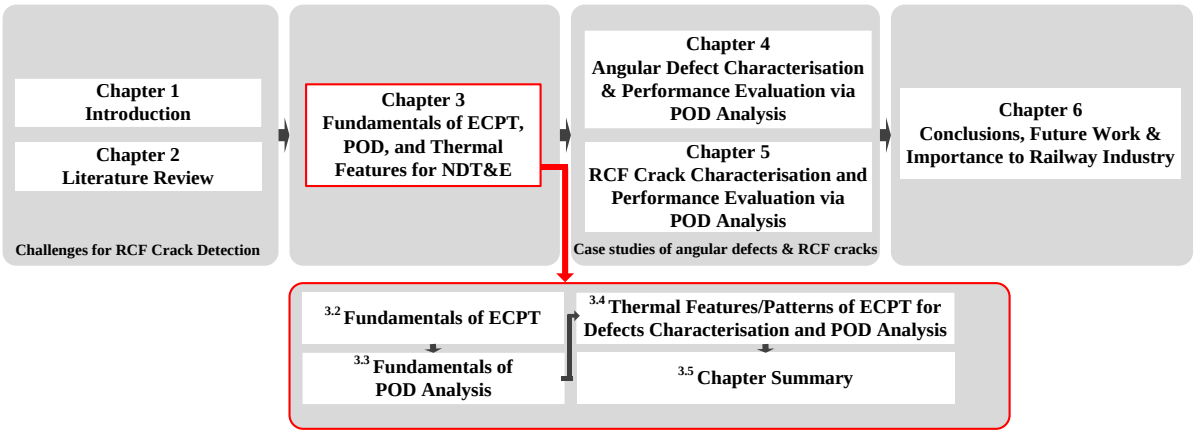

Figure 3.1 Flow chart of Chapter 3.

3.2 Fundamentals of ECPT

Briefly, ECPT technique takes the advantages of induction heating and infrared thermal imaging to achieve defect/flaw detection. Induction heating has the advantage of heating conductive materials without any direct contact via the electromagnetic induction. Figure 3.2 illustrates the basic idea of induction heating by using FEM. The blue arrows show currents running in a linear coil. The cyan arrows show the magnetic field induced by the coil. Electromagnetic induction leads to inductive heat generation and diffusion in the conductive specimen under test. An angular slot is simulated as a defect resulting in abnormal heat distributions. Greater simulation results of inclination angle characterisation are given in Section 4.4.2.

During the induction heating, four physical phenomena coexist, i.e., electromagnetic field formation, electromagnetic induction, heat generation, and heat diffusion. The coupled effects of these phenomena make up the whole heating process. In electromagnetic field formation, Ampère's law can mathematically describe this phenomenon. Electromagnetic induction can be described by Faraday-Lenz law. Heat generation mainly considers the Joule heating effect. As for heat diffusion, it can be described by Fourier's law.

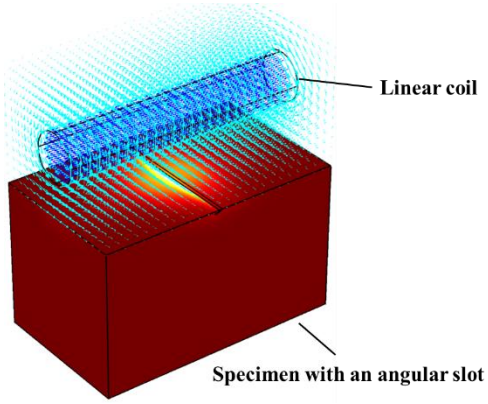

Figure 3.2 Illustration of induction heating using FEM.

Apart from induction heating, in real applications of ECPT, infrared thermal imaging is required to image temperature by sensing the infrared thermal radiation emitted from the material surface. The main advantage of infrared thermal imaging is that by using focal plane array it can easily visualise temperature effects which are impossible to be "seen" by human eyes.

Based on induction heating and infrared thermal imaging, ECPT becomes a fast and high-resolution method for defect detection and characterisation over a relatively large area. Defects such as RCF cracks within the range of effective skin depth disturb the eddy current density distribution, where higher levels of Joule heating are achieved in the regions of increased current density and thus influence the temperature distribution. Thus, defects can be detected from thermal images.

In addition, ECPT can exploit both induction heating and heat diffusion. At the start of the heating stage (normally shorter than 50 ms), induction/Joule heating plays a dominant role with its advantage of surface flaw detection. In the later heating and cooling stages (longer than 50 ms), heat diffusion takes over with the benefit of detecting subsurface and deeper flaws. Additionally, induction coils, excitation parameters (heating pulse duration, frequency, and intensity), and morphological parameters of defects (length, width, orientation, etc.) can also lead to various thermal distributions and patterns. Thus, thermal features based on various temporal- and spatial-thermal patterns can be used for defect detection and characterisation, as later discussed in Section 3.4.

3.2.1 *Electromagnetic wave propagation*

The electromagnetic wave propagation problem can be addressed by solving Maxwell's equations with specific boundary conditions. Maxwell's equations link six fundamental electromagnetic quantities together. These quantities are electric field (***E***), electric

displacement (***D***), magnetic field (***H***), magnetic induction (***B***), current density (***J***), and electric charge density (ρ). Maxwell's equations can be expressed either in integral form or differential form. Since in this work, all the simulation results are based on finite element modelling, only the differential forms of Maxwell's equations presented here. For the time-varying situation, they are generally expressed as [229]

$$\nabla \times \boldsymbol{H} = \boldsymbol{J} + \frac{\partial \boldsymbol{D}}{\partial t} \tag{3.1}$$

$$\nabla \times \boldsymbol{E} = -\frac{\partial \boldsymbol{B}}{\partial t} \tag{3.2}$$

$$\nabla \cdot \boldsymbol{D} = \rho \tag{3.3}$$

$$\nabla \cdot \boldsymbol{B} = 0 \tag{3.4}$$

Equations 3.1 and 3.2 show the Maxwell-Ampère's law and the Faraday's law, respectively. These two equations together express the evolution of coupled electromagnetic wave. Equations 3.3 and 3.4 are the electric and magnetic form of Gauss's law, respectively. These two equations together show the flux conservation. By combining Equations 3.1 and 3.3, another important equation showing the electric charge conservation law can be obtained [229]

$$\nabla \cdot \boldsymbol{J} = -\frac{\partial \rho}{\partial t} \tag{3.5}$$

The above five equations give the general Maxwell's equations in differential form. To describe the electromagnetic wave propagation in materials or a closed system, these equations should be added with constitutive relations that specify the macroscopic properties of materials. Typically, these relations are given as

$$\boldsymbol{J} = \sigma \boldsymbol{E} \tag{3.6}$$

$$\boldsymbol{D} = \varepsilon \boldsymbol{E} \tag{3.7}$$

$$\boldsymbol{B} = \mu \boldsymbol{H} \tag{3.8}$$

where, σ is the electrical conductivity. ε denotes the electrical permittivity. μ represents the magnetic permeability.

Maxwell's equations can be simplified and represented in terms of $\boldsymbol{B}$ field and $\boldsymbol{E}$ field by introducing potentials. The most used potentials are the magnetic vector potential ($\boldsymbol{A}$), the electric scalar potential (V), and the magnetic scalar potential (ψ).

For magnetic vector potential, it should be well-defined and continues to satisfy that no magnetic monopoles exist. It is well known that divergence of the curl of a vector field is zero. Thus, for magnetic vector potential, this relation is expressed as

$$\nabla \cdot (\nabla \times \boldsymbol{A}) = 0 \tag{3.9}$$

Via using this equation, equation 3.4, e.g., the magnetic form of Gauss's law, is rewritten as

$$\nabla \cdot \boldsymbol{B} = \nabla \cdot (\nabla \times \boldsymbol{A}) = 0 \tag{3.10}$$

Then, magnetic induction can be expressed as a function of $\boldsymbol{A}$

$$\boldsymbol{B} = \nabla \times \boldsymbol{A} \tag{3.11}$$

By combining equations 3.11 and 3.2, and introducing the electric scalar potential, equation 3.2, e.g., Faraday's law, is rewritten as

$$\nabla \times \boldsymbol{E} = \nabla \times (-\nabla V - \frac{\partial \boldsymbol{A}}{\partial t}) = -\frac{\partial}{\partial t}(\nabla \times \boldsymbol{A}) = -\frac{\partial \boldsymbol{B}}{\partial t} \tag{3.12}$$

where, $\nabla \times \nabla V$ is zero since the curl of the gradient of a scalar field is zero.

Then, the electric field can be expressed as a function of $\boldsymbol{A}$ and V

$$\boldsymbol{E} = -\nabla V - \frac{\partial \boldsymbol{A}}{\partial t} \tag{3.13}$$

Under certain circumstances, e.g., the magnetostatic condition where the electric charge density ρ is zero or is time-invariant, equation 3.1, e.g., Maxwell-Ampère's law, reduces to

$$\nabla \times \boldsymbol{H} = 0 \tag{3.14}$$

Similar to electric scalar potential, the magnetic scalar potential is introduced and the magnetic field can be expressed as

$$\boldsymbol{H} = -\nabla \psi \tag{3.15}$$

3.2.2 *Time-harmonic electromagnetic field and induction heating source*

3.2.2.1 *Time-harmonic electromagnetic field*

In the previous section, the general equations for calculating $\boldsymbol{B}$ field and $\boldsymbol{E}$ field are given by using potentials. As for ECPT technique, the time-harmonic case needs to be considered. Under this condition, the electromagnetic field harmonically oscillates with a specific sinusoidal function. In this section, the specific form describing the time-harmonic electromagnetic field is derived.

By using the vector phasor notation, any first-order partial differential of the phasor with respect to time can be easily represented by multiplying $j\omega$. Thus, equations 3.1 and 3.2 can be rewritten as

$$\nabla \times \boldsymbol{H} = \boldsymbol{J} + j\omega \boldsymbol{D} \tag{3.16}$$

$$\nabla \times \boldsymbol{E} = -j\omega \boldsymbol{B} \tag{3.17}$$

Where, ω is the angular frequency. j is the imaginary unit.

Then, by substituting constitutive relations of equations 3.6-3.8 into 3.16, it can be obtained as

$$\nabla \times \frac{1}{\mu} \boldsymbol{B} = \sigma \boldsymbol{E} + j\omega \varepsilon \boldsymbol{E} \tag{3.18}$$

Next, by substituting the magnetic vector potential ($\boldsymbol{A}$), the electric scalar potential (V), equation 3.18 is expressed as

$$\nabla \times (\frac{1}{\mu} \nabla \times \boldsymbol{A}) = \sigma(-\nabla V - j\omega \boldsymbol{A}) + j\omega \varepsilon(-\nabla V - j\omega \boldsymbol{A}) \tag{3.19}$$

After rearranging the terms, it is written as

$$(j\omega\sigma - \omega^2 \varepsilon)\, \boldsymbol{A} + \nabla \times (\frac{1}{\mu} \nabla \times \boldsymbol{A}) + (\sigma + j\omega \varepsilon) \nabla V = 0 \tag{3.20}$$

It is evident that equation 3.20 is a function of $\boldsymbol{A}$ and V, which means that $\boldsymbol{A}$ and V are coupled. In the following, the gauge transformation is introduced. By using a particular gauge, V can be vanished and equation 3.20 is reduced to the function of $\boldsymbol{A}$.

The gauge transformation is conducted by introducing two new potentials ($\tilde{\boldsymbol{A}}$ and $\tilde{V}$) defined as

$$\tilde{\boldsymbol{A}} = \boldsymbol{A} + \nabla\Psi \tag{3.21}$$

$$\tilde{V} = V - \frac{\partial\Psi}{\partial t} \tag{3.22}$$

These two transformations keep $\boldsymbol{B}$ and $\boldsymbol{E}$ fields unchanged, which can be verified by

$$\boldsymbol{E} = -\nabla V - \frac{\partial \boldsymbol{A}}{\partial t} = -\nabla(\tilde{V} + \frac{\partial\Psi}{\partial t}) - \frac{\partial(\tilde{\boldsymbol{A}} - \nabla\Psi)}{\partial t} = -\nabla\tilde{V} - \frac{\partial(\tilde{\boldsymbol{A}})}{\partial t} \tag{3.23}$$

$$\boldsymbol{B} = \nabla \times \boldsymbol{A} = \nabla \times (\tilde{\boldsymbol{A}} - \nabla\Psi) = \nabla \times \tilde{\boldsymbol{A}} \tag{3.24}$$

To vanish $\tilde{V}$, Ψ is chosen as

$$\Psi = -\frac{jV}{\omega} \tag{3.25}$$

Then, equations 3.21 and 3.22 are updated as

$$\tilde{\boldsymbol{A}} = \boldsymbol{A} + -\frac{j}{\omega}\nabla V \tag{3.26}$$

$$\tilde{V} = V - \frac{\partial(-jV/\omega)}{\partial t} = V + -\frac{j}{\omega}\frac{\partial V}{\partial t} = 0 \tag{3.27}$$

By substituting these two potentials into equation 3.20, it can be obtained as

$$(j\omega\sigma - \omega^2\varepsilon)\,\tilde{\boldsymbol{A}} + \nabla \times (\frac{1}{\mu}\nabla \times \tilde{\boldsymbol{A}}) = 0 \tag{3.28}$$

It is evident that equation 3.27 is the only function of $\tilde{\boldsymbol{A}}$. In addition, if $\tilde{\boldsymbol{A}}$ is known, the $\boldsymbol{B}$ field and $\boldsymbol{E}$ field can be calculated by

$$\boldsymbol{B} = \nabla \times \tilde{\boldsymbol{A}} \tag{3.29}$$

$$\boldsymbol{E} = -j\omega\tilde{\boldsymbol{A}} \tag{3.30}$$

3.2.2.2 *Induction heating source*

During the electromagnetic wave propagation, it carries electromagnetic power. Based on curl equations 3.1 and 3.2 and Poynting's theorem, in the following, different types of energies existing in the wave propagation will be derived. In addition, the induction heating source is specified as Ohmic/Joule power density.

Multiplying equation 3.2 by $\boldsymbol{H}$, equation 3.1 by $\boldsymbol{E}$ and subtracting former with latter, it can be obtained as

$$\boldsymbol{H}\cdot(\nabla\times\boldsymbol{E})-\boldsymbol{E}\cdot(\nabla\times\boldsymbol{H}) \;=\; -\boldsymbol{H}\cdot\frac{\partial\boldsymbol{B}}{\partial t}-\boldsymbol{E}\cdot\boldsymbol{J}-\boldsymbol{E}\cdot\frac{\partial\boldsymbol{D}}{\partial t} \tag{3.31}$$

Based on the identity of vector operation, the left side of equation 3.31 can be written as

$$\boldsymbol{H}\cdot(\nabla\times\boldsymbol{E})-\boldsymbol{E}\cdot(\nabla\times\boldsymbol{H}) \;=\; \nabla\cdot(\boldsymbol{E}\times\boldsymbol{H})=\;\nabla\cdot\boldsymbol{S} \tag{3.32}$$

where, $\boldsymbol{S}$ is the Poynting vector.

If the constitutive constants (σ, ε, μ) do not change with time, based on equations 3.6-3.8, the right side of equation 3.31 can then be written as

$$\begin{aligned}&-\frac{1}{2}\frac{\partial}{\partial t}(\mu\boldsymbol{H}\cdot\boldsymbol{H})-\frac{1}{2}\frac{\partial}{\partial t}(\varepsilon\boldsymbol{E}\cdot\boldsymbol{E})-\boldsymbol{E}\cdot\boldsymbol{J}\\&=-\frac{\partial}{\partial t}(\frac{1}{2}\mu H^2+\frac{1}{2}\varepsilon E^2)-\sigma E^2\end{aligned} \tag{3.33}$$

Then, equation 3.31 updates as

$$\nabla\cdot\boldsymbol{S} \;=\; -\frac{\partial}{\partial t}(\frac{1}{2}\mu H^2+\frac{1}{2}\varepsilon E^2)-\sigma E^2 \tag{3.34}$$

Then, the integral of equation 3.34 over an enclosed volume (*Vol*) can be expressed as

$$\int_{Vol}\nabla\cdot\boldsymbol{S}\,dv=-\frac{\partial}{\partial t}\int_{Vol}(\frac{1}{2}\mu H^2+\frac{1}{2}\varepsilon E^2)\,dv-\int_{Vol}\sigma E^2 dv \tag{3.35}$$

Via the divergence theorem (Gauss's theorem), equation 3.34 can be written as

$$-\oint_{Sur}\boldsymbol{S}\cdot d\boldsymbol{s}=\frac{\partial}{\partial t}\int_{Vol}(\frac{1}{2}\mu H^2+\frac{1}{2}\varepsilon E^2)\,dv+\int_{Vol}\sigma E^2 dv \tag{3.36}$$

where, *Sur* is the closed surface of *Vol*.

This equation is known as Poynting's theorem, which states that the surface integral of the Poynting vector $\boldsymbol{S}$ over a closed surface equals the power entering the enclosed volume.

If a time-harmonic electromagnetic field is described, equation 3.35 can be simplified as

$$-\oint_{Sur}\boldsymbol{S}\cdot d\boldsymbol{s}=j\omega\int_{Vol}(\frac{1}{2}\mu H^2+\frac{1}{2}\varepsilon E^2)\,dv+\int_{Vol}\sigma E^2 dv \tag{3.37}$$

And it is convenient to introduce the following quantities

$$W_m = \int_{Vol} (\frac{1}{2} \mu H^2)\, dv \tag{3.38}$$

$$W_e = \int_{Vol} (\frac{1}{2} \varepsilon E^2)\, dv \tag{3.39}$$

$$P_\sigma = \int_{Vol} \sigma E^2 dv \tag{3.40}$$

where, W_m and W_e denote the magnetic energy density and electric energy within the enclosed volume, respectively. P_σ denotes the ohmic power of the enclosed volume.

Based on these equations, Poynting's theorem can also specifically state as the power flowing into the surface of an enclosed volume equals to the changing rates of the stored magnetic energy and the electric energy, together with ohmic power within the enclosed volume.

It should be noted that P_σ will transform into Joule heat by eddy losses and this dissipated power is considered as the main induction heating source.

3.2.3 *Heat diffusion with induction heating source*

As is known to all, the heat transfer in solids is generally governed by

$$\rho C_p \frac{\partial T}{\partial t} + \rho C_p \boldsymbol{v} \cdot \nabla T + \nabla \cdot \boldsymbol{q} = p_s \tag{3.41}$$

where, ρ and C_p are the density and thermal capacity, respectively. T is the temperature as a function of both space and time. $\boldsymbol{v}$ is the velocity vector describing translational moving. $\boldsymbol{q}$ is the heat flux vector. p_s denotes the heating power per unit volume.

By introducing thermal conductivity λ, the relation between $\boldsymbol{q}$ and T is expressed as

$$\boldsymbol{q} = -\lambda \nabla T \tag{3.42}$$

This equation is Fourier's law of heat conduction. Since, in this work, all the relative positions between the tested specimens and the ECPT setup/coil are fixed, the translational motion term can be ignored. In addition, the major type of heat transfer is conduction without much considering other types, such as convection, and radiation. Based on the above concerns and by substituting equation 3.42 into equation 3.41, the heat transfer equation is reduced to the heat conduction/diffusion equation with the form of

$$\rho C_p \frac{\partial T}{\partial t} - \lambda \nabla^2 T = p_s \tag{3.43}$$

where, $\nabla^2 T$ means the divergence of the temperature gradient ∇T.

In the previous section, it is concluded that P_σ is the ohmic power of the enclosed volume which eventually transforms into Joule heat by eddy losses and is considered as the main induction heating source. For a point-function relation, this heating source is written as

$$p_\sigma = \sigma E^2 = p_s \tag{3.44}$$

Finally, by substituting equation 3.44 into equation 3.43, the heat diffusion equation with induction heating source can be then written as

$$\rho C_p \frac{\partial T}{\partial t} - \lambda \nabla^2 T = \sigma E^2 \tag{3.45}$$

3.2.4 Infrared imaging via uncooled infrared camera

One key process of ECPT technique is using an infrared camera to capture infrared radiation, i.e., convert infrared radiation into readable signals. An infrared detector plays as the core of an infrared imaging system/camera. Its capability mainly determines the performance of an infrared camera.

Generally, infrared detectors can be divided into two types, i.e., photon detectors and thermal detectors. The basic principle of photon detectors is that the absorption of photons causes changes in the mobility/concentration of free charge carriers [230]. These changes generate the electrical resistance changes or photocurrent changes which is proportional to the number of photons absorbed [231]. In thermal detectors, the absorbed radiation changes the physical property of the detector, e.g., the changes of electrical resistance in a resistive bolometer. Compared with photon detectors, although thermal detectors are characterised by lower sensitivities or time resolutions, they can satisfy most practical applications with much lower costs [231]. Additionally, thermal detectors can work at the ambient temperature without employing any type of cryogenic system [232]. Benefiting from these two advantages, nowadays uncooled infrared cameras equipped with the thermal detector take the leading position in most applications.

The performance of uncooled infrared cameras is assessed by a number of parameters, such as temperature accuracy, temperature resolution, spatial resolution, time resolution, etc. The temperature accuracy describes the absolute temperature measurement error of blackbody temperature measurement. The noise equivalent temperature difference (NETD) shows the temperature resolution of an infrared camera, which gives the minimum temperature difference between a blackbody object and blackbody background when the SNR of the infrared camera equals to one. The spatial resolution defines the total pixel number of a focal

plane array. The field of view (FOV) gives the angular extent of the observable object field. The frame rate shows the frequency at which consecutive images/frames are recorded by an infrared camera. The detector pitch is the pixel size of a detector array which is typically measured in microns. It is an important parameter to predict the spatial resolution and range performance of an infrared camera. A smaller detector pitch gets more image details (spatial resolution and FOV) if the area of the focal plane array is fixed. For instance, the infrared camera used in the work is FLIR A655sc, which is based on the uncooled microbolometer. Its main parameters are listed in table 3.1.

Table 3.1 Main parameters of FLIR A655sc

Parameters	Value	Unit
Temperature accuracy	± 2	℃
NETD	< 0.03	℃
HFOV/VFOV	25/19	°
Spatial resolution	640×480	Pixels
Maximum frame rate	200	Hz
Detector pitch	17	μm
Spectral range	7.5-14	μm
Detector time constant	~8	ms

3.3 Fundamentals of POD Analysis

POD analysis is a common and widely-accepted statistical tool, which can provide a quantitative assessment to evaluate the detectability of almost any NDT&E technique. POD analysis has been widely used for the detection capabilities of current NDT&E techniques, such as ultrasonic testing, eddy current testing. In this thesis, the aim of POD analysis is to quantitatively evaluate the performance of feature-based ECPT. In the following sections, some fundamentals of POD Analysis are introduced.

3.3.1 *POD curves*

Generally, POD curves are the direct results of POD analysis, which is normally a function of a chosen defect parameter (length, width, or depth) and presents some critical information to quantitatively characterise the detection capability and reliability [233-236]. Figure 3.3(a) illustrates three examples including a_{50} (the minimum defect size of 50% POD), a_{90} (the minimum defect size of 90% POD), and $a_{90/95}$ (the minimum defect size of 90% POD with a 95% degree of confidence). POD curves can be calculated from either experimental or simulated data. The inspection data can be recorded as two common types, i.e., binary data or signal response ($\hat{a}$). For the first one, the inspection results are denoted binary data by *1* indicating a defect is found or *0* indicating a defect is missed. Data of this type is called

hit/miss data. The data is called signal response data if the recorded response can be quantified and correlated with the flaw size, such as the maximum thermal response vs. the crack depth in ECPT testing.

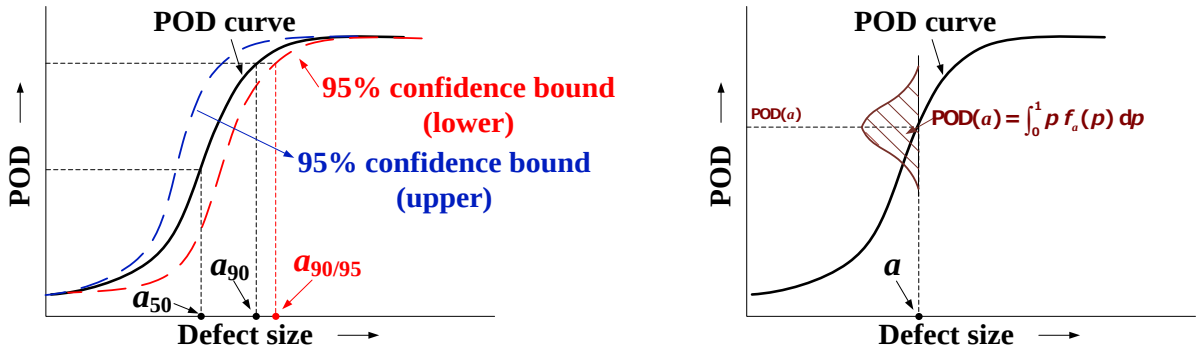

Figure 3.3 Schematic of a POD curve.
(a) POD curve with the 95% confidence bounds, a_{50}, a_{90}, and $a_{90/95}$. (b) Schematic of a probability density function and POD calculation.

The POD(a) function is defined as the proportion of all defects of size a that will be detected in a particular application of a NDT&E system, such as cracks detection by using ECPT technique. If a crack of size a has its own crack detection probability (p), the probability density function is given by $f_a(p)$, which is illustrated in figure 3.3(b). The conditional probability of a randomly selected crack detected at the inspection is given by $p\, f_a(p)\, dp$. The unconditional probability of a randomly selected and detected crack is the sum of the conditional probabilities over p, which is:

$$\mathrm{POD}(a) = \int_0^1 p\, f_a(p)\, \mathrm{d}p \tag{3.46}$$

Equation 3.46 suggests that the POD(a) function is the curve through the averages of individual density functions of the detection probabilities. This curve provides the basis for testing assumptions about the applicability of various POD(a) models.

3.3.2 *Hit/Miss data-based POD analysis*

For the hit/miss data, the recorded results are discrete and only have two possible outcomes, *1* or *0*. The distribution of random errors between outcomes and predicted values is not Gaussian (normal) but binomial. Thus, generalised linear models are needed first to transform hit/miss data into a linear domain, where the transformed probability can be modelled as an ordinary polynomial function. Usually, four transform functions are used. They are log-logistics function (also called log-odds or logit function), log-normal function (also called

probit function), loglog function, and complementary log-log function (also called Weibull function), which are expressed as

log-logistics (log-odds or logit) function: $$\ln\left(\frac{\mathrm{POD}(a)}{1-\mathrm{POD}(a)}\right)=f(a) \tag{3.47}$$

log-normal (probit) function: $$\Phi^{-1}\left(\mathrm{POD}(a)\right)=f(a) \tag{3.48}$$

loglog funcrtion: $$-\ln\left(-\ln\left(\mathrm{POD}(a)\right)\right)=f(a) \tag{3.49}$$

cloglog funcrtion: $$\ln\left(-\ln\left(1-\mathrm{POD}(a)\right)\right)=f(a) \tag{3.50}$$

where, $f(a)$ is any linear function of a and the most common forms are $f(a) = \alpha + \beta a$ and $f(a) = \alpha + \beta \ln(a)$. POD($a$) is the POD of defect with size of a. $\Phi(\cdot)$ is normal cumulative density function.

Among these four functions, the logit function is commonly used in analysing the hit/miss data because of its analytical tractability and close agreement with the cumulative log-normal distribution [233, 237]. The term on the left-hand side of equation 3.47 is called the log of the 'odds', i.e., odds equals to POD/(1-POD). This equation shows that the log of the odds of the POD is expressed as a linear function $f(a)$, which is the name of the log-odds model.

From the above four transform functions, their POD(a) models, as link functions to a, can be obtained as:

log-logistics (log-odds or logit) link: $$\mathrm{POD}(a)=\frac{\exp\left(f(a)\right)}{1+\exp\left(f(a)\right)} \tag{3.51}$$

log-normal (probit) link: $$\mathrm{POD}(a)=1-\Phi\left(f(a)\right) \tag{3.52}$$

loglog link: $$\mathrm{POD}(a)=-\exp\left(-\exp\left(-f(a)\right)\right) \tag{3.53}$$

cloglog link: $$\mathrm{POD}(a)=1-\exp\left(-\exp\left(f(a)\right)\right) \tag{3.54}$$

It should be noted that choosing the link function and using the logarithmic form of a may have a large influence on the value for $a_{90/95}$. For the symmetric data set, the POD link functions should be symmetric, either logit or probit. In the many situations when the data are skewed to the right, taking the log of size will produce a nearly symmetric data set. Thus, the use of a right-skewed link (the loglog link) is uncommon. In some situations, the data are left-skewed and using a symmetric link function penalises the inspection performance for

larger cracks due to lack-of-fit for the smaller cracks. In those situations, the left-skewed complementary loglog link function, cloglog, can provide adequate results [236].

3.3.3 Signal *response data-based POD analysis*

Apart from recording the inspection results as hit/miss data, flaw indications also can be interpreted as continuous responses to stimuli. For instance, the thermal response in active IRT. Assume the response can be quantified and recorded which is correlated with flaw size. If the response exceeds a defined decision threshold, a positive flaw indication can be given by the POD function.

The POD(a) function can be obtained from the relationship between the signal response ($\hat{a}$) and a. If $g_a(\hat{a})$ represents the probability density of the values for fixed flaw size a, then:

$$\mathrm{POD}(a) = \int_{\hat{a}_{dec}}^{+\infty} g_a(\hat{a})\,\mathrm{d}\hat{a} \tag{3.55}$$

This calculation is illustrated in figure 3.4, in which the shaded area under the density functions represents the probability of detection.

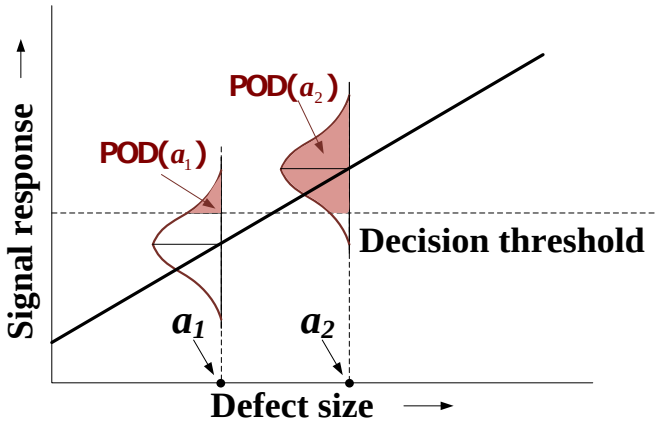

Figure 3.4 Schematic of POD calculation from $\hat{a}$ vs. a relationship.

It can be seen that the POD (a) function is derived from the relationship between $\hat{a}$ and a. Generally, the relationship between $\hat{a}$ and a defines the mean of $g_a(\hat{a})$, which is:

$$\hat{a} = g_a(\hat{a}) + \delta = \mu(a) + \delta \tag{3.56}$$

where $\mu(a)$ is the mean of $g_a(\hat{a})$ and δ is a random error term accounting for the differences between $\hat{a}$ and $\mu(a)$. The distributional property of δ determines the probability density $g_a(\hat{a})$ about $\mu(a)$. It is an acceptable assumption that δ is normally distributed with zero mean and constant standard deviation if the decision threshold is properly set.

For different kinds of the response data, there are always four $\hat{a}$ vs. a relationships, i.e., $\hat{a}$ vs. a, $\hat{a}$ vs. ln(a), ln($\hat{a}$) vs. a, ln($\hat{a}$) vs. ln(a). The following POD calculation process takes the $\hat{a}$ vs. a relationship as an example. Based on equation 3.56, this relationship is updated as:

$$\hat{a} = \alpha + \beta a + \delta \tag{3.57}$$

Equation 3.57 shows that $\hat{a}$ is normally distributed with mean $\alpha + \beta a$ and constant standard deviation σ_δ.

The POD(a) can be rewritten as:

$$\mathrm{POD}(a) = P\{\hat{a}_{dec} < \hat{a}\} \tag{3.58}$$

It is the area under $g_a(\hat{a})$ and above the threshold $\hat{a}_{dec}$. By using the notation of the standard normal distribution, equation 3.58 can be written as:

$$\mathrm{POD}(a) = 1 - \Phi\left(\frac{\hat{a}_{dec} - (\alpha + \beta a)}{\sigma_\delta}\right) \tag{3.59}$$

Based on the symmetry of normal distribution, equation 3.59 can be rewritten as:

$$\mathrm{POD}(a) = \Phi\left(\frac{a - (\hat{a}_{dec} - \alpha)/\beta}{\sigma_\delta / \beta}\right) \tag{3.60}$$

Equation 3.60 is a cumulative normal distribution function with its mean μ and standard deviation σ of the following forms:

$$\mu = (\hat{a}_{dec} - \alpha)/\beta \tag{3.61}$$

$$\sigma = \sigma_\delta / \beta \tag{3.62}$$

For estimating α, β, and σ_δ from $\hat{a}$ vs. a relationship can be achieved by using the maximum likelihood method.

3.3.4 *Parameter estimation and confidence bound calculation*

3.3.4.1 *Parameter estimation*

As a standard statistical technique, maximum likelihood estimates (MLE) analysis is widely used for parameter estimation based on the principle of choosing estimated values that are most likely to have produced the observed outcome, i.e., maximising the probability of the recorded data [238]. The following briefly shows how the MLE is used to estimate the model parameters from the recorded data.

Suppose Y_i represents the result of the i^{th} inspection and $f(y_i;\boldsymbol{\theta})$ gives the probability of obtaining Y_i, where $\boldsymbol{\theta}=(\theta_1, \theta_2,\ldots, \theta_k)'$ is the vector of the k parameters in the probability model. For the hit/miss data, Y_i can only be 0 or 1. For the signal response data as defined by equation 3.56, Y_i is the signal response, and $f(y_i;\boldsymbol{\theta})$ is a normal density function with mean and standard deviation given by $\boldsymbol{\theta}=(\alpha + \beta\, a, \sigma)'$. Let $Y_1,\ldots, Y_n$ represent the results of independent inspections of n defects. Given a group of the test results $\boldsymbol{Y}$, the likelihood function of $\boldsymbol{\theta}$ is equivalent to the joint probability function of $\boldsymbol{Y}$, which is expressed as:

$$L(\boldsymbol{\theta};\boldsymbol{y}) = \prod_{i=1}^{n} f(y_i;\boldsymbol{\theta}) \tag{3.63}$$

For a given result, Y_i is known and equation 3.63 is only a function of $\boldsymbol{\theta}$. For the models considered, it is more convenient to work with the natural log form and the log-likelihood function is:

$$\ln\{L(\boldsymbol{\theta})\} = \sum_{i=1}^{n} \ln\{f(y_i;\boldsymbol{\theta})\} \tag{3.64}$$

The maximum likelihood estimate is denoted $\hat{\boldsymbol{\theta}}$, which maximises ln $\{L(\boldsymbol{\theta})\}$. The maximum likelihood estimate $\hat{\boldsymbol{\theta}}$ can be obtained by solving the likelihood equation, also known as the score equation:

$$\frac{\partial \ln\{L(\boldsymbol{\theta})\}}{\partial \boldsymbol{\theta}} = \sum_{i=1}^{n} \frac{\partial \ln\{f(y_i;\boldsymbol{\theta})\}}{\partial \boldsymbol{\theta}} = 0, \quad i = 1, \ldots, k \tag{3.65}$$

Usually, Newton-Raphson method is used to find $\hat{\boldsymbol{\theta}}$.

3.3.4.2 *Confidence bound calculation*

Because the POD(a) function is equivalent to a cumulative distribution function and the parameters are estimated by using the maximum likelihood, a method developed by Cheng and Iles [239, 240] can be used to calculate lower confidence bounds. These bounds are calculated from the variance-covariance matrix of the estimates, which reflect the sensitivity to the number and sizes of flaws in the tested specimens.

The maximum likelihood estimates, $\hat{\theta}_i$, are asymptotically joint normally distributed with means given by the true parameter values, θ_i, and the variance-covariance matrix defined by:

$$\boldsymbol{V} = \boldsymbol{I}^{-1} \tag{3.66}$$

where, $\boldsymbol{I}$ is the information matrix with its elements $\boldsymbol{I}_{ij}$ are the expected values:

$$I_{ij} = -\mathrm{E}\left(\frac{\partial^2}{\partial\theta_i \partial\theta_j} \ln f(y_i;\boldsymbol{\theta})\right), \quad i, j = 1, \ldots, k \tag{3.67}$$

In many cases, the assumed models will be the logit and cumulative log-normal distribution functions. However, other models can also be used if the evidence is available to support their selection. If the POD(a) model is a cumulative log-normal distribution function with the parameter vector $\boldsymbol{\theta}=(\mu,\sigma)'$. The information matrix, $\boldsymbol{I}$, can be written in the form:

$$\boldsymbol{I}(\hat{\mu},\hat{\sigma}) = \frac{n}{\sigma^2}\begin{pmatrix} k_0 & -k_1 \\ -k_1 & k_2 \end{pmatrix} \tag{3.68}$$

where, n is the number of tests.

The lower one-sided confidence bound of the POD(a) function is given by:

$$\mathrm{POD}_{\alpha}(a) = \Phi(\hat{z} - h) \tag{3.69}$$

where, α is the significance level. $\Phi(\cdot)$ is the standard cumulative normal distribution.

$$\hat{z} = \frac{\ln a - \hat{\mu}}{\hat{\sigma}} \tag{3.70}$$

$$h = \left(\frac{\gamma}{nk_0}\left(1 + \frac{(k_0\hat{z} + k_1)^2}{k_0 k_2 - k_1^2}\right)\right)^{\frac{1}{2}} \tag{3.71}$$

where is γ obtained from table 3.2 for the number of cracks in the experiment and the desired confidence level.

Table 3.2 Values of γ for lower confidence bounds on the POD(a) function [233]

Sample size		20	25	30	40	50	60	80	100	∞
γ	90 %	3.903	3.884	3.871	3.855	3.846	3.839	3.831	3.827	3.808
	95 %	5.243	5.222	5.208	5.191	5.180	5.173	5.165	5.159	5.138

3.3.4.3 *Estimation of hit/miss data*

Estimation of the parameters of any POD(a) model for hit/miss data is based directly on the probability of each 0 or 1 result of an inspection. Assume that a balanced experiment has produced k inspections on each of n cracks. For this application, the likelihood function is given by:

$$L(\mu,\sigma)=\prod_{i=1}^{n}\prod_{j=1}^{k}p_i^{Z_{ij}}(1-p_i)^{Z_{ij}} \tag{3.72}$$

where Z_{ij} denotes the j^{th} inspection of the i^{th} flaw with a find (*1*) or a miss (*0*). The previous equations 3.51-3.54 define the probability of detecting a flaw of size *a*.

The log-likelihood form of equation 3.72 is:

$$\ln L(\mu,\sigma)=\sum_{i=1}^{n}\sum_{j=1}^{k}(Z_{ij}\ln(p_i)+(1-Z_{ij})\ln(1-p_i)) \tag{3.73}$$

The parameters to be estimated is μ and σ. Their maximum likelihood estimates, $\hat{\mu}$ and $\hat{\sigma}$, are the solutions to:

$$\frac{\partial \ln L(\mu,\sigma)}{\partial\mu}=\sum_{i=1}^{n}\sum_{j=1}^{k}\left(\frac{Z_{ij}}{p_i}\frac{\partial p_i}{\partial\mu}+\frac{1-Z_{ij}}{1-p_i}\frac{\partial p_i}{\partial\mu}\right)=0 \tag{3.74}$$

$$\frac{\partial \ln L(\mu,\sigma)}{\partial\sigma}=\sum_{i=1}^{n}\sum_{j=1}^{k}\left(\frac{Z_{ij}}{p_i}\frac{\partial p_i}{\partial\sigma}+\frac{1-Z_{ij}}{1-p_i}\frac{\partial p_i}{\partial\sigma}\right)=0 \tag{3.75}$$

Here, suppose the logit function (equation 3.47) is selected since it is the most commonly used model. If this model has a linear relationship with ln(*a*), it can be expressed as:

$$\ln\left(\frac{\mathrm{POD}(a)}{1-\mathrm{POD}(a)}\right)=\alpha+\beta\ln a \tag{3.76}$$

Further, the logit link (equation 3.51) is updated as:

$$\mathrm{POD}(a)=\frac{\exp(\alpha+\beta\ln a)}{1+\exp(\alpha+\beta\ln a)} \tag{3.77}$$

Since α and β in equation 3.77 are not interpretable in the physical meaning, a mathematically equivalent form is given by [237]:

$$\mathrm{POD}(a)=\frac{h(a)}{1+h(a)} \tag{3.78}$$

where, $h(a)$ has the form of:

$$h(a)=\exp\left(\frac{\pi}{\sqrt{3}}\left(\frac{\ln a-\mu}{\sigma}\right)\right) \tag{3.79}$$

where, μ and σ have the forms of:

$$\mu = -\alpha / \beta \tag{3.80}$$

$$\sigma = \pi / (\sqrt{3}\beta) \tag{3.81}$$

By substituting equations 3.78 into equations 3.74 and 3.75 and taking the derivatives, they become:

$$\sum_{i=1}^{n}\sum_{j=1}^{k}\frac{Z_{ij}}{k} - \sum_{i=1}^{n}\frac{h(a_i)}{1+h(a_i)} = 0 \tag{3.82}$$

$$\sum_{i=1}^{n}\sum_{j=1}^{k}\frac{Z_{ij}}{k}\ln(a_i) - \sum_{i=1}^{n}\frac{\ln(a_i)h(a_i)}{1+h(a_i)} = 0 \tag{3.83}$$

Any standard computational method, such as the Newton-Raphson iterative procedure can be used to find the solutions to equations 3.82 and 3.83. After obtaining the estimated parameters ($\hat{\mu},\hat{\sigma}$), the logit POD(a) can be easily calculated by:

$$\mathrm{POD}(a) = \Phi\left(\frac{\ln(a) - \hat{\mu}}{\hat{\sigma}}\right) \tag{3.84}$$

where, $\Phi(\cdot)$ is the standard cumulative normal distribution.

For the confidence bound calculation in hit/miss data, the information matrix is estimated from equation 3.67, using estimated $\hat{\boldsymbol{\theta}} = (\hat{\mu},\hat{\sigma})'$ for $\boldsymbol{\theta}$. For this POD(a) model, the elements of the information matrix are given by:

$$I_{11} = \frac{1}{\sigma^2}\frac{\pi^2}{3}\sum_{i=1}^{n}\frac{h(a_i)}{(1+h(a_i))^2} = \frac{nk_0}{\sigma^2} \tag{3.85}$$

$$I_{12} = I_{21} = \frac{1}{\sigma^2}\frac{\pi^2}{3\sigma}\sum_{i=1}^{n}\frac{\ln(a_i)h(a_i)}{(1+h(a_i))^2} = -\frac{nk_1}{\sigma^2} \tag{3.86}$$

$$I_{22} = \frac{1}{\sigma^2}\frac{\pi^2}{3\sigma^2}\sum_{i=1}^{n}\frac{\ln(a_i)^2 h(a_i)}{(1+h(a_i))^2} = \frac{nk_2}{\sigma^2} \tag{3.87}$$

$\hat{\boldsymbol{\theta}}$ together with the above equations gives all the parameters ($\hat{\mu}$, $\hat{\sigma}$, k_0, k_1, and k_2) required by equations 3.85-3.87 to calculate the lower confidence bound on the POD(a) function are available.

For other model functions (equations 3.48-3.50), the parameter estimation and confidence bound calculation can be achieved by following the similar steps above.

3.3.4.4 *Estimation of signal response data*

In the signal response data analysis, the parameter vector of the POD(a) function is calculated from the $\hat{a}$ versus a relationship. If all the $\hat{a}$ values are between the threshold value and the saturation limit, a simple regression analysis yields the necessary information to estimate the POD curve and its lower confidence bound. In this situation, the least-square estimates from the regression analysis also happen to be the maximum likelihood estimates. If the $\hat{a}$ values are censored below the threshold or above the saturation limit, a more general analysis will give answers identical to those of the regression analysis if all values are available for all the flaws [241].

In the response signal analysis, it is assumed that the $\hat{a}$ values for a flaw of size a have a normal distribution with mean $\alpha + \beta \ln a$ and constant standard deviation σ_δ. To simplify the notation, let $Y=\ln(\hat{a})$ and $X=\ln(a)$. The random variable has a standard normal distribution:

$$Z = \frac{Y - (\alpha + \beta X)}{\sigma_\delta} \tag{3.88}$$

Let $\phi(z)$ represent the density function of the standard normal distribution:

$$\phi(z) = \frac{1}{\sqrt{2\pi}} e^{-\frac{1}{2}z^2} \tag{3.89}$$

and $\Phi(z)$ represent the cumulative normal distribution:

$$\Phi(z) = \int_{-\infty}^{z} \phi(\xi) d\xi \tag{3.90}$$

The likelihood function is partitioned into three regions: (1) Region *R*, for which values are recorded; (2) Region *T*, for which only a maximum value is known (the values fall below the recording signal threshold and cannot be recorded); (3) Region *S*, for which only a minimum value is known (the values fall above the saturation limit and cannot be recorded).

The likelihood function for the entire sample is the product of the likelihood functions for the three regions:

$$L(\alpha, \beta, \sigma_\delta) = \prod_R L_R \prod_T L_T \prod_S L_S \tag{3.91}$$

By suppressing the dependency of L on α, β, and σ_δ:

$$L_R = \prod_{i=1}^{r} \frac{1}{\sigma_\delta} \phi(Z_i) \tag{3.92}$$

$$L_T = \prod_{i=1}^{t} \Phi_i(a_{th}) \tag{3.93}$$

$$L_S = \prod_{i=1}^{s} (1 - \Phi_i(a_{sat})) \tag{3.94}$$

where, $\frac{1}{\sigma_\delta}\phi(Z_i)$ is the probability of observing $\ln(\hat{a})$ for the i^{th} flaw in R. $\Phi_i(a_{th})$ is the probability of obtaining a $\ln(\hat{a})$ value below the recording threshold for the i^{th} flaw in T. $1-\Phi_i(a_{sat})$ is the probability of obtaining a $\ln(\hat{a})$ value above the saturation limit for the i^{th} flaw in S. r is the number of flaws in R. t is the number of the flaws with $\ln(\hat{a})$ below the recording threshold, a_{th}. s is the number of the flaws with $\ln(\hat{a})$ above the saturation limit, a_{sat}.

By substituting equations 3.92-3.94, the log form of the likelihood function is:

$$\begin{aligned} &\ln L(\alpha, \beta, \sigma_\delta) = \\ &-r \ln(\sigma_\delta) - \frac{1}{2\sigma_\delta^{\,2}} \sum_R (Y - (\alpha + \beta X))^2 + \sum_T \ln \Phi_i(a_{th}) + \sum_S \ln(1 - \Phi_i(a_{sat})) \end{aligned} \tag{3.95}$$

The parameters to be estimated is α, β, and σ_δ. Their maximum likelihood estimates are the solutions to:

$$\frac{\partial \ln L}{\partial \alpha} = \frac{1}{\sigma_\delta} \left(\sum_R Z_i + \sum_S V(Z_i) + \sum_T W(Z_i) \right) = 0 \tag{3.96}$$

$$\frac{\partial \ln L}{\partial \beta} = \frac{1}{\sigma_\delta} \left(\sum_R X_i Z_i + \sum_S X_i V(Z_i) + \sum_T X_i W(Z_i) \right) = 0 \tag{3.97}$$

$$\frac{\partial \ln L}{\partial \sigma_\delta} = \frac{1}{\sigma_\delta} \left(-r + \sum_R Z_i^2 + \sum_S Z_i V(Z_i) + \sum_T Z_i W(Z_i) \right) = 0 \tag{3.98}$$

where,

$$V(Z_i) = \frac{\phi(Z_i)}{1 - \Phi(Z_i)} \tag{3.99}$$

$$W(Z_i) = \frac{\phi(Z_i)}{\Phi(Z_i)} \tag{3.100}$$

Similarly, the Newton-Raphson iterative procedure can be used to find the solutions to equations 3.96-3.98.

The calculation of the lower confidence bound consists of five steps:

(1) The information matrix $\boldsymbol{I}(\hat{a}, \hat{\beta}, \hat{\sigma}_\delta)$ is obtained using equation 3.67;

(2) The variance-covariance matrix $\boldsymbol{V}(\hat{a}, \hat{\beta}, \hat{\sigma}_\delta)$ is obtained by inverting the information matrix $\boldsymbol{I}$ (equation 3.66);

(3) The variance-covariance matrix $\boldsymbol{V}(\hat{\mu}, \hat{\sigma})$ is calculated based on a first-order Taylor series expansion of the equations 3.61 and 3.62;

(4) The information matrix $\boldsymbol{I}(\hat{\mu}, \hat{\sigma})$ (equation 3.68) is obtained by inverting the variance-covariance matrix $\boldsymbol{V}(\hat{\mu}, \hat{\sigma})$;

(5) The calculated values are substituted into equations 3.69-3.71 to obtain the lower confidence bound.

The elements of the information matrix $\boldsymbol{I}(\hat{a}, \hat{\beta}, \hat{\sigma}_\delta)$ are given by:

$$I_{11} = -\frac{\partial^2 \ln(L)}{\partial \alpha^2} = \frac{1}{\sigma_\delta^2}(r + \sum_S \lambda(Z) - \sum_T \psi(Z)) \tag{3.101}$$

$$\begin{aligned} I_{12} = I_{21} &= -\frac{\partial^2 \ln(L)}{\partial \alpha \, \partial \beta} \\ &= \frac{1}{\sigma_\delta^2}(\sum_R X + \sum_S X\lambda(Z) - \sum_T X\psi(Z)) \end{aligned} \tag{3.102}$$

$$\begin{aligned} I_{13} = I_{31} &= -\frac{\partial^2 \ln(L)}{\partial \alpha \, \partial \sigma_\delta} \\ &= \frac{1}{\sigma_\delta^2}(2\sum_R Z + \sum_S V(Z) + \sum_S Z\lambda(Z) - \sum_T W(Z) - \sum_T Z\psi(Z)) \end{aligned} \tag{3.103}$$

$$\begin{aligned} I_{22} &= -\frac{\partial^2 \ln(L)}{\partial \beta^2} \\ &= \frac{1}{\sigma_\delta^2}(\sum_R X^2 + \sum_S X^2\lambda(Z) - \sum_T X^2\psi(Z)) \end{aligned} \tag{3.104}$$

$$I_{23} = I_{32} = -\frac{\partial^2 \ln(L)}{\partial\beta\,\partial\sigma_\delta} = \frac{1}{\sigma_\delta^2}(2\sum_R XZ + \sum_S XV(Z) + \sum_S XZ\lambda(Z) - \sum_T XW(Z) - \sum_T XZ\psi(Z)) \tag{3.105}$$

$$I_{22} = -\frac{\partial^2 \ln(L)}{\partial\sigma_\delta^2} = \frac{1}{\sigma_\delta^2}(-r + 3\sum_R Z^2 + 2\sum_S ZV(Z) + \sum_S Z^2\lambda(Z) - 2\sum_T ZW(Z) - \sum_T Z^2\psi(Z)) \tag{3.106}$$

where,

$$\lambda(Z) = V(Z)\ (V(Z) - Z) \tag{3.107}$$

$$\psi(Z) = W(Z)\ (W(Z) + Z) \tag{3.108}$$

Let $\boldsymbol{V}(\hat{a},\hat{\beta},\hat{\sigma}_\delta)$ represent the variance-covariance matrix of the maximum likelihood estimates and its elements are defined as:

$$\boldsymbol{V}(\hat{a},\hat{\beta},\hat{\sigma}_\delta) = \begin{pmatrix} \sigma_\alpha^2 & \sigma_{\alpha\beta} & \sigma_{\alpha\delta} \\ \sigma_{\alpha\beta} & \sigma_\beta^2 & \sigma_{\beta\delta} \\ \sigma_{\delta\alpha} & \sigma_{\delta\beta} & \sigma_\delta^2 \end{pmatrix} = \boldsymbol{I}(\hat{a},\hat{\beta},\hat{\sigma}_\delta)^{-1} \tag{3.109}$$

The Delta method is used for determining the asymptotic properties of $\boldsymbol{V}(\hat{\mu},\hat{\sigma})$ from $\boldsymbol{V}(\hat{a},\hat{\beta},\hat{\sigma}_\delta)$. Using a Taylor series approximation to linearize the relationships expressed by equations 3.61 and 3.62, $\boldsymbol{V}(\hat{\mu},\hat{\sigma})$ is given by:

$$\boldsymbol{V}(\hat{\mu},\hat{\sigma}) = \boldsymbol{T}^T\boldsymbol{V}(\hat{a},\hat{\beta},\hat{\sigma}_\delta)\boldsymbol{T} = \begin{pmatrix} \sigma_{\hat{\mu}}^2 & \sigma_{\hat{\mu}\hat{\sigma}} \\ \sigma_{\hat{\sigma}\hat{\mu}} & \sigma_{\hat{\sigma}}^2 \end{pmatrix} \tag{3.110}$$

where, $\boldsymbol{T}$ is the transformation matrix defined as:

$$\boldsymbol{T} = \begin{pmatrix} \frac{\partial\mu}{\partial\alpha} & \frac{\partial\sigma}{\partial\alpha} \\ \frac{\partial\mu}{\partial\beta} & \frac{\partial\sigma}{\partial\beta} \\ \frac{\partial\mu}{\partial\sigma_\delta} & \frac{\partial\sigma}{\partial\sigma_\delta} \end{pmatrix} = \frac{1}{\beta}\begin{pmatrix} 1 & 0 \\ \hat{\mu} & \hat{\sigma} \\ 0 & -1 \end{pmatrix} \tag{3.111}$$

The elements of $\boldsymbol{V}(\hat{\mu},\hat{\sigma})$ are:

$$\sigma_{\hat{\mu}}^2 = \frac{1}{\beta^2}(\sigma_\alpha^2 + 2\hat{\mu}\sigma_{\alpha\beta} + \hat{\mu}^2\sigma_\beta^2) \tag{3.112}$$

$$\sigma_{\hat{\mu}\hat{\sigma}} = \sigma_{\hat{\sigma}\hat{\mu}} = \frac{1}{\beta^2}(\hat{\sigma}\sigma_{\alpha\beta} - \sigma_{\alpha\delta} - \hat{\mu}\sigma_{\beta\delta} + \hat{\mu}\hat{\sigma}\sigma_\beta^2) \tag{3.113}$$

$$\sigma_{\hat{\sigma}}^2 = \frac{1}{\beta^2}(\sigma_\delta^2 - 2\hat{\sigma}\sigma_{\beta\delta} + \hat{\sigma}^2\sigma_\beta^2) \tag{3.114}$$

Inverting $\boldsymbol{V}(\hat{\mu},\hat{\sigma})$ yields $\boldsymbol{I}(\hat{\mu},\hat{\sigma})$ and the values of k_0, k_1, and k_2 can be obtained. These values are required in equation 3.71 to calculate the lower confidence bound on the POD(a) function.

3.4 Thermal Features/Patterns of ECPT for Defect Characterisation and POD Analysis

Based on the fundamentals of ECPT and POD analysis, this section briefly introduces and discusses various temporal- and spatial-thermal features/patterns, which will be used in the case studies. For a better illustration, the thermal data of testing an angular defect, i.e., Slot S_2 of Specimen *1* in figure 4.4(a), is used as an example to derive all the thermal features/patterns. In the case study chapters, the proposed features/patterns are used for characterising angular defects and RCF cracks. In this work, the simplest fitting function, linear fitting, is used to describe the relationships between various features and geometric parameters of defects. The main reason for using linear fitting is that RCF cracks investigated are in the light stage and the moderate stage. Geometric parameters of these RCF cracks are within narrow ranges and their relationships to features are approximated by linear fitting.

3.4.1 *Spatial domain-based features*

3.4.1.1 *Maximum thermal rise/response*

Figure 3.5(a) shows the thermal distribution of Slot S_2 in Specimen *1*, later introduced in Section 4.3.2. This thermal distribution is captured at 100 ms, i.e., at the end of 100 ms heating pulse. At this time, the pixel with the highest thermal rise/response is shown by the red dot, i.e., maximum thermal pixel which is denoted as P_m. Most of the thermal features/patterns introduced later are based on P_m. Figure 3.5(b) illustrates the transient response of this pixel within 1000 ms. In this case, its maximum thermal rise (T_{max}) is 10.12℃, which can be used as a simple but very basic feature to build the relationship to defect parameters.

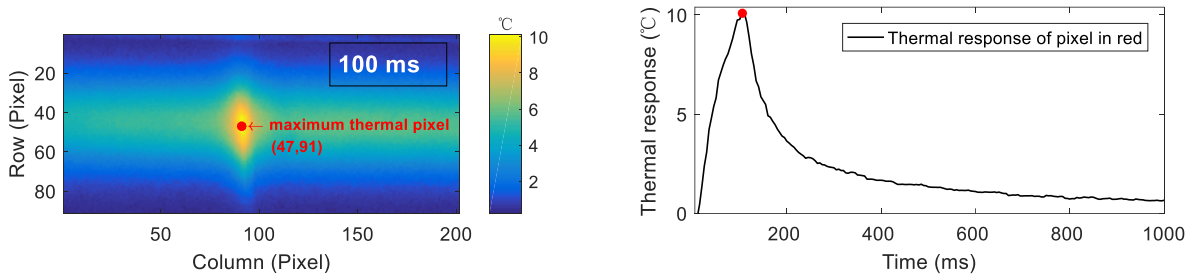

(a) (b)

Figure 3.5 Thermal distribution and response of Slot S_2 in Specimen *1*.
(a) Thermal distribution of ROI at 100 ms with background subtraction. (b) Thermal response of the pixel denoted by the red dot in (a).

3.4.1.3 *Spatial skewness- and kurtosis-based features*

Additionally, five parallel-neighbour lines are plotted on the thermal distribution of Slot S_2 in Specimen *1*, as shown in figure 3.6(a). Each of them contains 41 pixels (covering both sides of the inclined slot) and the middle line just goes across the P_m. Figure 3.6(b) shows the spatial thermal rise values of along five neighbour lines. Two spatial features, i.e., spatial skewness- and kurtosis-based features, are introduced here. These two features are derived from the thermal distribution at the end of the heating stage, which are denoted as SS_T and SK_T.

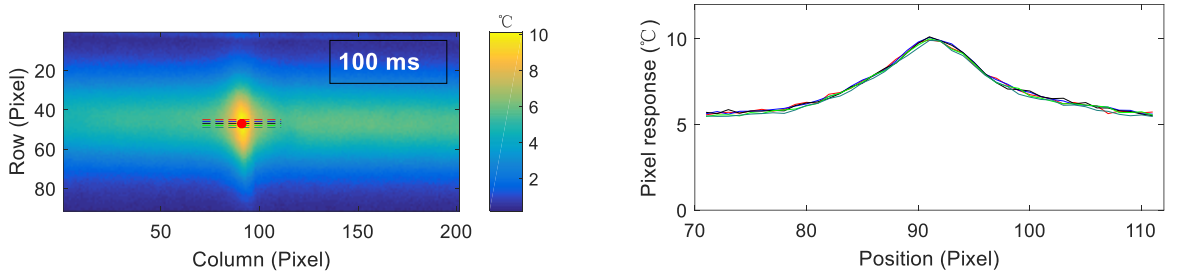

(a) (b)

Figure 3.6 Thermal distribution and line-scan results of Slot S_2 in Specimen *1*.
(a) Thermal distribution of ROI at 100 ms. Five parallel-neighbour lines in different colours are plotted with the middle line going across the P_m. (b) Line-scan results from (a).

Skewness measures the asymmetry (or lopsidedness) of a statistical distribution. The skewness for any symmetric distribution is zero. The skewness can also be either negative or positive to quantitatively show the difference from a symmetric distribution. A negative skewness means that a distribution is skewed to the left or the tail is on the left side of the distribution. On the other hand, a positive skewness shows a right-skewed distribution or a right-side tail. The skewness for a distribution is defined as:

$$s(X) = \frac{E(X-\mu)^3}{\sigma^3} \tag{3.115}$$

where, X represents the spatial (line-scan) thermal data at a specific time, which is 100 ms in this case. μ and σ are the mean and the standard deviation of X, respectively. $E(\cdot)$ is the expectation.

Different from skewness, kurtosis measures whether a data distribution is heavy-tailed or light-tailed compared to a normal distribution. The kurtosis for a standard normal distribution is three. Distributions with high kurtosis tend to have heavy tails (outliers), whereas distributions with low kurtosis tend to have light tails. The kurtosis is the normalised fourth central moment of a distribution:

$$k(X) = \frac{E(X-\mu)^4}{\sigma^4} \tag{3.116}$$

These two features can be used to measure the asymmetry and outlier of the statistically spatial thermal distribution shown in figure 3.6(b).

3.4.1.2 *First-order differential imaging*

First-order differential of original thermal data can be used to investigate the distribution and the response of heating/cooling rate. Figure 3.7(a) shows the first-order differential image of Slot S_2. This image is obtained by first sliding (neighbour frame difference) the original thermal video and then selecting at the specific time (30 ms). This specific time is when the first-order differential of P_m reaches its maximum value. Figure 3.7(b) shows the spatial values of the imaging result along five neighbour lines in figure 3.7(a). Each line has 121 pixels aiming to include the thermal response on both sides of the slot. The sum of the average values along the five neighbour lines is denoted by A_{diff1}.

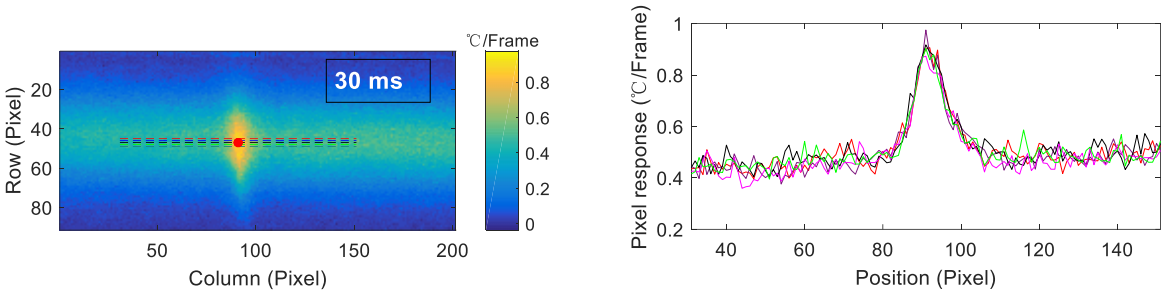

(a) (b)

Figure 3.7 First-order differential imaging of Slot S_2 in Specimen *1*.
(a) First-order differential imaging of ROI at 30 ms. Five parallel-neighbour lines are plotted with the middle line going across the P_m. (b) Spatial values along five neighbour lines.

3.4.2 *Temporal domain-based features*

Before introducing several temporal domain-based features, a zero-lag filter is first proposed here. Temporal domain-based features depend strongly on the calculation time slot. Commonly-used filters will introduce lag and then affect the time slot setting. To accurately retain key feature points, e.g., the maximum response time, in filtered data where they occur in the original-unfiltered data, a zero-lag filter based on the Hamming window is proposed. The idea of zero-lag filtering is processing the input temporal response data in both the forward and reverse directions [242]. The filtered data has the characteristics of zero-phase distortion.

Specifically, a 11-point symmetric Hamming window-based finite impulse response lowpass filter is used, which is defined as:

$$w[n] = a_0 + (1 - a_0)\cos(\frac{2\pi n}{N}), \qquad 0 \le n \le N \tag{3.117}$$

where, a_0 is 25/46, and N is 10.

This 11-point window can smooth signals without taking much computing time. Additionally, since the maximum frame rate (sample rate) of the FLIR A655sc is 200 Hz and low frequencies are of much interest to defect detection, the cut-off frequency is set to 15 Hz. The filter coefficients are given by the following equation:

$$x[n] = h[n] \cdot w[n] \tag{3.118}$$

where, h [n] is the unwindowed impulse response.

3.4.2.1 *Area-based feature*

Figure 3.8 further shows the normalised thermal response and its first-order differential response. Since we are more interested in the change rate of thermal response without consideration for the sign (+ -), only the absolute value of first-order differential response is plotted. Note that all the curves in this figure are normalised to (0,1). The peak of the thermal response separates the heating stage and the cooling stage. The first peak of the first-order differential response presents the highest heating rate, whereas the second peak gives the highest cooling rate. Based on selecting a time slot of the heating stage or the cooling stage, the sum-up value of the thermal response curve or the absolute value of first-order differential response curve, i.e., area under the curve, can be obtained. The sum-up values from the thermal response and the first-order differential response are denoted as SUM_{T} and SUM_{diff1},

respectively. For the heating stage, the time slot of calculating SUM_T or SUM_{diff1} can be set as any range varying from the start to the end of excitation. For the cooling stage, the time slot can be set varying from the end of excitation to the end of the recording time. Furthermore, the time slot can be chosen including both the heating and the cooling stages. The time slot selection depends on the period of interest to be investigated, e.g., early/later heating slots, early/later cooling slots.

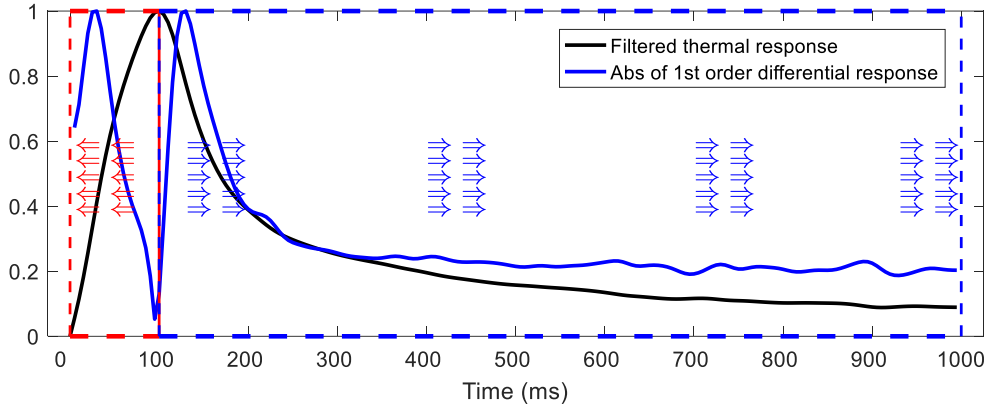

Figure 3.8 Normalised thermal response and first-order differential response. They are the response of P_m when Slot S_2 in Specimen *1* is tested. The heating stage and the cooling stage are shown by the red-dashed box and the blue-dashed box, and they are separated by the time when P_m reaches to T_{max}.

3.4.2.2 *Temporal skewness- and kurtosis-based features*

Apart from the area-based features (SUM_T and SUM_{diff1}), the characteristics of thermal response and its first-order differential responses in figure 3.8 can also be measured by skewness and kurtosis. Here, the skewness (denoted as S_T and S_{diff1}) is used to measure the asymmetry of the histogram derived from either the thermal or first-order differential response. The kurtosis (denoted as K_T and K_{diff1}) is used here to measure whether the histogram is heavy-tailed or light-tailed. It can be assumed that slots with different inclination angles and pocket lengths have individual thermal responses and further affect skewness and kurtosis values. The equation used to calculate the temporal skewness and kurtosis are the same as equations 3.115 and 3.116. The only difference is that the X in these two equations represents the transient normalised thermal response or first-order differential response within a specific time slot.

3.4.3 *Tempo-spatial-based patterns*

3.4.3.1 *Ratio mapping based on first-order differential result*

Figure 3.7(a) shows a spatial distribution at the early heating response (30 ms is about one-third of the 100 ms heating pulse). However, this image is based on the specific time when the first-order differential result reached to the maximum value and this time apparently will vary with different heating pulses. Here, the ratio mapping of the first-order differential result is introduced to automatically compress the video information of the ROI into one image. Note that the first-order differential data used here is the original data without taking normalised or absolute values. Figure 3.9(a) shows the ratio mapping result of Slot S_2. The ratio equation used here is:

$$R = \frac{T'_{max}(t) + T'_{min}(t)}{T'_{max}(t) - T'_{min}(t)} \tag{3.119}$$

where, T'_{max} and T'_{min} are the max and min first-order-differential values of each pixel.

Figure 3.9(b) gives the spatial values of the ratio mapping result along five neighbour lines. The sum of the average values along the five neighbour lines is denoted by A_{ratio}.

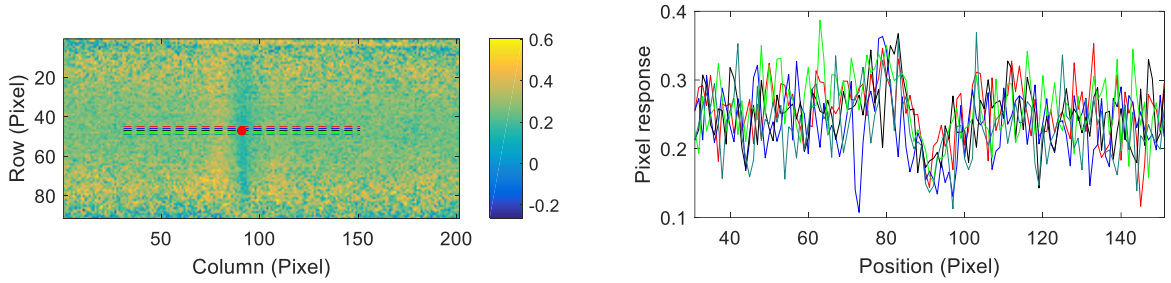

(a) (b)

Figure 3.9 Ratio mapping from first-order differential result of Slot S_2.
(a) Ratio mapping of ROI. (b) Spatial values along five neighbour lines.

3.4.3.2 *PCA-based thermal pattern*

Apart from using the ratio mapping to compress the thermal video information, the thermal data can also be presented by a set of linearly uncorrelated variables using principal component analysis (PCA). These principal components are arranged in order of decreasing variance. For the thermal video, the aim of using PCA is to maximise the contrast between defective and sound areas. Since the thermal video/sequences are stored as a three-dimensional matrix, in order to apply PCA this matrix need to be converted into a two-dimensional matrix (T) with the numbers of the columns and rows representing the total

pixels and frames, respectively. In this work, singular value decomposition is used to decompose the two-dimensional thermal matrix [243]:

$$T = URV^T \tag{3.120}$$

where, U is a matrix consisting of a set of empirical orthogonal functions (EOFs) as its columns. These EOFs characterise the spatial variations of T [244]. Typically, the first two or three EOFs can adequately represent the spatial variations of T. R is a diagonal matrix with the singular values of T. And V is an orthogonal matrix with its columns as the principal components, which describe the time variations of T.

Figure 3.10(a) shows the spatial distribution of the first EOF, which is manually selected and presents the most abnormal thermal pattern. Here, the time slot of calculating EOFs is 1000 ms. In fact, various time slots in the heating stage or cooling stage can be set for PCA, which means that the calculation of EOFs depends on both temporal and spatial inputs. Figure 3.10(b) shows the spatial values along five neighbour lines. The sum of the average values along the five neighbour lines is denoted as $A_{\text{T-PCA}}$.

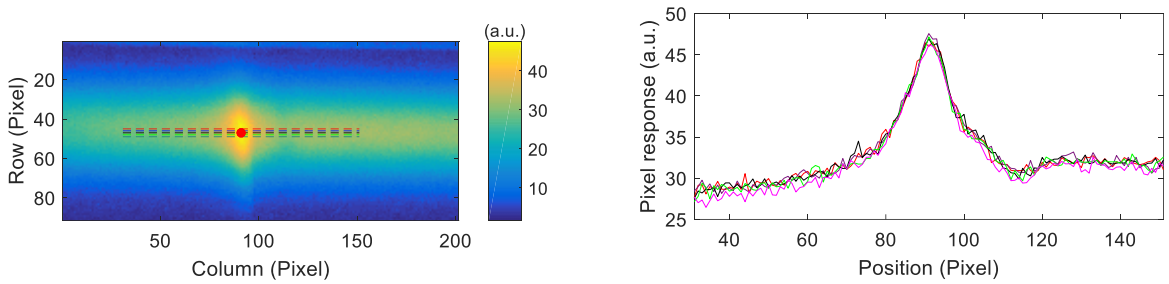

(a) (b)

Figure 3.10 PCA-based thermal pattern of Slot S_2.
(a) PCA-based thermal pattern of ROI (first EOF). (b) Pixel values along five neighbour lines.

3.4.3.3 *PCA-based first-order differential pattern*

Similarly, in equation 3.120, if the two-dimensional matrix (T) is converted from the first-order differential video/sequences, the calculated EOFs can represent the tempo-spatial information of the first-order differential results. Figure 3.11(a) presents the spatial distribution of the first EOF and figure 3.11(b) shows the spatial values along five neighbour lines. The sum of the average values along the five neighbour lines is denoted by $A_{\text{diff1-PCA}}$.

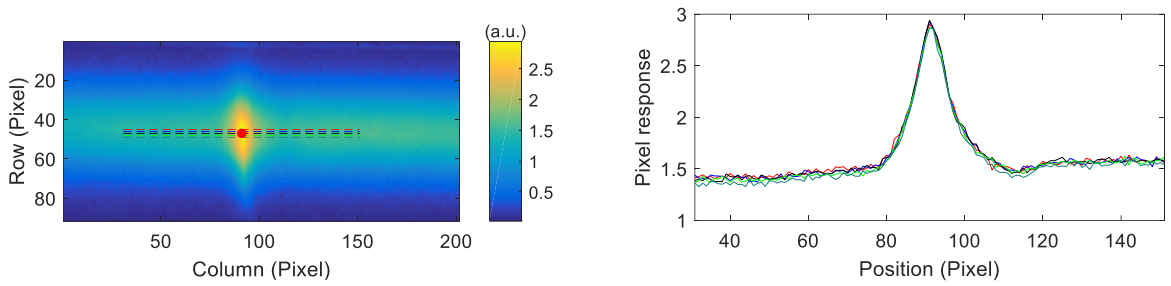

(a) (b)

Figure 3.11 PCA-based first-order differential pattern of Slot S_2.
(a) PCA-based first-order differential pattern of ROI (first EOF). (b) Pixel values along five neighbour lines.

From the above description, three types of thermal features/patterns are briefly introduced. They are four spatial domain-based features (T_{max}, SS_T, SK_T, and A_{diff1}), four temporal domain-based features (SUM_T, SUM_{diff1}, S_T, and S_{diff1}), and three tempo-spatial-based features (A_{ratio}, $A_{T\text{-}PCA}$, and $A_{diff1\text{-}PCA}$). All these features can be used for angular defect and RCF crack characterisation and POD analysis. The detailed discussions can be found in the following case study chapters.

3.5 Chapter Summary

In this chapter, the theoretical background related to ECPT technique is first introduced. The reasons of using ECPT for detecting surface-breaking cracks in metallic materials are theoretically explained. Fundamentals of POD analysis is then presented. By referring POD curves and some critical information (a_{50}, a_{90}, $a_{90/95}$), POD analysis can easily provide a quantitative assessment to evaluate the performance of ECPT for RCF defect characterisation. Based on these backgrounds, types of spatial/temporal domain-based and tempo-spatial-based thermal features/patterns are proposed for further defect characterisation and POD analysis.

By utilising the proposed features, the following two chapters carry out the case studies of detecting angular defects and natural RCF cracks, respectively. The capabilities and performances of these features are compared by POD analysis. Critical analyses and discussions of the experimental results are also provided.

Chapter 4. Angular Defect Characterisation and Performance Evaluation via POD Analysis

4.1 Introduction

Since angular defects are considered as one common representation of idealised RCF cracks, this chapter presents a case study of the angular defect characterisation and the evaluation of features' performances via POD analysis. It starts by proposing a POD analysis framework to guide the case study, which aims to quantitatively evaluate the performance of feature-based defect characterisation. Then, the ECPT configuration and three dedicated specimens that contain artificial angular slots are introduced. Types of features/patterns (introduced in Section 3.4) are used to characterise three main parameters, i.e., pocket length, inclination angle, and vertical depth, of angular defects. Based on the proposed POD analysis framework, the performances of angular defect characterisation using these features are evaluated in the last section. The flow chart of this chapter is shown in figure 4.1 and the detailed discussions are given the following sections.

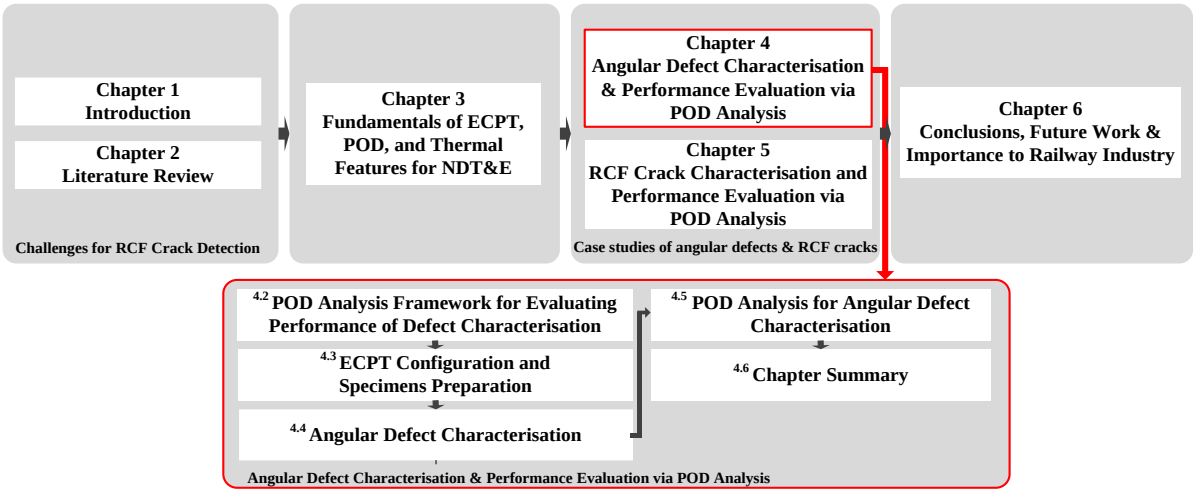

Figure 4.1 Flow chart of Chapter 4.

4.2 POD Analysis Framework for Evaluating Performance of Defect Characterisation

Since the probabilistic performance of feature-based characterisation is evaluated by POD analysis, here a POD analysis framework for defect characterisation is proposed, as shown in figure 4.2. It is initiated by setting the excitation parameters (such as the excitation currents and the heating pulse duration), the camera parameters (such as the resolution and the frame rate), and choosing the type of coil, to build an ECPT configuration. Then, thermal images/videos are preprocessed by choosing the region of interest (ROI), enhancing the contrast in ROI using background subtraction and noise filtering. Further, thermal

features/patterns are extracted for further characterising the geometric parameters of defects. Then, the *R*-squared (R^2), slope, and 2-norm of the residual are compared to evaluate the linearity of the relationship between the extracted features and a specific parameter of the defect. Finally, the POD curves derived from the test data are compared to evaluate different features' performance.

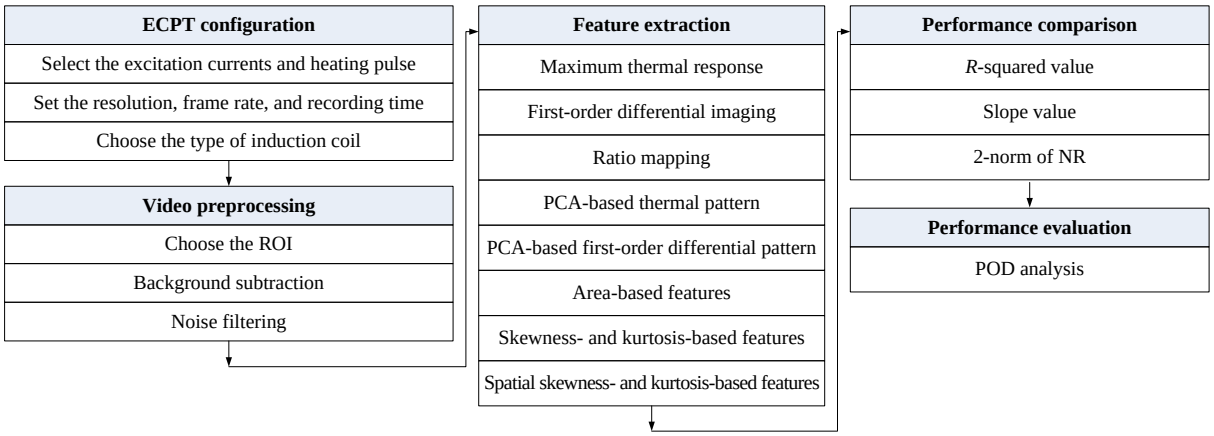

Figure 4.2 POD analysis framework for evaluating performance of defect characterisation.

4.3 ECPT Configuration and Specimens Preparation

In this section, the components and main parameters of ECPT configuration are introduced. The manufacturing of specimens and their material properties and geometric parameters are presented.

4.3.1 *ECPT configuration*

The ECPT configuration used in experimental studies is shown in figure 4.3. Figure 4.3(a) gives its physical layout. It mainly consists of four units, i.e. a heating module with a planar rectangular induction coil, a signal generator, an infrared (IR) camera and a personal computer. The heating module is Easyheat 224 from Cheltenham Induction Heating with the 150-400 kHz working frequency range (automatically tuned to the resonant frequency) and the maximum RMS current of 400 A. The inner and outer diameters of the rectangular coil are 4 mm and 6 mm and its bottom side is used for excitation (equivalent to the linear coil), as illustrated in figure 4.3(b). The signal generator is Agilent 33500B and it is used to synchronously trigger the heating module and the IR camera. The type of IR camera is the FLIR A655sc equipped with an uncooled microbolometer, which has the spectral range of 7.5-14.0 μm and the NETD < 30 mK.

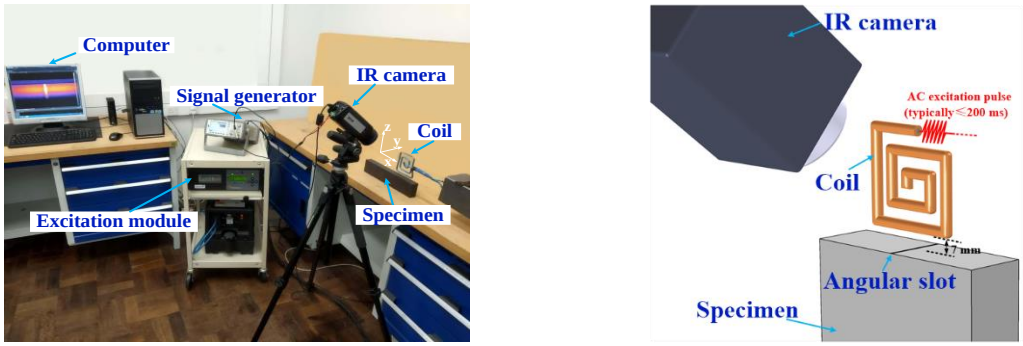

(a) (b)

Figure 4.3 ECPT configuration for angular defect characterisation.
(a) Layout of ECPT configuration. (b) Schematic diagram of ECPT configuration.

4.3.2 *Specimens preparation*

To avoid complexity in modelling RCF cracks, simplifications of the real crack shapes are often required. One common assumption is that the crack shape is semi-elliptical [245, 246], or angular slot [247-249], which lies in a single plane at a shallow angle below the rail surface. Based on the assumption of angular slots, three metal blocks (named as Specimens *1*, *2*, and *3*) made of AISI 1045 medium carbon steel are fabricated as specimens, as shown in figure 4.4. Comparing AISI 1045 with PD3 rail steel (see Section 5.2.2), their material properties are very similar and only the carbon level of AISI 1045 is slightly lower. Each steel block contains a group of artificial angular slots (cut by wire electric discharge machining) to simulate RCF cracks, as shown in figures 4.4(a)-(c). Specimens' material properties can be found in table 4.1. Geometric details of Specimens *2* and *3* can be seen in figures 4.4(d) and (e). Table 4.2 shows the parameters of angular slots. Specimen *1* is used to simulate RCF cracks with a constant inclination angle but different pocket lengths, whereas Specimens *2* and *3* are used to simulate RCF cracks with different inclination angles and varying pocket lengths, which is a more challenge case.

Before conducting the experimental, the top faces of all specimens are uniformly sprayed with the black matt paint to reduce surface reflection. The specimens are placed with the 7 mm lift-off under the coil.

Table 4.1 Material properties of the specimens

Material properties	Value	Unit
Density	7.8×10^{3}	kg/m^{3}
Specific heat capacity	486	J/(kg·K)
Thermal conductivity	49.8	W/(m·K)
Conductivity	6.17×10^{6}	S/m
Relative permeability	100	1

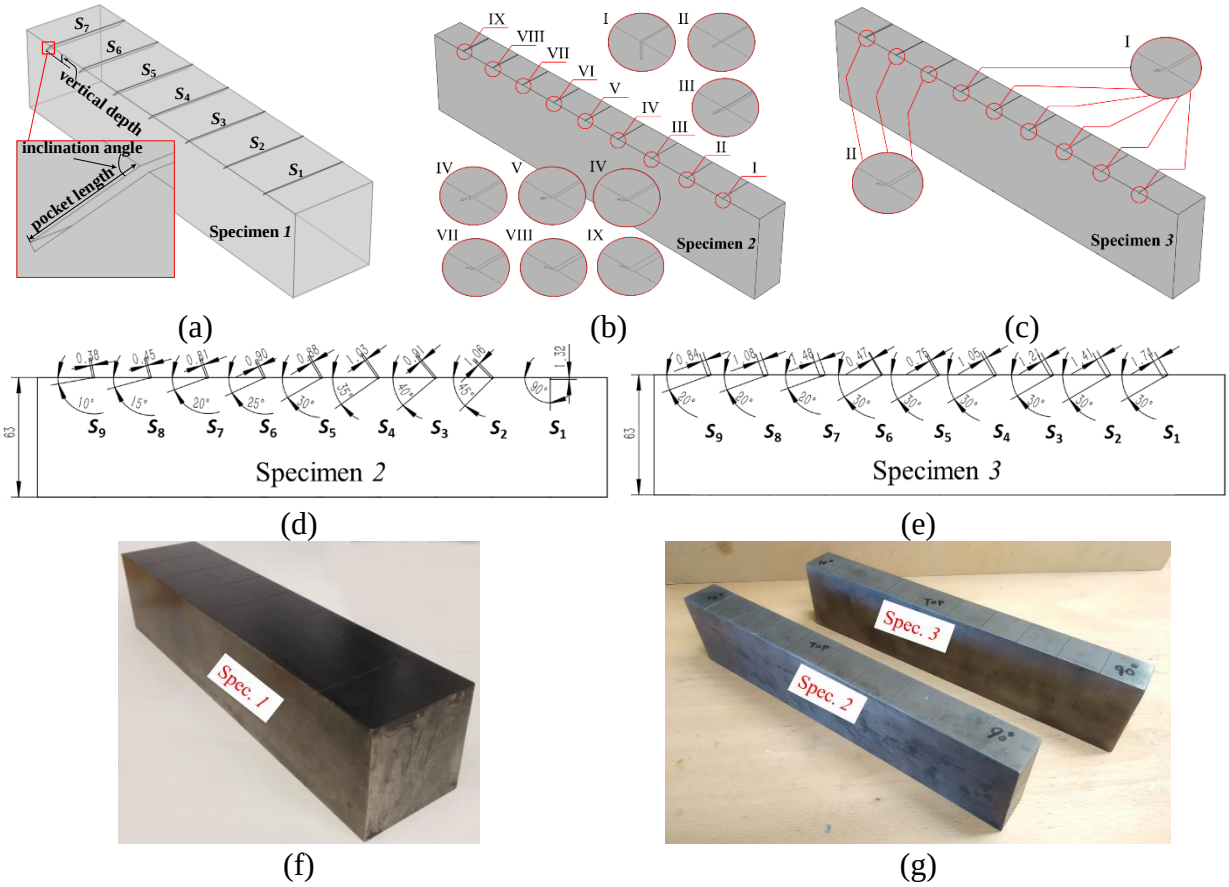

(f) (g)

Figure 4.4 Specimens *1-3*.

(a) is the schematic diagram of Specimen *1* with seven angular slots. Angular slots are cut with the same angle but different pocket lengths. (b)-(e) are the schematic diagrams of Specimens *2* and *3* with nine angular slots in each. Angular slots are cut with different angles and pocket lengths. 90° angle simulates the vertical slot and the rest angles cover the common angle range of RCF cracks [250]. (f) Photo of Specimen *1*. (g) Photo of Specimen 2 and *3*.

Table 4.2 Geometric parameters of the slots in Specimens *1-3*

Geometric parameters	Specimen	Value									Unit
		S_1	S_2	S_3	S_4	S_5	S_6	S_7			
Inclination angle	Specimen *1*	45	45	45	45	45	45	45			°
Pocket length	Specimen *1*[*1]	0.51	1.02	1.53	2.01	2.54	3.01	3.52			mm
Opening	Specimen *1*	0.44	0.43	0.44	0.42	0.43	0.44	0.45			mm
		S_1	S_2	S_3	S_4	S_5	S_6	S_7	S_8	S_9	
Inclination angle	Specimen *2*	90	45	40	35	30	25	20	15	10	°
Pocket length	Specimen *2*[*1]	1.32	1.06	0.91	1.03	0.88	0.90	0.81	0.45	0.38	mm
Vertical depth	Specimen *2*	1.32	0.74	0.59	0.58	0.44	0.37	0.27	0.12	0.08	mm
Opening	Specimen *2*[*2]	0.37	0.43	0.44	0.48	0.46	0.51	0.66	0.85	1.13	mm
		S_1	S_2	S_3	S_4	S_5	S_6	S_7	S_8	S_9	
Inclination angle	Specimen *3*	30	30	30	30	30	30	20	20	20	°
Pocket length	Specimen *3*[*1]	1.74	1.41	1.21	1.05	0.75	0.47	1.48	1.08	0.84	mm
Vertical depth	Specimen *3*	0.87	0.71	0.61	0.52	0.38	0.23	0.51	0.38	0.29	mm
Opening	Specimen *3*[*2]	0.43	0.42	0.45	0.43	0.41	0.27	0.27	0.26	0.28	mm

[*1]: Cut with different pocket lengths and all within 4 mm to simulate cracks in initial and propagation stage; [*2]: Changing openings due to different cutting (inclination) angles.

4.4 Angular Defect Characterisation

In this section, the above specimens are tested and features/patterns for the pocket length, the inclination angle, and the vertical depth characterisation are studied in detail. For evaluating and comparing the fitted relationships between the features and the geometric parameters, R^2, slope, and 2-norm of the residual are used. It is noteworthy that to eliminate the effects of different heating pulses, the residual values are normalised into the range of (-1, 1). Under each heating pulse, 2-norm of these normalised residuals (2-norm NR). Through comparisons, features' strengths and limitations are further summarised.

4.4.1 *Pocket length characterisation*

This section tests and compares several features for the pocket length characterisation. The main parameters of ECPT configuration used here are shown in table 4.3. The specimen used is Specimen *1*. Note that for simplicity all the features shown in Sections 4.4.1.1-4.4.1.5 are firstly extracted under only one typical heating pulse [251], i.e. 100 ms heating pulse. For each angular slot, five features, i.e., T_{max}, A_{diff1}, A_{ratio}, $A_{T\text{-}PCA}$, and $A_{diff1\text{-}PCA}$, are investigated. Features extracted under different heating pulses are further discussed and compared in Section 4.4.1.6.

Table 4.3 Main parameters of ECPT configuration in pocket length characterisation

Parameters	Value	Unit
Excitation frequency	260	Hz
Excitation currents (RMS)	300	A
Resolution of IR camera	640×120	pixels
Frame rate of IR camera	200	Hz
Recording time	1×10^3	ms

4.4.1.1 *Maximum thermal rise*

Figure 4.5 shows the relationship between T_{max} and the pocket length under the 100 ms heating pulse. All the T_{max} values of Slot S_1-S_7 are also given in the second row of table 4.4. This feature is extracted at pixel level which shows high repeatability with the largest standard deviation lower than 0.09 ℃. However, the relationship between this feature and the pocket length is nonlinear, which is clearly shown by the data deviation from the linear fitting line. In the following sections, four more features are extracted at area level to find a more linear relationship with the pocket length.

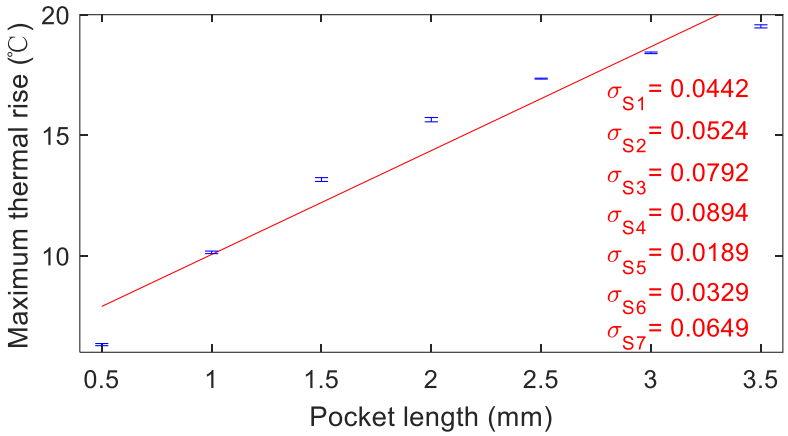

Figure 4.5 T_{max} vs. pocket length under the 100ms heating pulse.
Symmetric error bar gives two standard deviations of six repeated tests for each pocket length. The standard deviations for each pocket length are shown at the right bottom.

4.4.1.2 *First-order differential imaging*

Figure 4.6(a) shows the first-order differential image of Slot S_1 at 35 ms. As introduced in Section 3.4.1.2, this specific time is when the first-order differential of the maximum thermal pixel (P_m) reached to its maximum. Figure 4.6(b) gives the spatial values of the imaging result along the five neighbour lines in figure 4.6(a). Their average is shown by the bold-black-dashed curve and the shaded area under this curve is A_{diff1}. Based on the same steps, all the A_{diff1} of Slot S_2-S_7 are calculated and shown in the third row of table 4.4.

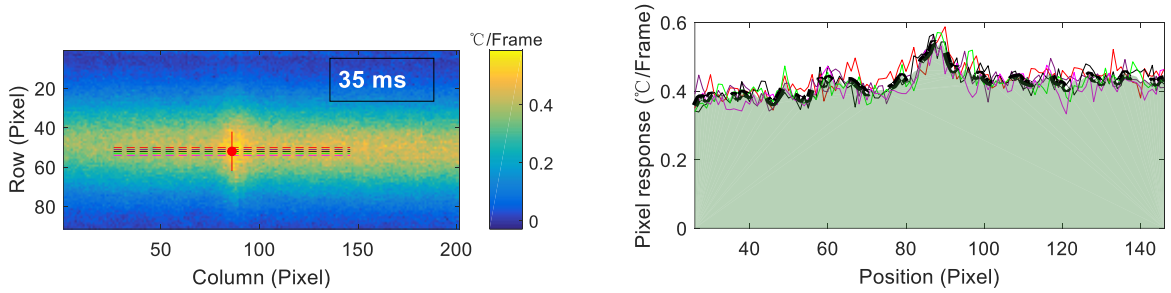

(a) (b)

Figure 4.6 First-order differential imaging of Slot S_1.
(a) First-order differential imaging of ROI at 35 ms. The red solid line denotes the slot's surface-length direction and red dot shows P_m. Five neighbour lines are plotted with the middle one across P_m. (b) Spatial values along five lines. Their average values are plotted by the bold-black-dashed curve.

4.4.1.3 *Ratio mapping based on first-order differential result*

Based on the first-order differential result, the ratio mapping is used to automatically compress the video information of the ROI into one image. Figure 4.7(a) shows the ratio mapping result of Slot S_1 based on equation 3.119. Figure 4.7(b) shows the spatial values along five lines. Their average is shown by the bold-black-dashed curve and the shaded area

under this curve is A_{ratio}. In addition, the fourth row of table 4.4 gives all the A_{ratio} of Slot S_1-S_7 from the ratio mapping.

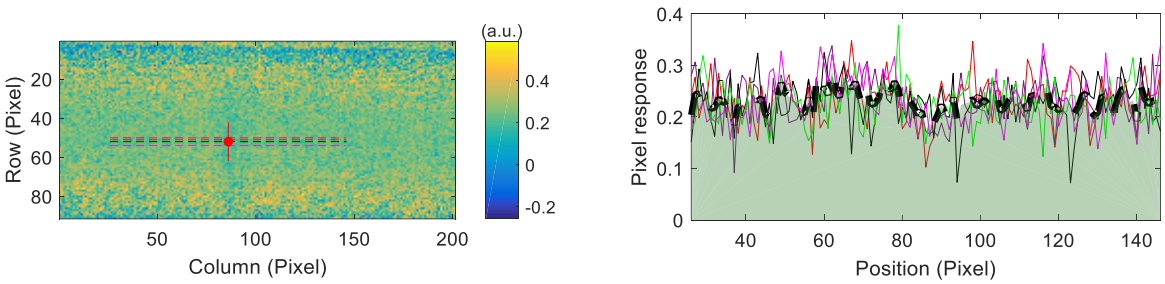

(a) (b)

Figure 4.7 Ratio mapping from first-order differential result of Slot S_1.
(a) Ratio mapping of ROI. Five neighbour lines are plotted with the middle one across P_m. (b) Spatial values along five lines. Their average values are plotted by the bold-black-dashed curve.

4.4.1.4 *PCA-based thermal pattern*

Figure 4.8(a) presents the PCA-based thermal pattern of the ROI under the 100 ms heating pulse. This image is obtained by applying PCA method (introduced in Section 3.4) to the thermal video and then choosing the first empirical orthogonal function (first EOF). Figure 4.8(b) shows the pixel/spatial values along five neighbour lines and a black-bold-dashed curve shows their average. The shaded area under this curve is $A_{T\text{-}PCA}$. Further, the fifth row of table 4.4 gives the $A_{T\text{-}PCA}$ of Slot S_1-S_7. The strengths of this feature are good linearity (high R^2 values) and high sensitivity (large slopes), as later shown in figure 4.11(b). However, this feature is not very sensitive to short pocket length (see figure 4.8(b)). Therefore, in the next section, another feature, derived from the PCA-based first-order differential pattern, is extracted to find a more sensitive corresponding with a short pocket length.

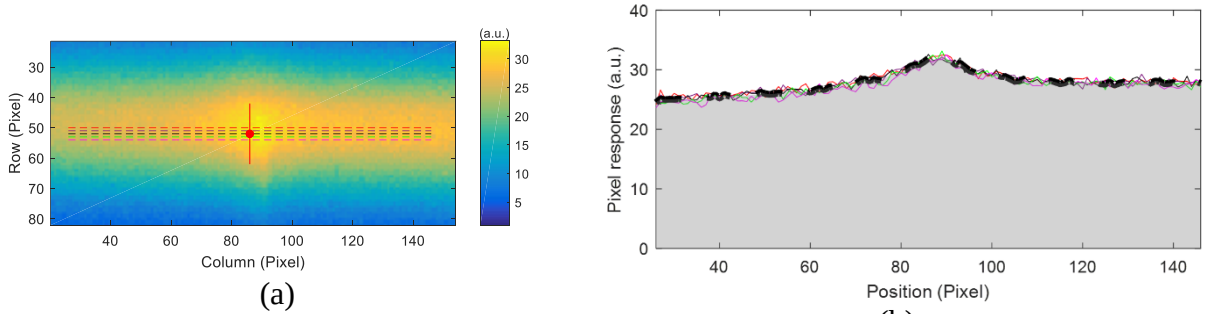

(a) (b)

Figure 4.8 PCA-based thermal pattern of Slot S_1.
(a) PCA-based thermal pattern of ROI (first EOF). Five neighbour lines are plotted with the middle one across P_m. (b) Spatial values along five lines. Their average values are plotted by the bold-black-dashed curve.

4.4.1.5 *PCA-based first-order differential pattern*

The PCA-based first-order differential pattern of ROI is shown in Figure 4.9(a). It is achieved by sliding the thermal video and then using PCA method to obtain the first EOF. Figure 4.9(b) shows pixel/spatial values along five neighbour lines and their average. The shaded area under this curve is $A_{\text{diff1-PCA}}$. By comparing figure 4.9(b) with figure 4.8(b), the strength of this feature is that it can detect a short pocket length with a sharp profile change. Further, the last row of table 4.4 gives the $A_{\text{diff1-PCA}}$ of Slot S_1-S_7.

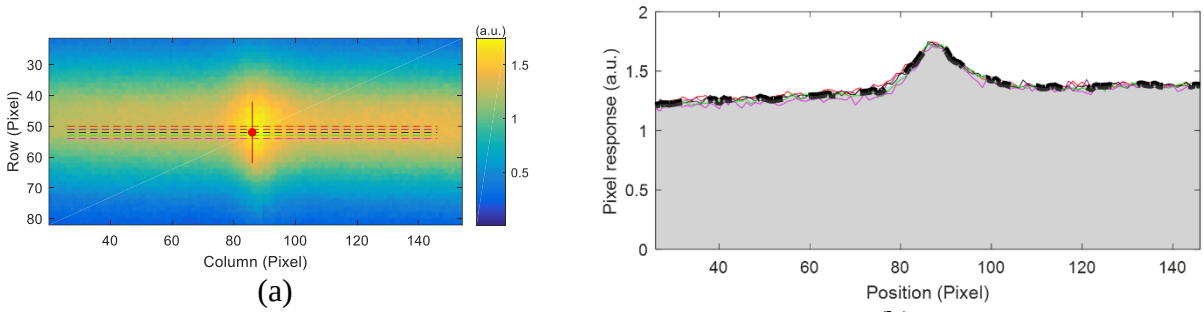

(a) (b)

Figure 4.9 PCA-based first-order differential pattern of Slot S_1.
(a) PCA-based first-order differential pattern of ROI (first EOF). Five neighbour lines are plotted with the middle one across P_m. (b) Spatial values along five lines. Their average values are plotted by the bold-black-dashed curve.

Table 4.4 The calculated $T_{\max}$, A_{diff1}, A_{ratio}, $A_{\text{T-PCA}}$, $A_{\text{diff1-PCA}}$ of Slot S_1-S_7.

Slot number	S_1	S_2	S_3	S_4	S_5	S_6	S_7
$T_{\max}$ (°C)	6.28	10.12	13.03	15.60	17.36	18.45	19.51
A_{diff1} (°C/Frame)	51.42	61.22	66.85	74.23	79.53	85.66	91.76
A_{ratio} (a.u.)	27.89	29.80	31.56	35.30	36.55	37.52	38.69
$A_{\text{T-PCA}}$ (a.u.)	3354.73	3963.58	4307.79	4945.66	5501.32	6088.82	6573.70
$A_{\text{diff1-PCA}}$ (a.u.)	165.26	196.21	210.04	233.38	251.81	271.34	287.86

4.4.1.6 *Features comparison of pocket length characterisation*

Table 4.4 shows that all five relationships are monotonic. For illustration, values in this table only show one test result for each slot. Repeatability uncertainty of the measurement can be calculated by conducting repeated tests [252-256]. Typically, at least five repeated tests are used to evaluate repeatability uncertainty. Here, each test is repeated six times. After six repeated tests for each slot, figure 4.10 presents all the relationships between five features and the pocket length. Here, R^2 and 2-norm NR (introduced at the start of Section 4.4) are used as two criteria to evaluate and compare the fitted relationships. Among these relationships, $T_{\max}$ shows a high reproducibility but a low linear relationship to the pocket length. $A_{\text{T-PCA}}$ vs. pocket length shows the best linearity with a 99.8 % R^2 value.

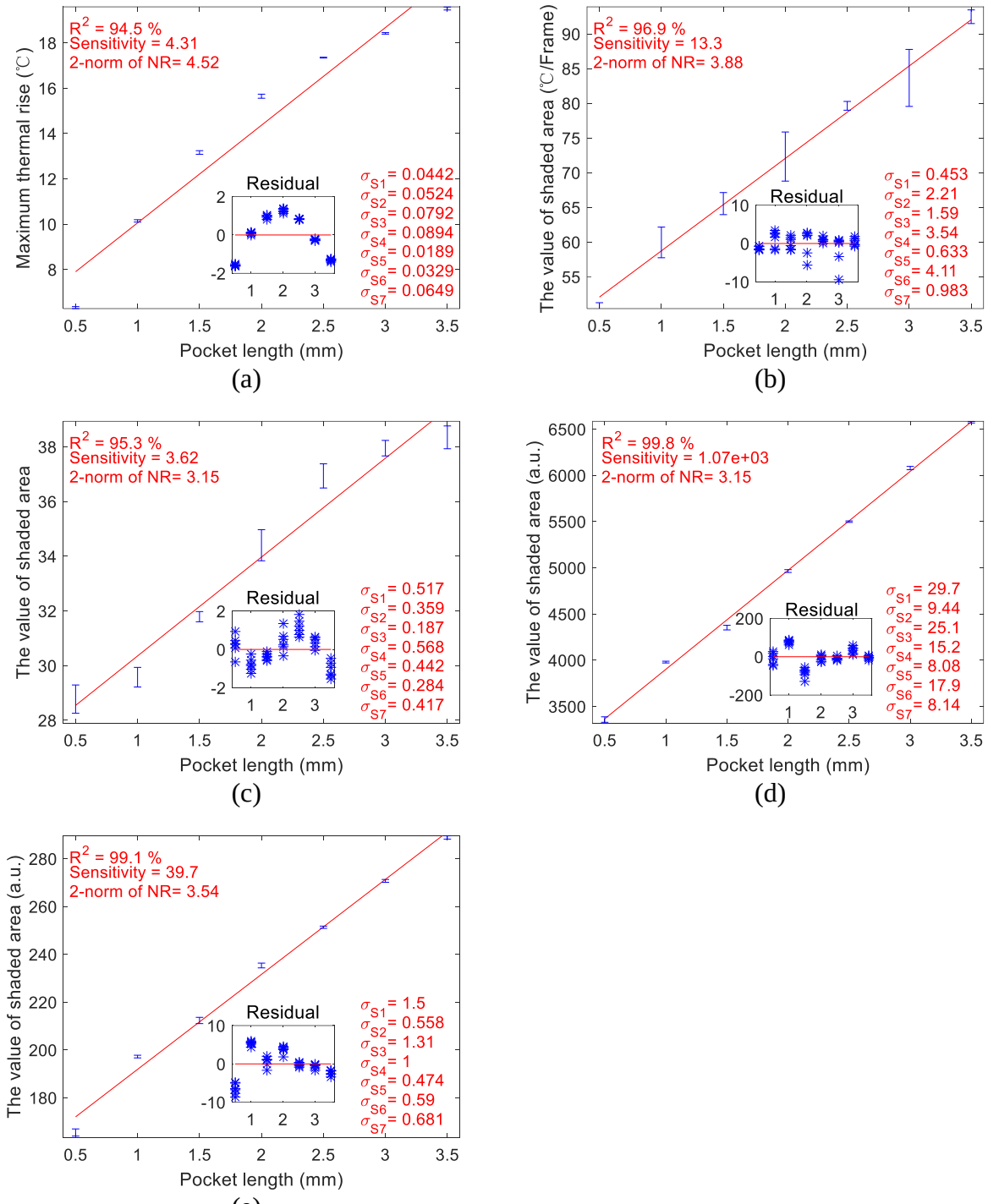

Figure 4.10 T_{max}, A_{diff1}, A_{ratio}, $A_{T\text{-}PCA}$, and $A_{diff1\text{-}PCA}$ vs. pocket length. (a) T_{max} vs. pocket length. (b) A_{diff1} vs. pocket length. (c) A_{ratio} vs. pocket length. (d) $A_{T\text{-}PCA}$ vs. pocket length. (e) $A_{diff1\text{-}PCA}$ vs. pocket length. Red lines are the linear fitting lines.

Next, in order to generalise the above results, the same features are extracted under eight heating pulses (10, 20, 30, 50, 80, 100, 150, and 200 ms). Specifically, the minimum heating pulse is 10 ms which is the shortest value the excitation module can achieve and the maximum heating pulse is 200 ms also commonly used in previous work [249].

Figure 4.11(a) shows T_{max} vs. the pocket length. It shows that under different heating pulses all the results present that the maximum thermal rise monotonically increases with pocket length. The reason is that the longer the heating pulse, the more the Joule heat is generated. Additionally, the longer the slot, the more heat is trapped at the slanted area. Both of them lead to a higher temperature rise at the inclination side than the other side. However, from the residuals vs. fitted linear plots shown in figure 4.11(b), their patterns show that residuals do not randomly distribute along both sides of the fitted lines which are more obvious under longer heating pulses and when pocket length is longer than 2 mm. This result is also presented by the decreasing R^2 and the increasing 2-norm NR (the T_{max} row of table 4.5). These patterns indicate the inappropriate linear fitting. In the following, A_{diff1} and A_{ratio} features are discussed.

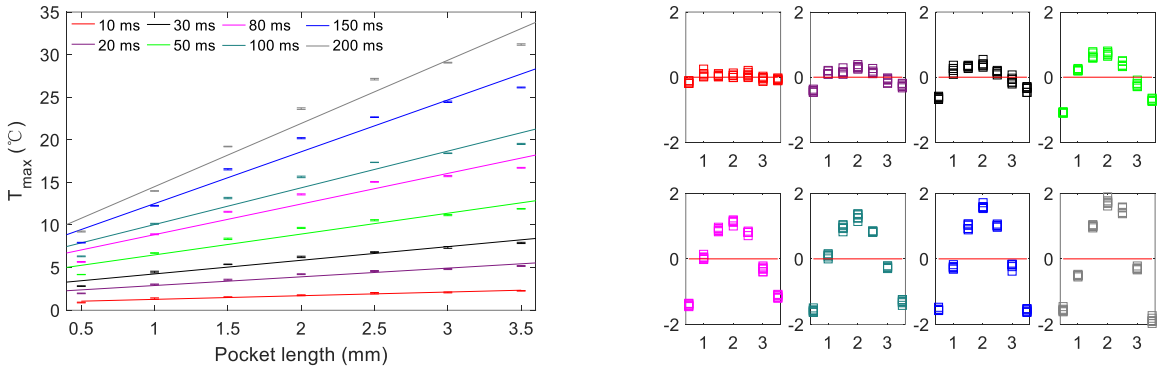

(a) (b)

Figure 4.11 T_{max} vs. pocket length under eight heating pulses.
(a) Linear fitting plots. (b) Residual plots. Residuals of each result are presented by squares.

Figure 4.12(a) shows A_{diff1} vs. the pocket length. This figure also verifies the monotonically increasing relationship. Compared with T_{max}, figure 4.12(b) shows that A_{diff1} has a better linear relationship with the pocket length. This relationship is still reasonable even when pocket lengths are longer than 2 mm, which is shown by the random pattern of the residuals and smaller values of the 2-norm of NR in the A_{diff1} row of table 4.5. Specifically, under 20 ms, 30 ms and 50 ms heating pulses, A_{diff1} and pocket length has linear relationships with higher R^2 ($>$96%) and smaller 2-norm of NR ($<$3.6).

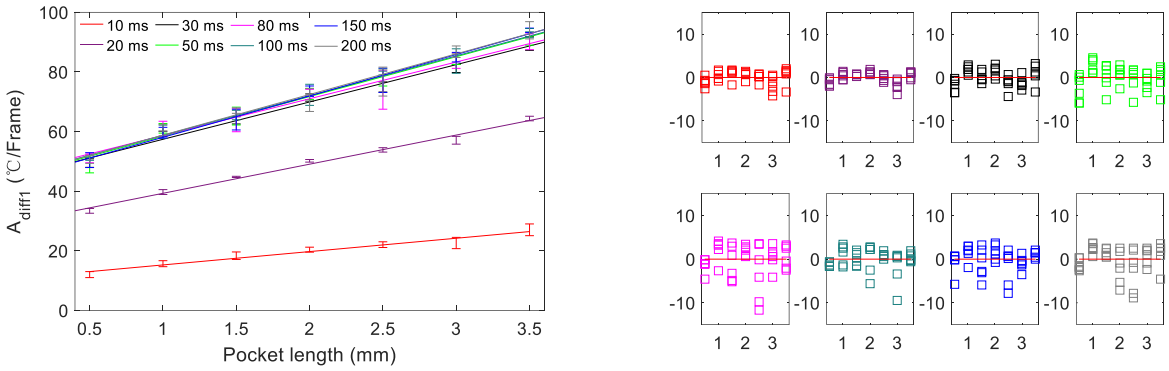

(a) (b)

Figure 4.12 A_{diff1} vs. pocket length under eight heating pulses.
(a) Linear fitting plots. (b) Residual plots.

Figure 4.13(a) shows A_{ratio} vs. the pocket length. By comparing figure 4.13(b) with figures 11(b) and 12(b), this feature has a larger standard deviation than T_{max} but the smaller than A_{diff1}. Additionally, when the heating pulse is larger than 50 ms, this feature also has a well-fitted linear relationship with the pocket length, as verified by the larger R^2 values and the random patterns of the residuals shown in the A_{ratio} row of table 4.5. Although the minimum 2-norm of NR (2.82) is obtained under the 20 ms heating pulse, the R^2 value (85.7%) is much lower compared to the values of T_{max} and A_{diff1}. Under longer heating pulses ($\geqslant$80 ms) A_{ratio} and pocket length has linear relationships with higher R^2 ($>$94%) and lower 2-norm of NR ($<$3.6).

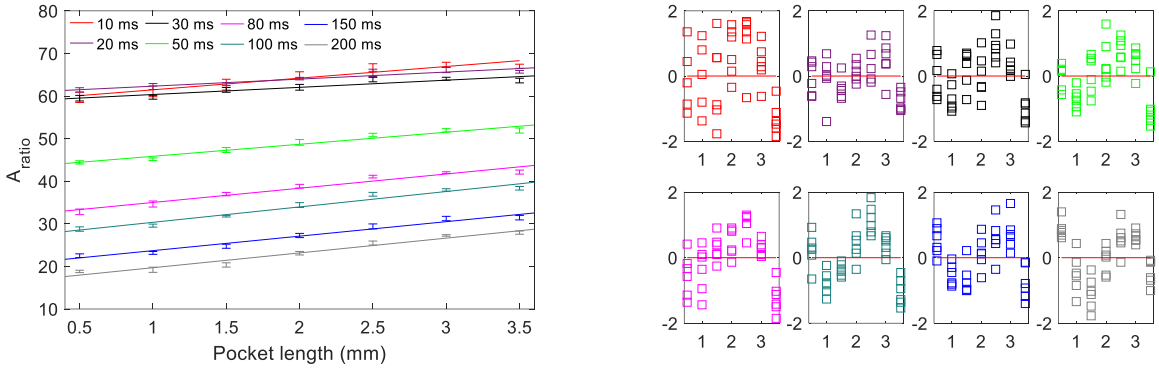

(a) (b)

Figure 4.13 A_{ratio} vs. pocket length under eight heating pulses.
(a) Linear fitting plots. (b) Residual plots.

In addition to A_{diff1} and A_{ratio}, two PCA-based features are discussed in the following. $A_{T\text{-}PCA}$ vs. the pocket length under eight heating pulses are in figure 4.14(a). By comparing figure. 4.14(b) with figure 4.11(b), the residuals plots show random patterns when using linear fittings. These patterns mean that residuals randomly distribute along both sides of the fitted lines and verify the rationality of using linear fitting to present the relationship between $A_{T\text{-}PCA}$ and the pocket

length. In addition, a longer heating pulse (＞80 ms) contributes a well-fitted linear relationship, as indicated by a larger R^2 and a smaller 2-norm NR (the $A_{\text{T-PCA}}$ rows in table 4.5). Among eight heating pulses, the 100 ms heating pulse achieve the minimum 2-norm NR (3.15) with a 99.9% R^2.

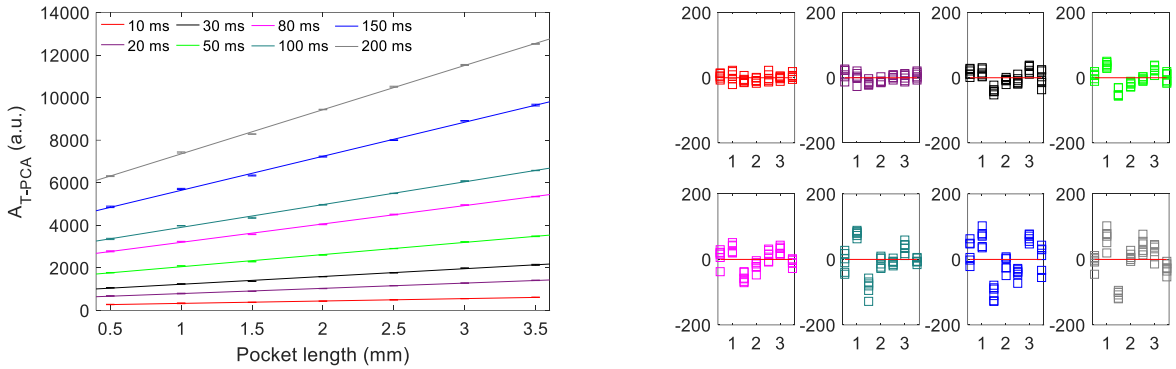

(a) (b)

Figure 4.14 $A_{\text{T-PCA}}$ vs. pocket length under eight heating pulses.
(a) Linear fitting plots. (b) Residual plots.

Similarly, $A_{\text{diff1-PCA}}$ vs. the pocket length under eight heating pulses are in shown figure 4.15(a). This figure also confirms the monotonically increasing relationships. Compared with figure 4.11(b), figure 4.15(b) shows that $A_{\text{diff1-PCA}}$ also presents a better linear relationship with the pocket length, which is indicated by smaller 2-norm NR and random patterns of the residuals (the $A_{\text{diff1-PCA}}$ row in table 4.5). However, the 2-norm NR shows an increasing trend if a longer heating pulse (＞80 ms) is used. Thus, the 20 ms heating pulse can be found with the minimum 2-norm NR (2.95) but a lower R^2 of 99.1%. The 80 ms heating pulse can be found with the highest R^2 value (99.5%) but a larger 2-norm NR of 3.26.

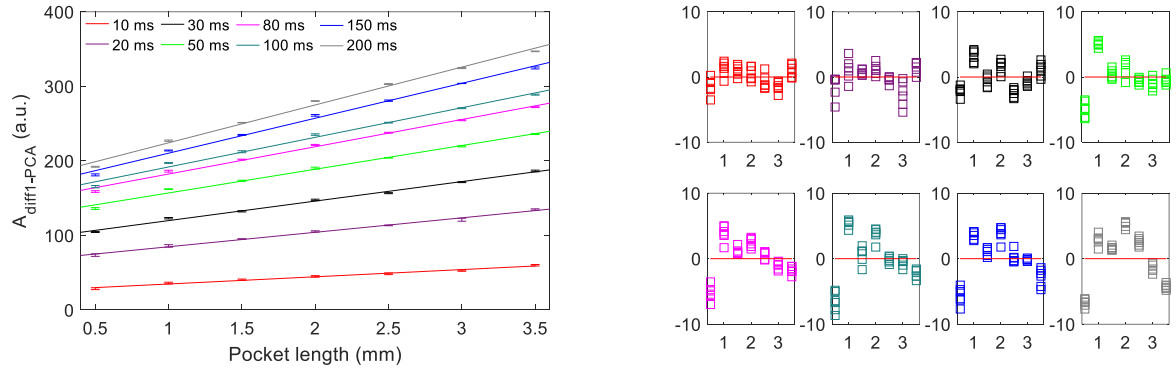

(a) (b)

Figure 4.15 $A_{\text{diff1-PCA}}$ vs. pocket length under eight heating pulses.
(a) Linear fitting plots. (b) Residual plots.

Table 4.5 Fitting parameters of T_{max}, A_{diff1}, A_{ratio}, $A_{T\text{-}PCA}$, and $A_{diff1\text{-}PCA}$ under different pulses

	Pulse duration	10 ms	20 ms	30 ms	50 ms	80 ms	100 ms	150 ms	200 ms
T_{max}	R^2	94.8%	94.4%	95.2%	93.5%	93.7%	94.5%	96.4%	96.9%
	Slope	0.43	1.02	1.60	2.45	3.59	4.31	6.08	7.42
	2-norm of NR	3.07	3.84	3.87	4.48	4.61	4.52	4.51	4.50
A_{diff1}	R^2	89.9%	98.5%	97.7%	96.1%	92.1%	96.9%	96.5%	95.1%
	Slope	4.47	9.77	12.50	13.40	12.30	13.30	13.90	13.60
	2-norm of NR	3.90	3.55	3.44	3.47	4.28	3.88	3.74	4.13
A_{ratio}	R^2	84.6%	85.7%	82.5%	93.5%	94.2%	95.3%	95.4%	95.3%
	Slope	2.74	1.66	1.68	2.83	3.34	3.62	3.40	3.47
	2-norm of NR	4.12	2.82	3.16	3.09	3.58	3.15	3.21	3.25
$A_{T\text{-}PCA}$	R^2	99.1%	99.7%	99.6%	99.8%	99.8%	99.9%	99.9%	99.9%
	Slope	112.35	246.13	365.88	571.93	863.72	1071.24	1601.08	2078.46
	2-norm of NR	3.41	3.30	3.53	3.34	3.54	3.15	3.49	3.26
$A_{diff1\text{-}PCA}$	R^2	97.8%	99.1%	99.4%	99.2%	99.5%	99.1%	99.4%	99.4%
	Slope	9.67	19.42	26.17	31.83	36.58	39.74	46.88	50.79
	2-norm of NR	3.40	2.95	3.57	3.16	3.26	3.54	3.72	4.03

From the above comparisons, the five features, i.e., T_{max}, A_{diff1}, A_{ratio}, $A_{T\text{-}PCA}$, and $A_{diff1\text{-}PCA}$, have their strengths and limitations. The T_{max} has the advantage of high repeatability but the relationship to the pocket length is nonlinear. Thus, only under shorter heating pulses (10, 20, 30 ms) and for a shorter pocket length characterisation, T_{max} feature can be used for linear fitting and it outperforms other features. Although A_{diff1} and A_{ratio} have lower repeatability, both features show well-fitted linear relationships to pocket length. Comparing both of them, A_{diff1} has a better linear relationship and higher sensitivity under shorter heating pulses, which can benefit the feature extraction of high-speed inspection. However, this feature needs to be obtained at a specific time. One the other hand, A_{ratio} has the advantage of taking values from automatically compressed video information, although its linear relationship is not as good as the first-order differential result under shorter heating pulses. Still, A_{ratio} can be considered under longer heating pulses ($\geqslant$80 ms) when its R^2 value is comparable to T_{max} and A_{diff1}. $A_{T\text{-}PCA}$ and $A_{diff1\text{-}PCA}$ show relatively better linear-fitting relationships to the pocket length but, similar to A_{diff1} and A_{ratio}, they suffer a low reproducibility. The strength of $A_{T\text{-}PCA}$ is that, according to the values of R^2 and 2-norm NR, it shows a better fitting relationship to the pocket length (with R^2 > 99% and 2-norm NR < 3.6). On the other hand, $A_{diff1\text{-}PCA}$ has the advantage of characterising angular defects with short pocket lengths.

4.4.2 *Inclination angle characterisation*

In this section, features for the inclination angle characterisation are investigated and compared by both experimental and simulation studies.

The main parameters of ECPT configuration are the same as those shown in table 4.3. The specimen used is Specimen *2*. In Section 4.4.1, it has been found that most of the relationships between different features and the pocket length become clearer by using a longer pulse duration. By knowing this, for investigating the temporal domain-based features, i.e., SUM_T, SUM_{diff1}, S_T, S_{diff1}, K_T, and K_{diff1}, this section selects the 200 ms heating pulse duration and investigates influences of different time slots on these features. For spatial-based features, SS_T and SK_T, still different heating pulses are used to verify their performances of characterising inclination angles. Note that since the simulation models proposed in this work only consider the heating stage, the temporal domain-based features depending on both the heating and cooling stage cannot be obtained. Therefore, only two spatial-based features are discussed in Section 4.4.2.4. The features comparison is further discussed in Section 4.4.2.6.

It is noteworthy that during the test of Specimen *2*, P_m of each slot is changing at different frames even in repeated tests, which is different from simulation studies. Figure 4.16(a) shows an example of the thermal distribution at 200 ms when S_2 of Specimen *2* is tested. P_m is marked as the red dot. From this figure, at 200 ms the red dot locates at the 55^{th} row and the 93^{rd} column. Furthermore, the characteristic location of P_m is statistically found by using histograms, as shown in figure 4.16(b). Six repeated tests are selected to obtain these two histograms. Specifically, six repeated tests include the first three under the 100 ms heating pulse and the additional three tests under the 200 ms heating pulse. For each test, P_m values from the 4^{th} (20 ms) to 13^{th} (65 ms) frame, i.e., during the stable heating stage, are recorded with their rows and columns. Thus, a total of 60 P_m values are recorded. In figure 4.16(b), the counts that fall into the 55^{th} row and the 93^{rd} column are 27 and 60, respectively. Thus, they are the dominant row and column of P_m. It is noteworthy that in six repeated tests the 93^{rd} column is the only column, which means that the transient location of P_m only moves along the surface length direction of S_2. This is because heat is trapped at the edge of S_2 and the main diffusion is along the surface length direction. Further, by bundling these two together, the characteristic location, denoted as P_c, can be obtained, i.e., 55^{th} row and the 93^{rd} column, as shown in figure 4.16(c). The above steps show an example of how to obtain P_c when S_2 of Specimen *2* is tested. Following the same procedures, it is easy to get the rest P_c of other slots.

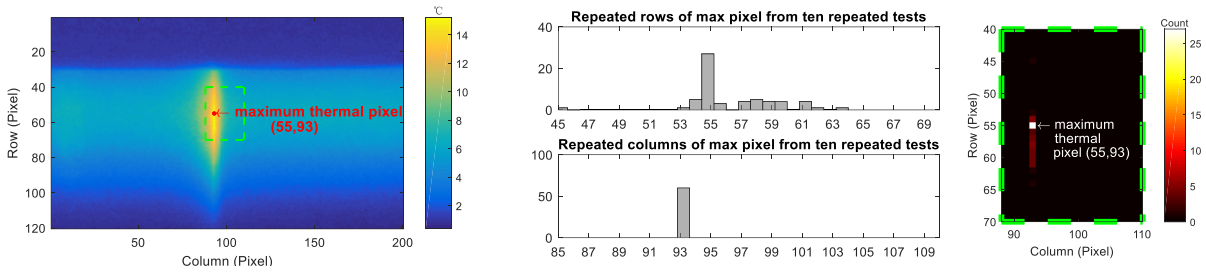

(a) (b) (c)

Figure 4.16 Thermal distribution and maximum thermal pixel's positions.
(a) Thermal distribution of slot vicinity after a 200 ms heating pulse when S_2 of Specimen *2* is tested. P_m is marked as the red dot. (b) Histograms of the maximum pixels' rows and columns. (c) Counts of P_m locations.

After obtaining P_c, its thermal response can be extracted from the raw infrared video, as shown in figure 4.17. By using the zero-lag filtering, the filtered thermal response is obtained. Further, the first-order differential response can be obtained by sliding the filtered thermal response. The absolute value of the first-order differential response is also plotted as the bold dotted curve in this figure. Note that all the curves in figure 4.17 are normalised to (0,1) or (-1,1). Before discussing thermal features, some reference locations and time slots are needed since some features are related to the temporal domain. Here, two periods, i.e., the later heating stage (shaded in light red), and the whole cooling stage (shaded in light blue), are utilised to investigate different features. The reason for using these two stages instead of the early heating stage is that even though the video recording and the pulse excitation are synchronised, a varying lag of the excitation still exists, as shown in the subfigure. In this case, the time lag is around 5 ms (one frame). Thus, a better way is to find the peak time (of the thermal response or the first-order differential response) first and then use time slots from its either side for further extracting different features.

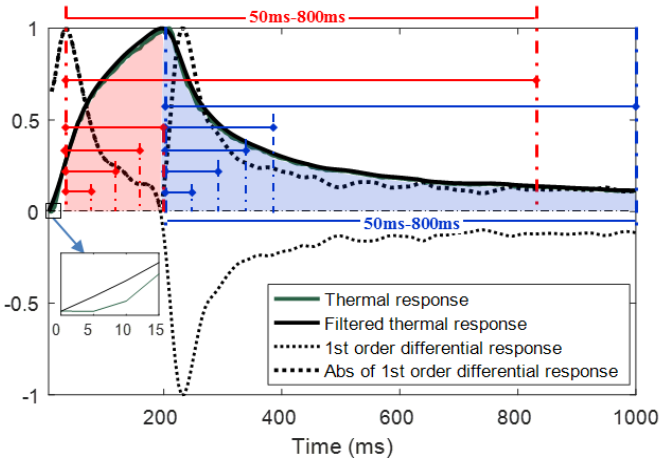

Figure 4.17 Normalised thermal response and first-order differential response of P_c.
They are the responses of P_c when S_2 of Specimen *2* is tested.

4.4.2.1 *Area-based features*

Figures 4.18(a) and (b) show the normalised thermal responses and the corresponding first-order differential responses for slots S_1-S_9 in Specimen *2*, respectively.

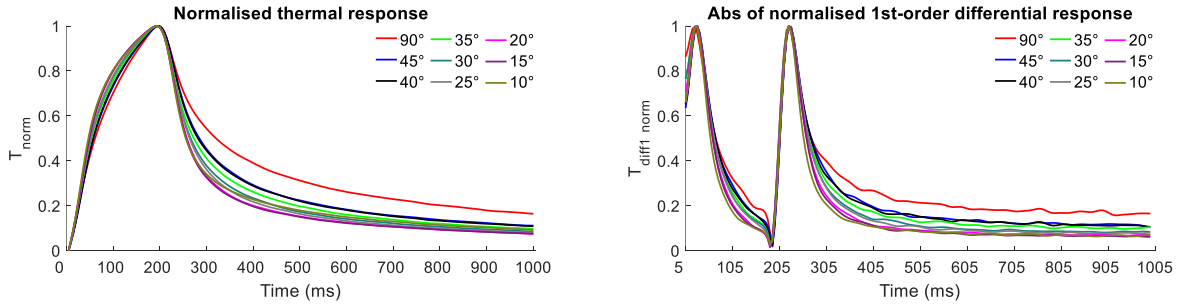

(a) (b)

Figure 4.18 Normalised thermal responses and the first-order differential responses. (a) Normalised thermal responses. (b) Normalised absolute first-order differential responses.

Based on the time slots of both the later heating and whole cooling stages (in figure 4.17), the sum-up values of the curves, i.e., areas under the curves, can be obtained. Figure 4.19(a) gives the values from the thermal responses, i.e., SUM_T. Similarly, figure 4.19(b) shows the values from the first-order differential responses, i.e., SUM_{diff1}. It is clear that both SUM_T and SUM_{diff1} increase with the time slot and they present the overall decreasing relationships to the inclination angle. From figure 4.19(a), the 800 ms time slot leads to the largest decreasing rate (slope). However, by selecting this time slot, the relationship between SUM_T and the inclination angle is nonmonotonic, as shown by the "+" sign on the value when the S_9 with the 10° inclination angle is tested. This is also shown in the SUM_T row, the last column of table 4.6. On the other hand, by selecting the 100 ms or 150 ms time slots, even if the absolute value of the slope is less than 0.5, SUM_T presents the monotonic relationship to the inclination angle with a higher R^2 and a smaller 2-norm NR. From figure 4.19(b), both the 200 ms and 800 ms time slots contribute to the monotonically decreasing relationships (all the SUM_{diff1} values are marked with "-" sign). These two time slots give smaller 2-norm NR and the latter gives a larger decreasing rate, as shown in SUM_{diff1} row, last two columns of table 4.6. Compared with SUM_T, it shows that by using the 800 ms time slot, SUM_{diff1} shows the best monotonically linear relationship to the inclination angle with the R^2 and absolute slope value of 98.6% and 2.12.

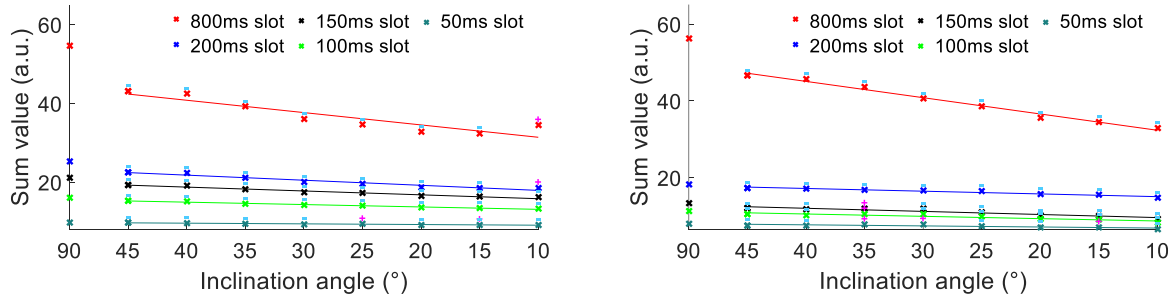

Figure 4.19 Area-based (SUM_T and SUM_{diff1}) vs. inclination angle.
(a) and (b) show the SUM_T and SUM_{diff1} vs. inclination angle, respectively. Solid lines show the linear fitting relationships. "+" and "-" signs marked on the top of feature points show the increase or decrease between two neighbour points from left to right. For each inclination angle, the test is repeated six times and the average value is used.

4.4.2.2 *Skewness-based features*

Apart from the area-based features, the characteristics of thermal responses and their first-order differential responses in figure 4.18 can also be measured by some statistical values, e.g., skewness and kurtosis. Here, the skewness is used to measure the asymmetry of the histogram derived from either the thermal or first-order differential response. It can be assumed that the slots with different inclination angles have individual thermal responses and further affect the skewness values. By using different time slots, figures 4.20(a) and (b) show the skewness values from the thermal responses and first-order differential responses (S_T and S_{diff1}), respectively. It can be seen that the linear fitting relationship can be improved by increasing the calculation time slot. However, from figure 4.20(a), none of the five time slots can give a monotonic relationship. On the other hand, in figure 4.20(b), only by using the 800 ms time slot, S_{diff1} shows the monotonic relationship to the inclination angle (all the values are marked with "+" sign). By comparing the S_T and S_{diff1} rows of table 4.6, it shows that by choosing the 800 ms time slot, S_T has a higher R^2 value and a lager absolute slope value, but this relationship is nonmonotonic. Although S_{diff1} has a lower R^2 value and a smaller absolute slope, it still shows the monotonically increasing relationship to the inclination angle.

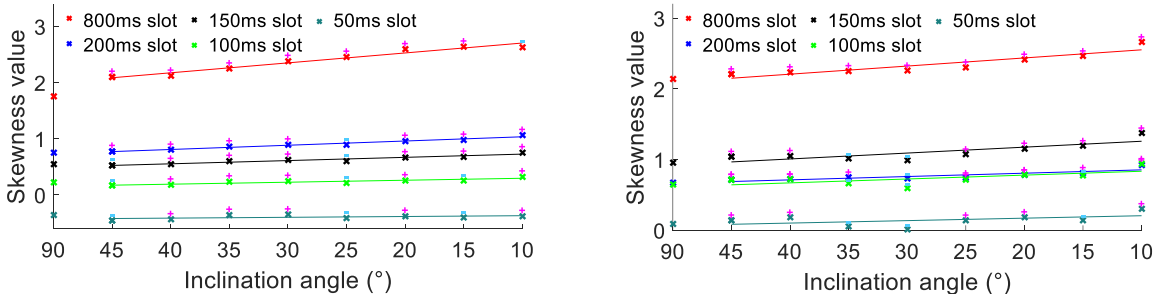

Figure 4.20 Skewness-based (S_T and S_{diff1}) vs. inclination angle.
(a) S_T vs. inclination angle. (b) S_{diff1} vs. inclination angle.

4.4.2.3 *Kurtosis-based features*

Similar to the previous section, the kurtosis is used here to measure whether the histograms from the thermal and first-order differential responses are heavy-tailed or light-tailed. Figures 4.21(a)-(b) present the kurtosis values from the thermal responses and first-order differential responses (K_T and K_{diff1}), respectively. The same as two skewness-based features, both K_T and K_{diff1} show better linear relationships by increasing the calculation time slot. Figure 4.21(a) shows only by using the 800 ms time slot, K_T shows the monotonic relationship to the inclination angle (marked with "+" sign). From figure 4.21(b), none of the five time slots can give a monotonic relationship. Comparing the K_T and K_{diff1} rows of table 4.6, by choosing the 800 ms time slot, K_T the best monotonically linear relationship to the inclination angle with the R^2 and absolute slope value of 97.5% and 0.45.

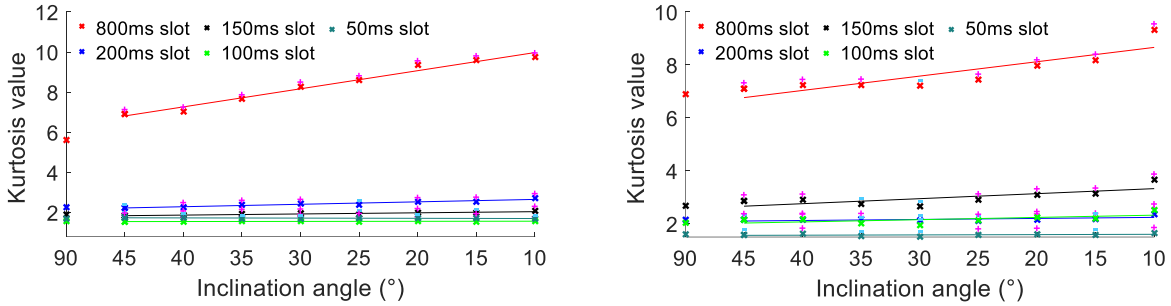

Figure 4.21 Kurtosis-based features (K_T and K_{diff1}) vs. inclination angle.
(a) K_T vs. inclination angle. (b) K_{diff1} vs. inclination angle.

Table 4.6 Fitting parameters under different calculation time slots

	Time slot (ms)	50	100	150	200	800
SUM_T	R^2	92.7 %	97.2 %	95.6 %	93.7 %	82.9 %
	Abs. slope	0.09	0.30	0.49	0.65	1.57
	2-norm of NR	2.00	1.89	1.85	1.99	2.03
	Mono-relationship	×	√	√	×	×
SUM_{diff1}	R^2	64.4 %	81.8 %	87.4 %	94.0 %	98.6 %
	Abs. slope	0.14	0.30	0.40	0.36	2.12
	2-norm of NR	1.90	1.98	1.96	1.67	1.80
	Mono-relationship	×	×	×	√	√
S_T	R^2	23.9 %	77.2 %	91.9 %	95.8 %	95.7 %
	Abs. slope	0.01	0.02	0.03	0.04	0.09
	2-norm of NR	2.14	2.03	1.78	1.71	1.73
	Mono-relationship	×	×	×	×	×
S_{diff1}	R^2	23.6 %	44.9 %	66.9 %	72.0 %	83.4 %
	Abs. slope	0.02	0.03	0.04	0.02	0.06
	2-norm of NR	1.88	1.88	1.79	1.77	1.73
	Mono-relationship	×	×	×	×	√

K_T	R^2	24.8 %	13.2 %	80.7 %	90.2 %	97.5 %
	Abs. slope	0.01	0	0.03	0.06	0.45
	2-norm NR	2.29	2.23	1.90	1.71	1.84
	Mono-relationship	×	×	×	×	√
K_{diff1}	R^2	10.0 %	36.5 %	55.3 %	36.8 %	75.9 %
	Abs. slope	0.01	0.04	0.09	0.02	0.27
	2-norm NR	2.02	1.76	1.76	1.91	1.94
	Mono-relationship	×	×	×	×	×

4.4.2.4 *Spatial skewness- and kurtosis-based features of simulation results*

Figure 4.22(a) shows the FEM model used for the simulation study. Four main parameters, e.g., inclination angle, pocket length, vertical depth, and opening, of an angular slot are illustrated in the zoomed-in subfigure. The FEM software used is COMSOL Multiphysics via the induction heating interface, which couples the magnetic field and the heat transfer. Material properties used are the same as those in table 4.1. During the model calculation, the parametric sweep function is used to automatically update the geometric parameters of the model to those of a specific angular slot in Specimen *2*, as shown in table 4.2. After calculation, figure 4.22(b) shows four examples of the thermal distributions at the end of a 50 ms heating. These distributions show two different thermal patterns. The first pattern is the very similar thermal distributions at both sides of the slot if its inclination angle is 90°. Another one is that the thermal rise at the inclined side is higher than the other side if the inclination angle is less than 90°. This is because with the inclination angle decreasing, a larger amount of heat is trapped in the inclined tip, which results in a higher thermal rise. Figure 4.22(b) also denotes the maximum thermal points by the black dots. Via the maximum thermal points of all nine slots, figures 4.22(c) to (g) further show the line-scan results across them under five different heating pulses. It can be seen that the slot with the 15° inclination angle has the largest values of T_{max} under the 10 and 20 ms heating pulses, whereas 20° slot gives the largest T_{max} under other heating pulses, as also shown in figure 4.23(a).

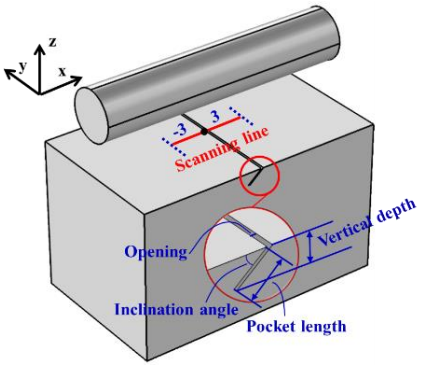

(a)

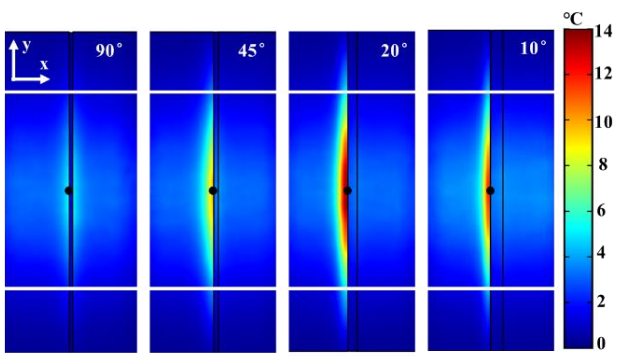

(b)

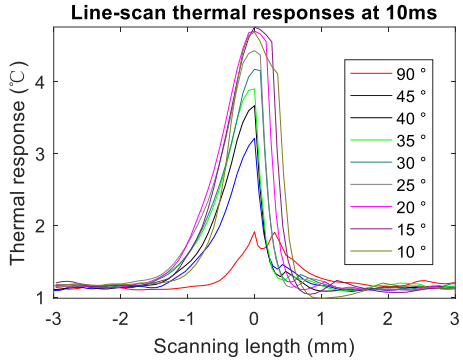

(c)

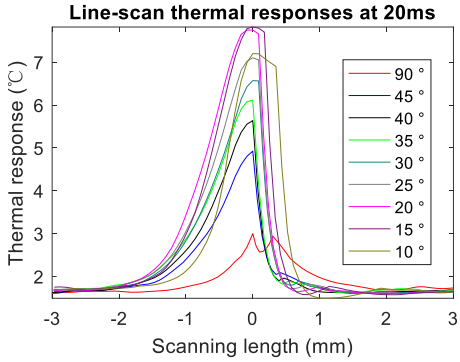

(d)

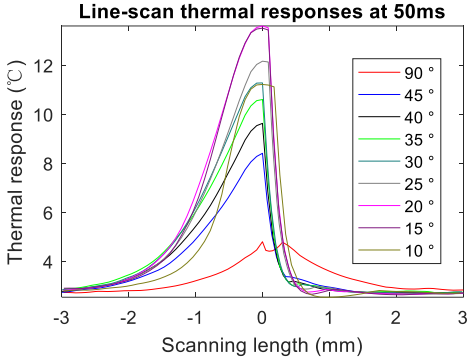

(e)

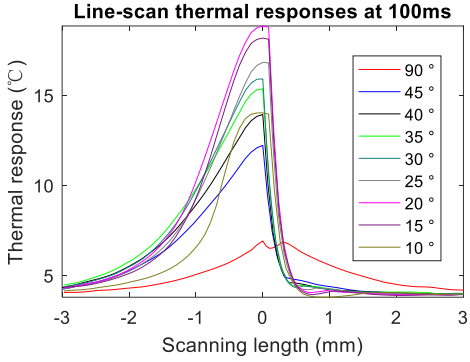

(f)

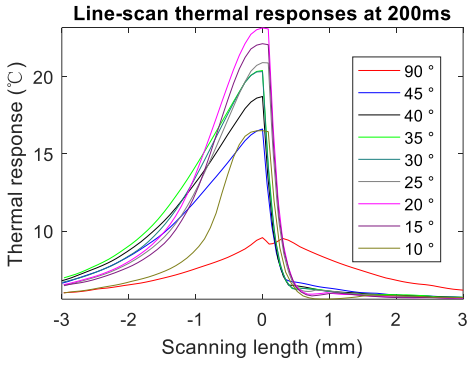

(g)

Figure 4.22 Simulation model and line scan results [257].
(a) FEM model. (b) Thermal distributions of the top surface at 50 ms with four different angles of the slot (90°, 45°, 20°, and 10°). The white-solid lines show the edges of the coil. (c)-(g) shows line-scan results of different inclination angles after 10, 20, 50, 100, and 200 ms heating pulses, respectively.

Based on the above line scan results, their spatial skewness and kurtosis, i.e., SS_T and SK_T, can be calculated. Figures 4.23 (b) and (c) shows the relationships of SS_T vs. inclination angle and SK_T vs. inclination angle, respectively. Results show that SS_T and SK_T under the 10 ms heating pulse always show the highest values with the asymmetrically-enhanced thermal distribution of the line scan. It also can be seen that although SS_T and SK_T have more positive correlations to the inclination angle under longer heating pulses ($\geqslant$100 ms), these relationships are non-monotonic.

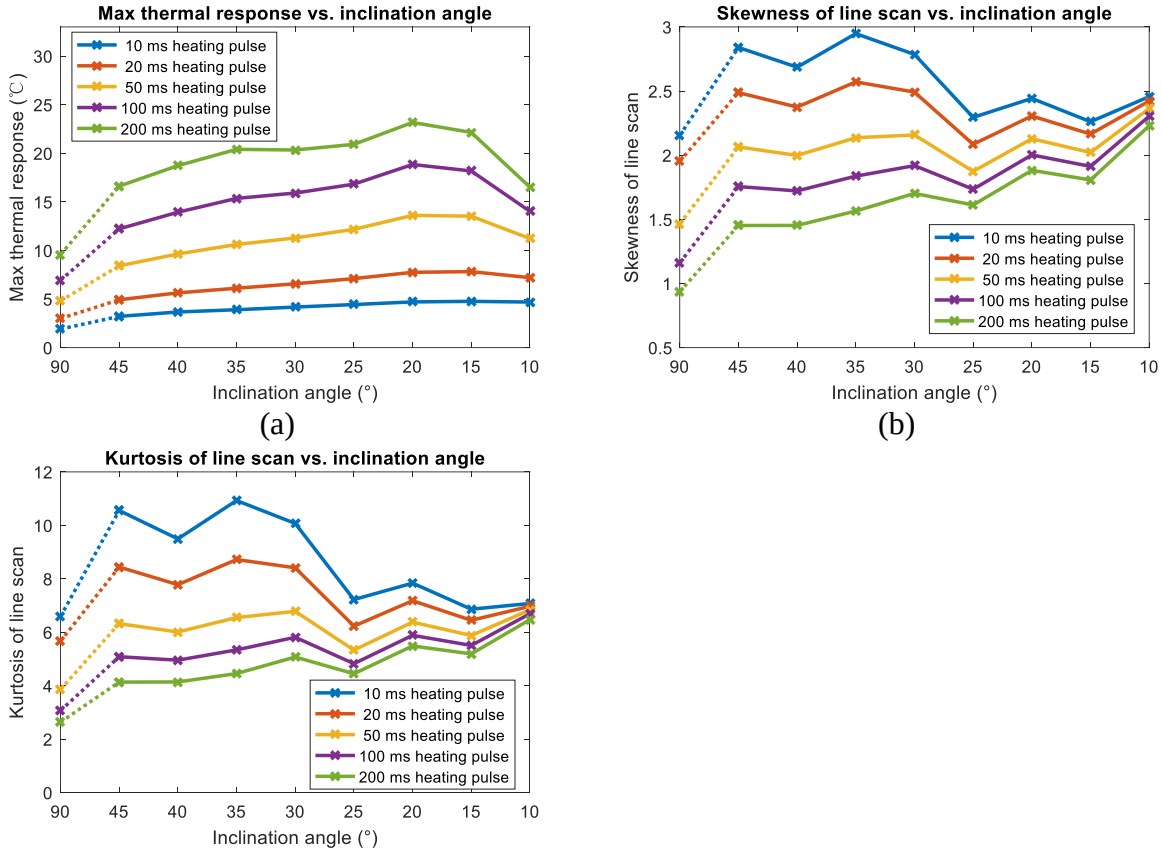

Figure 4.23 T_{max}, SS_T, and SK_T vs. inclination angle.
(a)-(c) gives T_{max}, SS_T, and SK_T vs. inclination angle under five different heating pulses, respectively.

4.4.2.5 *Spatial skewness- and kurtosis-based features*

In the above, SS_T and SK_T for inclination angle characterisation are numerically investigated. In the section, SS_T and SK_T, are further verified by experimental studies.

Figure 4.24 shows the line-scan thermal responses of nine inclination angles. Five different heating pulses are used. Figure 4.24(a) shows how to get the line-scan responses. Here, the same as figure 4.18, this figure takes S_2 of Specimen *2* as an example. Based on the previously calculated P_c, five parallel-neighbour line scans (black-dashed lines) are conducted.

After calculating the average of five line-scan values, it is shown as the blue-solid curve in figure 4.24(f). By using the same procedures, under different heating pulses, figures 4.24(b) to (f) give all the line-scan results of different inclination angles. These results verify that the thermal responses are increasing with the heating pulse. Additionally, for Specimen *2*, S_8 (15°) has the strongest thermal responses only under the 10 ms heating pulse, whereas S_7 (20°) gives the strongest thermal responses under longer heating pulses (⩾20 ms), which also can be seen in figure 4.24(g). These two results are in line with the simulation findings. Further, figures 4.24(h) and (i) show the SS_T and SK_T values of all the line-scan plots. It shows that SS_T and SK_T under the 10 or 20 ms heating pulse always show the highest value. In addition, these two figures show that both SS_T and SK_T have more positive correlations to the inclination angle when the heating pulse is longer than 100 ms. However, the same as simulation results, none of the five pulse durations can give a monotonic relationship. Comparing the SS_T and SK_T rows of table 4.7, it shows that by choosing the 200 ms pulse duration, SS_T has a better fitting relationship to the inclination angle with a higher R^2 value of 87.3 % and a smaller 2-norm NR of 1.73.

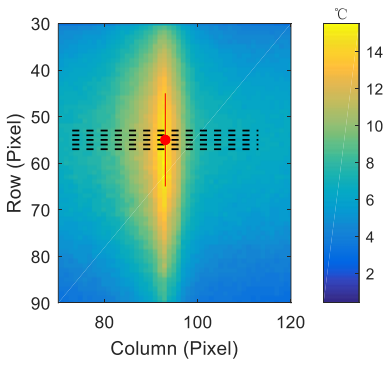

(a)

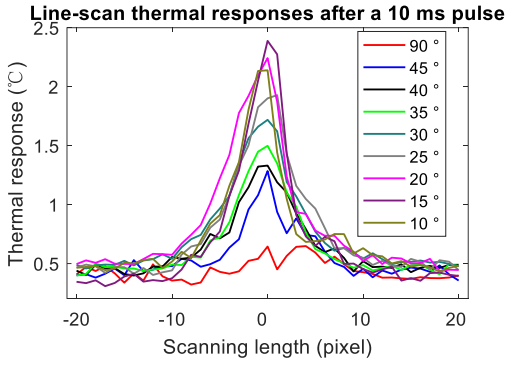

(b)

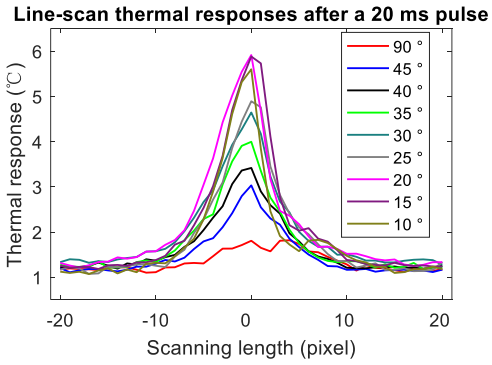

(c)

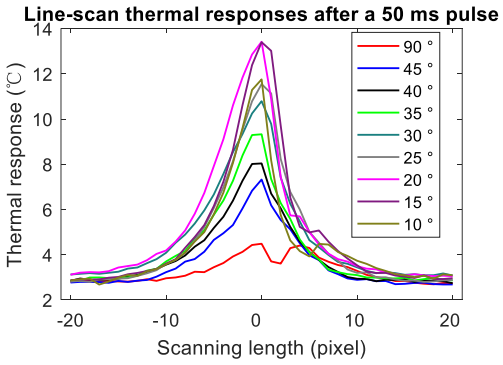

(d)

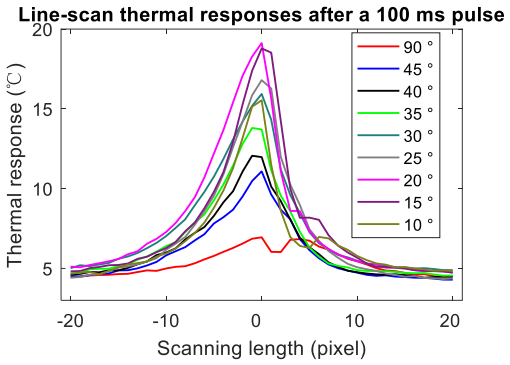

(e)

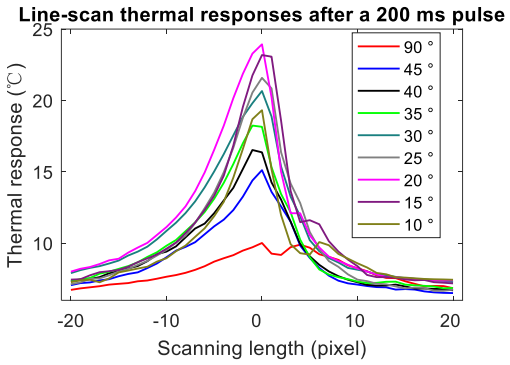

(f)

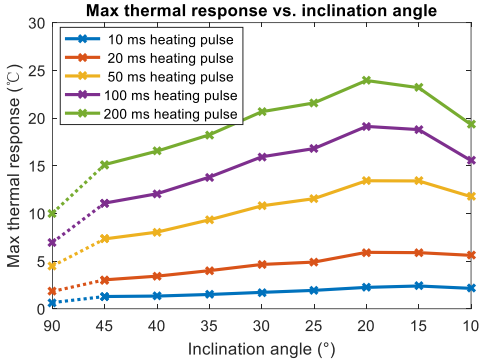

(g)

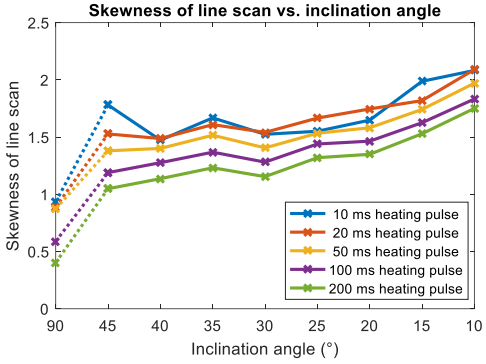

(h)

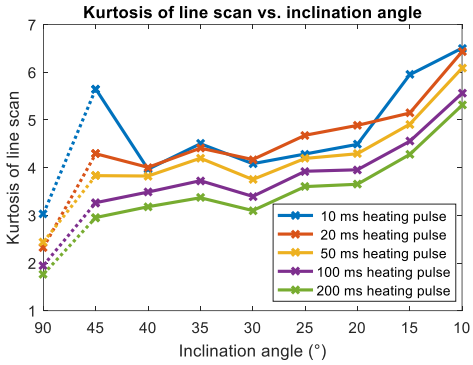

(i)

Figure 4.24 Line-scan results and three different features vs. inclination angle. Specimen *2* is tested. (a) Schematic diagram of performing the line scan when S_2 of Specimen *2* is tested. Five parallel-neighbour lines are plotted with the middle line going across P_c. The average of five line-scan values is shown as the black-solid curve in (e). (b)-(f) Line-scan results of different inclination angles after a 10, 20, 50, 100, 200 ms heating pulse, respectively. (g)-(i) T_{max}, SS_T, and SK_T vs. inclination angle under five different heating pulses, respectively.

Table 4.7 Fitting parameters under different heating pulse durations

	Pulse duration(ms)	10	20	50	100	200
SS_T	R^2	77.4 %	80.2 %	79.4 %	85.5 %	87.3 %
	Abs. slope	0.07	0.07	0.08	0.08	0.09
	2-norm NR	2.23	1.92	1.79	1.81	1.73
	Mono-relationship	×	×	×	×	×
SK_T	R^2	58.7 %	71.0 %	68.8 %	75.0 %	76.9 %
	Abs. slope	0.24	0.24	0.27	0.27	0.28
	2-norm NR	2.17	1.95	1.93	1.91	1.86
	Mono-relationship	×	×	×	×	×

4.4.2.6 *Features comparison of inclination angle characterisation*

From the above sections, six temporal and two spatial features are used for characterising inclination angles of angular defects under the influence of changing pocket lengths. In most cases, longer time slots or pulse durations can contribute the relationships between the proposed features and the inclination angle. SUM_T, SUM_{Diff1}, S_{Diff1}, and K_T show monotonic relationships for longer time slots. Of these four features, SUM_{Diff1} has the best linear relationship to the inclination angle upon using the 800 ms time slot. The relationship between T_{max} and the inclination angle is non-monotonic under all different heating pulses. T_{max} increases initially with the inclination angle, then reach a peak, and decreases afterwards. Under the condition that the pocket length is constant, this relationship is supposed to be monotonic. The main cause of the non-monotonic relationship is the changing pocket length. Consequently, it is difficult for T_{max} itself to characterise the inclination angle under the influence of the pocket length. The relationship between SS_T (or SK_T) and the inclination angle is still non-monotonic. But compared with T_{max}, SS_T (or SK_T) has more positive correlations to the inclination angle when longer heating pulses are used.

4.4.3 *Vertical depth characterisation*

In the above sections, different features for characterising pocket lengths and inclination angles are discussed. This section investigates a more challenge task, i.e., the vertical depth characterisation. The vertical depth can be considered as a function of both the pocket length and the inclination angle. All the proposed features are investigated to test their capabilities of characterising vertical depths. The parameters of ECPT configuration are the same as those used in Section 4.4.2. The only difference is that Specimen *3* is also tested. After the same calculation procedures, figure 4.25 shows the relationships of the features vs. the vertical depth. Note that, in figures 4.25(a)-(e), there is no linear fitting line plotted since it is hard to see any relationships (R^2 values are below 10%). Table 4.8 further shows the fitting parameters of the relationships between the eight effective features and the vertical depth. From this table, it can be seen that SS_T shows the best performance of characterising vertical depths, which has the highest R^2 value (82.8%) and smallest 2-norm of NR (2.14) compared with other features. In addition, SUM_T, SUM_{diff1}, S_T, and SK_T tend to have linear relationships to the vertical depth. But compared with SS_T, they have relatively lower R^2 values and larger 2-norm of NR.

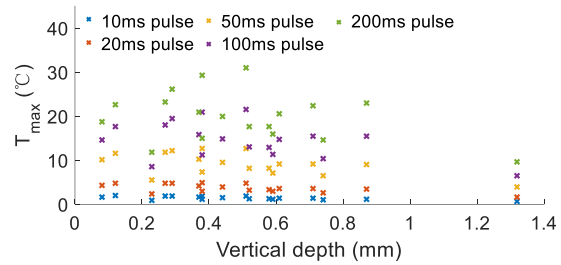

(a)

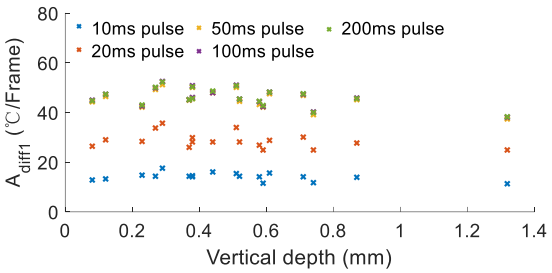

(b)

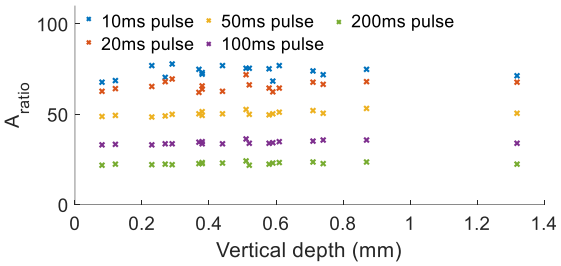

(c)

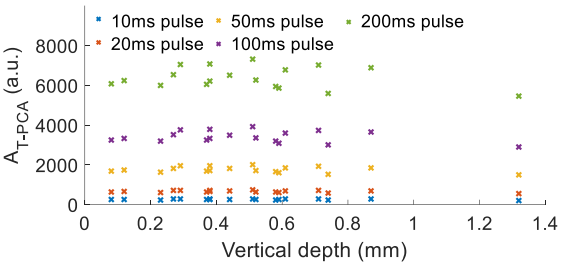

(d)

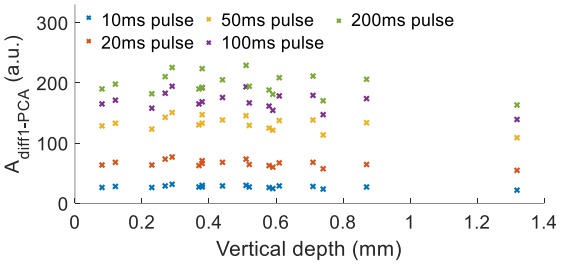

(e)

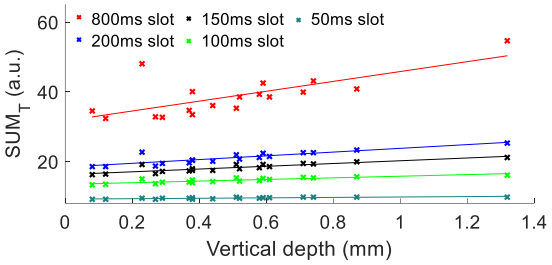

(f)

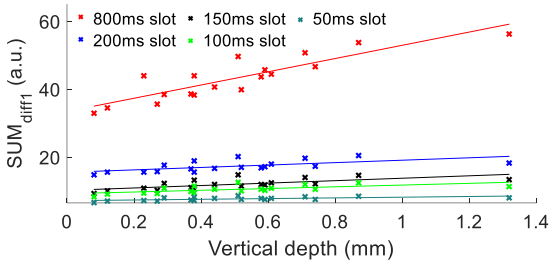

(g)

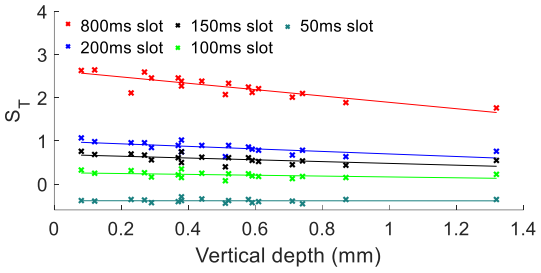

(h)

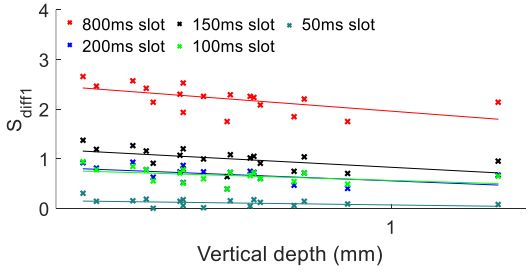

(i)

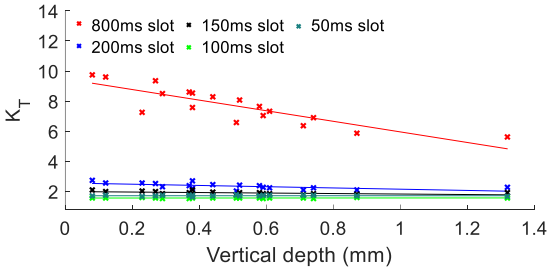

(j)

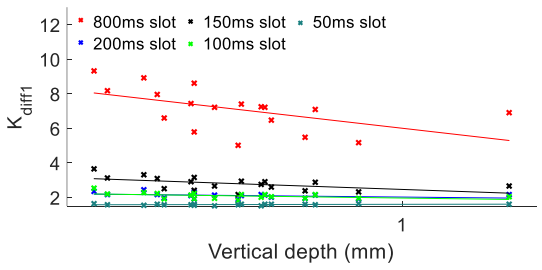

(k)

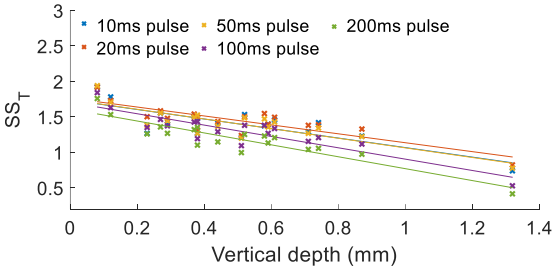

(l)

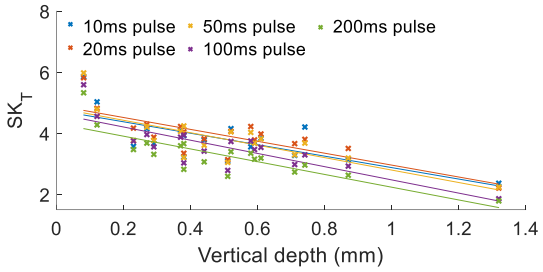

(m)

Figure 4.25 All the proposed features vs. vertical depth.
(a), (b), (l) and (m) show the spatial domain-based features vs. vertical depth. (c)-(e) give the tempo-spatial-based patterns vs. vertical depth. (f)-(k) show the temporal domain-based features vs. vertical depth. (a) T_{max} vs. vertical depth. (b) A_{diff1} vs. vertical depth. (c) A_{ratio} vs. vertical depth. (d) $A_{T\text{-}PCA}$ vs. vertical depth. (e) $A_{diff1\text{-}PCA}$ vs. vertical depth. (f) SUM_T vs. vertical depth. (g) SUM_{diff1} vs. vertical depth. (h) S_T vs. vertical depth. (i) S_{diff1} vs. vertical depth. (j) K_T vs. vertical depth. (k) K_{diff1} vs. vertical depth. (l) SS_T vs. vertical depth. (m) SK_T vs. vertical depth. Solid lines show the linear fitting relationships.

Table 4.8 Fitting parameters of different relationships

	SUM_T	SUM_{diff1}	S_T	S_{diff1}	K_T	K_{diff1}	SS_T	SK_T
Time slot	150ms	800ms	800ms	800ms	800ms	800ms	-	-
Pulse duration	-	-	-	-	-	-	200ms	200ms
R^2	75.8%	77.4%	74.8%	31.3%	72.4%	28.3%	82.8%	58.2%
Abs. slope	3.96	19.49	0.74	0.51	3.52	2.22	0.84	2.09
2-norm of NR	2.58	2.80	2.54	2.35	2.62	2.40	2.14	2.32

4.5 POD Analysis for Angular Defect Characterisation

Based on the proposed POD analysis framework, Sections 4.3 and 4.4 have finished the first four steps, i.e., ECPT configuration, video preprocessing, feature extraction, and performance comparison. This section carries out the last step, performance evaluation of defect characterisation via POD analysis. Note that not all the features/patterns but those presenting clear relationships (to the pocket length and the vertical depth) are chosen for POD analysis. POD analysis for evaluating features of inclination angle characterisation is not considered. The reason is that even several features (SUM_T, SUM_{diff1}, S_{diff1}, K_T) can be used to characterise inclination angles, there are no ready-made rules to decide the severity of the inclination angle, which is different from the severity of the pocket length (the longer the severer). In addition, since these features can be interpreted as continuous responses to the induction heating, in the following the signal response data is used for POD analysis.

4.5.1 *POD analysis for evaluating performance of pocket length characterisation*

According to equation 3.58, for T_{max}, A_{diff1}, A_{ratio}, $A_{T\text{-}PCA}$, and $A_{diff1\text{-}PCA}$, the calculated POD curves as functions of the pocket length are shown in figure 4.26. Note that these POD curves

are based on equation 3.56 with the Cartesian relationship, i.e., $\hat{a}$ vs. a relationship. The decision threshold is set as the maximum feature value of repeated tests when S_1 of Specimen *1* is tested, i.e., it is assumed that detecting an angular slot with its pocket length shorter than 0.5 mm is at 50% POD. Still, the decision threshold can be set by other assumptions.

It is found that POD curves increase with pocket length under all heating pulses. For different features, optimal heating pulses can be found to achieve high POD value. Specifically, from the POD curves in figure 4.26(a), it can be seen that when using T_{max}, the 50 ms heating pulse achieved the highest POD value. However, it is unrealistic to detect a zero pocket length with 40% POD. The reason is that if pocket lengths jump outside the minimum value (0.51 mm) of the slots used for experiments, its corresponding POD value is extrapolated based on the linear relationship, which is no more valid under the 50 ms heating pulse. Figure 4.26(b) shows that when using A_{diff1}, the 20 ms heating pulse benefits a longer slot ($>$0.5 mm) detection and has a narrower transition area. This advantage is in line with the previous discussion in Section 4.4.1.6. From figure 4.26(c), when using A_{ratio} for a longer slot ($>$0.3 mm) detection, the 50 ms or 80 ms heating pulse is preferred. Compared with other features, the POD curve of $A_{T\text{-}PCA}$ has the narrowest transition area even different heating pulses are used and longer heating pulses contribute to higher POD values, as shown in figure 4.26(d). By comparing figure 4.26(d) and 4.26(e), $A_{diff1\text{-}PCA}$ shows better detectability compared with $A_{T\text{-}PCA}$ and longer heating pulses are preferred to get higher POD values. However, in Section 4.4.1.6, it is found that the 2-norm NR shows an increasing trend if a longer heating pulse ($>$ 80 ms) is used. Thus, for $A_{diff1\text{-}PCA}$, there is a trade-off between the increase of detectability and the goodness of the linear relationship when selecting the heating pulse. Additionally, table 4.9 shows the pocket length with 90% POD (L_{90}) of different features under eight heating pulses. L_{90} means there is a 90% chance of detecting a defect longer than this value. For T_{max}, the optimal heating pulse is 50 ms with the L_{90} of 0.41 mm. However, this length is suspicious because the well-fitted linear relationship is satisfied only under shorter heating pulses (10, 20, 30 ms) as discussed in Section 4.4.1.6. For the A_{diff1}, the optimal heating pulse is 20 ms with the L_{90} of 0.66 mm. For the A_{ratio}, the optimal heating pulse is 80 ms with the L_{90} of 0.95 mm. For the $A_{T\text{-}PCA}$, the optimal heating pulse is 200 ms with the L_{90} of 0.54 mm. For the $A_{diff1\text{-}PCA}$, by considering a trade-off and taking the priority of the linear relationship, the 80 ms heating pulse is preferred with the L_{90} of 0.51 mm. From the above discussions, it can be concluded that by using any of eight heating pulses, $A_{diff1\text{-}PCA}$ has the best performance of characterising pocket lengths, which is demonstrated by the shortest L_{90} shown in last row of table 4.9.

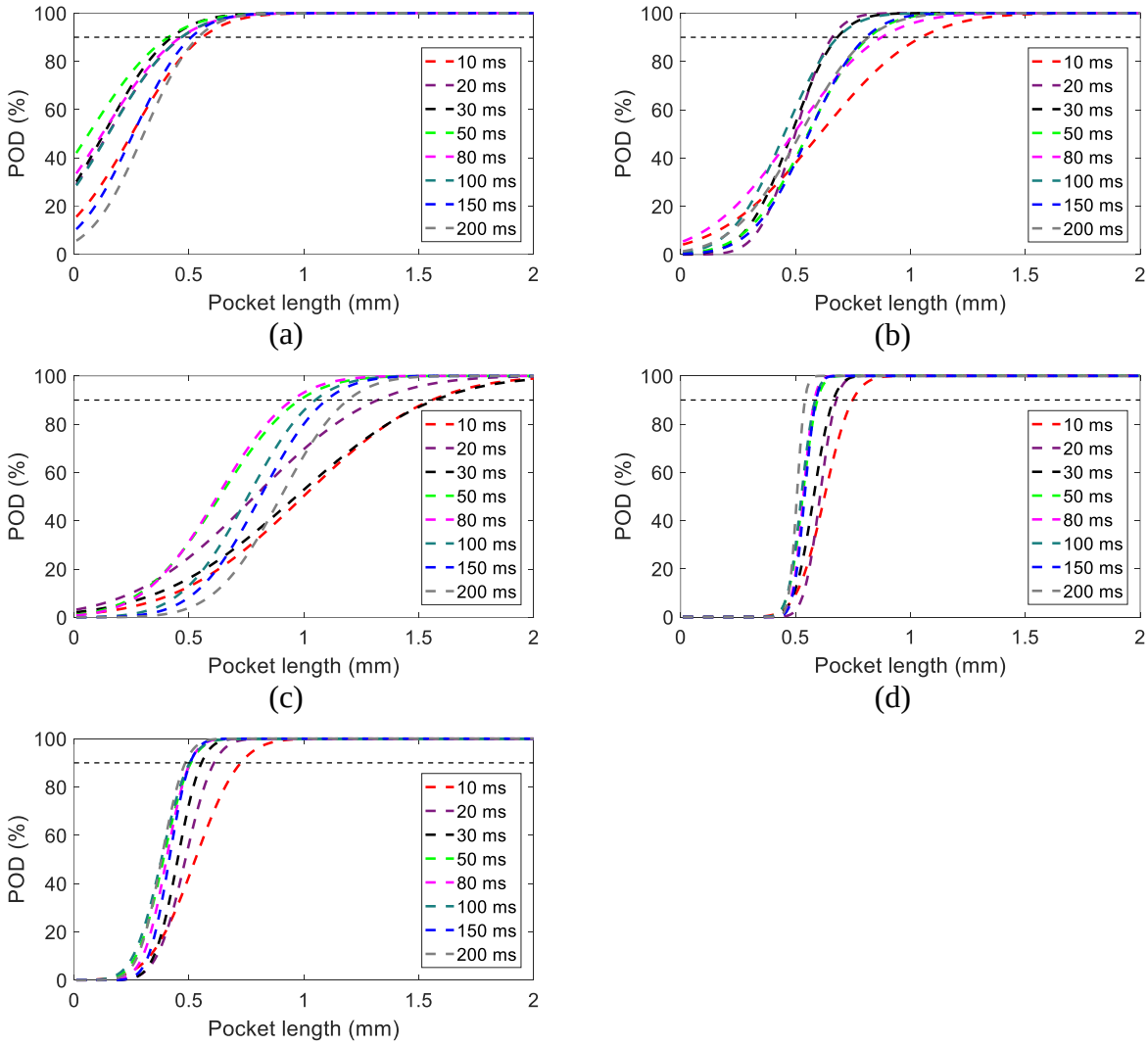

Figure 4.26 POD curve vs. pocket length under eight heating pulses.
(a) Based on T_{max}. (b) Based on A_{diff1}. (c) Based on A_{ratio}. (d) Based on $A_{T\text{-}PCA}$. (e) Based on $A_{diff1\text{-}PCA}$.

Table 4.9 Calculated results of L_{90} for different features and heating pulses

Feature	Heating pulse								Unit
	10	20	30	50	80	100	150	200	ms
T_{max}	0.56	0.47	0.43	0.41	0.47	0.47	0.51	0.54	mm
A_{diff1}	1.05	0.66	0.68	0.82	0.88	0.68	0.80	0.82	mm
A_{ratio}	1.56	1.32	1.57	0.98	0.95	1.05	1.10	1.19	mm
$A_{T\text{-}PCA}$	0.75	0.68	0.65	0.59	0.58	0.58	0.59	0.54	mm
$A_{diff1\text{-}PCA}$	0.73	0.61	0.56	0.51	0.51	0.50	0.51	0.48	mm

4.5.2 *POD analysis for evaluating performance of vertical depth characterisation*

For SUM_T, SUM_{diff1}, S_T, S_{diff1}, K_T, K_{diff1}, SS_T, and SK_T, the calculated POD curves as functions of the vertical depth are shown in figure 4.27. These POD curves are also based on equation 3.57. Similar to Section 4.5.1, the decision threshold is set as the maximum feature value of

repeated tests when S_9 of Specimen *2* is tested, i.e., it is a fifty-fifty chance to detect an angular slot with its vertical depth shorter than 0.08 mm. One problem is that by using S_T, S_{diff1}, K_T, K_{diff1}, SS_T, and SK_T for vertical depth characterisation, all the relationships present the decreasing trend, as shown in figures 4.25(h)-(m). To correctly conduct the POD analysis, the increasing trend is needed and the reciprocals of the feature values in these figures are used. Additionally, based on table 4.8 in Section 4.4.3, only the features calculated under a specific time slot or a pulse duration (presenting better linear relationships to the vertical depth) are discussed here. With more feature data collected, the 95% lower confidence bound is also estimated.

It can be seen that SUM_T, SUM_{diff1}, S_T, and K_T present similar POD curves. It is because the linear relationships between these features and the vertical depth are quite same, which are presented by similar R^2 values (around 75%) in the previous table 4.8. For S_{diff1}, K_{diff1}, and SK_T, their POD curves show unrealistic values for detecting slots with shallow vertical depths since if a vertical depth is shallower than the minimum depth (0.08 mm) used in the experiments, its corresponding POD value is extrapolated based on the assumption of a linear relationship. However, these features have poor linear relationships to the vertical depth. Compared with the above features, SS_T presents a reasonable curve with POD tending to zero for shallow vertical depths and to one for deep vertical depths. The reason is that SS_T enjoys a more linear relationship to the vertical depth. Further, table 4.10 gives the D_{90} and $D_{90/95}$ values for different features. $D_{90/95}$ means the minimum vertical depth of 90% POD with a 95% degree of confidence. It can be seen that SK_T gives the smallest values of D_{90} (0.14 mm) and $D_{90/95}$ (0.21 mm). Still, SK_T presents a poor linear relationship to the vertical depth. Although D_{90} and $D_{90/95}$ of SUM_T, SUM_{diff1}, S_T, K_T, and SS_T are larger than them of SK_T, these values are based on more linear relationships which are indicated by higher R^2 values in table 4.8. From the above discussions, it can be concluded that by choosing the 800 ms time slot, SUM_{diff1} has the best performance of characterising vertical depths, which is presented by the smallest D_{90} and $D_{90/95}$. On the other hand, SS_T can characterise vertical depths smaller than them used in experiments with reasonable POD values.

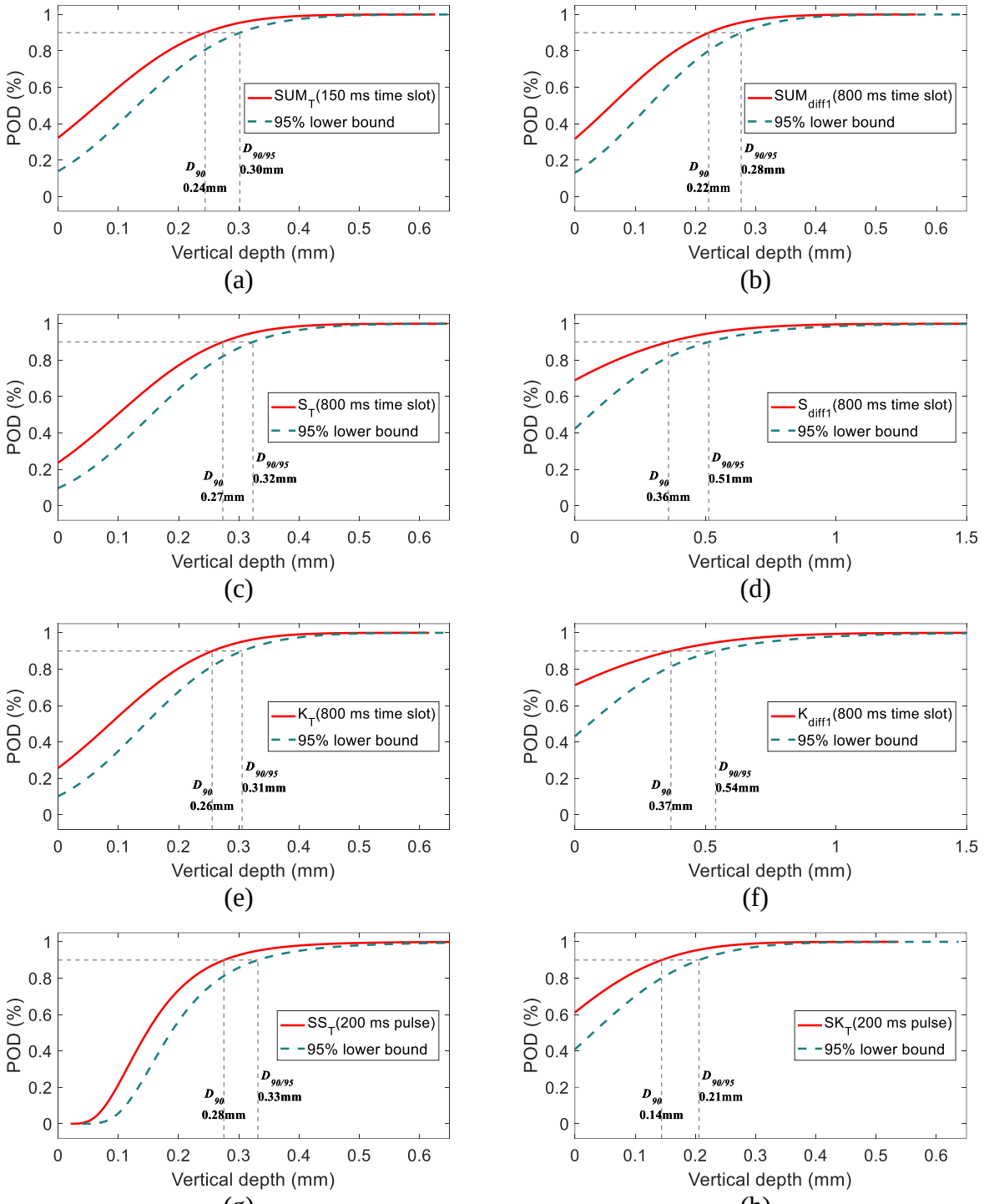

Figure 4.27 POD curve vs. pocket length under eight heating pulses.
(a) Based on SUM_T. (b) Based on SUM_{diff1}. (c) Based on S_T. (d) Based on S_{diff1}. (e) Based on K_T. (f) Based on K_{diff1}. (g) Based on SS_T. (h) Based on SK_T.

Table 4.10 Calculated results of D_{90} and $D_{90/95}$ for different features

	SUM_T	SUM_{diff1}	S_T	S_{diff1}	K_T	K_{diff1}	SS_T	SK_T	Unit
Time slot	150	800	800	800	800	800	-	-	ms
Pulse duration	-	-	-	-	-	-	200	200	ms
D_{90}	0.24	0.22	0.27	0.36	0.26	0.37	0.28	0.14	mm
$D_{90/95}$	0.30	0.28	0.32	0.51	0.31	0.54	0.33	0.21	mm

4.6 Chapter Summary

This chapter carries out a case study of features for angular defect characterisation and their performances evaluation based on POD analysis. A POD analysis framework is proposed to provide a guide on the performance evaluation of feature-based defect characterisation. The ECPT configuration and three specimens with artificial angular slots are introduced. Types of features/patterns are utilised to characterise three main parameters, i.e., pocket length, inclination angle, and vertical depth, of angular defects. The performances of different features are compared and evaluated by POD analysis. Results show that T_{max} has the advantage of high repeatability but its relationships to all three main parameters are nonlinear, especially under longer heating pulses. Although A_{diff1}, A_{ratio}, $A_{T\text{-}PCA}$, and $A_{diff1\text{-}PCA}$ have lower repeatability compared with T_{max}, these features show well-fitted linear relationships to pocket length. Among them, $A_{diff1\text{-}PCA}$ has the best performance of characterising pocket lengths, which is demonstrated by the shortest L_{90}. However, for $A_{diff1\text{-}PCA}$, special cares of the trade-off between increasing the POD and increasing the goodness of the $\hat{a}$ vs. a relationship needs to be taken. In the inclination angle characterisation, SUM_T presents the monotonic relationship by selecting specific time slots. Compared with SUM_T, SUM_{diff1} has a better monotonical relationship by using longer time slots. S_{diff1} and K_T show the monotonically increasing relationships to the inclination angle only by using 800ms time slot. Among these features, SUM_{diff1} shows the best linear relationship to the inclination angle. In the vertical depth characterisation, SUM_{diff1} has the best performance of characterising vertical depths, which is presented by the smallest D_{90} and $D_{90/95}$. On the other hand, SS_T has the highest R^2 value and the smallest 2-norm of NR and presents reasonable POD values for vertical depths outside the range used in experiments.

Chapter 5. RCF Crack Characterisation and Performance Evaluation via POD Analysis

5.1 Introduction

The previous chapter investigates the angular defect characterisation and the evaluation of the feature performance by POD analysis. In this chapter, another case study of RCF crack characterisation and performance evaluation via POD analysis is explored. Similar to the previous chapter, this chapter begins by configuring the ECPT setup and preparing three cut-off specimens containing natural RCF cracks. Then, the capabilities of the proposed features/patterns are further verified to characterise four main parameters, i.e., pocket length, inclination angle, vertical depth, and surface length, of RCF cracks. Lastly, based on the previously proposed POD analysis framework, the performances of RCF crack characterisation using these features are evaluated. The flow chart of this chapter is shown in figure 5.1 and detailed discussions will be given the following sections.

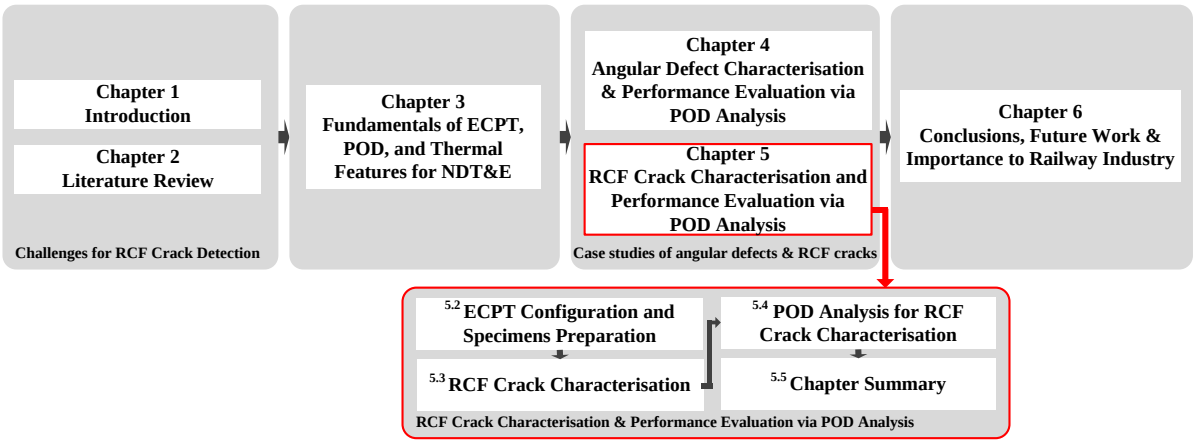

Figure 5.1 Flow chart of Chapter 5.

5.2 ECPT Configuration and Specimen Preparation

5.2.1 *ECPT configuration*

Figure 5.2(a) shows the four main units of the ECPT configuration, which are the same as those shown in figure 4.3. The only difference is that in characterising inclination angles using the first cut-off specimen (Specimen N_1 latter introduced), to capture the detailed spatial thermal patterns, a 2.9× close-up lens is mounted onto the standard lens of the IR camera, as shown in figure 5.2(b). The operational current and excitation frequency of the heating module are adjusted when testing different specimens. The frame rate and the spatial

resolution of the IR camera are set to 200 Hz, 640×120 pixels, respectively. The recording duration is 1000 ms for all the IR videos.

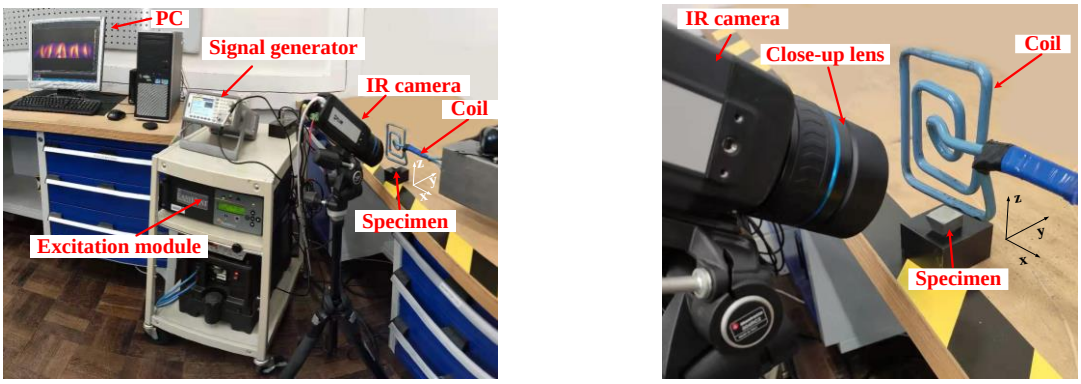

(a) (b)

Figure 5.2 ECPT configuration for RCF crack characterisation.
(a) Layout of ECPT configuration. (b) Zoom-in figure showing the close-up lens.

5.2.2 *Specimen preparation*

Three RCF specimens are carefully selected to further verify the features introduced in Section 3.4. Figure 5.3 shows the first cut-off specimen (Specimen N_1) from a PD3 (60 kg/m) rail removed from service. Compared with the AISI 1045 steel, its carbon level is slightly different within the range of 0.7 % to 0.8 % [258]. This specimen contains nine RCF cracks with different inclination angles and pocket lengths (penetration depths). Here, only eight RCF cracks (denoted as C_1-C_8) are marked and the reason will be later explained in Section 5.3. The inclination angles, pocket lengths (L), vertical depth (D) are estimated by the side view profile and 3D profile from X-ray tomography, as shown in figures 5.3(b)-(d). Note that all the vertical depths decrease along the y direction of the specimen and the deepest value of each crack is provided. Some cracks (C_2-C_5) have varying angles along the surface length direction and the estimated angles are considered as their effective values denoted by $\hat{\theta}$. This specimen is used for investigating the pocket length, the inclination angle, and the vertical depth characterisation.

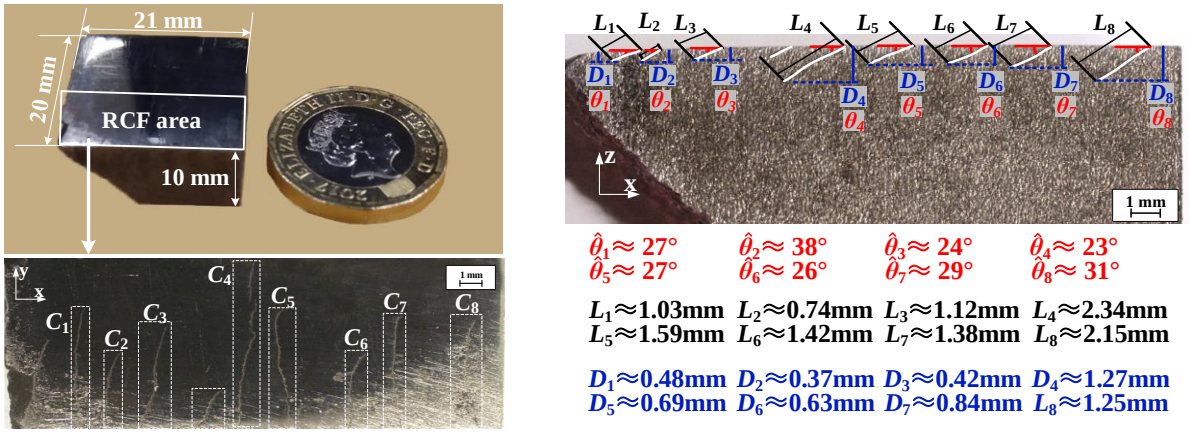

(a) (b)

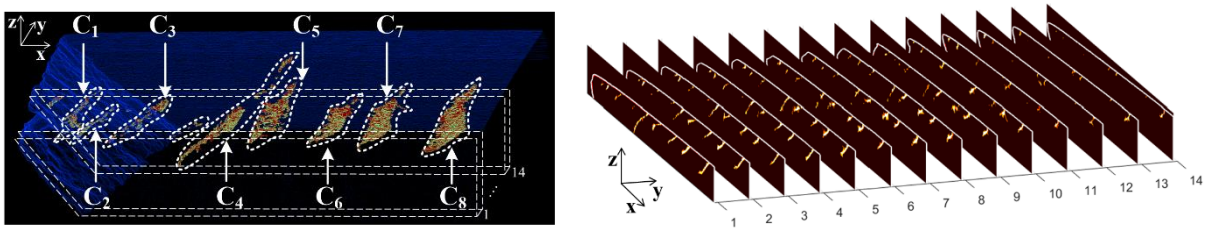

(c) (d)

Figure 5.3 Cut-off Specimen N_1 containing natural RCF cracks.
(a) Photos of the specimen. Bottom subfigure is the top view of the zoom-in RCF crack area from optical microscopy. (b) Side view of the specimen from optical microscopy. Cracks are delineated by white curves. (c)-(d) 3D profile from X-ray tomography.

Figure 5.4 shows another two cut-off specimens (Specimens N_2 and N_3) contain RCF cracks. These two specimens are used for investigating the surface length characterisation. They are selected because the RCF cracks in them are in the light stage and the moderate stage, respectively. And their clustered distributions are more complex than them of Specimen N_1. Surface lengths (SL) to be investigated are alternatively delineated by white and yellow curves, as shown in figures 5.4(c) and (d). Additionally, tables 5.1 and 5.2 give the roughly measured SL values from optical microscopy. Note that for Specimen N_3, the clustered distribution of cracks is severer, which leads to several cracks connected with each other. In figures 5.4(d), the connected cracks are delineated and considered as one clustered crack, e.g., SL_{10} and SL_{16}. In table 5.2, the SL value is the total lengths of the cracks if they are connected.

Table 5.1 Surface lengths of the cracks in Specimen N_2

Surface length number	Value (mm)									
SL_1 - SL_{10}	5.8	2.9	7.7	7.1	2.0	16.4	13.2	2.6	17.2	19.6
SL_{11} - SL_{20}	14.1	8.7	13.3	11.5	10.6	2.1	5.1	13.2	22.3	1.3
SL_{21} - SL_{30}	8.3	23.7	7.8	8.2	11.6	6.6	5.3	13.4	9.5	2.2
SL_{31} - SL_{39}	15.3	1.7	9.6	3.4	5.6	5.4	2.1	1.9	3.2	

Table 5.2 Surface lengths of the cracks in Specimen N_3

Surface length number	Value (mm)									
SL_1 - SL_{10}	2.8	12.8*	14.6*	17.7*	14.3	6.2	17.4	10.7	14.1	64.3*
SL_{11} - SL_{20}	31.7*	6.1	13.2	27.3	12.8	38.8*	23.2	13.7*	16.3	9.7

*: Total lengths of the connected cracks.

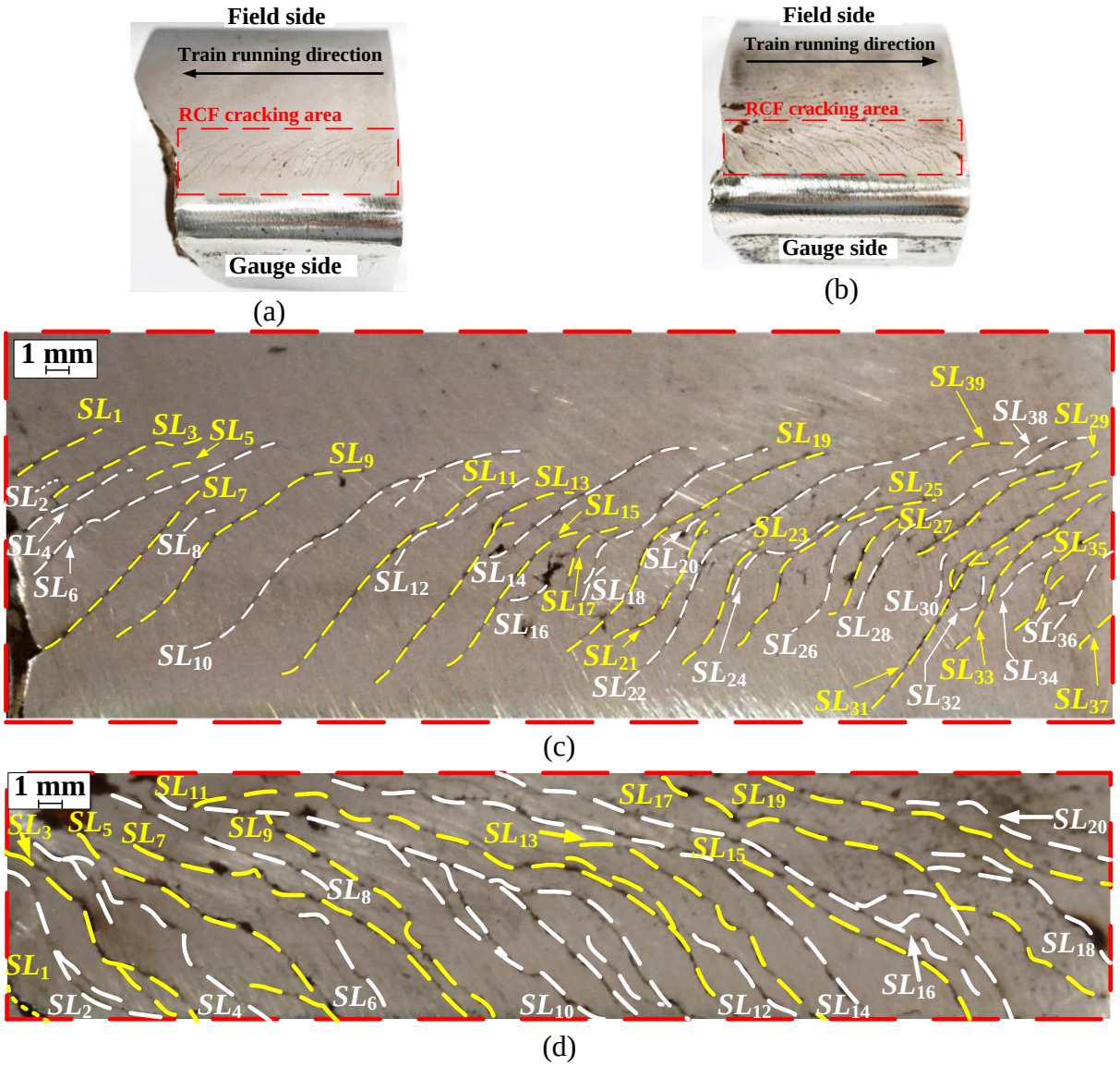

Figure 5.4 Cut-off Specimens N_2 and N_3.
(a) Photos of the Specimen N_2. (b) Photos of the Specimen N_3. (c) Zoom-in RCF crack area of Specimen N_2. (d) Zoom-in RCF crack area of Specimen N_3. Cracks to be investigated are alternatively delineated by yellow and white dashed curves.

Similarly, before carrying out experiments, all the top surfaces of three cut-off specimens are uniformly sprayed with the black matt paint to reduce the surface reflection. For the first specimen, a 7 mm lift-off distance between the bottom of the coil and the top face is kept. For the remaining two specimens, since the cracks are much longer, to avoid coil blocking the IR camera view, a 12 mm lift-off distance is used, which provides a good view of covering all the surface lengths of the cracks. In addition, to heat a clustered area of cracks, the previous coil is replaced by a larger rectangular coil.

5.3 RCF Crack Characterisation

In this section, the above RCF specimens are used for crack characterisation. At the beginning of this section, two crack reconstructors are designed to obtain the complex surface shapes of cracks. Features/patterns characterising for the pocket length, the inclination angle, the vertical depth, and the surface length are investigated in detail. For evaluating and comparing the fitted relationships between the features and the geometric parameters, the same criteria, i.e., R^2 and 2-norm NR, are used. Through comparisons, features' strengths and limitations are summarised.

5.3.1 *Design of crack shape reconstructors*

In this work, all three specimens contain natural RCF cracks. Due to the complex surface shapes of these cracks, the proposed features cannot be directly applied to characterise pocket lengths or inclination angles. Thus, two crack reconstructors are proposed to first reveal and highlight the surface shapes of cracks, and further obtain the characteristic pixels around the reconstructed shapes. Figures 5.5 shows the detailed reconstruction process and the method used in each step of the reconstructors and the example output of each step.

The crack reconstructor of Specimen N_1 is shown in figure 5.5(a). In the video preprocessing step, the previously introduced zero-lag filtering is used. In the crack response enhancement step, the PCA method is used to produce highly compressed descriptions of thermal responses. In Specimen N_1, since the crack distribution is simpler with larger crack spacings, the side effect of thermal diffusion is limited. Thus, both the heating and the cooling stages are used in this step. By properly choosing an empirical orthogonal function (EOF), underlying crack responses can be further revealed. For Specimen N_1, in the heating stage, the third EOF is selected ($EOF_{3,h}$). The further improved crack responses can be revealed by combining $EOF_{3,h}$ with $EOF_{3,c}$, which is another EOF_3 from the cooling stage. Here, the 200ms heating slot and 300ms cooling slot are found to achieve the expected result. In the crack shape reconstruction step, a set of image-processing procedures are used to reconstruct the shapes of the cracks, which include normalisation, Otsu-based binarization, linear element-based morphological opening, Euclidean distance transform, etc. Note that in the last procedure the right edges are extracted to obtain the crack shapes. It is because that all the cracks in Specimen N_1 incline to the left side as shown in figure 5.3(b) and the horizontal direction of heat propagation is from right to left. Based on the reconstruct shapes, the next step finds characteristic pixels via the histograms of local maxima at different frames. The results of this step then can be used to calculate the proposed features. The last step checks whether the

results are expected. If not, the process will return to the crack response enhancement step and update EOFs by using a new window/span of heating and cooling stages. A detailed discussion of this reconstructor will be given in Section 5.3.2.

The crack reconstructor of Specimens N_2 and N_3 is shown in figure 5.5(b). More complex and clustered distributions need to be properly addressed. In the crack response extraction step, different methods can be used, from simply choosing the thermogram or the first-order differential imaging at a specific time to utilising PCA-based patterns. In the crack shape reconstruction step, a set of image-processing procedures are used to reconstruct the shapes of the cracks. One of the key procedures is using a customised Frangi filter [259] to detection the crack shapes under complex and clustered distributions. The characteristic pixel extraction step is not considered since Specimens N_2 and N_3 are only used for investigating the surface length characterisation and the crack shapes are obtained in the third step. However, if needed, this step can be easily included. The last step checks whether the results are expected. If not, the process will return to the crack response extraction step by choosing another method and the crack shape reconstruction step by updating the parameters of the Frangi filter. A detailed application of this reconstructor will be given in Section 5.3.4.

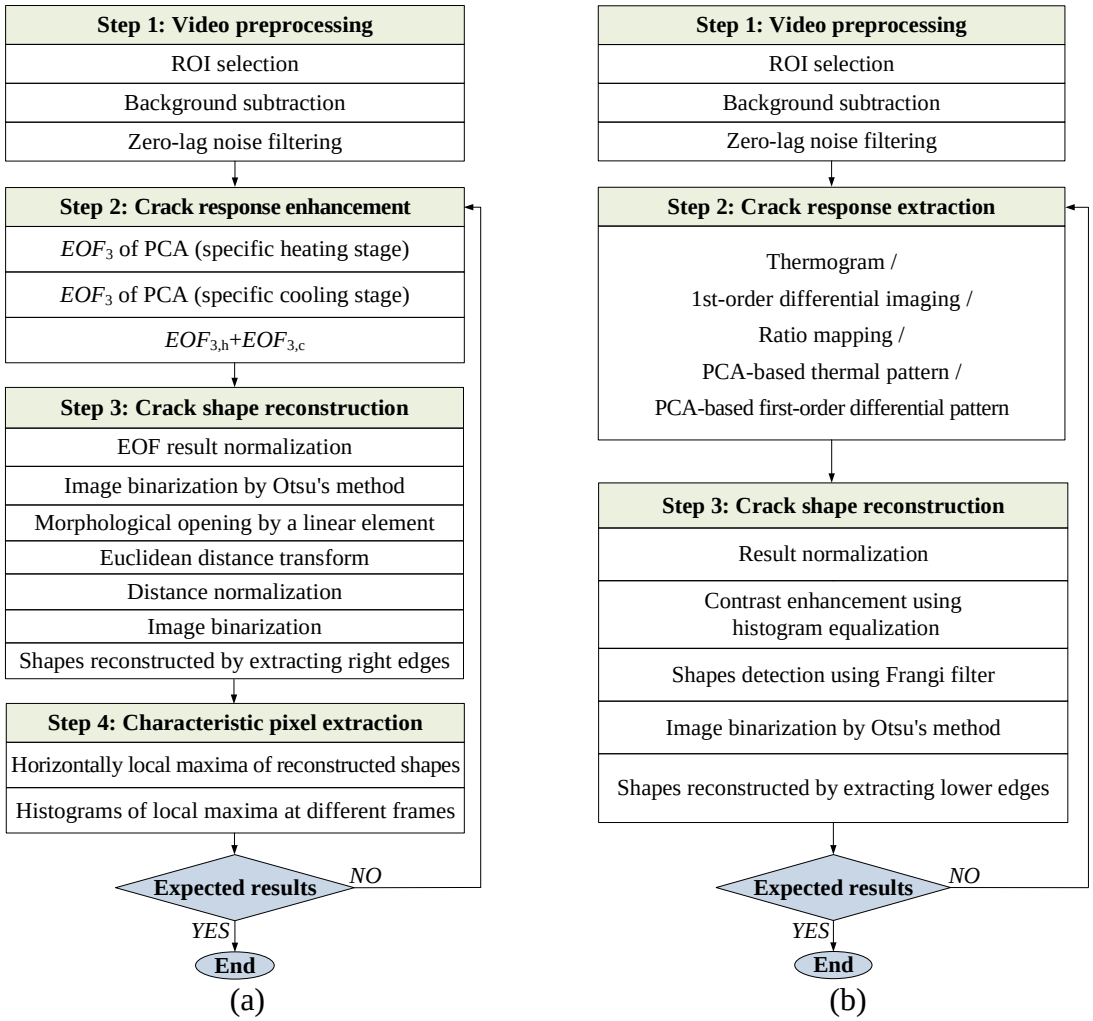

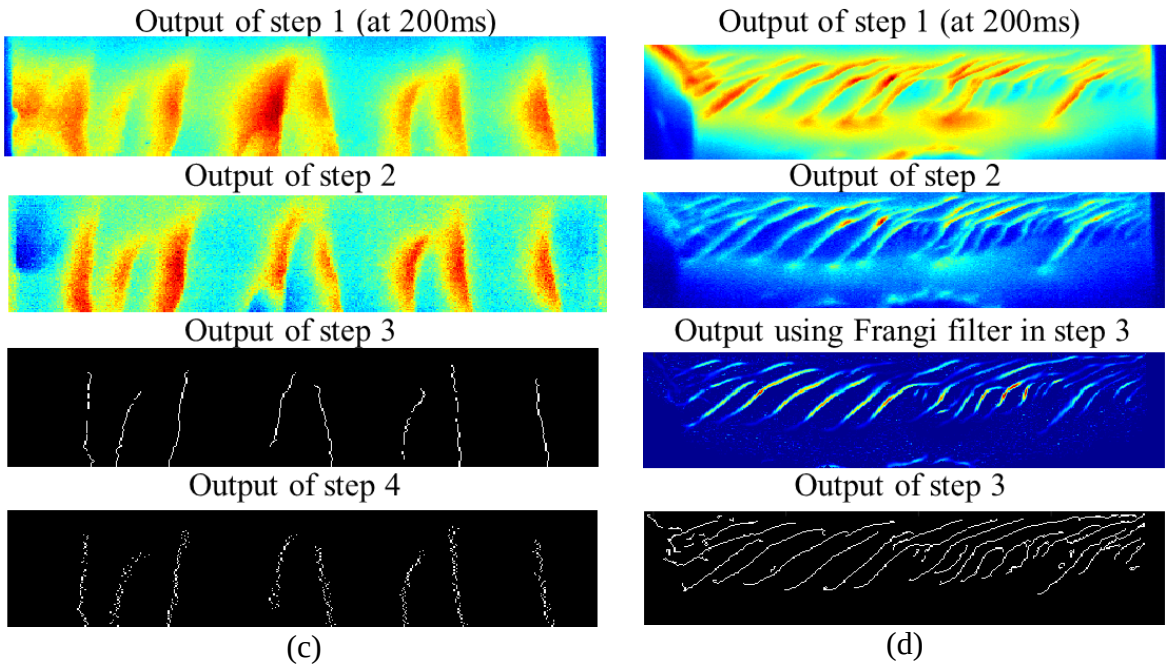

Figure 5.5 Crack reconstructors consisting of different steps.
(a) Crack reconstructor of Specimen N_1. (b) Crack reconstructor of Specimens N_2 and N_3. (c) and (d) show examples of output from each step by using these reconstructors, respectively. Note that the output of step 1 is thermal video. Here, only a thermogram at 200 ms is shown.

5.3.2 *Pocket length characterisation*

This section verifies and compares T_{max}, A_{diff1}, A_{ratio}, $A_{T\text{-}PCA}$, and $A_{diff1\text{-}PCA}$ for characterising pocket lengths of RCF cracks. Specimen N_1 is used. The heating module works with the operational RMS current of 300 A and the frequency of 262 kHz. From Chapter 4, it is found that shorter heating pulses contribute to the performance of T_{max} and A_{diff1}, whereas longer heating pulses benefits the performance of A_{ratio}, $A_{T\text{-}PCA}$, and $A_{diff1\text{-}PCA}$. Thus, five specific heating pulses (10 ms, 20 ms, 50ms, 100 ms, 200 ms) are selected.

Before extracting the above features, the first step is utilising a crack reconstructor to reveal and highlight the surface shapes of cracks. Figure 5.6(a) shows the optical image of the RCF crack area and its thermal distribution after a 200 ms heating pulse. For better observation, the red-dashed boxes show the relative positions of ROIs from the optical and thermal images. Note that the view angles of them are different. The optical one is almost vertical and the latter is around 40°-angled to avoid the view blocking from the coil. Then, via the crack reconstructor introduced in figure 5.5(a), the output of each step is shown in figures 5.6(b)-(d), respectively. By comparing the bottom subfigures of figures 5.6(a) and (b), it clearly shows that the PCA-based can effectively extract and enhance the defective areas. As previously mentioned, this study only focuses on eight RCF cracks (denoted as C_1-C_8) and the crack at the

left of C_4 is excluded. In figure 5.6(b), the response of this crack is not obvious. The reason is that this crack is at the bottom edge of the specimen and it locates outside the effective heating area of the coil. Consequently, in the crack shape reconstruction step, this crack disappeared from the reconstructed results, as shown in the bottom of figure 5.6(c). It is noteworthy that although this crack is missed in this study, an optimised coil design, e.g., using a larger diameter or multiple turns, can easily address this problem. The maximum thermal pixels around the reconstructed crack shapes are needed as the base points to calculate the proposed features. These maximum thermal pixels are changing at different frames due to measurement errors and uncertainty. In the characteristic pixel extraction step, the characteristic locations of these maximum thermal pixels of eight cracks are obtained by finding horizontally local maxima around the reconstructed shapes and their histograms at different frames, as shown in figure 5.6(d).

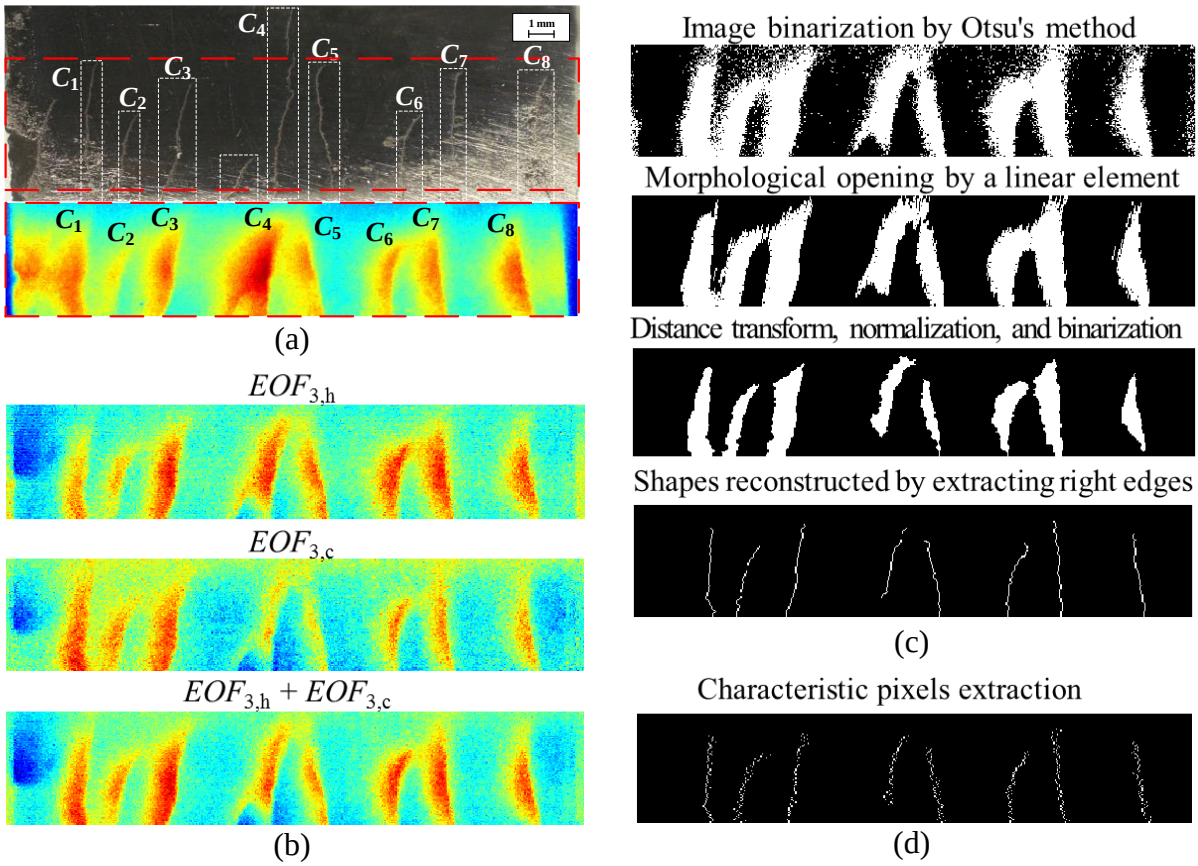

Figure 5.6 Reconstructed crack shapes and extracted characteristic pixels. (a) Preprocessed thermal frame after a 200 ms heating pulse by cropping ROI, background subtraction, and filtering. (b) Enhanced crack responses by PCA. (c) Reconstructed crack shapes by a set of image-processing procedures. (d) Extracted characteristic pixels by local maxima around the reconstructed shapes and their histograms at different frames.

Based on the above characteristic pixels, all the five features under different heating pulse durations can be calculated. Considering the complex geometry of each RCF crack, some

different procedures are used compared with the calculation of features for angular defect characterisation. Take the feature calculation of C_1 as an example. T_{max} is the average value of all the characteristic pixels from C_1. For A_{diff1}, A_{ratio}, $A_{T\text{-}PCA}$, and $A_{diff1\text{-}PCA}$, the line-scan responses are needed. Based on the characteristic pixels, horizontal-neighbour line scans are conducted. For each characteristic pixel (P_c), a 21-pixel line scan (going across it) is conducted and the middle point of this line scan is P_c. Compared with the pixel length (121 pixels) used in Section 4.4.1, it is much shorter. The reason is that a longer pixel length may reach to C_2. To avoid this, the line scan with 21 pixels is used here. After obtaining all the line scan results from first-order differential imaging, their average value is considered as A_{diff1}. Similarly, the average value of line scan results from ratio mapping, PCA-based thermal pattern, and PCA-based first-order differential pattern are considered as A_{ratio}, $A_{T\text{-}PCA}$, and $A_{diff1\text{-}PCA}$, respectively.

After all the calculation, figure 5.7 shows the relationships of these features vs. the pocket length. Figures 5.7(a) and (b) show that T_{max} and A_{diff1} tend to have positive correlations with the pocket length but neither can give a monotonic relationship. In figures 5.7(c), there is no linear fitting line plotted since it is hard to see any relationships (R^2 values are below 10%). From figures 5.7(d) and (e), it can be seen that both $A_{T\text{-}PCA}$ and $A_{diff1\text{-}PCA}$ increase with the pocket length and the relationships are more obvious under longer heating pulses. In addition, $A_{T\text{-}PCA}$ has monotonically increasing relationships to the pocket length under the 100 ms and the 200 ms heating pulse, whereas $A_{diff1\text{-}PCA}$ show the monotonical relationship to the pocket length only under the 200 ms heating pulse. Table 5.3 gives the fitting parameters of the relationships. From this table, it can be seen that for T_{max} and A_{diff1}, all the R^2 values are below 70% and it is difficult for them to present a clear relationship to pocket length. Compared with T_{max} and A_{diff1}, $A_{T\text{-}PCA}$ and $A_{diff1\text{-}PCA}$ have higher R^2 values by using longer heating pulses. In addition, longer heating pulses significantly increase their slope values and keep their 2-norm of NR values low. Thus, $A_{T\text{-}PCA}$ and $A_{diff1\text{-}PCA}$ show well-fitted linear relationships to pocket length. Comparing both, under longer heating pulses, $A_{T\text{-}PCA}$ shows better linear relationships to the pocket length (with $R^2 > 93\%$ and 2-norm NR < 1.7). On the other hand, $A_{diff1\text{-}PCA}$ shows better fitting relationships to the pocket length (with $R^2 > 75\%$ and 2-norm NR < 1.8) under shorter heating pulses.

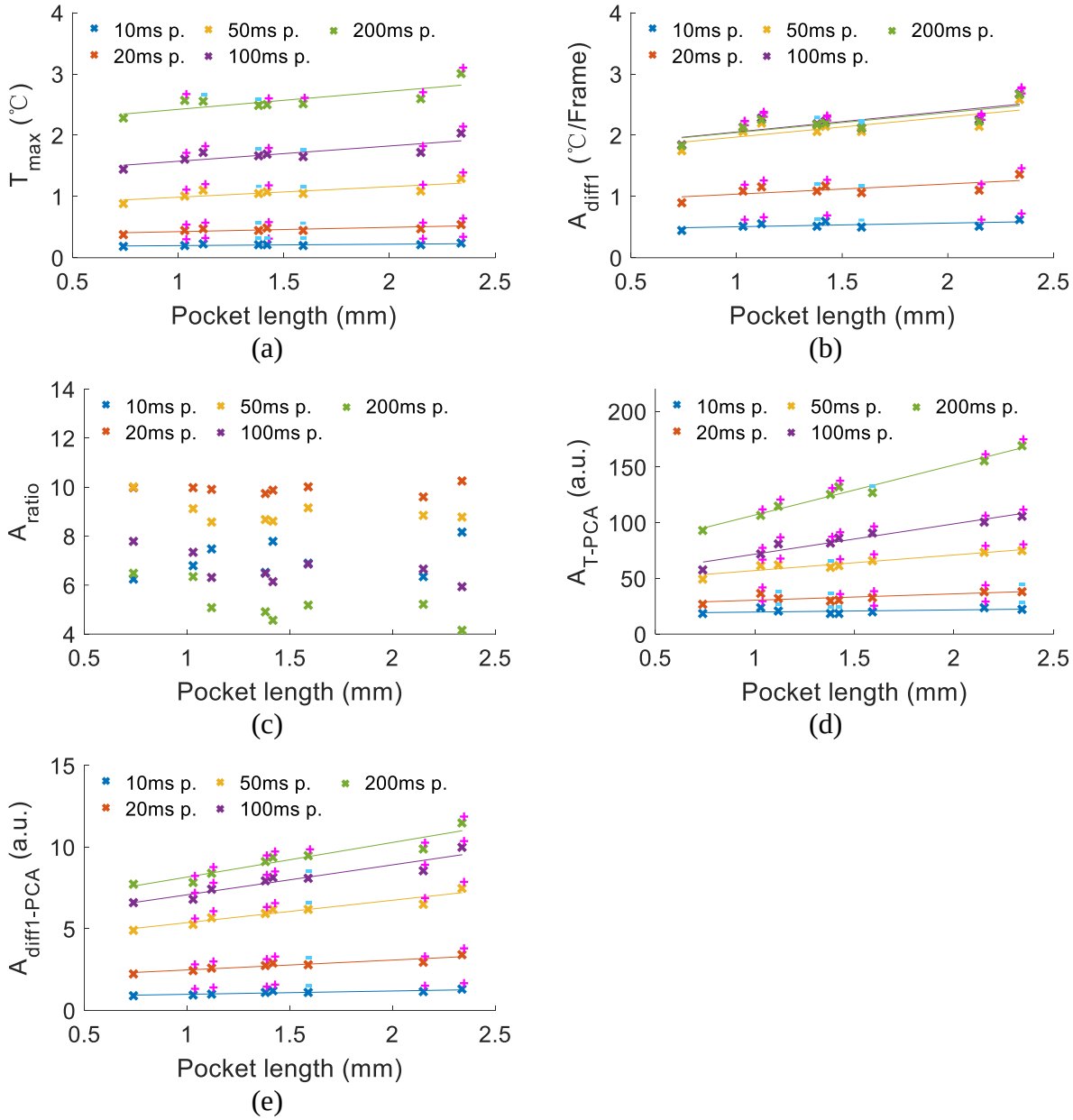

Figure 5.7 T_{max}, A_{diff1}, A_{ratio}, $A_{T\text{-}PCA}$, and $A_{diff1\text{-}PCA}$ vs. pocket length. "+" and "-" marked on the top of feature points show the increase or decrease between two neighbour points from left to right. (a) T_{max} vs. pocket length. (b) A_{diff1} vs. pocket length. (c) A_{ratio} vs. pocket length. (d) $A_{T\text{-}PCA}$ vs. pocket length (e) $A_{diff1\text{-}PCA}$ vs. pocket length.

Table 5.3 Fitting parameters of T_{max}, A_{diff1}, $A_{T\text{-}PCA}$, and $A_{diff1\text{-}PCA}$ under different pulses

	Pulse duration	10 ms	20 ms	50 ms	100 ms	200 ms
T_{max}	R^2	52.1%	65.0%	68.0%	68.4%	63.7%
	Slope	0.02	0.07	0.17	0.25	0.30
	2-norm of NR	1.94	2.02	1.82	1.80	1.88
	Mono-relationship	×	×	×	×	×
A_{diff1}	R^2	34.5%	50.0%	61.3%	63.1%	61.3%
	Slope	0.06	0.17	0.33	0.34	0.33
	2-norm of NR	2.11	2.11	1.94	1.98	2.00
	Mono-relationship	×	×	×	×	×

$A_{\text{T-PCA}}$	R^2	19.1%	56.2%	88.9%	93.2%	97.4%
	Slope	1.90	5.69	13.95	27.22	44.97
	2-norm of NR	1.92	1.98	1.87	1.63	1.65
	Mono-relationship	×	×	×	√	×
$A_{\text{diff1-PCA}}$	R^2	75.1%	85.3%	90.7%	89.2%	90.3%
	Slope	0.20	0.60	1.37	1.83	2.12
	2-norm of NR	1.65	1.73	1.87	1.74	1.76
	Mono-relationship	×	×	×	×	√

5.3.3 *Inclination angle characterisation*

This section verifies and compares SUM_{T}, SUM_{diff1}, S_{T}, S_{diff1}, K_{T}, K_{diff1}, SS_{T}, and SK_{T} for characterising inclination angles of RCF cracks. The specimen and main parameters of ECPT configuration are the same as Section 5.3.2.

Similarly, based on the characteristic pixels of each crack, the average of them is used to calculate all the eight features under different time slots and pulse durations. Figure 5.8 gives the relationships between these features and the pocket length. From figure 5.8(a), an unexpected outcome can be seen that the SUM_{T} of C_1-C_3, as shown by the circles, are much larger than others, which deviate from the decreasing trend. It probably results from the varying thickness in the left side of Specimen N_1. Under the condition, heat is easily trapped in this area and cannot diffuse through the z direction, which inevitably affects the responses of thermal features. To avoid this, the feature values of C_1-C_3 are excluded from the fitting points. The fitting results show that for SUM_{T}, SUM_{diff1}, S_{T}, S_{diff1}, K_{T}, $K_{\text{diff1,}}$ longer time slots lead to clearer relationships. However, SS_{T} and SK_{T} can hardly show any relationships to the inclination angle. Additionally, table 5.4 gives the fitting parameters and monotonic relationships. Only the best fitting results are shown this table, i.e., SUM_{T}, SUM_{diff1}, S_{T}, S_{diff1}, K_{T}, K_{diff1} are calculated by using the 800 ms time slot, and SS_{T}, SK_{T} are calculated by using the 200 ms pulse duration. Among different features, SUM_{T}, SUM_{diff1}, S_{T}, and K_{T} have better fitting relationships, which is in line with the results discussed in Section 4.4.2. However, for the S_{diff1}, K_{diff1}, SS_{T}, and SK_{T}, even under the 800 ms time slot or 200 ms pulse duration, the R^2 values lie below 35% and the absolute values of slopes are less than 0.1. Together these results provide that in testing natural RCF cracks, SUM_{T}, SUM_{diff1}, S_{T}, and K_{T} are more fit for the inclination angle characterisation.

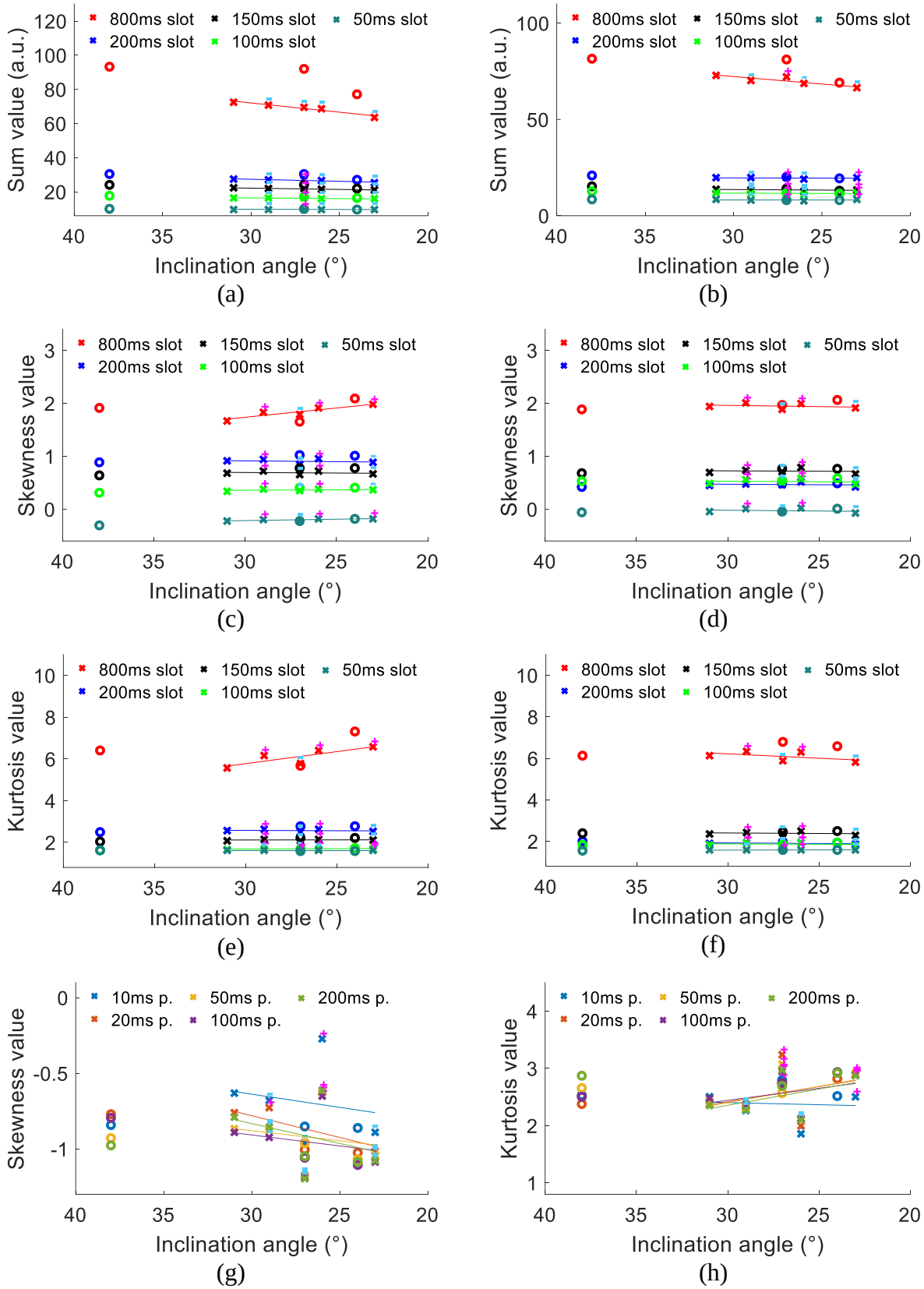

Figure 5.8 SUM_T, SUM_{diff1}, S_T, S_{diff1}, K_T, K_{diff1}, SS_T, and SK_T vs. inclination angle. Circles show the feature values of C_1-C_3,which are excluded from the fitting points. (a) and (b) show the SUM_T and SUM_{diff1} vs. inclination angle, respectively. (c) and (d) show the S_T and S_{diff1} vs. inclination angle, respectively. (e) and (f) show the K_T and K_{diff1} vs. inclination angle, respectively. (g) and (h) show SS_T and SK_T vs. inclination angle.

Table 5.4 Fitting parameters of different relationships

	SUM_T	SUM_{diff1}	S_T	S_{diff1}	K_T	K_{diff1}	SS_T	SK_T
R^2	92.4 %	74.5 %	83.0 %	7.6 %	67.6 %	30.2 %	15 %	20.2 %
Abs. slope	1.08	0.78	0.03	0.00	0.12	0.04	0.03	0.06
2-norm NR	1.76	1.65	1.59	1.73	1.56	1.76	1.44	1.47
Mono-relationship	√	×	×	×	×	×	×	×

5.3.4 *Vertical depth characterisation*

In addition to characterising pocket lengths and inclination angles, this section further investigates and verifies the capabilities of all the proposed features for the vertical depth characterisation. After the same calculation procedures, figure 5.9 shows the relationships of the features vs. the vertical depth. It can be seen that only T_{max}, A_{diff1}, A_{ratio}, $A_{T\text{-}PCA}$, and $A_{diff1\text{-}PCA}$ show positive correlations with the vertical depth. For other features, it is hard to find any clear relationships and there is no linear fitting line plotted (R^2 values are below 10%). Considering the findings in the vertical depth characterisation of angular defects, it is expected that SUM_T, SUM_{diff1}, S_T, S_{diff1}, K_T, K_{diff1}, SS_T, and SK_T should present clear relationships to the vertical depth. The outcomes are just opposite to those in Section 4.4.3. One possible reason is that the pocket length dominates the feature response. This explains why T_{max}, A_{diff1}, A_{ratio}, $A_{T\text{-}PCA}$, and $A_{diff1\text{-}PCA}$ have positive correlations with the vertical depth since these features should be more correlated to the pocket length. In fact, the average pocket length of this specimen is 1.47 mm, which is much longer than the average value (0.99 mm) of Specimens *2* and *3*. Another possible reason is that the feature responses are affected by the varying thickness in the left side of Specimen N_1, as mentioned in the previous section. Table 5.5 further shows the fitting parameters of the relationships. From this table, it can be seen that the best linear relationship to the vertical depth is obtained by using $A_{T\text{-}PCA}$. Still, the relationship probably results from the pocket length.

Table 5.5 Fitting parameters of different relationships

	T_{max}	A_{diff1}	$A_{T\text{-}PCA}$	$A_{diff1\text{-}PCA}$
Pulse duration	100ms	100ms	200ms	200ms
R^2	54.0%	49.5%	88.9%	78.8%
Slope	0.34	0.46	66.54	3.07
2-norm of NR	1.90	2.08	2.06	1.94
Mono-relationship	×	×	×	×

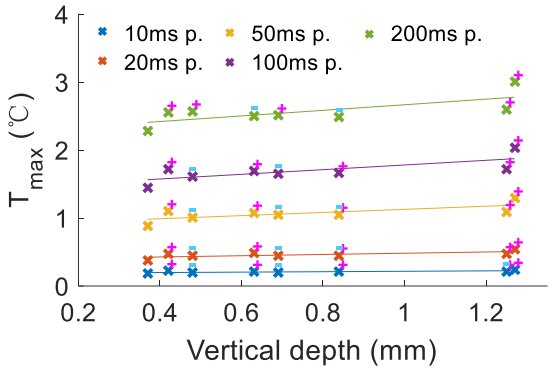
10ms p.
20ms p.
50ms p.
100ms p.
200ms p.
T_{max} (℃)
Vertical depth (mm)

(a)

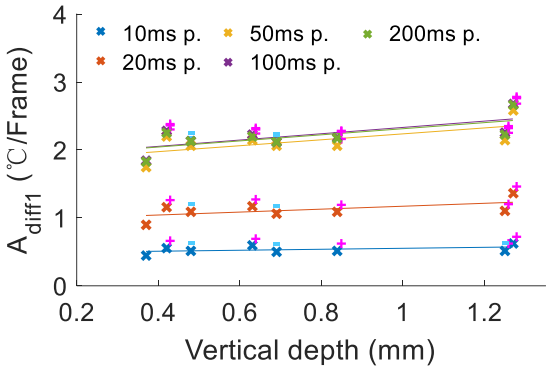
10ms p.
20ms p.
50ms p.
100ms p.
200ms p.
A_{diff1} (℃/Frame)
Vertical depth (mm)

(b)

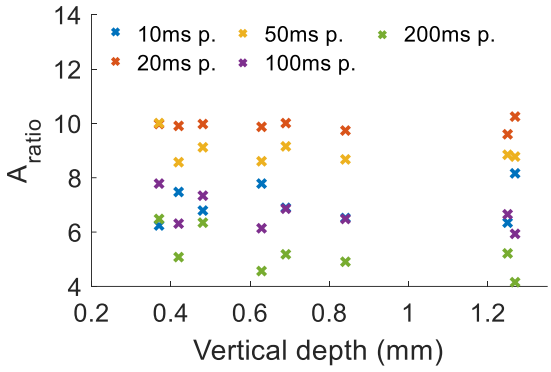
10ms p.
20ms p.
50ms p.
100ms p.
200ms p.
A_{ratio}
Vertical depth (mm)

(c)

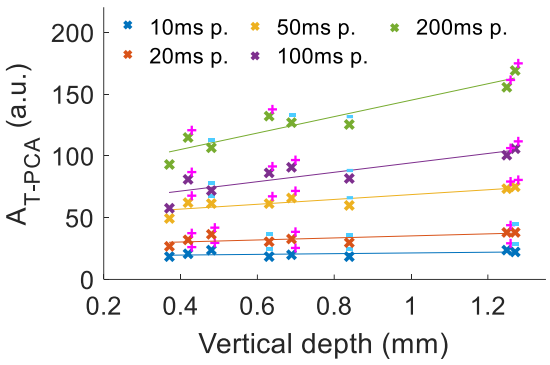
10ms p.
20ms p.
50ms p.
100ms p.
200ms p.
$A_{T\text{-}PCA}$ (a.u.)
Vertical depth (mm)

(d)

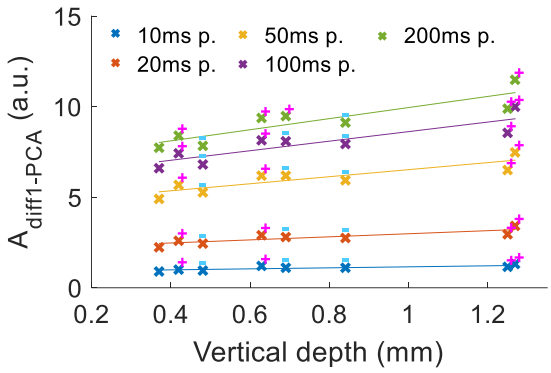
10ms p.
20ms p.
50ms p.
100ms p.
200ms p.
$A_{diff1\text{-}PCA}$ (a.u.)
Vertical depth (mm)

(e)

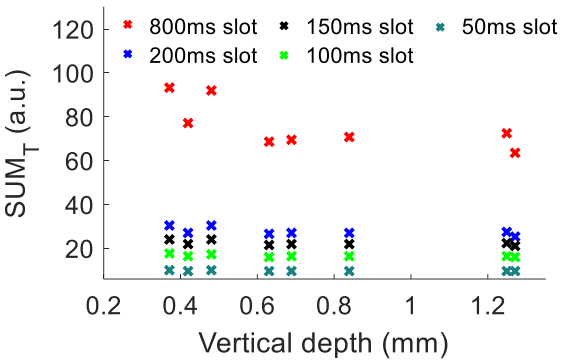
800ms slot
200ms slot
150ms slot
100ms slot
50ms slot
SUM_T (a.u.)
Vertical depth (mm)

(f)

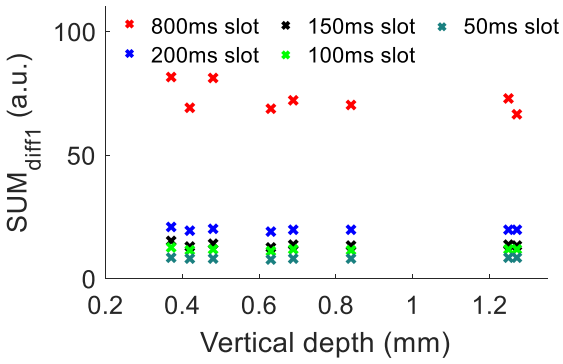
800ms slot
200ms slot
150ms slot
100ms slot
50ms slot
SUM_{diff1} (a.u.)
Vertical depth (mm)

(g)

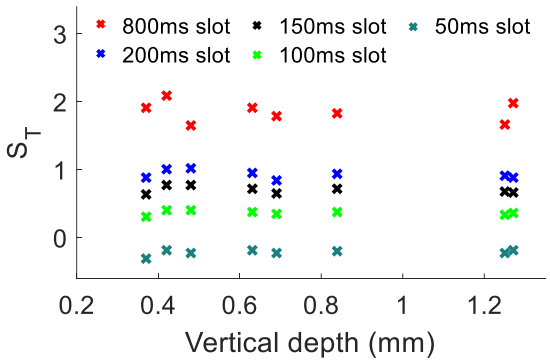
800ms slot
200ms slot
150ms slot
100ms slot
50ms slot
S_T
Vertical depth (mm)

(h)

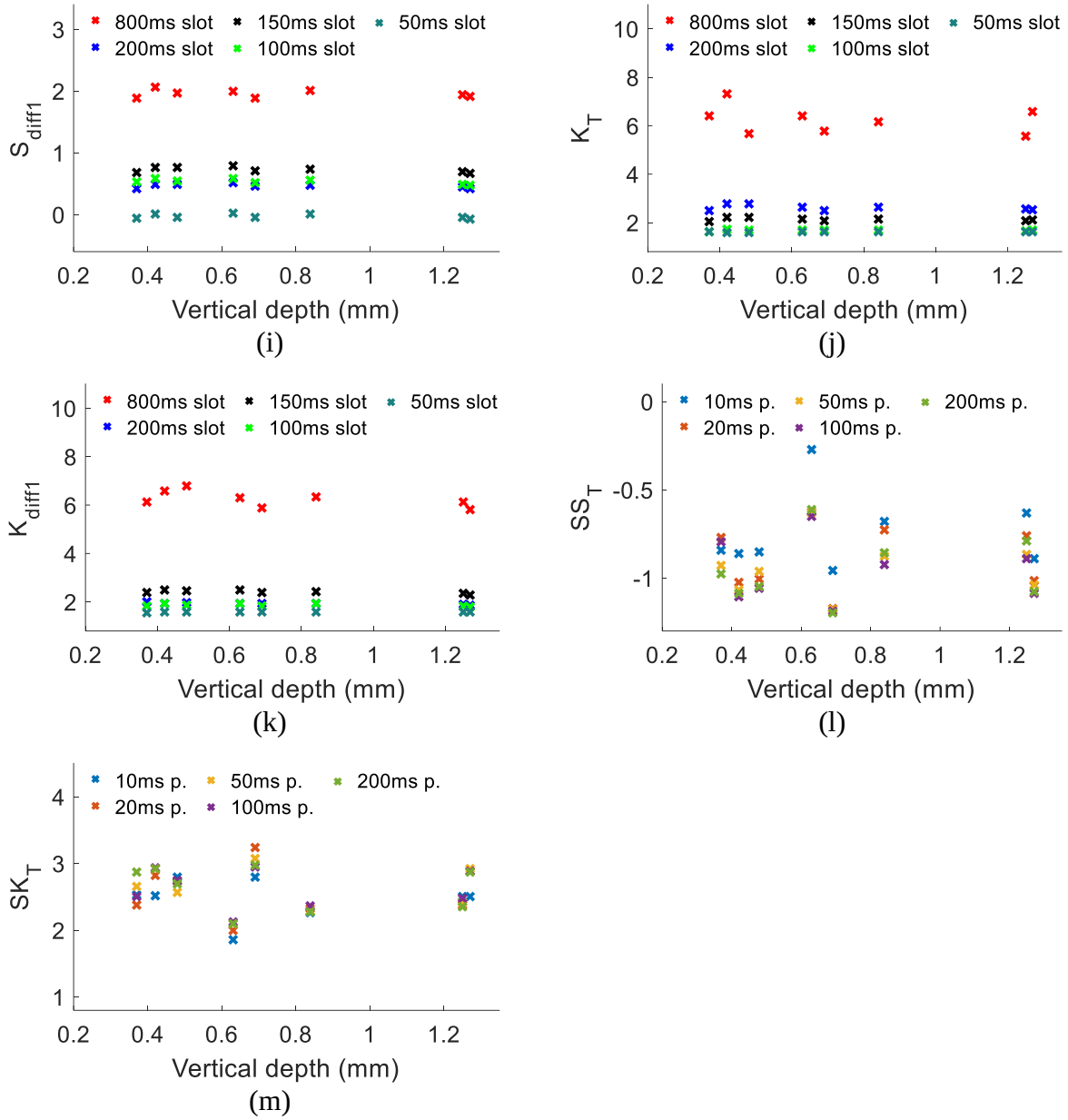

Figure 5.9 All the proposed features vs. vertical depth of testing Specimen N_1. (a), (b), (l) and (m) show the spatial domain-based features vs. vertical depth. (c)-(e) give the tempo-spatial-based patterns vs. vertical depth. (f)-(k) show the temporal domain-based features vs. vertical depth. (a) T_{max} vs. vertical depth. (b) A_{diff1} vs. vertical depth. (c) A_{ratio} vs. vertical depth. (d) $A_{T\text{-}PCA}$ vs. vertical depth. (e) $A_{diff1\text{-}PCA}$ vs. vertical depth. (f) SUM_T vs. vertical depth. (g) SUM_{diff1} vs. vertical depth. (h) S_T vs. vertical depth. (i) S_{diff1} vs. vertical depth. (j) K_T vs. vertical depth. (k) K_{diff1} vs. vertical depth. (l) SS_T vs. vertical depth. (m) SK_T vs. vertical depth. For each vertical depth, the test is repeated six times and the average value is shown as a feature point in the figures. "+" and "-" marked on the top of feature points show the increase or decrease between two neighbour points from left to right. Solid lines show the linear fitting relationships.

5.3.5 *Surface length characterisation*

Another important aspect for RCF crack characterisation is the surface length characterisation since the severity of a crack is strongly linked to its surface length. This section investigates the surface length characterisation by using the second crack reconstructor introduced Section 5.3.1. Here, Specimens N_2 and N_3 are used. Compared with Specimen N_1, Specimens N_2 and N_3 contain more cracks and their clustered distributions are more complex. Additionally, since a high lift-off distance is used, the operational current of the heating module is adjusted to a higher value of 350 A for testing Specimens N_2 and N_3.

From the crack reconstructor shown in figure 5.5(b), different methods can be used in the crack response extraction step, including simple thermograms, first-order differential imaging, ratio mapping, PCA-based thermal pattern, and PCA-based first-order differential pattern. These methods have been introduced in Section 3.4 and the features derived from them have been used for the pocket length and the inclination angle characterisation. Here, two-dimensional images instead of the proposed features from these methods are considered as the outputs of the crack response extraction step. These images are taken as the inputs of the crack shape reconstruction step, as shown in figure 5.10.

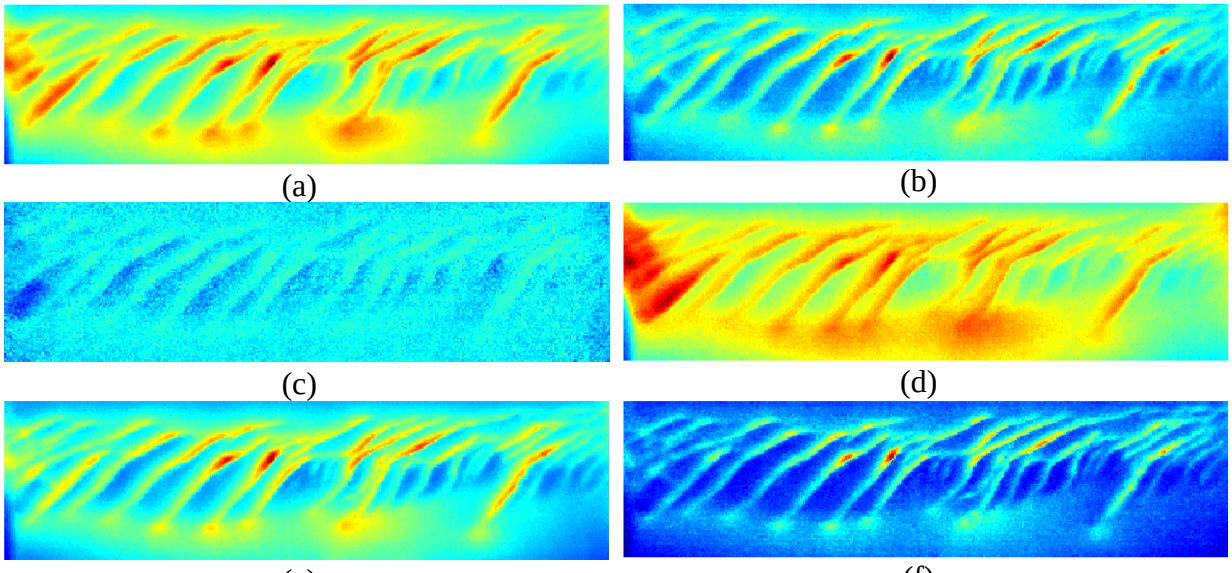

Figure 5.10 Crack response extraction of Specimen N_2.
(a) Thermogram at 200 ms, $I_{T\text{-}200}$. (b) First-order differential imaging at 30 ms, $I_{diff1\text{-}30}$. (c) Ratio mapping under 200 ms heating pulse, I_{ratio}. (d) PCA-based thermal pattern under 200 ms heating pulse, $I_{T\text{-}PCA}$. (e) PCA-based first-order differential pattern under 200 ms heating pulse, $I_{diff1\text{-}PCA}$. (f) Refined PCA-based thermal pattern in the early heating stage, $I_{ET\text{-}PCA}$.

Specifically, figure 5.10(a) shows the thermogram at the end of the 200 ms heating pulse, denoted as $I_{T\text{-}200}$. Figure 5.10(b) gives the first-order differential imaging at the 30 ms, when

an averaged first-order differential response of 100 selected pixels in the defective areas reach to its maximum, and it is denoted as $I_{\text{diff1-30}}$. Figure 5.10(c) presents the ratio mapping based on the first-order differential result, denoted as I_{ratio}. Figures 5.10(d)-(e) show the PCA-based thermal pattern and first-order differential pattern under the 200ms heating pulse, denoted as $I_{\text{T-PCA}}$, $I_{\text{diff1-PCA}}$, respectively. From the above figures, all of them can give the two-dimensional presentations of the cracks' clustered distributions. Among them, I_{ratio} shows the lowest contrast of the defective areas. The remaining four images have higher contrasts, but they suffer from the edge effect, i.e., trapping heat from diffusion, in the left side of the specimen, which is especially obvious in figures 5.10(a) and (d). In addition, it is difficult to identify some small cracks, such as SL_{30}, SL_{37}. To avoid the edge effect and missing small cracks, a refined PCA-based thermal pattern is proposed here (denoted as $I_{\text{ET-PCA}}$) to strengthen the crack response extraction step. For the refined one, two early heating stages with different time slots are considered. $EOF_{1,\text{h1}}$ is obtained by selecting EOF_1 from the first heating stage ($EOF_{1,\text{h1}}$) and a further improvement is conducted by combining $EOF_{1,\text{h1}}$ with another $EOF_{1,\text{h2}}$, which the EOF_1 from the second heating stage. It is found that the expected results are achieved by using the heating stages with the 0-15ms and the 15-30ms time slots, respectively. The result of $I_{\text{ET-PCA}}$ is shown in figures 5.10(f).

By individually inputting the above two-dimensional images into the crack shape reconstruction step, the reconstructed shapes are shown in figures 5.11(a)-(f), respectively. Note that in each subfigure, the top one is the result by using the customised Frangi filter with its parameter σ (the standard deviation) ranging from 0.2 to 2.0. The middle one is the final reconstructed shapes. The bottom one gives the automatically labelled crack shapes by different colours. By comparing these figures, the worst case is the result of using I_{ratio} as the input data, as shown in figure 5.11(c). For the remaining figures, most of the crack shapes can be successfully revealed. Better results are obtained by using $I_{\text{diff1-30}}$ and $I_{\text{ET-PCA}}$, as shown in figures 5.11(b) and (f). Even the shapes of small cracks can be reconstructed. By comparing these two, $I_{\text{ET-PCA}}$ outperforms $I_{\text{diff1-30}}$, which is shown by the reconstructed shapes of SL_2, SL_{30}, and SL_{37}.

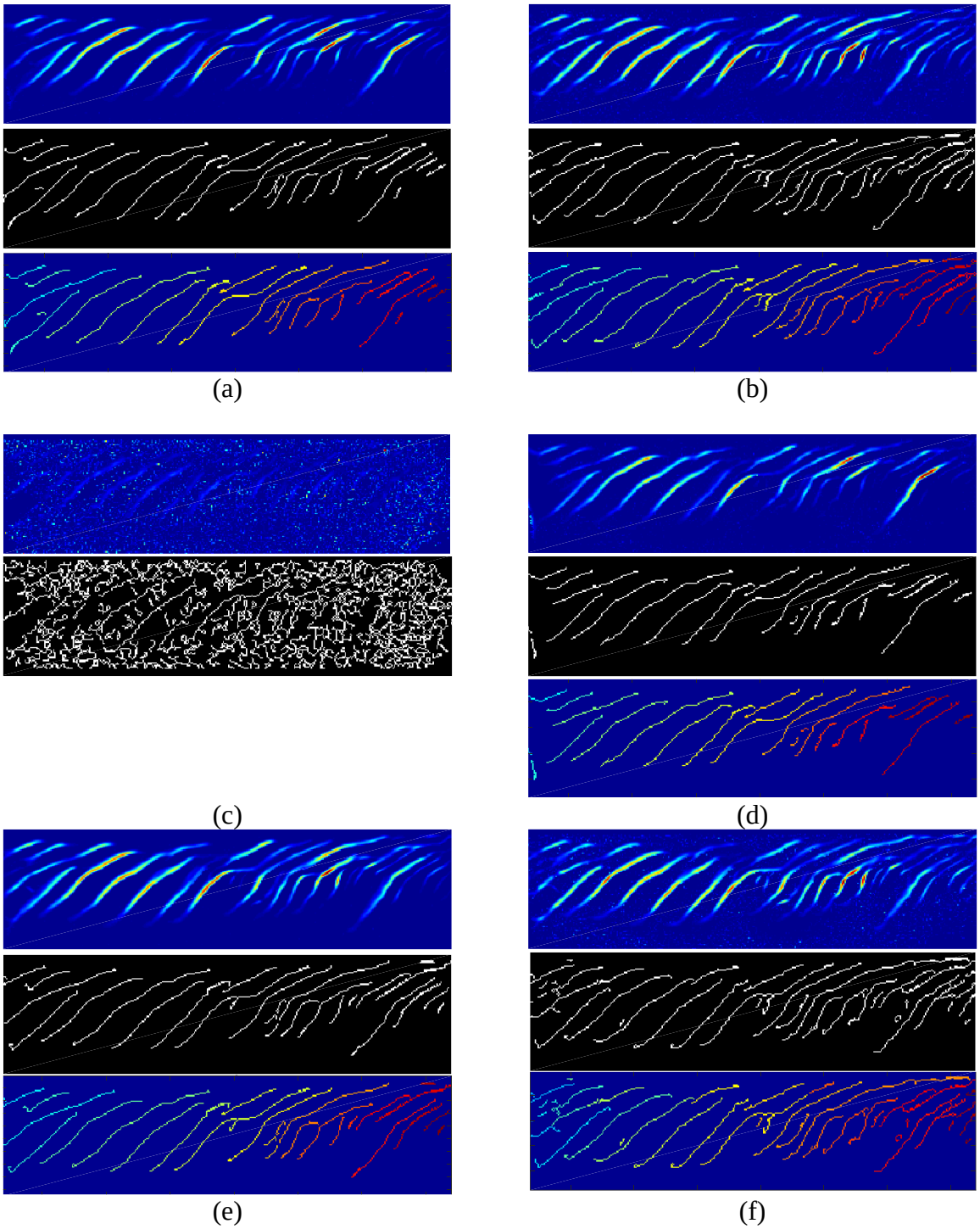

Figure 5.11 Crack shape reconstruction of Specimen N_2.
In each subfigure, the top, middle, and bottom show the result of Frangi filter, the final reconstructed shapes and the automatically labelled crack shapes, respectively. (a) Reconstructed results by using $I_{\text{T-200}}$. (b) Reconstructed results by using $I_{\text{diff1-30}}$. (c) Reconstructed results by using I_{ratio}. (d) Reconstructed results by using $I_{\text{T-PCA}}$. (e) Reconstructed results by using $I_{\text{diff1-PCA}}$. (f) Reconstructed results by using $I_{\text{ET-PCA}}$.

Based on the reconstructed crack shapes, the pixel length (*PL*) of each crack shape can be calculated, as shown in table 5.6. Note that some of the reconstructed shapes are connected and they are considered as one crack. For instance, in figure 5.11(a), PL_{15}, PL_{17}, and PL_{18} cannot be separated and they are considered as one crack with the length of 115 pixels, which

is corresponding to the sum of SL_{15}, SL_{17}, and SL_{18}, i.e., 28.9 mm. Based on this rule, the relationships between PL and SL (see table 5.1) of Specimen N_2 are shown in figure 5.12. Here, only non-null values in table 5.6 are used as the fitting data. In addition, table 5.7 shows the fitting parameters of these relationships. It shows that by using $I_{T\text{-}200}$, $I_{diff1\text{-}30}$, $I_{T\text{-}PCA}$, $I_{diff1\text{-}PCA}$, $I_{ET\text{-}PCA}$, PL positively correlates with SL. Among these crack response extraction methods, $I_{ET\text{-}PCA}$ provides the best PL vs. SL relationship, with the highest R^2 (92.8 %) and smallest 2-norm of NR (2.24).

Table 5.6 Pixel lengths of the cracks in Specimen N_2

	Surface length number	Value (pixels)									
$I_{T\text{-}200}$	PL_1 - PL_{10}	30	null	37	null	null	89	65	null	77	111
	PL_{11} - PL_{20}	70	null	76	48	115[*1]	null	115[*1]	115[*1]	87	null
	PL_{21} - PL_{30}	21	105	36	null	61	23	null	111[*2]	111[*2]	null
	PL_{31} - PL_{39}	69	null	39	null	22	null	null	null	null	
$I_{diff1\text{-}30}$	PL_1 - PL_{10}	36	null	47	21	null	94	62	null	87	121
	PL_{11} - PL_{20}	87	null	81	49	149[*1]	null	149[*1]	149[*1]	89	null
	PL_{21} - PL_{30}	36	140[*3]	46	null	71	25	22	48	87	null
	PL_{31} - PL_{39}	164[*4]	null	164[*4]	null	33	18	null	28	140[*3]	
$I_{T\text{-}PCA}$	PL_1 - PL_{10}	20	null	38	null	null	70	47	null	81	113
	PL_{11} - PL_{20}	74	null	72	45	100[*1]	null	100[*1]	100[*1]	82	null
	PL_{21} - PL_{30}	16	107	35	null	65	23	null	93[*2]	93[*2]	null
	PL_{31} - PL_{39}	75	null	null	null	22	null	null	null	null	
$I_{diff1\text{-}PCA}$	PL_1 - PL_{10}	36	null	40	null	null	90	62	null	82	114
	PL_{11} - PL_{20}	78	null	85	44	130[*1]	null	130[*1]	130[*1]	89	null
	PL_{21} - PL_{30}	26	106	44	null	72	24	15	46	91	null
	PL_{31} - PL_{39}	81	null	64	null	24	13	null	22	null	
$I_{ET\text{-}PCA}$	PL_1 - PL_{10}	36	8	46	8	null	102	63	null	86	128
	PL_{11} - PL_{20}	79	null	78	50	151[*1]	null	151[*1]	151[*1]	94	null
	PL_{21} - PL_{30}	39	184[*5]	47	null	47	62	18	126[*2]	126[*2]	8
	PL_{31} - PL_{39}	173[*6]	null	173[*6]	173[*6]	30	26	8	184[*5]	184[*5]	

[*1]: PL_{15}, PL_{17}, and PL_{18} are connected and they are considered as one crack.
[*2]: PL_{28} and PL_{29} are connected and they are considered as one crack.
[*3]: PL_{22} and PL_{39} are connected and they are considered as one crack.
[*4]: PL_{31} and PL_{33} are connected and they are considered as one crack.
[*5]: PL_{22}, PL_{38}, and PL_{39} are connected and they are considered as one crack.
[*6]: PL_{31}, PL_{33}, and PL_{34} are connected and they are considered as one crack.

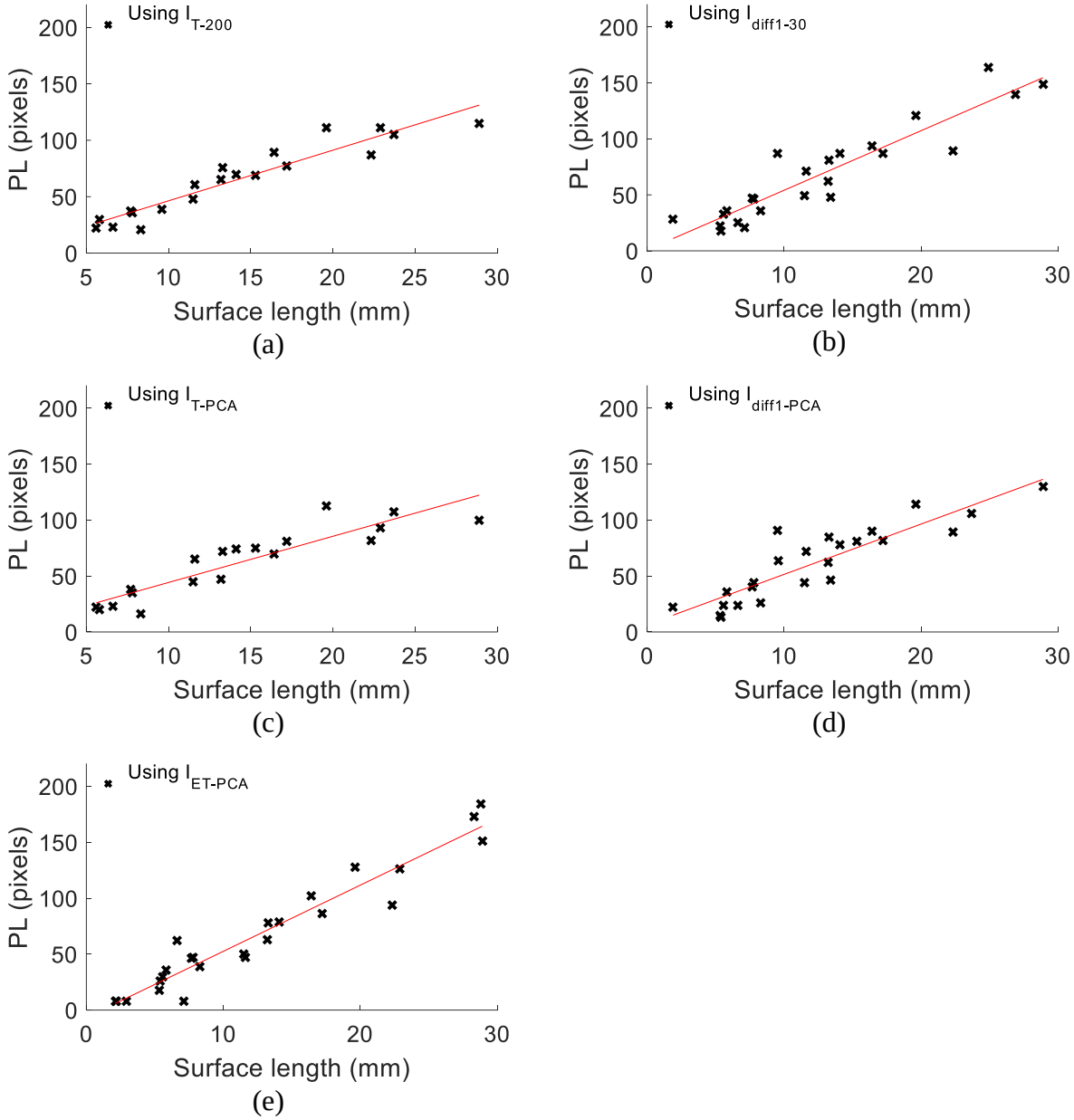

Figure 5.12 *PL* vs. *SL* of Specimen N_2 in the crack response extraction step. (a) *PL* vs. *SL* by using $I_{T\text{-}200}$. (b) *PL* vs. *SL* by using $I_{diff1\text{-}30}$. (c) *PL* vs. *SL* by using $I_{T\text{-}PCA}$. (d) *PL* vs. *SL* by using $I_{diff1\text{-}PCA}$. (e) *PL* vs. *SL* by using $I_{ET\text{-}PCA}$.

Table 5.7 Fitting parameters of different relationships

	$I_{T\text{-}200}$	$I_{diff1\text{-}30}$	$I_{T\text{-}PCA}$	$I_{diff1\text{-}PCA}$	$I_{ET\text{-}PCA}$
R^2	89.6 %	86.3 %	82.6 %	79.6 %	92.8 %
Slope	4.49	5.32	4.13	4.50	5.91
2-norm of NR	2.31	2.31	2.40	2.84	2.24

Following the same steps, figure 5.13 shows $I_{T\text{-}200}$, $I_{diff1\text{-}30}$, I_{ratio}, $I_{T\text{-}PCA}$, $I_{diff1\text{-}PCA}$, and $I_{ET\text{-}PCA}$ of RCF crack area in Specimen N_3. From this figure, it can be seen that all the results are affected by the clustered distribution of the cracks. Among these methods, I_{ratio} still shows the

lowest contrasts of defective areas. $I_{T\text{-}200}$ and $I_{T\text{-}PCA}$ suffer from the side effect of thermal diffusion and some cracks cannot be clearly distinguished, such as SL_2 and SL_6. For $I_{diff1\text{-}30}$, $I_{diff1\text{-}PCA}$, and $I_{ET\text{-}PCA}$, they present higher contrasts of the cracks. Since $I_{diff1\text{-}30}$, and $I_{ET\text{-}PCA}$ are obtained by using the early heating stage, they are less influenced by the thermal diffusion, thereby revealing more distinct crack shapes, e.g., SL_2, SL_{10}, and SL_{12}.

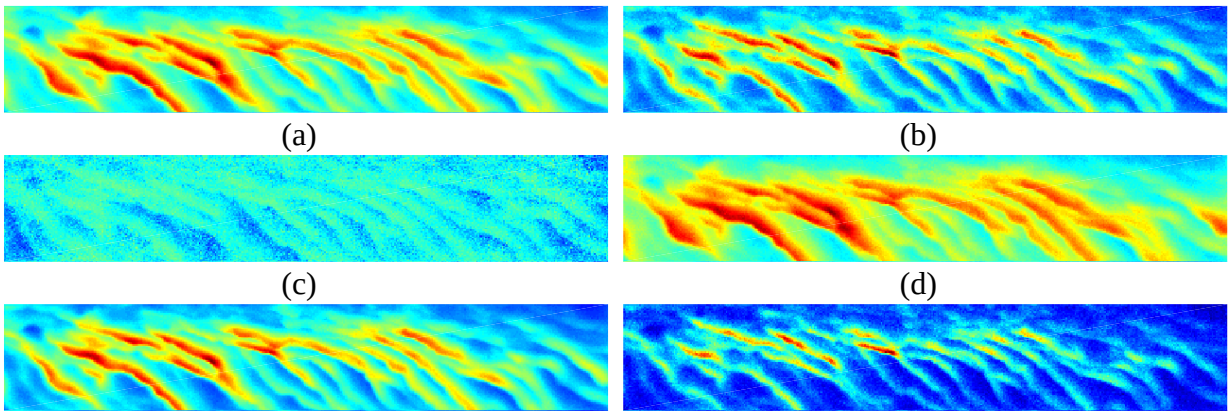

Figure 5.13 Crack response extraction of Specimen N_3.
(a) Thermogram at 200 ms, $I_{T\text{-}200}$. (b) First-order differential imaging at 30 ms, $I_{diff1\text{-}30}$. (c) Ratio mapping under 200 ms heating pulse, I_{ratio}. (d) PCA-based thermal pattern under 200 ms heating pulse, $I_{T\text{-}PCA}$. (e) PCA-based first-order differential pattern under 200 ms heating pulse, $I_{diff1\text{-}PCA}$. (f) Refined PCA-based thermal pattern in the early heating stage, $I_{ET\text{-}PCA}$.

Figures 5.14 show the reconstructed shapes by using the above results in the crack shape reconstruction step. As shown in figures 5.14(b) and (f), better results revealing more crack shapes are obtained by using $I_{diff1\text{-}30}$ and $I_{ET\text{-}PCA}$. Based on the reconstructed crack shapes, *PL* of each crack shape is calculated, as shown in table 5.8. Similarly, if the reconstructed crack shapes are connected, they are considered as one crack. Further, the relationships between *PL* and *SL* of Specimen N_3 are shown in figure 5.15. Table 5.9 gives the fitting parameters of these relationships. Results show that by using $I_{T\text{-}200}$, $I_{diff1\text{-}30}$, $I_{T\text{-}PCA}$, $I_{diff1\text{-}PCA}$, $I_{ET\text{-}PCA}$, *PL* presents positive correlations with *SL*. Among these crack response extraction methods, $I_{diff1\text{-}30}$, $I_{diff1\text{-}PCA}$, and $I_{ET\text{-}PCA}$ provide better fitting relationships. Different from the results from Specimen N_2, the best *PL* vs. *SL* relationship is obtained by using $I_{diff1\text{-}30}$, which has a R^2 and a 2-norm of NR of 85.8 % and 2.24, respectively.

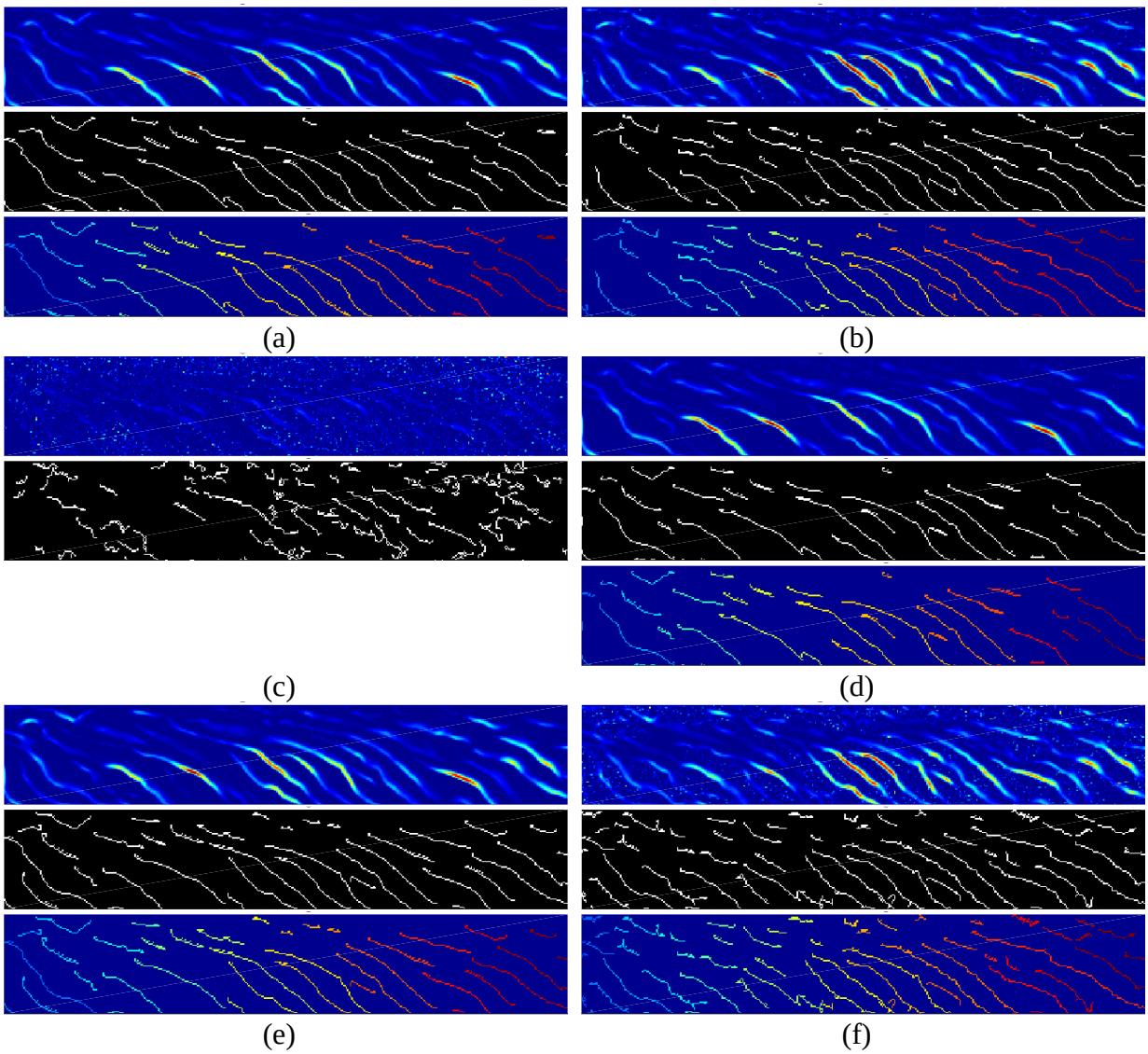

Figure 5.14 Crack shape reconstruction of Specimen N_3.
In each subfigure, the top, middle, and bottom show the result of Frangi filter, the final reconstructed shapes and the automatically labelled crack shapes, respectively. (a) Reconstructed results by using $I_{\text{T-200}}$. (b) Reconstructed results by using $I_{\text{diff1-30}}$. (c) Reconstructed results by using I_{ratio}. (d) Reconstructed results by using $I_{\text{T-PCA}}$. (e) Reconstructed results by using $I_{\text{diff1-PCA}}$. (f) Reconstructed results by using $I_{\text{ET-PCA}}$.

Table 5.8 Pixel lengths of the cracks in Specimen N_3

	Surface length number	Value (pixels)									
$I_{\text{T-200}}$	PL_1 - PL_{10}	10	27	84	23	102	null	71	78	47	259
	PL_{11} - PL_{20}	121	null	62	92	50	95	121	54	33	22
$I_{\text{diff1-30}}$	PL_1 - PL_{10}	16	45	null	42	104	15	98	74	61	267
	PL_{11} - PL_{20}	129	27	88	100	61	131	147	57	61	28
$I_{\text{T-PCA}}$	PL_1 - PL_{10}	10	12	82	24	104	null	85	76	23	207
	PL_{11} - PL_{20}	112	25	64	83	50	79	98	53	27	null
$I_{\text{diff1-PCA}}$	PL_1 - PL_{10}	11	41	82	33	112	null	70	86	44	261
	PL_{11} - PL_{20}	128	22	61	91	55	132	125	56	42	22
$I_{\text{ET-PCA}}$	PL_1 - PL_{10}	17	45	66	97	75	39	149	58	55	257
	PL_{11} - PL_{20}	121	29	96	152	66	134	152	59	97	49

Table 5.9 Fitting parameters of different relationships

	$I_{T\text{-}200}$	$I_{diff1\text{-}30}$	$I_{T\text{-}PCA}$	$I_{diff1\text{-}PCA}$	$I_{ET\text{-}PCA}$
R^2	77.9 %	85.8 %	67.5 %	83.8 %	84.5 %
Slope	3.61	3.88	2.78	3.81	3.75
2-norm of NR	2.32	2.24	2.45	2.36	2.58

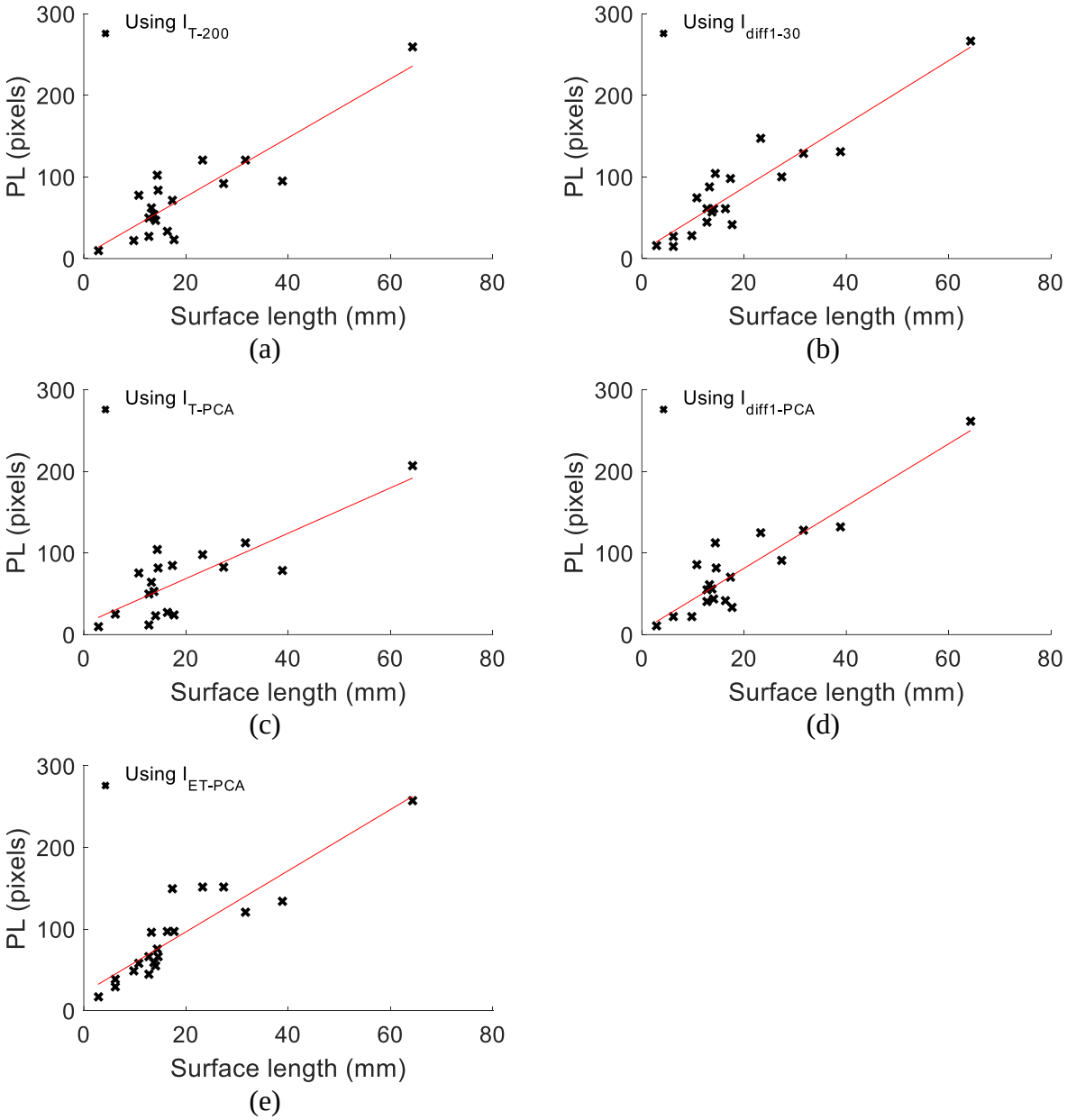

Figure 5.15 *PL* vs. *SL* of Specimen N_3 in crack response extraction step.
(a) *PL* vs. *SL* by using $I_{T\text{-}200}$. (b) *PL* vs. *SL* by using $I_{diff1\text{-}30}$. (c) *PL* vs. *SL* by using $I_{T\text{-}PCA}$. (d) *PL* vs. *SL* by using $I_{diff1\text{-}PCA}$. (e) *PL* vs. *SL* by using $I_{ET\text{-}PCA}$.

Since the camera view and the objective distance are fixed during the tests of Specimens N_2 and N_3, *PL* values from the reconstructed results of these two should be on the same scale. Thus, by combining these values together, the relationships between *PL* and *SL* of both specimens are shown in figure 5.16. Table 5.10 gives the fitting parameters of these relationships. In summary, the surface length can be characterised by using the crack reconstructor introduced in figure 5.5(b). In the crack response extraction step, different methods can be used to generate two-dimensional images as the inputs of the crack shape reconstruction step. Better reconstructed results are achieved by using $I_{\text{diff1-30}}$, $I_{\text{diff1-PCA}}$, and $I_{\text{ET-PCA}}$, which further contribute to the surface length characterisation.

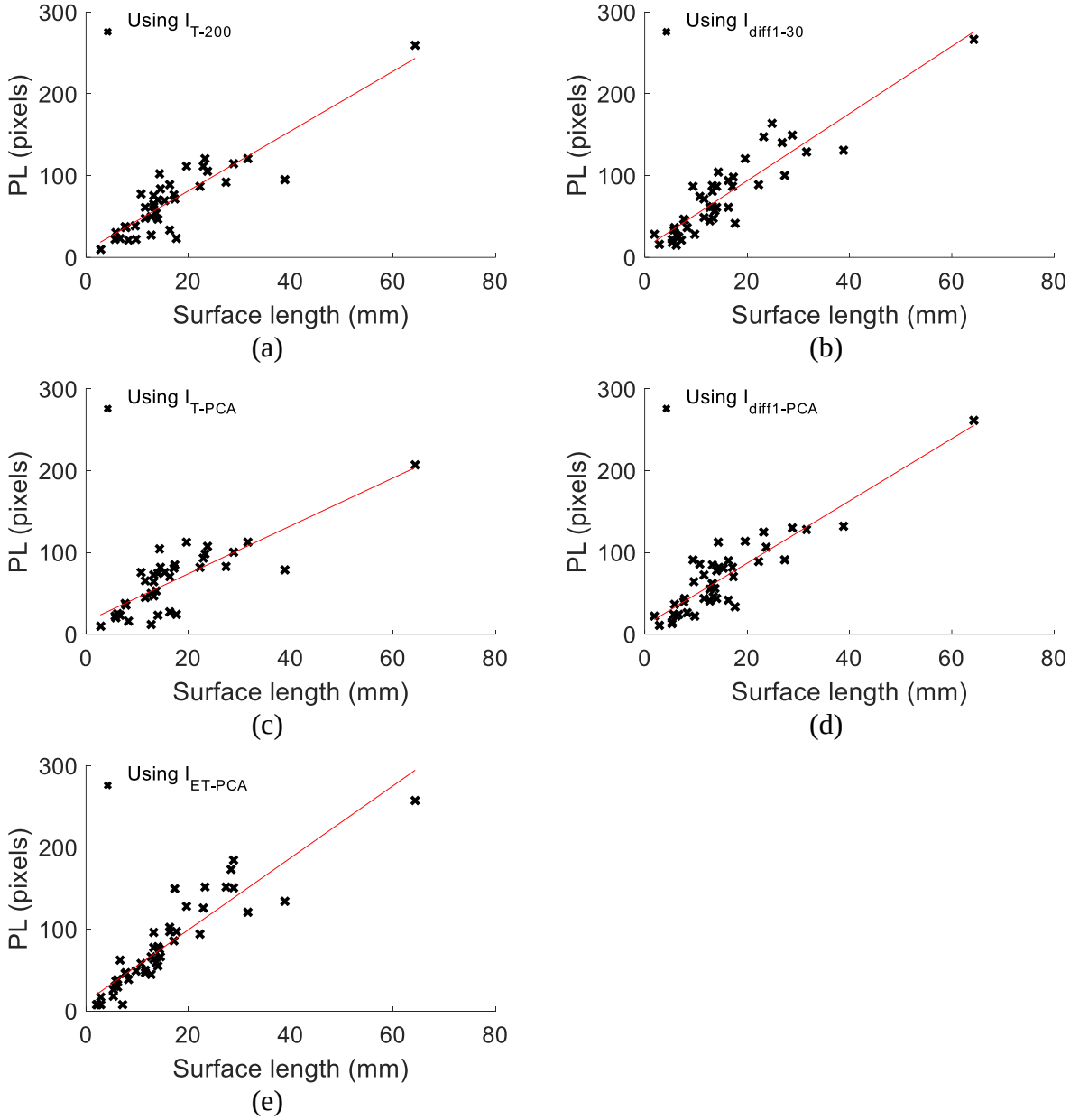

Figure 5.16 *PL* vs. *SL* of Specimens N_2 and N_3 in the crack response extraction step. (a) *PL* vs. *SL* by using $I_{\text{T-200}}$. (b) *PL* vs. *SL* by using $I_{\text{diff1-30}}$. (c) *PL* vs. *SL* by using $I_{\text{T-PCA}}$. (d) *PL* vs. *SL* by using $I_{\text{diff1-PCA}}$. (e) *PL* vs. *SL* by using $I_{\text{ET-PCA}}$.

Table 5.10 Fitting parameters of different relationships

	$I_{T\text{-}200}$	$I_{diff1\text{-}30}$	$I_{T\text{-}PCA}$	$I_{diff1\text{-}PCA}$	$I_{ET\text{-}PCA}$
R^2	79.1 %	83.1 %	68.4 %	81.4 %	84.2 %
Slope	3.66	4.11	2.93	3.81	4.40
2-norm of NR	2.75	2.97	2.76	2.80	2.67

5.4 POD Analysis for RCF Crack Characterisation

The above section has investigated and compared various features/patterns for RCF crack characterisation. To evaluate the probabilistic performance of these features, this section carries out the POD analysis. Specifically, based on the signal response data, Sections 5.4.1 and 5.4.2 provide the POD analysis for the features of characterising pocket lengths and vertical depths, respectively. Section 5.4.3 presents the POD analysis for the features of characterising surface lengths. The signal response data is first used for POD analysis. In addition, the reconstruction results of the surface lengths can be also considered as two possible outcomes, i.e., a surface length is reconstructed or a surface length is missed. Thus, the hit/miss data is also used for POD analysis.

5.4.1 *POD for evaluating performance of pocket length characterisation*

For T_{max}, A_{diff1}, $A_{T\text{-}PCA}$, and $A_{diff1\text{-}PCA}$, the calculated POD curves as functions of the pocket length are shown in figure 5.17. Additionally, table 5.11 shows L_{90} of these features under eight heating pulses. These POD curves are based on equation 3.57. Similar to Section 4.5.1, the decision threshold is set as the maximum feature value of six repeated tests when L_2 of Specimen N_1 is tested, i.e., it is assumed that detecting a RCF crack with its pocket length shorter than 0.74 mm is fifty-fifty chance. However, the decision threshold can be set by other assumptions. Note that only the relationships with R^2 higher than 60% are investigated here (see table 5.3). Figure 5.17(a) shows that for characterising a specific pocket length, T_{max} achieves higher POD values under the 20 ms and 50 ms heating pulses, which verifies that under shorter heating pulses, T_{max} has better performances. By using the 20 ms heating pulse, T_{max} gives the shortest L_{90}. Figure 5.17(b) shows that when a pocket length is longer than 0.7 mm, A_{diff1} gives similar POD values even under different heating pulses. Compared with T_{max}, A_{diff1} has shorter L_{90}, which is not in line with the findings in Section 4.5.1. In addition, both figures show that a zero pocket length can still be detected with the POD value higher than 10% which is unrealistic. The reason is that the fitting relationships of the two features to the pocket length are inadequate. Especially, for A_{diff1}, the R^2 values are all lower than 65%, which may result in unrealistic values for L_{90}. If pocket lengths are outside the minimum value (0.74 mm) used in experiments, its corresponding POD value is no more valid.

Compared with other features, the POD curve of $A_{\text{T-PCA}}$ has the narrowest transition area even under different heating pulses and longer heating pulses contribute to smaller L_{90} values, as shown in figure 5.17(c). By comparing figures 5.17(c) and (d), it shows that $A_{\text{diff1-PCA}}$ has shorter L_{90} compared with $A_{\text{T-PCA}}$ and longer heating pulses are preferred to get higher POD values. These results are in line with the previous results in Section 4.5.1. From the above discussions, it can be concluded that by using longer heating pulses, $A_{\text{diff1-PCA}}$ has the best performance of characterising pocket lengths, which is demonstrated by the shortest L_{90}.

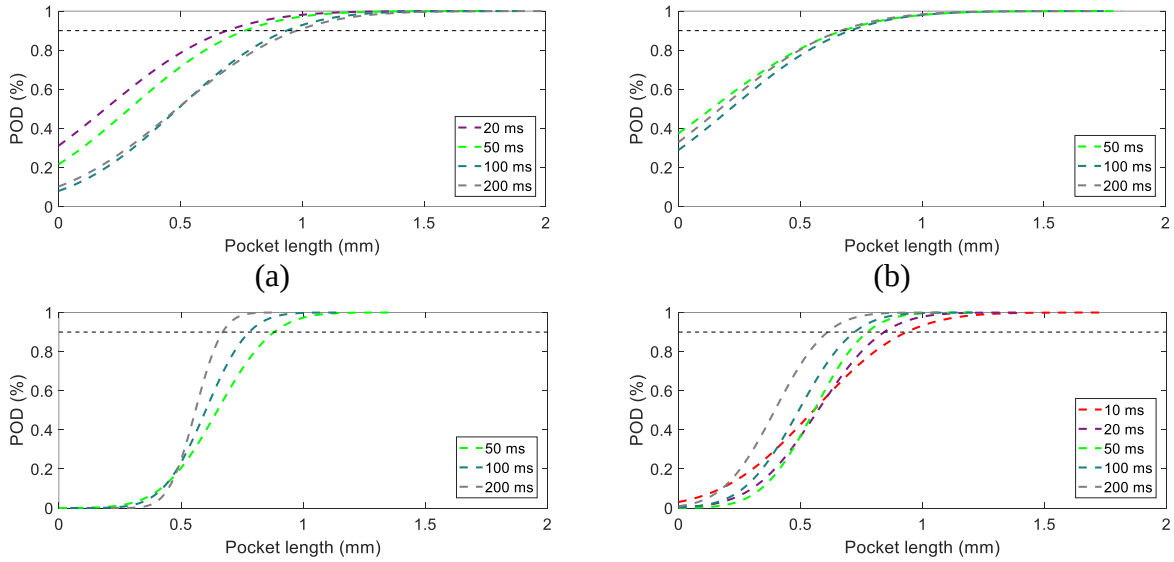

Figure 5.17 POD curve vs. pocket length under different heating pulses.
(a) Based on $T_{\max}$. (b) Based on A_{diff1}. (c) Based on $A_{\text{T-PCA}}$. (d) Based on $A_{\text{diff1-PCA}}$.

Table 5.11 Calculated results of L_{90} for different features and heating pulses

Feature	Heating pulse					Unit
	10	20	50	100	200	ms
$T_{\max}$	-	0.69	0.76	0.93	0.98	mm
A_{diff1}	-	-	0.67	0.70	0.67	mm
$A_{\text{T-PCA}}$	-	-	0.88	0.78	0.67	mm
$A_{\text{diff1-PCA}}$	0.93	0.84	0.77	0.72	0.61	mm

5.4.2 *POD for evaluating performance of vertical depth characterisation*

From the discussions in Section 5.3.4, only $A_{\text{T-PCA}}$ and $A_{\text{diff1-PCA}}$ show positive correlations with the vertical depth, which requires the use of the 200ms heating pulse. For these two features, the calculated POD curves as functions of the vertical depth are shown in figure 5.18. These POD curves are based on equation 3.57. Similarly, the decision threshold is set as the maximum feature value of six repeated tests when D_2 of Specimen N_1 is tested, i.e., it has a 50% probability of detecting a crack with its vertical depth shorter than 0.37 mm.

Additionally, D_{90} of these features are shown in figures 5.18(a) and (b). Comparing these figures, the POD curve of $A_{T\text{-}PCA}$ has a narrower transition area and a shorter D_{90}. However, as mentioned before, the relationship of $A_{T\text{-}PCA}/A_{diff1\text{-}PCA}$ vs. the vertical depth probably results from the pocket length, which dominates the responses of these two features.

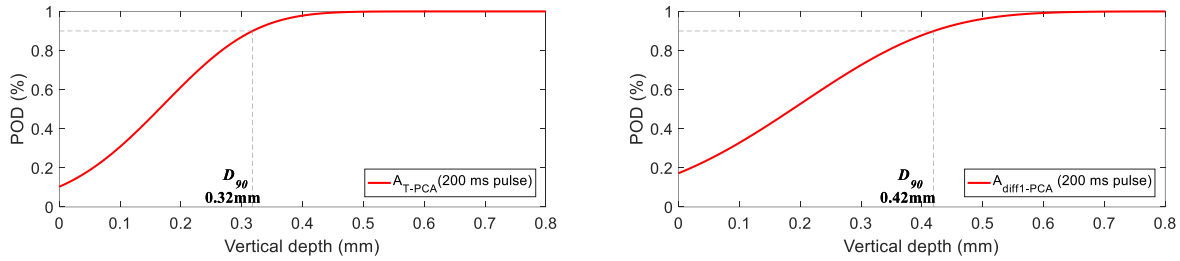

(a) (b)

Figure 5.18 POD curve vs. vertical depth.
(a) Based on $A_{T\text{-}PCA}$. (b) Based on $A_{diff1\text{-}PCA}$.

5.4.3 *POD for evaluating performance of surface length characterisation*

For evaluating the performances of characterising surface lengths by using $I_{T\text{-}200}$, $I_{diff1\text{-}30}$, $I_{diff1\text{-}PCA}$, and $I_{ET\text{-}PCA}$. Both the signal response and the hit/miss data-based POD analyses are conducted here. The 95% lower confidence bound is also estimated since the number of surface lengths in Specimens N_2 and N_3 is around 60, which can provide reasonable estimates of confidence bounds for both signal response and hit/miss data.

Figure 5.19 shows the signal response data-based POD curves by using $I_{T\text{-}200}$, $I_{diff1\text{-}30}$, $I_{diff1\text{-}PCA}$, and $I_{ET\text{-}PCA}$. Note that $I_{T\text{-}PCA}$ is not considered here since its R^2 (68.4%) is much lower than others. These curves are derived from the relationships between *PL* and *SL* discussed in Section 5.3.5. For $I_{T\text{-}200}$, the decision threshold is set as the maximum *PL* of six repeated tests when SL_1 of Specimen N_3 is tested since SL_{38} of Specimen N_2 cannot be successfully reconstructed by using $I_{T\text{-}200}$. For $I_{diff1\text{-}30}$, $I_{diff1\text{-}PCA}$, and $I_{ET\text{-}PCA}$, the decision threshold is individually set as the maximum *PL* of six repeated tests when SL_{38} of Specimen N_2 is tested. By comparing figures 5.19(a)-(d), $I_{ET\text{-}PCA}$ gives the best performance of characterising surface lengths, which is shown by the shortest SL_{90} and $SL_{90/95}$. These values are also listed in table 5.12.

Table 5.12 Calculated results of SL_{90} and $SL_{90/95}$ based on different methods

	$I_{T\text{-}200}$	$I_{diff1\text{-}30}$	$I_{diff1\text{-}PCA}$	$I_{ET\text{-}PCA}$
SL_{90} (mm)	8.36	10.80	10.05	6.99
$SL_{90/95}$ (mm)	10.78	12.54	11.93	8.79

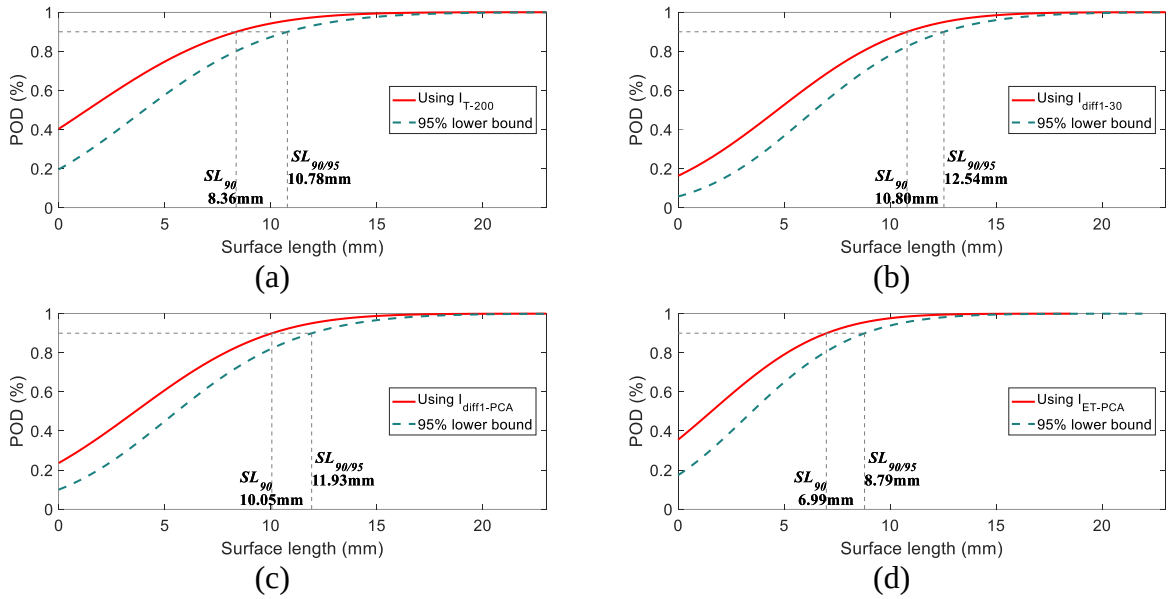

Figure 5.19 POD curve vs. surface length.
(a) Based on $I_{T\text{-}200}$. (b) Based on $I_{diff1\text{-}30}$. (c) Based on $I_{diff1\text{-}PCA}$. (d) Based on $I_{ET\text{-}PCA}$.

From the above, the signal response data is used for POD analysis. In addition, the reconstruction results of the surface lengths can be also considered as hit/miss data. Based on tables 5.6 and 5.8, the signal response data can be converted into binary data with *1* indicating a reconstructed surface length and *0* indicating a missed surface length. The converted results are shown in table 5.13. Since the surface lengths are uniformly distributed providing a symmetrical data set, the POD link functions used should also be symmetrical. Two typical links, i.e., logit link and probit link, are used to transform hit/miss data into the generalised linear domain. Based on these links and the binary data in table 5.13, hit/miss data-based POD curves can be derived, as shown in figure 5.20. Additionally, table 5.14 shows SL_{90} and $SL_{90/95}$ of the POD curves by using $I_{T\text{-}200}$, $I_{diff1\text{-}30}$, $I_{diff1\text{-}PCA}$, and $I_{ET\text{-}PCA}$. It can be seen that the POD curves based the logit link always have narrower transition area and lower SL_{90} and $SL_{90/95}$ no matter which method is used. By comparing figures 5.20(a)-(d), it can be seen that $I_{ET\text{-}PCA}$ has the shortest SL_{90} by using the logit link. However, its $SL_{90/95}$ is a little bit larger than $I_{diff1\text{-}PCA}$.

From the discussions of both the signal response and the hit/miss data, it can be concluded $I_{ET\text{-}PCA}$ has the best performance of characterising surface lengths, which is shown by the shortest SL_{90} and $SL_{90/95}$ of the signal response data and the shortest SL_{90} of the hit/miss data.

Table 5.13 Hit/miss results of surface lengths in Specimens N_2 and N_3

	Surface length number	Value (pixels)									
	PL_1 - PL_{10}	*1*	*0*	*1*	*0*	*0*	*1*	*1*	*0*	*1*	*1*
$I_{T\text{-}200}$	PL_{11} - PL_{20}	*1*	*0*	*1*	*1*	*1*	*0*	*1*	*1*	*1*	*0*
(Specimen N_2)	PL_{21} - PL_{30}	*1*	*1*	*1*	*0*	*1*	*1*	*0*	*1*	*1*	*0*
	PL_{31} - PL_{39}	*1*	*0*	*1*	*0*	*1*	*0*	*0*	*0*	*0*	
$I_{T\text{-}200}$	PL_1 - PL_{10}	*1*	*1*	*1*	*1*	*1*	*0*	*1*	*1*	*1*	*1*
(Specimen N_3)	PL_{11} - PL_{20}	*1*	*0*	*1*	*1*	*1*	*1*	*1*	*1*	*1*	*1*
	PL_1 - PL_{10}	*1*	*0*	*1*	*1*	*0*	*1*	*1*	*0*	*1*	*1*
$I_{diff1\text{-}30}$	PL_{11} - PL_{20}	*1*	*0*	*1*	*1*	*1*	*0*	*1*	*1*	*1*	*0*
(Specimen N_2)	PL_{21} - PL_{30}	*1*	*1*	*1*	*0*	*1*	*1*	*1*	*1*	*1*	*0*
	PL_{31} - PL_{39}	*1*	*0*	*1*	*0*	*1*	*1*	*0*	*1*	*1*	
$I_{diff1\text{-}30}$	PL_1 - PL_{10}	*1*	*1*	*0*	*1*	*1*	*1*	*1*	*1*	*1*	*1*
(Specimen N_3)	PL_{11} - PL_{20}	*1*	*1*	*1*	*1*	*1*	*1*	*1*	*1*	*1*	*1*
	PL_1 - PL_{10}	*1*	*0*	*1*	*0*	*0*	*1*	*1*	*0*	*1*	*1*
$I_{diff1\text{-}PCA}$	PL_{11} - PL_{20}	*1*	*0*	*1*	*1*	*1*	*0*	*1*	*1*	*1*	*0*
(Specimen N_2)	PL_{21} - PL_{30}	*1*	*1*	*1*	*0*	*1*	*1*	*1*	*1*	*1*	*0*
	PL_{31} - PL_{39}	*1*	*0*	*1*	*0*	*1*	*1*	*0*	*1*	*0*	
$I_{diff1\text{-}PCA}$	PL_1 - PL_{10}	*1*	*1*	*1*	*1*	*1*	*0*	*1*	*1*	*1*	*1*
(Specimen N_3)	PL_{11} - PL_{20}	*1*	*1*	*1*	*1*	*1*	*1*	*1*	*1*	*1*	*1*
	PL_1 - PL_{10}	*1*	*1*	*1*	*1*	*0*	*1*	*1*	*0*	*1*	*1*
$I_{ET\text{-}PCA}$	PL_{11} - PL_{20}	*1*	*0*	*1*	*1*	*1*	*0*	*1*	*1*	*1*	*0*
(Specimen N_2)	PL_{21} - PL_{30}	*1*	*1*	*1*	*0*	*1*	*1*	*1*	*1*	*1*	*1*
	PL_{31} - PL_{39}	*1*	*0*	*1*	*1*	*1*	*1*	*1*	*1*	*1*	*1*
$I_{ET\text{-}PCA}$	PL_1 - PL_{10}	*1*	*1*	*1*	*1*	*1*	*1*	*1*	*1*	*1*	*1*
(Specimen N_3)	PL_{11} - PL_{20}	*1*	*1*	*1*	*1*	*1*	*1*	*1*	*1*	*1*	*1*

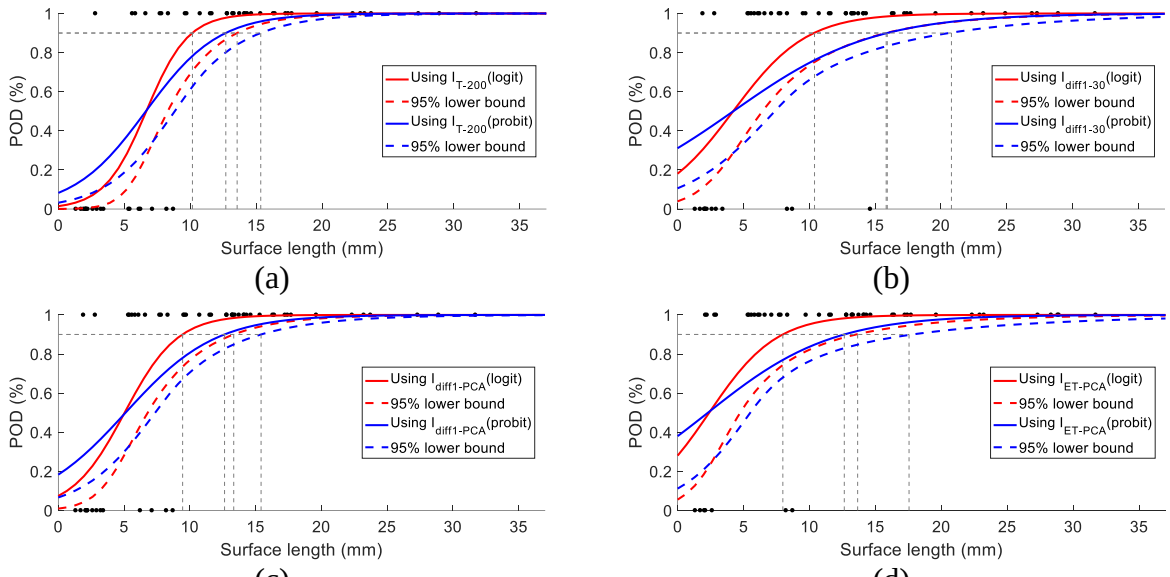

Figure 5.20 POD curve vs. surface length by hit/miss data.
Black dots represent hit/miss data with *1* indicating a reconstructed surface length and *0* indicating a missed surface length. (a) Based on $I_{T\text{-}200}$. (b) Based on $I_{diff1\text{-}30}$. (c) Based on $I_{diff1\text{-}PCA}$. (d) Based on $I_{ET\text{-}PCA}$.

Table 5.14 Calculated results of SL_{90} and $SL_{90/95}$ based on different methods

	POD link functions	$I_{T\text{-}200}$	$I_{diff1\text{-}30}$	$I_{diff1\text{-}PCA}$	$I_{ET\text{-}PCA}$
SL_{90} (mm)	logit link	10.17	10.40	9.46	7.98
	probit link	12.70	15.93	12.64	12.64
$SL_{90/95}$ (mm)	logit link	13.56	15.84	13.34	13.65
	probit link	15.35	20.80	15.42	17.55

5.5 Chapter Summary

In this chapter, three specimens containing natural cracks are used to further verify the capabilities of different features for RCF crack characterisation and their performances are evaluated by POD analysis. Results show that it is difficult for T_{max} and A_{diff1} to build a clear relationship to pocket length. $A_{T\text{-}PCA}$ and $A_{diff1\text{-}PCA}$ show well-fitted linear relationships to pocket length. Under longer heating pulses $A_{T\text{-}PCA}$ has the best performance of characterising pocket lengths, which is demonstrated by the shortest L_{90}. In the inclination angle characterisation, SUM_T, SUM_{diff1}, S_T, and K_T shows better performances. However, only SUM_T presents the monotonic relationship by using 800 ms time slot. In the vertical depth characterisation, it is unexpected that $A_{T\text{-}PCA}$, instead of SS_T, shows the best linear relationship to the vertical depth. The most possible reason is that the pocket length dominates the feature response since the average pocket length of the RCF cracks is much longer than the average value of the angular slots used in the first case study. Limited by this, it is difficult to use the current specimen, i.e., Specimens N_1, to verify different features. Future work will carry out the X-ray tomography scan for both Specimens N_2 and N_3 and take the reconstructed inclination angles and pocket lengths of RCF crack as the ground truth to justify the proposed features. In the surface length characterisation, $I_{diff1\text{-}30}$, $I_{diff1\text{-}PCA}$, $I_{ET\text{-}PCA}$ shows better performances. Via POD analysis, $I_{ET\text{-}PCA}$ gives the best performance of characterising surface lengths, which is shown by the shortest SL_{90}.

Chapter 6. Conclusions, Future Work and Importance to Railway Industry

This final chapter summarises the whole work of this thesis and draws the conclusions of using ECPT technique with quantitatively describable detectability as a promising candidate for RCF cracks detection and characterisation. Future work is briefly outlined which includes feature selection for crack characterisation, three-dimensional heating source/crack reconstruction, and model-assisted POD frameworks for improving the effectiveness of POD analysis.

6.1 Conclusions

With transportation volumes continuously increasing, the railway networks are now facing the problems of greater axle loads and increasing vehicle speeds, which may pose significant risks to the safe operation of railway transportation.

From the literature review chapter, the most direct consequence of increasing transportation volumes is the initiation of RCF defects in rails, which have become a severe safety issue for all types of railway networks and received more attention due to lack of examination and management. Among different RCF defects, the RCF crack probably presents the biggest hazard in rails. Up to date, different types of NDT&E techniques, e.g., ultrasonic testing, eddy current testing, alternating current field measurement, magnetic flux leakage testing, radiography, visual inspection, have been developed to detect and characterise RCF cracks. The main goal of detecting RCF cracks is to provide detailed guidelines for safety management and preventative grinding. Unfortunately, most of the current NDT&E techniques are still facing several challenges. One of the challenges is the characterisation of RCF cracks under their clustered distributions. Another one is the evaluation of the probabilistic performance in crack characterisation. By combining the advantages of eddy current pulse excitation and infrared thermography, the use of ECPT technique for the detection and characterisation of RCF cracks in rails has been proposed in this thesis. The probabilistic performance in crack characterisation has been investigated by utilising POD analysis.

In Chapter 3, this research work starts by describing and understanding the fundamentals of ECPT technique and POD analysis in NDT&E, and proposing thermal features/pattern for defect characterisation. Particular attention has been paid to the theoretical feasibility of ECPT for detecting and characterising surface-breaking cracks in metallic materials. For the theoretical background of ECPT, a three-dimensional model for conductive materials has been introduced to describe the transient thermal distribution with an induction heating source.

In the theoretical background of POD analysis, two types, hit/miss data-based and signal response data-based, of POD analysis have been discussed. The parameter estimation and confidence bound calculation of these two data types have been introduced, respectively. Based on understanding the fundamentals of ECPT and the requirements of POD analysis, types of spatial/temporal domain-based and tempo-spatial-based thermal features/patterns have been proposed. Via the proposed features and the evaluation of their performances by POD analysis, the experimental studies of characterising angular defects and natural RCF cracks can be accordingly carried out.

Major work of this thesis is detailed in Chapter 4 and Chapter 5. Since angular defects are considered as one common representation of idealised RCF cracks, Chapter 4 conducts a case study of angular defect characterisation and the evaluation of different features via POD analysis. Main considerations for angular defect characterisation using ECPT include experimental setup configuration, dedicated specimen preparation, thermal feature extraction, and features' performance evaluation. This chapter starts by proposing a POD analysis framework to guide the performance evaluation of feature-based defect characterisation. The ECPT setup (camera frame rate and resolution, coil shape, excitation pulse duration and current, etc.) is carefully configured and three dedicated specimens with artificial angular slots are prepared. Then, the proposed features/patterns have been used to characterise three main geometric parameters, i.e., pocket length, inclination angle, and vertical depth, of the angular defect. Further, the POD analysis has been carried out to evaluate the probabilistic performance of these features. Specifically, five features, i.e. T_{max}, A_{diff1}, A_{ratio}, $A_{T\text{-}PCA}$, and $A_{diff1\text{-}PCA}$, have been used to characterise the pocket length. Eight features, i.e., SUM_T, SUM_{diff1}, S_T, S_{diff1}, K_T, K_{diff1}, SS_T and SK_T, have been used for characterising the inclination angle. Additionally, the vertical depth can be considered as a function of both the pocket length and the inclination angle. All the above features have been investigated to test their capabilities of characterising vertical depths. Results show that T_{max} has the advantage of high repeatability. A_{diff1}, A_{ratio}, $A_{T\text{-}PCA}$, and $A_{diff1\text{-}PCA}$ show well-fitted linear relationships to pocket length. Among them, $A_{diff1\text{-}PCA}$ has the best performance of characterising pocket lengths. For $A_{diff1\text{-}PCA}$, the trade-off between increasing the POD and the goodness of the $\hat{a}$ vs. a relationship needs to be taken. In the inclination angle characterisation, SUM_T presents the monotonic relationship by selecting specific time slots. SUM_{diff1} has a better monotonical relationship by using longer time slots. S_{diff1} and K_T show the monotonically increasing relationships to the inclination angle only by using 800ms time slot. Among these features, SUM_{diff1} shows the best linear relationship to the inclination angle. In the vertical depth characterisation, SUM_{diff1} has the best performance of characterising vertical depths. SS_T has

the highest R^2 value and the smallest 2-norm of NR and presents reasonable POD values for vertical depths outside the range used in experiments.

In Chapter 5, to further verify the capabilities of different features for RCF crack characterisation, another case study of RCF crack characterisation and performance evaluation via POD analysis has been carried out. Similar to the previous chapter, this chapter starts by configuring the ECPT setup and preparing three cut-off specimens contains natural RCF cracks. Different from angular defect characterisation, the major challenges for RCF crack characterisation are their complex geometries and clustered distributions. For the ECPT setup, the solution is that a 2.9× close-up lens is mounted onto the standard lens to capture the detailed transient-spatial thermal patterns. For the specimen preparation, three typical cut-off specimens have been carefully selected. Among them, a small cut-off specimen contains nine RCF cracks with intermediate spacings, which consist of a relatively simple clustered distribution. This specimen is used for investigating the characterisation of the pocket length, the inclination angle, and the vertical depth. In addition, this specimen is scanned by X-ray computed tomography, which provides the three-dimensional profiles of all the cracks as the ground truth data. The remaining two cut-off specimens are used for investigating the surface length characterisation. These two specimens are selected because the RCF cracks in them are in different stages (light stage and moderate stage) and their clustered distributions are more complex. After these preparations and the thermal data collection, the proposed features/patterns have been verified by characterising four main parameters, i.e., pocket length, inclination angle, vertical depth, and surface length, of RCF cracks. Results show that it is difficult for T_{max} and A_{diff1} to build a clear relationship to pocket length. $A_{T\text{-}PCA}$ and $A_{diff1\text{-}PCA}$ show well-fitted linear relationships to pocket length. In the inclination angle characterisation, SUM_T, SUM_{diff1}, S_T, and K_T show better performances. However, only SUM_T presents the monotonic relationship by using 800 ms time slot. In the vertical depth characterisation, it is unexpected that $A_{T\text{-}PCA}$, instead of SS_T, shows the best linear relationship to the vertical depth. The most possible reason is that the pocket length dominates the feature response since the average pocket length of RCF cracks is much longer than the average value of angular slot used in the first case study. In the surface length characterisation, $I_{diff1\text{-}30}$, $I_{diff1\text{-}PCA}$, $I_{ET\text{-}PCA}$ shows better performance. Via POD analysis, $I_{ET\text{-}PCA}$ gives the best performance of characterising surface lengths.

6.2 Main Contributions

The main contributions of this thesis are detailed into five salient parts as follows:

(1) A thorough review of NDT&E techniques for detecting RCF defects in rails has been carried out. Based on the existing problems of current NDT&E techniques, the use of multi-physics-based ECPT method for RCF crack characterisation has been proposed. The challenges of ECPT for RCF crack characterisation are presented and two of them are particularly addressed throughout this thesis, i.e., the influences of clustered distributions on crack characterisation and probabilistic performance in crack characterisation.

(2) Implementations of three-dimensional FEM models and a lab-based ECPT system have been fulfilled for numerically and experimentally investigating the characterisation of RCF cracks under the clustered distributions and geometric influences:

- The FEM models are built in the COMSOL Multiphysics environment by considering the transient-time-harmonic induction heating process, which couples the electromagnetic field and the heat transfer together. The advantage of these models is that the electromagnetic field distribution is computed in the frequency domain, which makes the model-solving more time-efficient. Additionally, via these FEM models, a better understanding of the electromagnetic and the thermal distributions inside the modelled specimen can be achieved;
- The lab-based ECPT system together with dedicated specimens is used to experimentally verify the FEM models and investigate the probabilistic performance in crack characterisation since it is difficult for the FEM models to consider material factor, geometry factor, equipment factor and human factor without any prior knowledge.

These contributions are parts of the work published in *Infrared Physics & Technology* (vol. 100, pp. 73-81, 2019) and *IEEE Transactions on Industrial Informatics* (vol. 14, pp. 5658-5666, 2018).

(3) Three dedicated man-made specimens with angular slots and three cut-off specimens containing natural RCF cracks have been prepared for the case studies to investigate the capability of ECPT system for characterising idealised defects and RCF cracks:

- Three man-made specimens are made of AISI 1045 medium carbon steel. Each steel block contains a group of artificial angular cracks with different pocket lengths and inclination angles to simulate simplified RCF cracks. These man-made specimens are tested by the proposed ECPT system to verify the FEM models, and investigate the proposed features for angular defect characterisation and the evaluation of the features' performances via POD Analysis.

- Another three specimens cut off from PD3 (60 kg/m) rails removed from service are carefully selected for studying natural RCF crack characterisation. A challenge is that only the surface profiles of these RCF cracks are known and it is difficult to obtain their inner profiles. To provide the three-dimensional profiles of the cracks, one specimen with simple clustered distributions of cracks is fully scanned by X-ray computed tomography. This specimen is used for investigating the characterisation of the pocket length, the inclination angle, as well as the vertical depth. The remaining two cut-off specimens are selected because the RCF cracks in them are in the light stage and the moderate stage, respectively. And their clustered distributions are more complex. These two specimens are used for investigating the surface length characterisation.

These contributions are parts of the work published in *IEEE Transactions on Industrial Informatics* (vol. 14, pp. 5658-5666, 2018), *IEEE Transactions on Instrumentation and Measurement* (vol. 68, pp. 1373-1381, 2019), and *Infrared Physics & Technology* (vol. 100, pp. 73-81, 2019).

(4) Types of temporal/spatial thermal features for angular slots and RCF cracks localization and characterisation have been proposed and compared:

For the pocket length characterisation, $A_{\text{T-PCA}}$ and $A_{\text{diff1-PCA}}$ show well-fitted linear relationships to pocket length. For the inclination angle characterisation, SUM_{T} shows the best performances. For the vertical depth characterisation, $A_{\text{T-PCA}}$ shows the best linear relationship to the vertical depth. The most possible reason is that the pocket length dominates the feature response since the average pocket length of the RCF cracks is much longer than the average value of the angular slot. For the surface length characterisation, $I_{\text{ET-PCA}}$ gives the best performance of characterising surface lengths.

These contributions are parts of the work published in *IEEE Transactions on Industrial Informatics* (vol. 14, pp. 5658-5666, 2018), *IEEE Transactions on Instrumentation and Measurement* (vol. 68, pp. 1373-1381, 2019), and *Infrared Physics & Technology* (vol. 100, pp. 73-81, 2019) and a detailed features comparison is discussed in another paper to be published in *IEEE Transactions on Industrial Informatics*.

(5) A POD analysis framework has been proposed to guide the evaluation of the performance of feature-based characterisation.

This contribution is part of the work published in *IEEE Transactions on Industrial Informatics* (vol. 14, pp. 5658-5666, 2018).

6.3 Future Work

Although the thesis shows promising outcomes of using ECPT for RCF crack characterisation, there are still several issues need to be further addressed in future work. They are discussed as follows:

(1) Feature selection for crack characterisation is required for future investigations.

Although many features, as well as their capabilities of characterising different parameters of RCF cracks, have been investigated, the contributions of each parameter to these features are not fully understood. By using different machine learning algorithms, such as sparse regression, least absolute shrinkage and selection operator (LASSO), decision tree, autoencoder, manifold learning, feature selection can provide a better understanding of the underlying connects between the features and the crack parameters, and identify and remove irrelevant features.

(2) Three-dimensional RCF crack reconstruction based on direct and inverse problems is also essential for future research.

This thesis uses the feature-based method for crack characterisation. One limitation is that the performance of characterisation depends on the correlation of the proposed features to the crack parameters. A higher correlation ensures a better characterisation performance. However, any features with low correlations cannot be used for crack characterisation. Thus, loads of investigations need to conduct until a proper feature is obtained, which is time-consuming and somehow depends on experiences. A better way is proposing proper three-dimensional models to describe the thermal distribution under the influences of RCF cracks. By using idealised representations of RCF cracks [22, 247-249], it is possible to model the heat source distribution and the thermal distribution under induction heating. By inverting the thermal distribution, the shape and size of the heat source can be reconstructed. By investigating the relationships between the shapes and sizes of the cracks and the heat sources, RCF crack reconstruction can be further achieved.

(3) Model-assisted POD (MAPOD) frameworks for evaluating the performance of crack characterisation should be implemented in the future.

The idea of MAPOD is reducing the physical specimens by using the simulation results to evaluate performances of the inspection [260-264]. The core of a MAPOD framework is proposing a physical-based model, which can properly simulate the behaviour of the defect. A recent study has applied MAPOD to evaluating the performance of induction thermography

[265]. However, this study only uses a thin open crack to simulate crack in reactor vessel shells, which is too idealised to be used in the real situation. For RCF cracks with their complex and cluttered distributions, proper physical-based models are of urgent needs. They are left for future investigations since loads of simulation studies are needed to validate their performances, which is beyond the scope of the thesis.

(4) To increase cracks detectability and achieve high-speed inspection, potential future improvements of the ECPT setup, and developments of automated and integrated crack characterisation programs are required:

- The rectangular coil used in this thesis can provide a relatively uniform, simple, and rectangular heating region by using its bottom side. Its limitation is also obvious that the heating region is limited to the diameter and direction of the coil. Because of this limitation, the crack at the left of C_4 in Specimen N_1 is missed after applying the crack shape reconstructor. Thus, an optimised coil design by using a larger diameter or multiple turns can address this problem. Additionally, different coil types and ferrite-yoke based coil can also be used to cover a larger heating region [214].
- As used in the thesis, the single pulse excitation with a specific duration is a fast and effective way to characterise RCF cracks. However, the vertical depth, i.e., subsurface structures and discontinuities, is not very well characterised. In this case, a depth-resolved excitation is needed to visualise three-dimensional subsurface features [184]. Additionally, for ferromagnetic materials, such as rail steels, the DC-biased magnetisation can be used to extend the ECPT's detectable depth range, which relies on the nonlinear μ-H relation and the permeability distortion in the skin-depth layer [266].
- It is deemed that rail test trains will, within the foreseeable future, include the onboard ECPT for high-speed inspection. Future consideration ought to be given to video deblurring, fast video processing and crack characterisation, quantitative assessment, automated performance evaluation, and big data management.

6.4 Importance to Railway Transportation

For railway transportation, the first priority is ensuring safe and reliable railway networks. Currently, this priority is ensured by on-line monitoring and off-line inspections. As the key component of the railway network, rails are facing very high contact stresses from the wheel-rail contact, which inevitably leads to rail degradation and induces rail flaws. The investigations carried out in this thesis have shown the potential of ECPT as a promising NDT&E technique for RCF crack characterisation. One of its future developments is on

high-speed and machine-mounted systems with the combination of other NDT&E techniques, e.g., ultrasonic testing, to provide the ability of scanning both surface and subsurface defects. Research gaps before commercialisation needs to include integration and optimisation of techniques, fast video processing, automated performance evaluation, and big data management. Another foreseeable trend is developing portable and intelligent ECPT walking sticks/trolleys to provide an efficient way of verifying the results obtained by machine-mounted systems. This is because machine-mounted systems usually generate lots of false alarms at high speeds and this problem can be addressed by carrying out on-site checks using walking sticks/ trolleys. Addressing this main research gap requires the design of user-friendly operating systems with fully automated evaluation procedures, which can minimise manual intervention. It seems to be a matter of time before these two types of systems become commercially available. Such systems will provide more powerful and efficient ways to monitor and assess the integrity of railway networks, and detailed guidelines for preventative grinding. The aim of proposing these systems is to elevate the automation level of railway networks maintenance, improve the maintenance procedure, and reduce the maintenance time and cost, which contributes to a safe and reliable running environment.

References

[1] A.P. Juna, “On the characterisation and detection of rolling contact fatigue (RCF) type cracks in railway vehicle wheels using an alternating current field measurement (ACFM) technique,” Ph.D. dissertation, School of Metallurgy and Materials, University of Birmingham, 2017.

[2] Independent Investigation Board, “Train derailment at Hatfield: A final report by the independent investigation board,” Report. Office of Rail Regulation, 2006.

[3] S.L. Grassie, “Rolling contact fatigue on the British railway system: treatment,” *Wear*, vol. 258, pp. 1310-1318, 2005.

[4] W. Schoech, “Rail maintenance-At the core of vehicle rail interaction,” In *Conference on Railway Engineering*, 2008, pp. 181-188.

[5] R. Lewis and R.S. Dwyer-Joyce, “Wear mechanisms and transitions in railway wheel steels,” *Proceedings of the Institution of Mechanical Engineers, Part J: Journal of Engineering Tribology*, vol. 218, pp. 467-478, 2004.

[6] G. Donzella, M. Faccoli, A. Ghidini, A. Mazzu, and R. Roberti, “The competitive role of wear and RCF in a rail steel,” *Engineering fracture mechanics*, vol. 72, pp. 287-308, 2005.

[7] R. Stock and R. Pippan, “RCF and wear in theory and practice-the influence of rail grade on wear and RCF,” *Wear*, vol. 271, pp. 125-133, 2011.

[8] U. Olofsson and T. Telliskivi, “Wear, plastic deformation and friction of two rail steels—a full-scale test and a laboratory study,” *Wear*, vol. 254, pp. 80-93, 2003.

[9] R. Lewis, R.S. Dwyer-Joyce, S.R. Lewis, C. Hardwick, and E.A. Gallardo-Hernandez, “Tribology of the wheel-rail contact: The effect of third body materials,” *International Journal of Railway Technology*, vol. 1, pp. 167-194, 2012.

[10] R. Lewis and U. Olofsson, eds., *Wheel-rail interface handbook*. Elsevier, 2009.

[11] J. Tunna, J. Sinclair, and J. Perez, “A review of wheel wear and rolling contact fatigue,” *Proceedings of the Institution of Mechanical Engineers, Part F: Journal of Rail and Rapid Transit*, vol. 221, pp. 271-289, 2007.

[12] M. Sato, P.M. Anderson, and D.A. Rigney, “Rolling-sliding behavior of rail steels,” *Wear*, vol. 162, pp. 159-172, 1993.

[13] K. Kato, “Classification of wear mechanisms/models,” *Proceedings of the Institution of Mechanical Engineers, Part J: Journal of Engineering Tribology*, vol. 216, pp. 349-355, 2002.

[14] F.J. Franklin, T. Chung, and A. Kapoor, “Ratcheting and fatigue-led wear in rail-wheel contact,” *Fatigue & Fracture of Engineering Materials & Structures*, vol. 26, pp. 949-955, 2003.

[15] A. Kapoor, D.I. Fletcher, and F.J. Franklin, “The role of wear in enhancing rail life,” *Tribology Series*, vol. 41, pp. 331-340, 2003.

[16] A. Kapoor, F. Schmid, and D. Fletcher, “Managing the critical wheel/rail interface,” *Railway Gazette International*, vol. 158, pp. 25-28, 2002.

[17] E.E. Magel, “Rolling contact fatigue: a comprehensive review,” Office of Railroad Policy and Development, Federal Railroad Administration, The United States, 2011.

[18] P.A. Cuervo, J.F. Santa, and A. Toro, “Correlations between wear mechanisms and rail grinding operations in a commercial railroad,” *Tribology International*, vol. 82, pp. 265-273, 2015.

[19] F.J. Franklin, J.E. Garnham, D.I. Fletcher, C.L. Davis, and A. Kapoor, “Modelling rail steel microstructure and its effect on crack initiation,” *Wear*, vol. 265, pp. 1332-1341, 2008.

[20] U. Zerbst and S. Beretta, “Failure and damage tolerance aspects of railway components,” *Engineering Failure Analysis*, vol. 18, pp. 534-542, 2011.

[21] H.D. Grohmann, K. Hempelmann, and A. Groß-Thebing, “A new type of RCF, experimental investigations and theoretical modelling,” *Wear*, vol. 253, pp. 67-74, 2002.

[22] J. Zhu, G.Y. Tian, Q. Min, and J. Wu, “Comparison Study of Different Features for Pocket Length Quantification of Angular Defects Using Eddy Current Pulsed Thermography,” *IEEE Transactions on Instrumentation and Measurement*, vol. 68, pp. 1373-1381, 2019.

[23] D.F. Cannon and H. Pradier, “Rail rolling contact fatigue research by the European Rail Research Institute,” *Wear*, vol. 191, pp. 1-13, 1996.

[24] S.L. Grassie, “Squats and squat-type defects in rails: the understanding to date,” *Proceedings of the Institution of Mechanical Engineers, Part F: Journal of Rail and Rapid Transit*, vol. 226, pp. 235-242, 2012.

[25] M. Steenbergen and R. Dollevoet, “On the mechanism of squat formation on train rails-Part I: Origination,” *International Journal of fatigue*, vol. 47, pp. 361-372, 2013.

[26] A. Pyzalla, L. Wang, E. Wild, and T. Wroblewski, “Changes in microstructure, texture and residual stresses on the surface of a rail resulting from friction and wear,” *Wear*, vol. 251, pp. 901-907, 2001.

[27] E.E. Magel, P. Sroba, K. Sawley, and J. Kalousek, “Control of rolling contact fatigue of rails,” Center for Surface Transportation Technology, National Research Council, Canada, 2005.

[28] A. Ekberg, B. Åkesson, and E. Kabo, “Wheel/rail rolling contact fatigue-probe, predict, prevent,” *Wear*, vol. 314, pp. 2-12, 2014.

[29] W. Schoech, R. Heyder, and H.D. Grohmann, “Contact geometry and surface fatigue guidelines for appropriate rail maintenance,” In *Proceedings of the 7th International Conference on Contact Mechanics and Wear of Rail/Wheel Systems,* 2006. pp. 23-29.

[30] A. Bevan, P. Molyneux-Berry, B. Eickhoff, and M. Burstow, “Development and validation of a wheel wear and rolling contact fatigue damage model,” *Wear*, vol. 307, pp. 100-111, 2013.

[31] J.W. Ringsberg and A. Bergkvist, “On propagation of short rolling contact fatigue cracks,” *Fatigue & Fracture of Engineering Materials & Structures*, vol. 26, pp. 969-983, 2003.

[32] J.E. Garnham and C.L. Davis, 2008. “The role of deformed rail microstructure on rolling contact fatigue initiation,” *Wear*, vol. 265, pp. 1363-1372, 2008.

[33] I. Persson and S.D. Iwnick, “Optimisation of railway wheel profiles using a genetic algorithm,” *Vehicle System Dynamics*, vol. 41, pp. 517-526, 2004.

[34] I. Zobory, “Prediction of wheel/rail profile wear,” *Vehicle System Dynamics*, vol. 28, pp. 221-259, 1997.

[35] M. Ignesti, M. Malvezzi, L. Marini, E. Meli, and A. Rindi, “Development of a wear model for the prediction of wheel and rail profile evolution in railway systems,” *Wear*, vol. 284, pp. 1-17, 2012.

[36] H. Harrison, T. McCanney, and J. Cotter, “Recent developments in coefficient of friction measurements at the rail/wheel interface,” *Wear*, vol. 253, pp. 114-123, 2002.

[37] M. Tomeoka, N. Kabe, M. Tanimoto, E. Miyauchi, and M. Nakata, “Friction control between wheel and rail by means of on-board lubrication,” *Wear*, vol. 253, pp. 124-129, 2002.

[38] M. Steenbergen, “Rolling contact fatigue in relation to rail grinding,” *Wear*, vol. 356, pp. 110-121, 2016.

[39] E.E. Magel and J. Kalousek, “The application of contact mechanics to rail profile design and rail grinding,” *Wear*, vol. 253, pp. 308-316, 2002.

[40] M.P. Papaelias, C. Roberts, and C.L. Davis, “A review on non-destructive evaluation of rails: State-of-the-art and future development,” *Proceeding of the Institution of Mechanical Engineer Part F: Journal of Rail and Rapid Transit*, vol. 222, pp. 367-384, 2008.

[41] R. Clark, “Rail flaw detection: Overview and needs for future developments,” *NDT&E International*, vol. 37, pp. 111-118, 2004.

[42] D.F. Cannon, K.O. Edel, S.L. Grassie, and K. Sawley, “Rail defects: an overview,” *Fatigue & Fracture of Engineering Materials & Structures*, vol. 26, pp. 865-886, 2003.

[43] R. Pohl, A. Erhard, H.J. Montag, H.M. Thomas, and H. Wüstenberg, “NDT techniques for railroad wheel and gauge corner inspection,” *NDT&E International*, vol. 37, pp. 89-94, 2004.

[44] L. Roger, “Ultra-sonic apparatus for the detection of defects in railway rails,” United States Patent 2951365, 1960.

[45] V. Jemec and J. Grum, “Automated non-destructive testing and measurement systems for rails,” In *10th European Conference on Non-Destructive Testing*, 2010. [Online]. Available: http://www.idspektr.ru/10_ECNDT/reports/1_10_42.pdf.

[46] J. Krautkramerand and H. Kraukramer, *Ultrasonic testing of materials*, Berlin: Springer, 2002, pp. 368.

[47] H.M. Thomas, T. Heckel, and G. Hanspach, “Advantage of a combined ultrasonic and eddy current examination for railway inspection trains,” *Insight-non-Destructive Testing and Condition Monitoring*, vol. 46, pp. 341-344, 2007.

[48] R. Aharoni and E. Glikman, “A novel high-speed rail inspection system,” In *Proceedings of the 8th ECNDT*, vol. 7, 2002. [Online]. Available:

https://www.ndt.net/article/ecndt02/156/156.htm.

[49] J.N. Barshinger, S.K. Dewangan, S. Ramaswamy, and J. Li, "Method and apparatus for phased array based ultrasonic evaluation of rail," United States Patent 7305885, 2007.

[50] D. Utrata, "Exploring enhanced rail flaw detection using ultrasonic phased array inspection," In *AIP Conference Proceeding*, 2002, pp. 1813-1818.

[51] D. Utrata and R. Clark, "Groundwork for rail flaw detection using ultrasonic phased array inspection," In *AIP Conference Proceeding*, 2003, pp. 799-805.

[52] G. Garcia and J. Zhang, "Application of ultrasonic phased arrays for rail flaw inspection," TTCI Report for the US Department of Transportation, United States, 2006.

[53] P. Coperet, "Fast automated angle scan technique," In *17th World Conference on Nondestructive Testing*, 2008. [Online]. Available:

https://www.ndt.net/article/wcndt2008/papers/93.pdf.

[54] J. L. Rose, M. J. Afioli, and W.J. Song, "Application and potential of guided wave rail inspection," *Insight: Non-Destructive Testing and Condition Monitoring*, vol. 44, pp. 353-358, 2002.

[55] T. Hayashi, W.J. Song, and J. L. Rose, "Guided wave dispersion curves for a bar with an arbitrary cross-section, a rod and rail example," *Ultrasonics*, vol. 41, pp. 175-183, 2003.

[56] P. Cawley, P. Wilcox, D.N. Alleyne, B. Pavlakovic, M. Evans, K. Vine, and M.J. Lowe, "Long range inspection of rail using guided waves-field experience," In *Proceedings of the 16th World Conference on Non-Destructive Testing*, 2004. [Online]. Available:

http://citeseerx.ist.psu.edu/viewdoc/download?doi=10.1.1.159.6462&rep=rep1&type=pdf

[57] P. Wilcox, B. Pavlakovic, M. Evans, K. Vine, P. Cawley, M.J. Lowe, and D. Alleyne, "Long range inspection of rail using guided waves," In *AIP Conference Proceedings*, 2003, pp. 236-243.

[58] I. Bartoli, F.L. di Scalea, M. Fateh, and E.Viola, "Modelling guided wave propagation with application to the long-range defect detection in railroad tracks," *NDT&E International*, vol. 38, pp. 325-334, 2005.

[59] F.L. di Scalea, P. Rizzo, S. Coccia, I. Bartoli, M. Fateh, E. Viola, and G. Pascale, "Non-contact ultrasonic inspection of rails and signal processing for automatic defect

detection and classification," *Insight-No-Destructive Testing and Condition Monitoring*, vol. 47, pp. 1-8, 2005.

[60] WavesInSolids PRISM system. Available: www.wavesinsolids.com.

[61] J.L. Rose, C.M. Lee, T.R. Hay, Y. Cho, and I.K. Park, "Rail inspection with guided waves," In *Proceedings of the 12th Asia-Pacific Conference on NDT*, 2006. [Online]. Available:

http://citeseerx.ist.psu.edu/viewdoc/download?doi=10.1.1.216.5038&rep=rep1&type=pdf

[62] S. Kenderian, B. Djordjevic, and R.E. Green, "Laser based and air coupled ultrasound as non-contact and remote techniques for testing of railroad tracks," *Materials Evaluation*, vol. 60, pp. 65-70, 2002.

[63] S. Kenderian, D. Cerniglia, B.B. Djordjevic, G. Garcia, J. Sun, and M. Snell, "Rail track field testing using laser/air hybrid ultrasonic technique," *Materials Evaluation*, vol. 61, pp. 1129-1133, 2003.

[64] S. Kenderian, B.B. Djordjevic, D. Cerniglia, and G. Garcia, "Dynamic railroad inspection using the laser-air hybrid ultrasonic technique," *Insight-Non-Destructive Testing and Condition Monitoring*, vol. 48, pp. 336-341, 2006.

[65] D. Cerniglia, G. Garcia, S. Kalay, and F. Prior, "Application of laser induced ultrasound for rail inspection," In *7th World Congress on Railway Research*, 2006, pp. 4-8.

[66] M. Hirao and H. Ogi, *EMATs for science and industry: noncontacting ultrasonic measurements*. New York: Springer Science & Business Media, 2003, pp. 4.

[67] A. Chahbaz, "Development of a mobile inspection system for rail integrity assessment," Tektrend International Report for the Transportation Development Centre, Canada, 2000.

[68] A. Chahbaz, M. Brassard, and A. Pelletier, "Mobile inspection system for rail integrity assessment," In *Proceedings of the 15th World Conference of Non-Destructive Testing*, 2000. [Online]. Available:

https://www.ndt.net/article/wcndt00/papers/idn533/idn533.htm.

[69] V.P. Sebko, G.M. Suchkov, and A.V. Malakhov, "Using the electromagnetic-acoustic method," Russian Journal of Nondestructive Testing, vol. 40, pp. 442-448, 2004.

[70] S. Dixon, R.S. Edwards, and X. Jian, "Inspection of the railtrack head surfaces using electromagnetic acoustic transducers," *Insight-Non-Destructive Testing and Condition Monitoring*, vol. 46, pp. 326-330, 2004.

[71] R.S. Edwards, X. Jian, and S. Dixon, "Rail defect detection using ultrasonic surface waves," *AIP Conference Proceedings*, 2006, pp. 1601-1608.

[72] R.S. Edwards, S. Dixon, and X. Jian, "Characterisation of defect in the railhead using ultrasonic surface waves," *NDT&E International*, vol. 39, pp. 468-475, 2006.

[73] R.S. Edwards, S. Dixon, and X. Jian, "Depth gauging of defects using low frequency wideband Rayleigh waves," *Ultrasonics*, vol. 44, pp. 93-98, 2006.

[74] P.A. Petcher, M.D.G. Potter, and S. Dixon "A new electromagnetic acoustic transducer (EMAT) design for operation on rail," *NDT & E International*, vol. 65, pp. 1-7, 2014.

[75] Y. Fan, S. Dixon, R.S. Edwards, and X. Jian, "Ultrasonic surface wave propagation and interaction with surface defects on rail track head," *NDT&E International*, vol. 40, pp. 471-477, 2007.

[76] R.S. Edwards, C. Holmes, Y. Fan, M.P. Papaelias, S. Dixon, C.L. Davis, B.W. Drinkwater, and C. Roberts, "Ultrasonic detection of surface-breaking railhead defects," In *Proceedings of the BINDT Conference*, vol. 50, 2008, pp. 369-373.

[77] R.S. Edwards, A. Sophian, S. Dixon, G.Y. Tian, and X. Jian, "Dual EMAT and PEC non-contact probe: applications to defect testing," *NDT&E International*, vol. 39, pp. 45-52, 2006.

[78] Y. He, G.Y. Tian, H. Zhang, M. Alamin, A. Simm, and P. Jackson, "Steel Corrosion Characterisation Using Pulsed Eddy Current Systems," *IEEE Sensors Journal*, vol. 12, pp. 2113-2120, 2012.

[79] A. Sophian, G. Tian, and M. Fan, "Pulsed eddy current non-destructive testing and evaluation: A review," *Chinese Journal of Mechanical Engineering*, vol. 30, pp. 500-514, 2017.

[80] B.A. Auld and J.C. Moulder, "Review of advances in quantitative eddy current nondestructive evaluation," *Journal of Nondestructive Evaluatio*n, vol. 18, pp. 3-36, 1999.

[81] J. García-Martín, J. Gómez-Gil, and E. Vázquez-Sánchez, "Non-destructive techniques based on eddy current testing," *Sensors*, vol. 11, pp. 2525-2565, 2011.

[82] R. Ghoni, M. Dollah, A. Sulaiman, and F.M. Ibrahim, “Defect characterisation based on eddy current technique: Technical review,” *Advances in Mechanical Engineering*, vol. 6, pp. 182496, 2014.

[83] A. Sophian, G.Y. Tian, D. Taylor, and J. Rudlin, “Design of a pulsed eddy current sensor for detection of defects in aircraft lap-joints,” *Sensors and Actuators A: Physical*, vol. 101, pp. 92-98, 2002.

[84] Y. He, F. Luo, M. Pan, F. Weng, X. Hu, J. Gao, and B. Liu, “Pulsed eddy current technique for defect detection in aircraft riveted structures,” *NDT&E International*, vol. 43, pp. 176-181, 2010.

[85] H. Shaikh, N. Sivaibharasi, B. Sasi, T. Anita, R. Amirthalingam, B.P.C. Rao, T. Jayakumar, H.S. Khatak, and B. Raj, “Use of eddy current testing method in detection and evaluation of sensitisation and intergranular corrosion in austenitic stainless steels,” *Corrosion Science*, vol. 48, pp. 1462-1482, 2006.

[86] N. Yusa, S. Perrin, K. Mizuno, Z. Chen, and K. Miya, “Eddy current inspection of closed fatigue and stress corrosion cracks,” *Measurement Science and Technology*, vol. 18, pp. 3403-3408, 2007.

[87] Z. Song, T. Yamada, H. Shitara, and Y. Takemura, “Detection of damage and crack in railhead by using eddy current testing,” *Journal of Electromagnetic Analysis and Applications*, vol. 3, pp. 546-550, 2011.

[88] H.M. Thomas, M. Junger, H. Hintze, R. Krull, and S. Rühe, “Pioneering inspection of railroad rails with eddy currents,” In *Proceedings of the 15th World Conference on Non-Destructive Testing*, 2000. [Online]. Available: https://www.ndt.net/article/wcndt00/papers/idn796/idn796.htm.

[89] M. Junger, H.M. Thomas, R. Krull, and S. Rühe, “The potential of eddy current technology regarding railroad inspection and its implementation,” In *16th World Conference on Nondestructive Testing*, 2004. [Online]. Available: https://www.ndt.net/abstract/wcndt2004/331.htm.

[90] T. Heckel, H.M. Thomas, and S. Ruhe, “New developments for non-destructive rail testing,” In *Proceedings of National Seminar & Exhibition on Non-Destructive Evaluation*, 2009, pp. 261-265.

[91] R. Pohl, R. Krull, and R. Meierhofer, “A new eddy current instrument in a grinding train,” In *Proceedings of ECNDT*, 2006. [Online]. Available:

http://www.ultrasonic.de/article/ecndt2006/doc/P178.pdf.

[92] J. Rajamäki, M. Vippola, A. Nurmikolu, and T. Viitala, "Limitations of eddy current inspection in railway rail evaluation," In *Proceedings of the Institution of Mechanical Engineers, Part F: Journal of Rail and Rapid Transit*, vol. 232, 2018, pp. 121-129.

[93] J.C. Munoz, F.G. Márquez, and M.P. Papaelias, "Railroad inspection based on ACFM employing a non-uniform B-spline approach," *Mechanical Systems and Signal Processing*, vol. 40, pp. 605-617, 2013.

[94] G.L. Nicholson and C.L. Davis, "Modelling of the response of an ACFM sensor to rail and rail wheel RCF cracks," *NDT&E International*, vol. 46, pp. 107-114, 2012.

[95] M.P. Papaelias, C. Roberts, C.L. Davis, M. Lugg, and M. Smith, "Detection and quantification of rail contact fatigue cracks in rails using ACFM technology," *Insight-Non-Destructive Testing and Condition Monitoring*, vol. 50, pp. 364-368, 2008.

[96] H. Rowshandel, M.P. Papaelias, C. Roberts, and C. Davis, "Development of autonomous ACFM rail inspection techniques," *Insight-Non-Destructive Testing and Condition Monitoring*, vol. 53, pp. 85-89, 2011.

[97] G.L. Nicholson, H. Rowshandel, X.J. Hao, and C.L. Davis, "Measurement and modelling of ACFM response to multiple RCF cracks in rail and wheels," *Ironmaking & Steelmaking*, vol. 40, pp. 87-91, 2013.

[98] H. Rowshandel, G.L. Nicholson, J.L. Shen, and C.L. Davis, "Characterisation of clustered cracks using an ACFM sensor and application of an artificial neural network," *NDT&E International*, vol. 98, pp. 80-88, 2018.

[99] M. Lugg, and D. Topp, "Recent developments and applications of the ACFM inspection method and ACSM stress measurement method," In *Proceedings of ECNDT*, 2006. [Online]. Available: https://www.ndt.net/article/ecndt2006/doc/Tu.3.6.5.pdf.

[100] D. Topp and M.Smith, "Application of the ACFM inspection method to rail and rail vehicles," *Insight-Non-Destructive Testing and Condition Monitoring*, vol. 47, pp. 354-357, 2005.

[101] D.E. Bray, and R.K. Stanley, *Non-destructive evaluation: a tool in design, manufacturing, and service*, Florida: CRC Press, 1997, pp. 217.

[102] M. Kenzo, "Recent advancement of electromagnetic non-destructive inspection technology in Japan," *IEEE Transactions on magnetics*, vol. 38, pp. 321-326, 2002.

[103] Y. Li, G.Y. Tian, and S. Ward, "Numerical simulation on magnetic flux leakage evaluation at high speed," *NDT&E International*, vol. 39, pp. 367-373, 2006.

[104] S. Mandayam, L. Udpa, S.S. Udpa, and W. Lord, "Invariance transformations for magnetic flux leakage signals," *IEEE Transactions on magnetics*, vol. 32, pp. 1577-1580, 1996.

[105] A. Khodayari-Rostamabad, J.P. Reilly, N.K. Nikolova, J.R. Hare, and S. Pasha, "Machine learning techniques for the analysis of magnetic flux leakage images in pipeline inspection," *IEEE Transactions on magnetics*, vol. 45, pp. 3073-3084, 2009.

[106] Z.D. Wang, Y. Gu, and Y.S. Wang, "A review of three magnetic NDT technologies," *Journal of Magnetism and Magnetic Materials*, vol. 324, pp. 382-388, 2012.

[107] A.G. Antipov and A.A. Markov, "3D simulation and experiment on high speed rail MFL inspection," *NDT&E International*, vol. 98, pp. 177-185, 2018.

[108] P. Boyacioglu, A. Bevan, and A. Vickerstaff, "Use of NDT Inspection Data to Improve Rail Damage Prediction Models," In *8th International Conference on Railway Engineering*, 2018, pp. 1-6.

[109] A.G. Antipov and A.A. Markov, "Evaluation of transverse cracks detection depth in MFL rail NDT," *Russian Journal of Nondestructive Testing*, vol. 50, pp. 481-490, 2014.

[110] M. Naeimi, Z. Li, Z. Qian, Y. Zhou, J. Wu, R.H. Petrov, J. Sietsma, and R. Dollevoet, "Reconstruction of the rolling contact fatigue cracks in rails using X-ray computed tomography," *NDT&E International*, vol. 92, pp. 199-212, 2017.

[111] C. Jessop, J. Ahlström, L. Hammar, S. Fæster, and H.K. Danielsen, "3D characterisation of rolling contact fatigue crack networks," *Wear*, vol. 366, pp. 392-400, 2016.

[112] Y. Zhou, X. Zheng, J. Jiang, and D. Kuang, "Modeling of rail head checks by X-ray computed tomography scan technology," *International Journal of Fatigue*, vol. 100, pp. 21-31, 2017.

[113] T. Makino, Y. Neishi, D. Shiozawa, S. Kikuchi, S. Okada, K. Kajiwara, and Y. Nakai, "Effect of defect shape on rolling contact fatigue crack initiation and propagation in high strength steel," *International Journal of Fatigue*, vol. 92, pp. 507-516, 2016.

[114] S. Dhar, H.K. Danielsen, S. Fæster, C.J. Rasmussen, and D.J. Jensen, "2D and 3D characterization of rolling contact fatigue cracks in manganese steel wing rails from a crossing," *Wear*, vol. 436, p. 202959, 2019.

[115] C.J. Rasmussen, S. Fæster, S. Dhar, J.V. Quaade, M. Bini, and H.K. Danielsen, "Surface crack formation on rails at grinding induced martensite white etching layers," *Wear*, vol. 384, pp. 8-14, 2017.

[116] J. Kelleher, M.B. Prime, D. Buttle, P.M. Mummery, P.J. Webster, J. Shackleton, and P.J. Withers, "The measurement of residual stress in railway rails by diffraction and other methods," *Journal of Neutron Research*, vol. 11, pp. 187-193, 2003.

[117] M.E. Turan, F. Aydin, Y. Sun, and M. Cetin, "Residual stress measurement by strain gauge and X-ray diffraction method in different shaped rails," *Engineering Failure Analysis*, vol. 96, pp. 525-529, 2019.

[118] T. Sasaki, S. Takahashi, Y. Kanematsu, Y. Satoh, K. Iwafuchi, M. Ishida, and Y. Morii, "Measurement of residual stresses in rails by neutron diffraction," *Wear*, vol. 265, pp. 1402-1407, 2008.

[119] R. Clark and S. Singh, "The inspection of thermite welds in railroad rail-a perennial problem," *Insight-Non-Destructive Testing and Condition Monitoring*, vol. 45, pp. 387-393, 2003.

[120] X. Gibert, V.M. Patel, and R. Chellappa, "Deep multitask learning for railway track inspection," *IEEE Transactions on Intelligent Transportation Systems*, vol. 18, pp. 153-164, 2016.

[121] C. Alippi, E. Casagrande, F. Scotti, and V. Piuri, "Composite real-time image processing for railways track profile measurement," *IEEE Transactions on instrumentation and measurement*, vol. 49, pp. 559-564, 2000.

[122] M. Guerrieri, G. Parla, and D. Ticali, "Mono and stereoscopic image analysis for detecting the transverse profile of worn-out rails," *Procedia-Social and Behavioral Sciences*, vol. 53, pp. 611-621, 2012.

[123] F. Marino, A. Distante, P.L. Mazzeo, and E. Stella, "A real-time visual inspection system for railway maintenance: automatic hexagonal-headed bolts detection," *IEEE Transactions on Systems, Man, and Cybernetics, Part C*, vol. 37, pp. 418-428, 2007.

[124] E. Stella, P. Mazzeo, M. Nitti, G. Cicirelli, A. Distante, and T. D'Orazio, "Visual recognition of missing fastening elements for railroad maintenance," In *Proceedings of the IEEE-ITSC International Conference on Intelligent Transportation systems*, 2002, pp. 94-99.

[125] P. Mazzeo, M. Nitti, E. Stella, and A. Distante, "Visual recognition of fastening bolts for railroad maintenance," *Pattern recognition letters*, vol. 25, pp. 669-677, 2004.

[126] M. Singh, S. Singh, J. Jaiswal, and J. Hempshall, "Autonomous rail track inspection using vision based system," In *IEEE International Conference on Computational Intelligence for Homeland Security and Personal Safety*, 2006, pp. 56-59.

[127] S. Faghih-Roohi, S. Hajizadeh, A. Núñez, R. Babuska, and B. De Schutter, "Deep convolutional neural networks for detection of rail surface defects," In *International joint conference on neural networks*, 2016, pp. 2584-2589.

[128] M.F. Hashmi and A.G. Keskar, "Computer-vision based visual inspection and crack detection of railroad tracks," *Recent Advances in Electrical and Computer Engineering*, pp. 102-110, 2014.

[129] L. Jie, L. Siwei, L. Qingyong, Z. Hanqing, and R. Shengwei, "Real-time rail head surface defect detection: A geometrical approach," In *IEEE International Symposium on Industrial Electronics*, 2009, pp. 769-774.

[130] The MERMEC track inspection system, Available: www.mermecgroup.com.

[131] E.E. Magel and K. Sawley, "Rail Surface Condition Alert-stage 1: Evaluation and calibration of surface crack measuring devices," Centre for Transportation Technology, National Research Council, Canada, 2006.

[132] E. Deutschl, C. Gasser, A. Niel, and J. Werschonig, "Defect detection on rail surfaces by a vision based system," In *IEEE Intelligent Vehicles Symposium*, 2004, pp. 507-511.

[133] R.A. Osornio-Rios, J.A. Antonino-Daviu, and R. de Jesus Romero-Troncoso, "Recent Industrial Applications of Infrared Thermography: A Review," *IEEE Transactions on Industrial Informatic*s, vol. 15, pp. 615-625, 2018.

[134] C. Meola, "Infrared thermography of masonry structures," *Infrared physics & technology*, vol. 49, pp. 228-233, 2007.

[135] M. Manana, A. Arroyo, A. Ortiz, C.J. Renedo, S. Perez, and F. Delgado, "Field winding fault diagnosis in DC motors during manufacturing using thermal monitoring," *Applied Thermal Engineering*, vol. 31, pp. 978-983, 2011.

[136] S. Stipetic, M. Kovacic, Z. Hanic, and M. Vrazic, "Measurement of excitation winding temperature on synchronous generator in rotation using infrared thermography," *IEEE Transactions on Industrial Electronics*, vol. 59, pp. 2288-2298, 2012.

[137] A.N. Huda and S. Taib, "Application of infrared thermography for predictive/preventive maintenance of thermal defect in electrical equipment," *Applied Thermal Engineering*, vol. 61, pp. 220-227, 2013.

[138] Y. Hu, W. Cao, J. Ma, S.J. Finney, and D. Li, "Identifying PV module mismatch faults by a thermography-based temperature distribution analysis," *IEEE Transactions on Device and Materials Reliability*, vol. 14, pp. 951-960, 2014.

[139] D.B. Durocher and D. Loucks, "Infrared windows applied in switchgear assemblies: Taking another look," *IEEE Transactions on Industry Applications*, vol. 51, pp. 4868-4873, 2015.

[140] X.P. Maldague, "Introduction to NDT by active infrared thermography," *Materials Evaluation*, vol. 60, pp. 1060-1073, 2002.

[141] R. Usamentiaga, Y. Mokhtari, C. Ibarra-Castanedo, M. Klein, M. Genest, and X.P. Maldague, "Automated Dynamic Inspection Using Active Infrared Thermography," *IEEE Transactions on Industrial Informatics*, vol. 14, pp. 5648-5657, 2018.

[142] S. Doshvarpassand, C. Wu, and X. Wang, "An overview of corrosion defect characterisation using active infrared thermography," *Infrared Physics & Technology*, vol. 96, pp. 366-389, 2018.

[143] Y.Y. Hung, Y.S. Chen, S.P. Ng, L. Liu, Y.H. Huang, B.L. Luk, R.W.L. Ip, C.M.L. Wu, and P.S. Chung, "Review and comparison of shearography and active thermography for nondestructive evaluation," *Materials Science and Engineering: R: Reports*, vol. 64, pp. 73-112, 2009.

[144] C. Ibarra-Castanedo, J.M. Piau, S. Guilbert, N.P. Avdelidis, M. Genest, A. Bendada, and X.P. Maldague, "Comparative study of active thermography techniques for the nondestructive evaluation of honeycomb structures," *Research in Nondestructive Evaluation*, vol. 20, pp. 1-31, 2009.

[145] B.B. Lahiri, S. Bagavathiappan, P.R. Reshmi, J. Philip, T. Jayakumar, and B. Raj, "Quantification of defects in composites and rubber materials using active thermography," *Infrared Physics & Technology*, vol. 55, pp. 191-199, 2012.

[146] S.K. Lau, D.P. Almond, and J.M. Milne, "A quantitative analysis of pulsed video thermography," *NDT&E International*, vol. 24, pp. 195-202, 1991.

[147] X.P. Maldague, F. Galmiche, and A. Ziadi, "Advances in pulsed phase thermography," *Infrared physics & technology*, vol. 43, pp. 175-181, 2002.

[148] S.M. Shepard, "Advances in pulsed thermography," In *Thermosense XXIII*, 2001, pp. 511-515.

[149] A. Sirikham, Y. Zhao, H.Y. Nezhad, W. Du, and R. Roy, "Estimation of Damage Thickness in Fiber-Reinforced Composites using Pulsed Thermography," *IEEE Transactions on Industrial Informatics*, vol. 15, pp. 445-453, 2018.

[150] Y. Zhao, S. Addepalli, A. Sirikham, and R. Roy, "A confidence map based damage assessment approach using pulsed thermographic inspection," *NDT&E International*, vol. 93, pp. 86-97, 2018.

[151] A. Sirikham, Y. Zhao, and J. Mehnen, "Determination of thermal wave reflection coefficient to better estimate defect depth using pulsed thermography," *Infrared Physics & Technology*, vol. 86, pp. 1-10, 2017.

[152] Y. Zhao, J. Mehnen, A. Sirikham, and R. Roy, "A novel defect depth measurement method based on Nonlinear System Identification for pulsed thermographic inspection," *Mechanical Systems and Signal Processing*, vol. 85, pp. 382-395, 2017.

[153] D.P. Almond, S.L. Angioni, and S.G. Pickering, "Long pulse excitation thermographic non-destructive evaluation," *NDT&E International*, vol. 87, pp. 7-14, 2017.

[154] V. Vavilov, T. Kauppinen, and E. Grinzato, "Thermal characterisation of defects in building envelopes using long square pulse and slow thermal wave techniques," *Journal of Research in Nondestructive Evaluation*," vol. 9, pp. 181-200, 1997.

[155] Z. Wang, G.Y. Tian, M. Meo, and F. Ciampa, "Image processing based quantitative damage evaluation in composites with long pulse thermography," *NDT&E International*, vol. 99, pp. 93-104, 2018.

[156] S.G. Pickering, “LED optical excitation for the long pulse and lock-in thermographic techniques,” *NDT&E International*, vol. 58, pp. 72-77, 2013.

[157] D. Wu and G. Busse, “Lock-in thermography for nondestructive evaluation of materials,” *Revue générale de thermique*, vol.37, pp. 693-703, 1998.

[158] G. Busse, D. Wu, and W. Karpen, “Thermal wave imaging with phase sensitive modulated thermography,” *Journal of Applied Physics*, vol. 71, pp. 3962-3965, 1992.

[159] J. Rantala, D. Wu, and G. Busse, “Amplitude-modulated lock-in vibrothermography for NDE of polymers and composites,” *Research in Nondestructive Evaluation*, vol. 7, pp. 215-228, 1996.

[160] N. Rajic and C. Antolis, “An investigation of noise performance in optical lock-in thermography,” *Infrared Physics & Technology*, vol. 87, pp. 1-10, 2017.

[161] P. Daryabor and M.S. Safizadeh, “Investigation of defect characteristics and heat transfer in step heating thermography of metal plates repaired with composite patches,” *Infrared Physics & Technology*, vol. 76, pp. 608-620, 2016.

[162] J.M. Roche and D.L. Balageas, “Common tools for quantitative pulse and step-heating thermography–part II: experimental investigation,” *Quantitative InfraRed Thermography Journal*, vol. 12, pp. 1-23, 2015.

[163] S. Grys, W. Minkina, and L. Vokorokos, “Automated characterisation of subsurface defects by active IR thermographic testing-Discussion of step heating duration and defect depth determination,” *Infrared Physics & Technology*, vol. 68, pp. 84-91, 2015.

[164] K. Ghadermazi, M.A. Khozeimeh, F. Taheri-Behrooz, and M.S. Safizadeh, “Delamination detection in glass-epoxy composites using step-phase thermography,” *Infrared Physics & Technology*, vol. 72, pp. 204-209, 2015.

[165] S. Laureti, S. Sfarra, H. Malekmohammadi, P. Burrascano, D.A. Hutchins, L. Senni, G. Silipigni, X.P. Maldague, and M. Ricci, “The use of pulse-compression thermography for detecting defects in paintings,” *NDT&E International*, vol. 98, pp. 147-154, 2018.

[166] S. Laureti, G. Silipigni, L. Senni, R. Tomasello, P. Burrascano, and M. Ricci, “Comparative study between linear and non-linear frequency-modulated pulse-compression thermography,” *Applied Optics*, vol. 57, pp. D32-D39, 2018.

[167] K. Chatterjee, D. Roy, and S. Tuli, “A novel pulse compression algorithm for frequency modulated active thermography using band-pass filter,” *Infrared Physics & Technology*, vol. 82, pp. 75-84, 2017.

[168] G. Silipigni, P. Burrascano, D.A. Hutchins, S. Laureti, R. Petrucci, L. Senni, L. Torre, and M. Ricci, “Optimization of the pulse-compression technique applied to the infrared thermography nondestructive evaluation,” *NDT&E International*, vol. 87, pp. 100-110, 2017.

[169] W.J. Parker, R.J. Jenkins, C.P. Butler, and G.L. Abbott, “Flash method of determining thermal diffusivity, heat capacity, and thermal conductivity,” *Journal of applied physics*, vol. 32, pp. 1679-1684, 1961.

[170] V. Vavilov, E. Grinzato, P.G. Bison, S. Marinetti, and M.J. Bales, “Surface transient temperature inversion for hidden corrosion characterisation: theory and applications,” *International journal of heat and mass transfer*, vol. 39, pp. 355-371, 1996.

[171] Y. Li, W. Zhang, Z.W. Yang, J.Y. Zhang, and S.J. Tao, “Low-velocity impact damage characterisation of carbon fiber reinforced polymer (CFRP) using infrared thermography,” *Infrared Physics & Technology*, vol. 76, pp. 91-102, 2016.

[172] V. Vavilov, A. Chulkov, A. Smotrov, S. Smotrova, and A. Moskovchenko, “Characterizing impact damage in GFRP/CFRP composites by determining thermal effusivity/diffusivity,” *Measurement Science and Technology*, vol. 30, p. 034003, 2019.

[173] Y. Zhao, L. Tinsley, S. Addepalli, J. Mehnen, and R. Roy, “A coefficient clustering analysis for damage assessment of composites based on pulsed thermographic inspection,” *NDT&E International*, vol. 83, pp. 59-67, 2016.

[174] C. Ibarra-Castanedo, N.P. Avdelidis, E.G. Grinzato, P.G. Bison, S. Marinetti, C.C. Plescanu, A. Bendada, and X.P. Maldague, “Delamination detection and impact damage assessment of GLARE by active thermography,” *International Journal of Materials and Product Technology*, vol. 41, pp. 5-16, 2011.

[175] C. Bu, Q. Tang, J. Liu, and Y. Wang, “Inspection on CFRP sheet with subsurface defects using pulsed thermographic technique.” *Infrared Physics & Technology*, vol. 65, pp. 117-121, 2014.

[176] C. Maierhofer, M. Röllig, K. Ehrig, D. Meinel, and G. Céspedes-Gonzales, “Validation of flash thermography using computed tomography for characterizing

inhomogeneities and defects in CFRP structures," *Composites Part B: Engineering*, vol. 64, pp. 175-186, 2014.

[177] P.H. Shin, S.C. Webb, and K.J. Peters, "Pulsed phase thermography imaging of fatigue-loaded composite adhesively bonded joints," *NDT&E International*, vol. 79, pp. 7-16, 2016.

[178] N. Sharp, D. Adams, J. Caruthers, A. David, and M. Suchomel, "Lithium-ion battery electrode inspection using pulse thermography," *NDT&E International*, vol. 64, pp. 41-51, 2014.

[179] A. Manohar and F.L. di Scalea, "Determination of defect depth and size using virtual heat sources in pulsed infrared thermography," *Experimental Mechanics*, vol. 53, pp. 661-671, 2013.

[180] J. Schlichting, C. Maierhofer, and M. Kreutzbruck, "Crack sizing by laser excited thermography," *NDT&E International*, vol. 45, pp. 133-140, 2012.

[181] T. Li, D.P. Almond, and D.A.S. Rees, "Crack imaging by scanning pulsed laser spot thermography," *NDT&E International*, vol. 44, pp. 216-225, 2011.

[182] C. Pei, J. Qiu, H. Liu, and Z. Chen, "Simulation of surface cracks measurement in first walls by laser spot array thermography," *Fusion Engineering and Design*, vol. 109, pp. 1237-1241, 2016.

[183] X. Lu, Z. He, L. Su, M. Fan, F. Liu, G. Liao, and T. Shi, "Detection of Micro Solder Balls Using Active Thermography Technology and K-Means Algorithm," *IEEE Transactions on Industrial Informatics*, vol. 14, pp. 5620-5628, 2018.

[184] S. Kaiplavil and A. Mandelis, "Truncated-correlation photothermal coherence tomography for deep subsurface analysis," *Nature Photonics*, vol. 8, p. 635, 2014.

[185] Y.K. An, J. Yang, S. Hwang, and H. Sohn, "Line laser lock-in thermography for instantaneous imaging of cracks in semiconductor chips," *Optics and Lasers in Engineering*, vol. 73, pp. 128-136, 2015.

[186] J. Yang, S. Hwang, Y.K. An, K. Lee, and H. Sohn, "Multi-spot laser lock-in thermography for real-time imaging of cracks in semiconductor chips during a manufacturing process," *Journal of Materials Processing Technology*, vol. 229, pp. 94-101, 2016.

[187] P. Broberg, “Surface crack detection in welds using thermography,” *NDT&E International*, vol. 57, pp. 69-73, 2013.

[188] S.E. Burrows, S. Dixon, S.G. Pickering, T. Li, and D.P. Almond, “Thermographic detection of surface breaking defects using a scanning laser source,” *NDT&E International*, vol. 44, pp. 589-596, 2011.

[189] D. Cerniglia, and N. Montinaro, “Defect Detection in Additively Manufactured Components: Laser Ultrasound and Laser Thermography Comparison,” *Procedia Structural Integrity*, vol. 8, pp. 154-162, 2018.

[190] N. Montinaro, D. Cerniglia, and G. Pitarresi, “Detection and characterisation of disbonds on Fibre Metal Laminate hybrid composites by flying laser spot thermography,” *Composites Part B: Engineering*, vol. 108, pp. 164-173, 2017.

[191] J. Renshaw, J.C. Chen, S.D. Holland, and R.B. Thompson, “The sources of heat generation in vibrothermography,” *NDT&E International*, vol. 44, pp. 736-739, 2011.

[192] J. Liu, J. Gong, L. Qin, H. Wang, and Y. Wang, “Study of inspection on metal sheet with subsurface defects using linear frequency modulated ultrasound excitation thermal-wave imaging (LFMUTWI),” *Infrared Physics & Technology*, vol. 62, pp. 136-142, 2014.

[193] X. Guo and V. Vavilov, “Crack detection in aluminum parts by using ultrasound-excited infrared thermography,” *Infrared Physics & Technology*, vol. 61, pp. 149-156, 2013.

[194] X. Guo and Y. Mao, “Defect identification based on parameter estimation of histogram in ultrasonic IR thermography,” *Mechanical Systems and Signal Processing*, vol. 58, pp. 218-227, 2015.

[195] Y. Jia, R.M. Zhang, W. Zhang, G.F. Jin, J.F. Liu, G. Tian, and Z.W. Yang, “Rapid Detection of Cracks in Turbine Blades Using Ultrasonic Infrared Thermography,” In *IOP Conference Series: Materials Science and Engineering*, 2018, p. 012023.

[196] Y. Li, G. Tian, Z.W. Yang, W.Y. Luo, W. Zhang, A.B. Ming, S.Q. Wu, and B.Q. Liu, “The use of vibrothermography for detecting and sizing low energy impact damage of CFRP laminate,” *Advanced Composites Letters*, vol. 26, pp. 162-167, 2017.

[197] G.P.M. Fierro, D. Ginzburg, F. Ciampa, and M. Meo, “Imaging of barely visible impact damage on a complex composite stiffened panel using a nonlinear ultrasound

stimulated thermography approach," *Journal of Nondestructive Evaluation*, vol. 36, p. 69, 2017.

[198] A. Gleiter, G. Riegert, T. Zweschper, and G. Busse, "Ultrasound lock-in thermography for advanced depth resolved defect selective imaging," In *9th European Conference on Non-Destructive Testing*, 2006. [Online]. Available: https://www.ndt.net/article/ecndt2006/doc/We.3.8.2.pdf.

[199] M. Matsushita-Tokugawa, J. Miura, Y. Iwami, T. Sakagami, Y. Izumi, N. Mori, M. Hayashi, S. Imazato, F. Takeshige, and S. Ebisu, "Detection of dentinal microcracks using infrared thermography," *Journal of endodontics*, vol. 39, pp. 88-91, 2013.

[200] T. Pahlberg, M. Thurley, D. Popovic, and O. Hagman, "Crack detection in oak flooring lamellae using ultrasound-excited thermography," *Infrared physics & technology*, vol. 88, pp. 57-69, 2018.

[201] J.S. Vaddi, S.D. Holland, and M.R. Kessler, "Absorptive viscoelastic coatings for full field vibration coverage measurement in vibrothermography," *NDT&E International*, vol. 82, pp. 56-61, 2016.

[202] M. Rahammer and M. Kreutzbruck, "Local defect resonance excitation thermography for damage detection in plastic composites," In *AIP Conference Proceeding*, 2019, p. 120004.

[203] J. Renshaw, S.D. Holland, R.B. Thompson, and J. Anderegg, "Vibration-induced tribological damage to fracture surfaces via vibrothermography," *International Journal of Fatigue*, vol. 33, pp. 849-857, 2011.

[204] S.A. Keo, F. Brachelet, F. Breaban, and D. Defer, "Steel detection in reinforced concrete wall by microwave infrared thermography," *NDT&E International*, vol. 62, pp. 172-177, 2014.

[205] A. Foudazi, C.A. Edwards, M.T. Ghasr, and K.M. Donnell, "Active microwave thermography for defect detection of CFRP-strengthened cement-based materials," *IEEE Transactions on Instrumentation and Measurement*, vol. 65, pp. 2612-2620, 2016.

[206] H. Zhang, R. Yang, Y. He, A. Foudazi, L. Cheng, and G.Y. Tian, "A review of microwave thermography nondestructive testing and evaluation," *Sensors*, vol. 17, p. 1123, 2017.

[207] B. Weekes, D.P. Almond, P. Cawley, and T. Barden, "Eddy-current induced thermography: probability of detection study of small fatigue cracks in steel, titanium and nickel-based superalloy," *NDT&E International*, vol. 49, pp. 47-56, 2012.

[208] B. Gao, X. Li, W.L. Woo, and G.Y. Tian, "Quantitative validation of Eddy current stimulated thermal features on surface crack," *NDT&E International*, vol. 85, pp. 1-12, 2017.

[209] X. Li, B. Gao, W.L. Woo, G.Y. Tian, X. Qiu, and L. Gu, "Quantitative Surface Crack Evaluation Based on Eddy Current Pulsed Thermography," *IEEE Sensors Journal*, vol. 17, pp. 412-421, 2017.

[210] J. Vrana, M. Goldammer, J. Baumann, M. Rothenfusser, and W. Arnold, "Mechanisms and models for crack detection with induction thermography," In *AIP conference Proceedings*, 2008, pp. 475-482.

[211] G. Zenzinger, J. Bamberg, W. Satzger, and V. Carl, "Thermographic crack detection by eddy current excitation," *Nondestructive Testing and Evaluation*, vol. 22, pp. 101-111, 2007.

[212] J. Wilson, G.Y. Tian, I.Z. Abidin, S. Yang, and D. Almond, "Pulsed eddy current thermography: system development and evaluation," *Insight-Non-Destructive Testing and Condition Monitoring*, vol. 52, pp. 87-90, 2010.

[213] D.P. Almond, B. Weekes, T. Li, S.G. Pickering, E. Kostson, J. Wilson, G.Y. Tian, S. Dixon, and S. Burrows, "Thermographic techniques for the detection of cracks in metallic components," *Insight-Non-Destructive Testing and Condition Monitoring*, vol. 53, pp. 614-620, 2011.

[214] Y. Gao, G.Y. Tian, P. Wang, H. Wang, B. Gao, W.L. Woo, and K. Li, "Electromagnetic pulsed thermography for natural cracks inspection," *Scientific Reports*, vol. 7, p. 42073, 2017.

[215] W. Ren, J. Liu, G.Y. Tian, B. Gao, L. Cheng, and H. Yang, "Quantitative non-destructive evaluation method for impact damage using eddy current pulsed thermography," *Composites Part B: Engineering*, vol. 54, pp. 169-179, 2013.

[216] T. Liang, W. Ren, G.Y. Tian, M. Elradi, and Y. Gao, "Low energy impact damage detection in CFRP using eddy current pulsed thermography," *Composite Structures*, vol. 143, pp. 352-361, 2016.

[217] Y. He, B. Du, and S. Huang, “Non-contact Electromagnetic Induction Excited Infrared Thermography for Photovoltaic Cells and Modules Inspection,” *IEEE Transactions on Industrial Informatics*, vol. 14, pp. 5585-5593, 2018.

[218] K. Li, G.Y. Tian, L. Cheng, A. Yin, W. Cao, and S. Crichton, “State detection of bond wires in IGBT modules using eddy current pulsed thermography,” *IEEE Transactions on Power Electronics*, vol. 29, pp. 5000-5009, 2014.

[219] H. Zhang, S. Sfarra, A. Osman, F. Sarasini, U. Netzelmann, S. Perilli, C. Ibarra-Castanedo, and X.P. Maldague, “Eddy current pulsed thermography for ballistic impact evaluation in basalt-carbon hybrid composite panels,” *Applied optics*, vol. 57, pp. 74-81, 2018.

[220] B. Gao, Y. He, W.L. Woo, G.Y. Tian, J. Liu, and Y. Hu, “Multidimensional tensor-based inductive thermography with multiple physical fields for offshore wind turbine gear inspection,” *IEEE Transactions on Industrial Electronics*, vol. 63, pp. 6305-6315, 2016.

[221] B. Oswald-Tranta and M. Sorger, “Detection of subsurface defects in aluminium with thermo-inductive inspection,” In *Thermosense: Thermal Infrared Applications XXXIII*, 2011, p. 801310.

[222] X. Li, B. Gao, Y. Zhu, W.L. Woo, G.Y. Tian, G. Tang, J. Li, and C. Sun, “Periodic Pulsed Thermography for Inner Defects Detection of Lead-Steel Bonded Structure,” *IEEE Sensors Journal*, vol. 18, pp. 4679-4688, 2018.

[223] C. Xu, N. Zhou, J. Xie, X. Gong, G. Chen, and G. Song, “Investigation on eddy current pulsed thermography to detect hidden cracks on corroded metal surface,” *NDT&E International*, vol. 84, pp. 27-35, 2016.

[224] P. Jäckel and U. Netzelmann, “The influence of external magnetic fields on crack contrast in magnetic steel detected by induction thermography,” *Quantitative InfraRed Thermography Journal*, vol. 10, pp. 237-247, 2013.

[225] Y. Wang, B. Gao, W.L. Woo, G.Y. Tian, X.P. Maldague, L. Zheng, Z. Guo, and Y. Zhu, “Thermal Pattern Contrast Diagnostic of Microcracks With Induction Thermography for Aircraft Braking Components,” *IEEE Transactions on Industrial Informatics*, vol. 14, pp. 5563-5574, 2018.

[226] Y. Wu, B. Gao, J. Zhao, Y. Wang, Z. Liu, J. Chen, Y. Ying, and G.Y. Tian, "Weld Crack Detection Based on Region Electromagnetic Sensing Thermography," *IEEE Sensors Journal*, vol. 19, pp. 751-762, 2018.

[227] R. Yang, Y. He, B. Gao, G.Y. Tian, and J. Peng, "Lateral heat conduction based eddy current thermography for detection of parallel cracks and rail tread oblique cracks," *Measurement*, vol. 66, pp. 54-61, 2015.

[228] J. Schlobohm, O. Bruchwald, W. Frąckowiak, Y. Li, M. Kästner, A. Pösch, W. Reimche, H.J. Maier, and E. Reithmeier, "Advanced characterisation techniques for turbine blade wear and damage," *Procedia CIRP*, vol. 59, pp. 83-88, 2017.

[229] D.K. Cheng, *Field and wave electromagnetics*. Beijing: Pearson Education Asia Ltd. and Tsinghua University Press, 2006.

[230] A. Rogalski, *Infrared detectors*, Florida: CRC Press, 2010, pp. 27.

[231] M. Vollmer and K.P. Möllmann, *Infrared thermal imaging: fundamentals, research and applications*, Weinheim: Wiley-VCH, 2018, pp. 107.

[232] P.W. Kruse. *Uncooled thermal imaging: arrays, systems, and applications*. Washington: SPIE Press, 2001, pp. 1.

[233] A. P. Berens, "NDE reliability data analysis," in *ASM Handbook*, Ohio: ASM International, 1989.

[234] W.D. Rummel, "Recommended practice for a demonstration of NDE reliability on aircraft production parts," *Materials Evaluation*, vol. 40, 1982, pp. 922-932.

[235] J.C. Aldrin, E.A. Medina, D.A. Allwine, M. QadeerAhmed, J. Fisher, J.S. Knopp, and E.A. Lindgren, "Probabilistic risk assessment: impact of human factors on NDE and sensor degradation on structural health monitoring," in *AIP Conference Proceedings*, 2007, pp. 1461-1468.

[236] *Nondestructive Evaluation System Reliability Assessment*, MIL-HDBK-1823, Department of Defense, U.S., 2007. [Online]. Available: https://statistical-engineering.com/wp-content/uploads/2017/10/MIL-HDBK-1823A2009.pdf.

[237] J. Berkson, "Why I prefer logits to probits," *Biometrics*, vol. 7, pp. 327-339, 1951.

[238] R.V. Hogg, J. McKean, and A.T. Craig, *Introduction to mathematical statistics*. Boston: Pearson Education, 2019, pp. 355-356.

[239] R.C. Cheng and T.C. Lies, "One-sided confidence bands for cumulative distribution functions," *Technometrics*, vol. 30, pp. 155-159, 1988.

[240] R.C. Cheng and T.C. Iles, "Confidence bands for cumulative distribution functions of continuous random variables," *Technometrics*, vol. 25, pp. 77-86, 1983.

[241] M. Glasser, "Regression analysis with dependent variable censored," *Biometrics*, pp. 300-307, 1965.

[242] A.V. Oppenheim and R.W. Schafer, *Discrete-Time Signal Processing*. New Jersey: Pearson Education, 2010, pp. 370-371.

[243] N. Rajic, "Principal component thermography for flaw contrast enhancement and flaw depth characterisation in composite structures," *Composite Structures*, vol. 58, pp. 521-528, 2002.

[244] S. Marinetti, E. Grinzato, P.G. Bison, E. Bozzi, M. Chimenti, G. Pieri, and O. Salvetti, "Statistical analysis of IR thermographic sequences by PCA," *Infrared Physics & Technology*, vol. 46, pp. 85-91, 2004.

[245] R. Collins, "The development of the ACPD and ACFM techniques at UCL," *Nondestructive Testing of Materials*, vol. 8, pp. 65-74, 1995.

[246] J.E. Garnham, D.I. Fletcher, C.L. Davis, and F.J. Franklin, "Visualization and modelling to understand rail rolling contact fatigue cracks in three dimensions," *Proceedings of the Institution of Mechanical Engineers, Part F: Journal of Rail and Rapid Transit*, vol. 225, pp. 165-178, 2011.

[247] I.Z. Abidin, G.Y. Tian, J. Wilson, S. Yang, and D. Almond, "Quantitative evaluation of angular defects by pulsed eddy current thermography," *NDT&E International*, vol. 43, pp. 537-546, 2010.

[248] G.L. Nicholson, A.G. Kostryzhev, X.J. Hao, and C.L. Davis, "Modelling and experimental measurements of idealised and light-moderate RCF cracks in rails using an ACFM sensor," *NDT&E International*, vol. 44, pp. 427-437, 2011.

[249] J. Peng, G.Y. Tian, L. Wang, Y. Zhang, K. Li, and X. Gao, "Investigation into eddy current pulsed thermography for rolling contact fatigue detection and characterization," *NDT&E International*, vol. 74, pp. 72-80, 2015.

[250] H.C. Eden, J.E. Garnham, and C.L. Davis, “Influential microstructural changes on rolling contact fatigue crack initiation in pearlitic rail steels,” *Materials science and technology*, vol. 21, pp. 623-629, 2005.

[251] B. Gao, W.L. Woo, Y. He, and G.Y. Tian, “Unsupervised sparse pattern diagnostic of defects with inductive thermography imaging system,” *IEEE Transactions on Industrial Informatics*, vol. 12, pp. 371-383, 2015.

[252] T. Kohler, M. Beyeler, D. Webster, and R. Müller, “Compartmental bone morphometry in the mouse femur: reproducibility and resolution dependence of microtomographic measurements,” *Calcified Tissue International*, vol. 77, pp. 281-290, 2005.

[253] M. Faifer, R. Ottoboni, S. Toscani, and L. Ferrara, “Nondestructive testing of steel-fiber-reinforced concrete using a magnetic approach,” *IEEE Transactions on Instrumentation and Measurement*, vol. 60, pp.1709-1717, 2010.

[254] B. Yan, D. Kennedy, R.L. Miller, J.P. Cowin, K.H. Jung, M. Perzanowski, M. Balletta, F.P. Perera, P.L. Kinney, and S.N. Chillrud, “Validating a nondestructive optical method for apportioning colored particulate matter into black carbon and additional components,” *Atmospheric Environment*, vol. 45, pp.7478-7486, 2011.

[255] L. Ferrara, M. Faifer, and S. Toscani, “A magnetic method for non destructive monitoring of fiber dispersion and orientation in steel fiber reinforced cementitious composites-part 1: method calibration,” *Materials and Structures*, vol. 45, pp. 575-589, 2012.

[256] G. Villain, Z.M. Sbartaï, X. Dérobert, V. Garnier, and J.P. Balayssac, “Durability diagnosis of a concrete structure in a tidal zone by combining NDT methods: laboratory tests and case study,” *Construction and Building Materials*, vol. 37, pp.893-903, 2012.

[257] F. Liu, J. Zhu, G.Y. Tian, C. Ulianov, and Z. Wang, “Investigations for inclination angle characterization of angular defects using eddy current pulsed thermography,” *Infrared Physics & Technology*, vol. 100, pp. 73-81, 2019.

[258] W.J. Wang, R. Lewis, B. Yang, L.C. Guo, Q.Y. Liu, and M.H. Zhu, “Wear and damage transitions of wheel and rail materials under various contact conditions,” *Wear*, vol. 362, pp.146-152, 2016.

[259] A.F. Frangi, W.J. Niessen, K.L. Vincken, and M.A. Viergever, "Multiscale vessel enhancement filtering," In *International conference on medical image computing and computer-assisted intervention*, 1998, pp. 130-137.

[260] P. Calmon, "Trends and stakes of NDT simulation," *Journal of Nondestructive Evaluation*, vol. 31, pp. 339-341, 2012.

[261] L.L. Gratiet, B. Iooss, G. Blatman, T. Browne, S. Cordeiro, and B. Goursaud, "Model assisted probability of detection curves: New statistical tools and progressive methodology," *Journal of Nondestructive Evaluation*, vol. 36, p. 8, 2017.

[262] G. Ribay, X. Artusi, F. Jenson, C. Reece, and P.E. Lhuillier, "Model-based POD study of manual ultrasound inspection and sensitivity analysis using metamodel," In *AIP Conference Proceedings*, 2016, p. 200006.

[263] A. Rosell and G. Persson, "Model based capability assessment of an automated eddy current inspection procedure on flat surfaces," *Research in Nondestructive Evaluation*, vol. 24, pp. 154-176, 2013.

[264] R. Jarvis, P. Cawley, and P.B. Nagy, "Performance evaluation of a magnetic field measurement NDE technique using a model assisted Probability of Detection framework," *NDT&E International*, vol. 91, pp. 61-70, 2017.

[265] B.A. Zouraq, H.K. Bui, A. Peterzol, G. Wasselynck, G. Berthiau, D. Trichet, and M. Taglione, "A Model-Assisted Probability of Detection Study on Induction Thermography Technique," *IEEE Transactions on Magnetics*, vol. 55, pp. 1-4, 2019.

[266] J. Wu, J. Zhu, H. Xia, C. Liu, X. Huang, and G.Y. Tian, "DC-biased Magnetization Based Eddy Current Thermography for Subsurface Defect Detection," *IEEE Transactions on Industrial Informatics*, vol. 15, pp. 6252-6259, 2019.